

# Synthesis of Cyanine Polyelectrolytes and Anions for Organic Electronic Devices

THÈSE N° 7478 (2017)

PRÉSENTÉE LE 9 FÉVRIER 2017

À LA FACULTÉ DES SCIENCES ET TECHNIQUES DE L'INGÉNIEUR  
UNITÉ DE RATTACHEMENT POUR SCIENTIFIQUES IMX  
PROGRAMME DOCTORAL EN CHIMIE ET GÉNIE CHIMIQUE

ÉCOLE POLYTECHNIQUE FÉDÉRALE DE LAUSANNE

POUR L'OBTENTION DU GRADE DE DOCTEUR ÈS SCIENCES

PAR

Lei WANG

acceptée sur proposition du jury:

Prof. J.-E. Moser, président du jury  
Prof. F. Nüesch, Prof. C. R. Hinderling, directeurs de thèse  
Prof. E. Constable, rapporteur  
Dr F. Castro, rapporteur  
Prof. K. Sivula, rapporteur



ÉCOLE POLYTECHNIQUE  
FÉDÉRALE DE LAUSANNE

Suisse  
2017



## Zusammenfassung

In den letzten Jahrzehnten wurden zahlreiche praktische Anwendungen von organischen elektronischen Bauelementen gezeigt. Aufgrund des Potenzials einer kostengünstigen Herstellung, ausgezeichneter Leistung und vielseitiger Funktionalitäten wie Flexibilität, Portabilität und Transparenz, werden sie als vielversprechende Alternativen zu anorganischen Halbleitertechnologien angesehen. In dieser Arbeit konzentrierte ich mich vor allem auf die Untersuchung einer speziellen Klasse organischer Halbleiter, Cyanin-Farbstoffen. Beginnend mit der Synthese von Cyaninpolyelektrolyten (Cy-Poly) und neuen Anionen wurden neue Funktionalitäten wie orthogonale Löslichkeit, Vernetzungsfähigkeit und Photosensibilisierungsfähigkeit eingeführt und die entsprechenden Materialien als aktive Komponenten in organischen elektronischen Bauelementen untersucht. Die Verwendung von Cyaninsalzen ermöglicht ein gemischtes ionisches/elektronisches Leitvermögen in festen organischen halbleitenden Dünnschichten. Aufgrund der Anwesenheit von mobilen Anionen und ihrer Beförderung zu den jeweiligen Metallelektroden wird ein Ionenübergang erzeugt. Dies führt zu einer elektrochemischen Oxidation und Reduktion innerhalb des organischen Dünnschichtfilms und zum Aufbau eines eingebauten elektrischen Feldes im intrinsischen Bereich mit Veränderung der potentiellen Energie. Die elektronische Leitfähigkeit wird in den dotierten Zonen erheblich verbessert, was die Ladungsinjektion an den Elektroden erleichtert. Der bemerkenswerte Potentialabfall im Übergangsbereich ermöglicht die Lichtemission der elektrolumineszenten Materialien sowie einen photovoltaischen Effekt bei der Beleuchtung mit weißem Licht. Ein besonderes Interesse galt der Stabilisierung ionischer Verbindungen in organischen elektronischen Bauelementen aus Cyanin-Farbstoffen, durch chemische Fixierung der ionischen Träger in der gewünschten Position. In den Bauteilen, welche die immobilisierbaren Phenylazid-Anionen enthalten, wurde ein unerwartetes Exiton-Quenching-Verhalten beobachtet, das der Triplet Sensibilisierung von Trimethincyaninen auf die Photodekomposition von 4-Azidobenzoat-Ionen zugeschrieben wurde.

**Stichwörter:** organische Photovoltaik, lichtemittierende elektrochemische Zelle, Photoleitfähigkeit, Triplet Photosensibilisator, Cyanin-Farbstoff, Phenylazid

## Abstract

Many practical applications among organic electronic devices have been demonstrated over the last decades. They are considered as promising alternatives to inorganic semiconductor technologies due to the potential of cost-effective fabrication, excellent performance and versatile functionalities such as flexibility, portability and transparency. In this work, I mainly focused on the investigation of a special class of organic semiconductors, cyanine dyes. Starting with the synthesis of cyanine polyelectrolytes (Cy-Poly) and novel anions, new functionalities such as orthogonal solubility, crosslinking capability and photosensitizing ability were introduced and the corresponding materials as active components in organic electronic devices were explored. The utilization of cyanines allows for the mixed ionic/electronic conduction in solid organic semiconducting thin films. Due to the presence of mobile anions, an ionic junction is created as a result of the ionic motion towards respective metal electrodes. This leads to electrochemical oxidation and reduction within the organic thin film and the establishment of a built-in electric field across the intrinsic region with potential energy shifts. The electronic conductivity is considerably enhanced in the doped zones, which facilitates charge injection from the electrodes. The remarkable potential drop in the intrinsic region enables light emission of the electroluminescent materials as well as a photovoltaic response upon white light illumination. A special interest was given to the stabilization of ionic junctions in cyanine dye organic electronic devices by chemically fixing the ionic carriers in the desired position. Unexpected exciton quenching behavior was observed in the devices containing the immobilizable phenyl azide anions, which was attributed to the triplet sensitization effect of trimethine cyanines on the photodecomposition of 4-azido benzoate ions.

**Keywords:** organic photovoltaics, light-emitting electrochemical cells, photoconductivity, triplet photosensitizer, cyanine dye, phenyl azides

## Acknowledgements

I had a great honor to spend four years, which took one seventh of my life up to now, to pursue a PhD degree in this fantastic country Switzerland. (Un)fortunately this is going to come to an end. Before saying goodbye to everything here, I take this excellent opportunity to acknowledge all the people that have been involved in my life within this period.

To start with, I would like to acknowledge my supervisor, Prof. Frank Nüesch, for accepting me as his PhD student, which initiated the whole story. He is always very kind and nice, and with a bit sense of humor. He regularly gives important scientific inputs during the group meetings and tries to offer key advice on my PhD project. Although he is quite busy, he is able to balance his efforts and offer opportunities to each student. It is a great pleasure for me to accomplish my study under his supervision.

I would like to extend my deep gratitude to my co-supervisor, Prof. Christian Hinderling. He looks very energetic all the time and always smiles to everybody. He provides me with a spacious laboratory and a nice office, and he contributes to my PhD project significantly with precious ideas and fruitful discussions. Also, many thanks are given to him again for offering me the opportunities to undertake responsibilities for AFM and some scientific tasks in addition to the PhD project.

Furthermore, I am very grateful to my group leader, Dr. Roland Hany. He is very patient and has an easy-going personal character. He predominantly guides my project with his solid knowledge and rich experience and constantly modifies the direction of my work with brilliant ideas to achieve our mutual goals.

I would also like to thank my mentor, Prof. Kevin Sivula, for several helpful scientific discussions and nice conversations in his office or during the workshops in the Swiss mountains.

Special thanks go to Prof. Andreas Lendlein (HZG, Germany), Prof. Manfred Wagner (TU Berlin, Germany) and Prof. Jin Xu (Xiamen University, China) for generously offering me recommendation letters, which were crucial for the successful enrollment at EPFL.

I heartfelt thank all my colleagues at Empa and ZHAW who helped me with their time and expertise, which considerably contributed to the success of my work. Particularly Dr. Jakob Heier for fluorescence, profilometry and AFM measurements, Dr. Hui Zhang for initially

## Acknowledgements

---

teaching me the fabrication and characterization of devices, Sandra Jenatsch for sharing the same SNF project and exploring the potential application of my dyes, Dr. Daniel Rentsch for NMR measurements, Dr. Mohammed Makha for lamination experiments and frequently transporting nitrogen tanks together with vital information exchange, Claudia Konrad and Fabian Deuber for their numerous little helps at the initial stage of my PhD, Beatrice Fischer for TGA, DSC, IR and GPC measurements, Dr. Peter Lienemann, Samuel Menzi and Jasmin Keist for XRF measurements, Dr. Sebastian Opitz for ESI-MS measurements, Dr. Dalin Wu, Dr. Manolis Tzirakis and Yongzen Tan for various chats about work, career and life during lunches and coffee breaks, Thibaud Fleurieau-Lintz for being the other chemist working with PFB anions besides me, Yeesong Ko, Simon Dünki, Anna Véron, Jean-Nicolas Tisserant, Jose Enrico Quinsaot, Chuyao Peng, Nicolas Leclaire, Donatas Gesevicius, Surendra Babu Anantharaman, Philip Caspari, Roland Steim and Anand Verma for many good moments together during everyday work and group events.

I also thank the numerous friends that I have met and worked with in ACSSZ and that I have played with during badminton, skiing and swimming. All these people and activities significantly enriched my experience, brought much joy to me and made my life in Switzerland truly colorful.

Last but not least, I must thank my wife, Yuting Zhang, for accompanying me in a foreign country. She understands me and believes in me. She spares no effort to take care of our little daughter, Ziyang Wang, without bothering me as far as possible. However, I feel quite sorry for them since I am very often not able to be with them during the evenings or over the weekends. Moreover, I feel shame that the first illness of my daughter in her life was because of me. So, be stronger, overcome various difficulties, WEILAIWOMENHUINIUBIDEBUDELIAO (translation: we have a bright future).

Yes, the end is here.

Lei Wang

Oct. 2016 in Dübendorf

## Table of Contents

Zusammenfassung .....	i
Abstract .....	ii
Acknowledgements .....	iii
Table of Contents .....	v
List of Figures .....	x
List of Schemes.....	xix
List of Tables.....	xx
Chapter 1: Introduction .....	1
1.1 Thesis Outline.....	1
1.2 Organic Electronics.....	3
1.2.1 Organic photovoltaic and electroluminescent devices .....	3
1.2.2 Synthesis and properties of organic semiconductors.....	8
1.3 Ionic Junctions .....	13
1.3.1 Mixed ionic/electronic conduction in organic materials.....	13
1.3.2 Dynamic junction in organic electronic devices.....	13
1.3.3 Attempts towards a fixed ionic junction .....	17
1.4 Phenyl Azides .....	24
1.4.1 Photo-induced decomposition and reaction .....	24
1.4.2 Application for nanostructure modification .....	30
1.5 References .....	33
Chapter 2: Synthesis of Cyanine Dyes and Polyelectrolytes.....	51
2.1 Introduction .....	51
2.2 Experimental.....	51
2.2.1 Materials and methods.....	51

## Table of Contents

---

2.2.2 Synthesis of Cy-Poly .....	52
2.2.3 Synthesis of Cy-FN3.....	54
2.2.4 Synthesis of Cy-N3.....	55
2.2.5 Synthesis of Cy-MES.....	56
2.2.6 Synthesis of Cy-PF6.....	56
2.3 Results and Discussion.....	57
2.3.1 Synthesis and characterization of Cy-Poly .....	57
2.3.2 Synthesis of perfluorophenyl azides.....	61
2.3.3 Anion exchange of cyanine dyes .....	62
2.4 Conclusions.....	66
2.5 References.....	67
2.6 Supporting Information.....	68
2.6.1 NMR characterization for Cy-Poly.....	68
2.6.2 NMR characterization for Cy-FN3 .....	82
2.6.3 NMR characterization for Cy-N3.....	92
2.6.4 NMR characterization for Cy-MES.....	96
2.6.5 NMR characterization for Cy-PF6 .....	101
Chapter 3: Cyanine Dye Light-emitting Electrochemical Cells .....	105
3.1 Introduction.....	105
3.2 Experimental.....	107
3.2.1 Materials and methods.....	107
3.2.2 Device fabrication and characterization.....	107
3.3 Results and Discussion.....	108
3.3.1 Determination of junction position and width .....	108
3.3.2 Photovoltaic effect of the p-i-n junction .....	113
3.3.3 Host-guest light-emitting electrochemical cells.....	117



## Table of Contents

---

3.4 Conclusions.....	119
3.5 References.....	120
3.6 Supporting Information.....	124
3.6.1 LECs with different Cy3-PF6 film thickness.....	124
3.6.2 Reversely biased Cy3-PF6 LECs.....	125
Chapter 4: Photoconductivity in Ionic Cyanine Films.....	126
4.1 Introduction.....	126
4.2 Experimental.....	127
4.2.1 Device fabrication.....	127
4.2.2 Methods.....	128
4.3 Results.....	129
4.4 Discussion.....	135
4.5 Conclusions.....	140
4.6 References.....	140
4.7 Supporting Information.....	142
Chapter 5: Visible-Light Induced Azide Decomposition in Trimethine Cyanine/Azido-Benzoate Films.....	145
5.1 Introduction.....	145
5.2 Experimental.....	147
5.2.1 Materials.....	147
5.2.2 Methods.....	148
5.3 Results.....	149
5.3.1 Decarboxylation of fluorobenzoate anion.....	149
5.3.2 Thermal stability of Cy-FN3 and Cy-N3 films.....	150
5.3.3 Visible light induced decomposition of phenyl azide.....	152
5.4 Discussion.....	153

## Table of Contents

---

5.4.1 Decarboxylation of 4-azido-2,3,5,6-tetrafluoro benzoate.....	153
5.4.2 Visible light sensitization of 4-azido benzoate.....	154
5.4.3 Photorelaxation of cyanine dyes.....	157
5.4.4 Photolysis of azides.....	159
5.4.5 Quenching of cyanine triplets by 4-azido benzoate .....	160
5.5 Conclusions.....	161
5.6 References.....	163
5.7 Supporting Information.....	167
5.7.1 NMR measurements of stored Cy3-FN3 film.....	167
5.7.2 ATR-IR measurements .....	169
5.7.3 Thermal stability of Cy3-N3 films at elevated temperatures.....	169
5.7.4 Effect of thermal evaporation .....	170
5.7.5 White light irradiation on Na-N3 and Cy3-N3 .....	171
Chapter 6: Cyanine Dye Polyelectrolytes for Organic Bilayer Heterojunction Solar Cells.....	173
6.1 Introduction .....	173
6.2 Experimental.....	175
6.2.1 Materials and methods.....	175
6.2.2 Solar cell fabrication and characterization .....	176
6.3 Results and Discussion.....	177
6.3.1 Characterization of Cy-Poly thin films .....	177
6.3.2 Cy-Poly/PCBM bilayer solar cells .....	178
6.3.3 Hole mobility measurement .....	183
6.4 Conclusions.....	185
6.5 References .....	185
6.6 Supporting Information.....	188
6.6.1 Absorption spectra and IPCE in the near-infrared wavelength region .....	188

## Table of Contents

---

6.6.2 Electronic and ionic charges in cyanine dyes.....	189
Chapter 7: Conclusions and Outlook .....	193
7.1 Conclusions.....	193
7.2 Outlook.....	195
Abbreviations and Symbols.....	197
Curriculum Vitae .....	203

---

## List of Figures

<b>Figure 1-1:</b> Schematic illustration of organic bilayer or BHJ devices.....	4
<b>Figure 1-2:</b> Schematic illustration of exciton dissociation process in a heterojunction solar cell. .....	5
<b>Figure 1-3:</b> Schematic illustration of a LEC with or without an external voltage. ....	6
<b>Figure 1-4:</b> J-V characteristics of a solar cell under dark (dotted line) or white light illuminated conditions (solid line). ....	7
<b>Figure 1-5:</b> Chemical structures of conducting polymers PANI, PPV and PT. ....	9
<b>Figure 1-6:</b> Chemical structures of small molecule organic semiconductors MePc, pentacene, BCP and C <sub>60</sub> . ....	10
<b>Figure 1-7:</b> Schematic illustration of (a) cationic CPEs and (b) anionic CPEs. ....	11
<b>Figure 1-8:</b> Typical absorbance spectra of Cy3, Cy5 and Cy7 thin films. ....	12
<b>Figure 1-9:</b> Schematic illustration of stabilization of ions by lowering the temperature. ....	17
<b>Figure 1-10:</b> Schematic illustration of stabilization of ions by polymerizing the ionic monomers. ....	20
<b>Figure 1-11:</b> Schematic illustration of stabilization of ions by curing the ionic conductors. ....	21
<b>Figure 1-12:</b> Schematic illustration of stabilization of ions by solvent-soaking under device charging. ....	22
<b>Figure 1-13:</b> Schematic illustration of stabilization of ions by ion diffusion after lamination. ....	23
<b>Figure 1-14:</b> Schematic illustration of singlet and triplet phenyl nitrenes. ....	24
<b>Figure 1-15:</b> Schematic illustration for direct photogeneration of phenyl nitrenes upon UV light irradiation. ....	25
<b>Figure 1-16:</b> Schematic illustration for triplet sensitized photolysis of phenyl azides, (TS: triplet sensitizer). ....	26
<b>Figure 1-17:</b> Simplified schemes for typical reactions of singlet and triplet phenyl nitrenes. ....	29
<b>Figure 1-18:</b> Simplified scheme for surface functionalization via direct binding of PFPAs. ....	31
<b>Figure 1-19:</b> Simplified schemes for surface functionalization with PFPAs by a two-step approach. ....	31

---

<b>Figure 1-20:</b> Chemical structures of photocrosslinkers bis(PFBA), sFPA, BABP and DAZH.....	32
<b>Figure 2-1:</b> $^1\text{H}$ NMR spectrum of Poly20 (DMSO- $d_6$ ).....	69
<b>Figure 2-2:</b> $^1\text{H}$ diffusion-edited NMR spectra of Poly20 (DMSO- $d_6$ ). .....	70
<b>Figure 2-3:</b> $^{13}\text{C}\{^1\text{H}\}$ NMR spectrum of Poly20 (DMSO- $d_6$ ). .....	70
<b>Figure 2-4:</b> HSQC and HMBC NMR spectra of Poly20 (DMSO- $d_6$ ).....	71
<b>Figure 2-5:</b> $^1\text{H}$ NMR spectrum of Poly30 (DMSO- $d_6$ ).....	71
<b>Figure 2-6:</b> $^1\text{H}$ diffusion-edited NMR spectra of Poly30 (DMSO- $d_6$ ). .....	72
<b>Figure 2-7:</b> $^1\text{H}$ NMR spectrum of Poly50 (DMSO- $d_6$ ).....	72
<b>Figure 2-8:</b> $^1\text{H}$ diffusion-edited NMR spectra of Poly50 (DMSO- $d_6$ ). .....	73
<b>Figure 2-9:</b> $^1\text{H}$ NMR spectrum of PEG25Poly50 (methanol- $d_4$ ).....	74
<b>Figure 2-10:</b> $^1\text{H}$ NMR spectrum of PEG50Poly50 (methanol- $d_4$ ).....	74
<b>Figure 2-11:</b> $^{13}\text{C}\{^1\text{H}\}$ NMR spectrum of PEG50Poly50 (methanol- $d_4$ ). .....	75
<b>Figure 2-12:</b> $^1\text{H}$ NMR spectrum of Cy5-Poly20 (methanol- $d_4$ ).....	76
<b>Figure 2-13:</b> HSQC and HMBC spectra of Cy5-Poly20 (methanol- $d_4$ ). .....	76
<b>Figure 2-14:</b> $^1\text{H}$ NMR spectrum of Cy5-Poly30 (methanol- $d_4$ ).....	77
<b>Figure 2-15:</b> $^1\text{H}$ NMR spectrum of Cy5-Poly50 (methanol- $d_4$ ).....	77
<b>Figure 2-16:</b> $^1\text{H}$ NMR spectrum of Cy3-Poly20 (methanol- $d_4$ ).....	79
<b>Figure 2-17:</b> $^1\text{H}$ diffusion-edited NMR spectra of Cy3-Poly20 (methanol- $d_4$ ). .....	79
<b>Figure 2-18:</b> $^{13}\text{C}\{^1\text{H}\}$ NMR spectrum of Cy3-Poly20 (methanol- $d_4$ ).....	80
<b>Figure 2-19:</b> $^1\text{H}$ NMR spectrum of Cy3-Poly30 (methanol- $d_4$ ).....	80
<b>Figure 2-20:</b> $^1\text{H}$ NMR spectrum of Cy3-Poly50 (methanol- $d_4$ ).....	81
<b>Figure 2-21:</b> $^1\text{H}$ NMR spectrum of Cy5-PEG25Poly50 (methanol- $d_4$ ).....	82
<b>Figure 2-22:</b> $^1\text{H}$ NMR spectrum of Cy5-PEG50Poly50 (methanol- $d_4$ ).....	82
<b>Figure 2-23:</b> $^1\text{H}$ NMR spectrum of methyl pentafluorobenzoate (1) (chloroform- $d$ ).....	83
<b>Figure 2-24:</b> $^{19}\text{F}$ NMR spectrum of methyl pentafluorobenzoate (1) (chloroform- $d$ ).....	83
<b>Figure 2-25:</b> $^{13}\text{C}$ NMR spectrum of methyl pentafluorobenzoate (1) (chloroform- $d$ ).....	84
<b>Figure 2-26:</b> $^1\text{H}$ NMR spectrum of methyl 4-azido-2,3,5,6-tetrafluorobenzoate (2) (chloroform- $d$ ).....	84

---

<b>Figure 2-27:</b> $^{19}\text{F}$ NMR spectrum of methyl 4-azido-2,3,5,6-tetrafluorobenzoate (2) (chloroform-d <sub>3</sub> ).....	85
<b>Figure 2-28:</b> $^{13}\text{C}$ NMR spectrum of methyl 4-azido-2,3,5,6-tetrafluorobenzoate (2) (chloroform-d <sub>3</sub> ).....	85
<b>Figure 2-29:</b> $^1\text{H}$ NMR spectrum of methyl 4-azido-2,3,5,6-tetrafluorobenzoic acid (3) (DMSO-d <sub>6</sub> ).....	86
<b>Figure 2-30:</b> $^{19}\text{F}$ NMR spectrum of methyl 4-azido-2,3,5,6-tetrafluorobenzoic acid (3) (DMSO-d <sub>6</sub> ).....	86
<b>Figure 2-31:</b> $^{13}\text{C}$ NMR spectrum of methyl 4-azido-2,3,5,6-tetrafluorobenzoic acid (3) (DMSO-d <sub>6</sub> ).....	86
<b>Figure 2-32:</b> $^1\text{H}$ NMR spectrum of TFP (methanol-d <sub>4</sub> ).....	87
<b>Figure 2-33:</b> $^{19}\text{F}$ NMR spectrum of TFP (methanol-d <sub>4</sub> ).....	87
<b>Figure 2-34:</b> $^1\text{H}$ NMR spectrum of Cy5-FN3 (with TFP) (methanol-d <sub>4</sub> ).....	88
<b>Figure 2-35:</b> $^{19}\text{F}$ NMR spectrum of Cy5-FN3 (with TFP) (methanol-d <sub>4</sub> ).....	89
<b>Figure 2-36:</b> $^{13}\text{C}$ NMR spectrum of Cy5-FN3 (methanol-d <sub>4</sub> ).....	89
<b>Figure 2-37:</b> $^1\text{H}$ NMR spectrum of Cy3-FN3 (with TFP) (methanol-d <sub>4</sub> ).....	90
<b>Figure 2-38:</b> $^{19}\text{F}$ NMR spectrum of Cy3-FN3 (with TFP) (methanol-d <sub>4</sub> ).....	90
<b>Figure 2-39:</b> $^{13}\text{C}$ NMR spectrum of Cy3-FN3 (methanol-d <sub>4</sub> ).....	91
<b>Figure 2-40:</b> $^1\text{H}$ NMR spectrum of Cy7-FN3 (with TFP) (methanol-d <sub>4</sub> ).....	92
<b>Figure 2-41:</b> $^{19}\text{F}$ NMR spectrum of Cy7-FN3 (with TFP) (methanol-d <sub>4</sub> ).....	92
<b>Figure 2-42:</b> $^1\text{H}$ NMR spectrum of 4-azido benzoic acid (5) (methanol-d <sub>4</sub> ).....	93
<b>Figure 2-43:</b> $^1\text{H}$ NMR spectrum of Cy5-N3 (methanol-d <sub>4</sub> ).....	94
<b>Figure 2-44:</b> $^1\text{H}$ NMR spectrum of Cy3-N3 (methanol-d <sub>4</sub> ).....	95
<b>Figure 2-45:</b> $^1\text{H}$ NMR spectrum of Cy7-Cl (methanol-d <sub>4</sub> ) extracted after washing with NaOH aqueous solution (pH = 9).....	95
<b>Figure 2-46:</b> $^1\text{H}$ NMR spectrum of Cy5-MES (methanol-d <sub>4</sub> ).....	97
<b>Figure 2-47:</b> $^{13}\text{C}\{^1\text{H}\}$ NMR spectrum of Cy5-MES (methanol-d <sub>4</sub> ).....	97
<b>Figure 2-48:</b> HSQC, HMBC and DQF-COSY NMR spectra of Cy5-MES (methanol-d <sub>4</sub> ).....	98
<b>Figure 2-49:</b> $^1\text{H}$ NMR spectrum of Cy3-MES (methanol-d <sub>4</sub> ).....	99

---

<b>Figure 2-50:</b> $^{13}\text{C}\{^1\text{H}\}$ NMR spectrum of Cy3-MES (methanol- $d_4$ ).....	100
<b>Figure 2-51:</b> HSQC, HMBC and DQF-COSY NMR spectra of Cy3-MES (methanol- $d_4$ ). .....	100
<b>Figure 2-52:</b> $^1\text{H}$ NMR spectrum of bCy3-PF6 (with TFP) (DMSO- $d_6$ ).....	101
<b>Figure 2-53:</b> $^{19}\text{F}$ NMR spectrum of bCy3-PF6 (with TFP) (DMSO- $d_6$ ).....	102
<b>Figure 2-54:</b> $^1\text{H}$ NMR spectrum of STCy3-PF6 (with TFP) (DMSO- $d_6$ ).....	102
<b>Figure 2-55:</b> $^{19}\text{F}$ NMR spectrum of STCy3-PF6 (with TFP) (DMSO- $d_6$ ).....	103
<b>Figure 2-56:</b> $^1\text{H}$ NMR spectrum of Cy1-PF6 (with TFP) (DMSO- $d_6$ ).....	103
<b>Figure 2-57:</b> $^{19}\text{F}$ NMR spectrum of Cy1-PF6 (with TFP) (DMSO- $d_6$ ). .....	104
<b>Figure 3-1:</b> Chemical structures of Cy-PF6. ....	107
<b>Figure 3-2:</b> Schematic of device architecture for Cy3-PF6 LECs.....	108
<b>Figure 3-3:</b> (a) Transient current density (open squares) and luminance (filled circles) in ITO/PEDOT/Cy3-PF6(30 nm)/Alq <sub>3</sub> /Ag LECs operated under constant bias at 3 V, (b) PL spectra recorded after biasing for different time.....	110
<b>Figure 3-4:</b> (a) Experimental IPCE spectra for pristine (black squares) and biased device at maximum current under light irradiated through ITO (blue circles) or Ag (red triangles) and simulated intrinsic layer absorbance spectra for light irradiated through ITO (blue dotted) or Ag (red dotted), (b) ratio of the absorbance for light irradiated through ITO and Ag for different junction thicknesses and positions, the vertical lines indicate the active layer thickness, experimental results of three different cells are marked by orange stars.....	111
<b>Figure 3-5:</b> Schematic of p-doped, intrinsic and n-doped zones of active layer in a Cy3-PF6 LEC at maximum current situation.....	112
<b>Figure 3-6:</b> White light (solid lines) and dark (dotted lines) J-V characteristics of ITO/PEDOT/Cy3-PF6(30 nm)/Alq <sub>3</sub> /Ag devices measured before bias (pristine), after bias at 3 V for ~3 h to the maximum current and relaxation for 17 h after the bias is switched off.....	113
<b>Figure 3-7:</b> White light (solid lines) and dark (dotted lines) J-V characteristics of ITO/PEDOT/Cy3-PF6((a) 30 nm, (b) 90 nm)/Alq <sub>3</sub> /Ag devices measured before bias (pristine), after bias at (a) 4 V, (b) 6 V for 10 – 20 min to the maximum current. ....	114
<b>Figure 3-8:</b> Evolution of $V_{oc}$ and $J_{sc}$ in ITO/PEDOT/Cy3-PF6(90 nm)/Alq <sub>3</sub> /Ag device after biasing at 5 V (a) to different current or (b) for different time after maximum current is reached.....	115

- Figure 3-9:** Photovoltaic performance of ITO/PEDOT/Cy3-PF6(90 nm)/Alq<sub>3</sub>/Ag LECs before bias (pristine) and after bias at 5 V to the maximum current, after white light illumination for 65 min and storage at -20 °C for 12 days. .... 116
- Figure 3-10:** Variation of absorbance spectra of (a) bCy3-PF6 and (b) STCy3-PF6 thin films during storage in the dark in N<sub>2</sub> at RT. .... 118
- Figure 3-11:** PL spectra of host-guest blend films in different ratio. .... 119
- Figure 3-12:** White light (solid lines) and dark (dotted lines) J-V characteristics of ITO/PEDOT/Cy3-PF6((a) 45 nm, (b) 60 nm, (c) 130 nm, (d) 155 nm)/Alq<sub>3</sub>/Ag and (e) ITO/MoO<sub>3</sub>/Cy3-PF6(60 nm)/Alq<sub>3</sub>/Ag devices measured before bias (pristine) and after bias at (a) 4 V, (b) 5 V, (c) 9 V, (d) 10 V, (e) 6 V for 10 – 20 min to the maximum current. .... 124
- Figure 3-13:** Photovoltaic performance of ITO/PEDOT/Cy3-PF6/Alq<sub>3</sub>/Ag LECs with different Cy3-PF6 thickness after biasing to the maximum current. .... 125
- Figure 3-14:** (a) White light (solid lines) and dark (dotted lines) J-V characteristics of ITO/PEDOT/Cy3-PF6(90 nm)/Alq<sub>3</sub>/Ag LECs before and after bias at -6.5 V for ~20 min, (b) transient current and luminance in ITO/PEDOT/Cy3-PF6(90 nm)/Alq<sub>3</sub>/Ag LECs operated under constant bias at -5 V. .... 125
- Figure 4-1:** (a) Chemical structure of Cy5-PF6 and energy level diagram of the layers used in the thin film diodes. (b) Current-voltage curves of single layer Cy5-PF6 (40 nm) devices using MoO<sub>3</sub> as anode buffer layer in the dark and under 1 or 3 sun irradiation. .... 130
- Figure 4-2:** Current-voltage curves of single layer Cy5-PF6 (40 nm) devices using (a) MoO<sub>3</sub> or (b) PEDOT anode buffer layers. The cathode buffer layers (Al or Ag) are indicated in the figure legend. Curves monitored in the dark are marked by dashed lines while curves measured under AM1.5 simulated solar light are drawn as full lines. Dotted lines correspond to the difference between current-voltage curves in the dark and under irradiation. .... 131
- Figure 4-3:** (a) Conductivity  $\sigma$  extracted from the linear slope of the current-voltage characteristics of an ITO/MoO<sub>3</sub>/Cy5-PF6 (40 nm)/Alq<sub>3</sub>/Al device measured at different light intensities (full curves are shown in 4.7 Supporting Information, **Figure 4-9**). (b) Absorbance spectra of glass/MoO<sub>3</sub> (10 nm)/Cy5-PF6 (40 nm) and IPCE spectra of the same device as in (a) at different bias voltages under 1 sun irradiation. (c) Relative conductivity  $\sigma$  extracted from the linear slope of the current-voltage characteristics of ITO/PEDOT/Cy5-PF6 (x nm)/Alq<sub>3</sub>/Ag as a function of device thickness x. (d) Simulated absorptance spectra of the devices in (c). 132



<b>Figure 4-4:</b> (a) IPCE spectra of ITO/MoO <sub>3</sub> (10 nm)/Cy5-PF6 (130 nm)/Alq <sub>3</sub> (2 nm)/Ag(12 nm) devices at (a) -3V or (b) 0 V bias under 1 sun irradiation from the front (ITO) and back side (Ag). (c) Current density-voltage curves in the dark and under illumination. ....	133
<b>Figure 4-5:</b> (a) Poling curve of ITO/MoO <sub>3</sub> /Cy5-PF6 (40 nm)/Alq <sub>3</sub> /Al devices in forward direction at +3V. The luminescence emission is indicated in the graph. (b) Corresponding current-voltage characteristics of the same device after a poling time of 25 minutes in forward direction. Dashed and solid lines stand for dark and light J-V characteristics, respectively. ....	134
<b>Figure 4-6:</b> (a) Absorbance and luminescence spectra of a 40 nm thick Cy5-PF6 layer sandwiched between ITO/MoO <sub>3</sub> and Alq <sub>3</sub> /Al electrodes. The film was excited with a 4.5 mW laser emitting at 532 nm. (b) Field induced quenching efficiency Q <sub>PL</sub> (E) of Cy5-PF6 luminescence monitored at 730 nm. Q <sub>PL</sub> (E) was calculated from equation (Eq. 4-3). ....	135
<b>Figure 4-7:</b> Photo-CELIV measurements of ITO/MoO <sub>3</sub> /Cy5-PF6 (40 nm or 130 nm)/Alq <sub>3</sub> /Al devices (a) Recombination kinetics measured by time delayed charge carrier extraction. (b) Extracted charge carrier mobility at different sweep rates (film thicknesses indicated in the graph).....	138
<b>Figure 4-8:</b> V <sub>oc</sub> and J <sub>sc</sub> values of ITO/MoO <sub>3</sub> /Cy5-PF6 (40 nm)/Alq <sub>3</sub> /Al devices irradiated at different light intensities.....	142
<b>Figure 4-9:</b> J-V characteristics of ITO/MoO <sub>3</sub> /Cy5-PF6 (40 nm)/Alq <sub>3</sub> /Al devices irradiated at different light intensities.....	143
<b>Figure 4-10:</b> IPCE spectra of ITO/MoO <sub>3</sub> /Cy5-PF6 (130 nm)/Alq <sub>3</sub> (2 nm)/Al (8 nm) devices at 0 V under 1 sun irradiation from the front (ITO) and back side (Al). ....	143
<b>Figure 4-11:</b> Ellipsometry measurements of Cy5-PF6. ....	143
<b>Figure 4-12:</b> J-V characteristics of ITO/PEDOT/Cy3-PF6 (130 nm)/Alq <sub>3</sub> /Ag before and after bias at +3V to maximum current.....	144
<b>Figure 4-13:</b> (a) Poling curve of ITO/MoO <sub>3</sub> /Cy5-PF6 (40 nm)/Alq <sub>3</sub> /Al devices in reverse direction at different voltages. (b) White light (solid lines) and dark (dotted lines) J-V characteristics before and after biasing at -3 V to maximum current.....	144
<b>Figure 5-1:</b> Chemical structures of Cy-FN3, Cy-N3 and Cy3-T.....	148
<b>Figure 5-2:</b> (a) <sup>1</sup> H and (b) <sup>19</sup> F NMR spectra of Na-FN3 in DMSO-d <sub>6</sub> measured freshly, 2 hours or 7 hours after sample preparation. ....	149

---

<b>Figure 5-3:</b> Absorbance and PL spectra of (a, b) Cy3-FN3 and (c, d) Cy3-N3 thin films coated from ACN and stored in the dark at RT in N <sub>2</sub> .....	151
<b>Figure 5-4:</b> (a) Absorbance spectra of pristine Na-N3, Cy3-PF6, Cy3-N3 films and irradiated Cy3-N3 film using UV light and (b) PL spectra of Cy-N3 films before and after UV light irradiation.....	152
<b>Figure 5-5:</b> ATR-IR spectra of Cy3-N3 films before and after 2 h visible light (> 400 nm) irradiation.....	153
<b>Figure 5-6:</b> (a) CV spectra of Cy3-N3, Cy3-PF6 and Fc/Fc <sup>+</sup> , (b) frontier energy levels of Cy3 and 4-azido benzoate anion.....	156
<b>Figure 5-7:</b> Schematic mechanism of sensitized azide photodecomposition via triplet energy transfer.....	157
<b>Figure 5-8:</b> Absorbance spectra for Cy3-N3, Cy5-N3 and Cy7-FN3 films before (solid lines) and after (dotted lines) monochromatic light irradiation for 1 h.....	161
<b>Figure 5-9:</b> <sup>1</sup> H NMR spectrum of freshly coated Cy3-FN3 film from TFP (redissolved in methanol-d <sub>4</sub> ).....	167
<b>Figure 5-10:</b> <sup>19</sup> F NMR spectrum of freshly coated Cy3-FN3 film from TFP (redissolved in methanol-d <sub>4</sub> ).....	168
<b>Figure 5-11:</b> <sup>1</sup> H NMR spectrum of 21 days stored Cy3-FN3 film (redissolved in methanol-d <sub>4</sub> ).....	168
<b>Figure 5-12:</b> <sup>19</sup> F NMR spectrum of 21 days stored Cy3-FN3 film (redissolved in methanol-d <sub>4</sub> ).....	168
<b>Figure 5-13:</b> ATR-IR spectra of Cy3-FN3 films before and after 21 days storage in the dark at RT in N <sub>2</sub> .....	169
<b>Figure 5-14:</b> ATR-IR spectra of Cy7-FN3 before and after storage in ACN for 23 hours (ACN removed before measure).....	169
<b>Figure 5-15:</b> (a) Absorbance and (b) PL spectra of Cy3-N3 films after different time of heating at 50 °C in the dark in N <sub>2</sub> .....	169
<b>Figure 5-16:</b> (a) Absorbance and (b) PL spectra of Cy3-N3 films after different time of heating at 70 °C in the dark in N <sub>2</sub> .....	170

<b>Figure 5-17:</b> (a) Absorbance and (b) PL spectra of Cy3-N3 films before and after 1 h thermal evaporation.....	170
<b>Figure 5-18:</b> Absorbance spectra of Na-N3 aqueous solution over time for (a) white light or (b) visible light (> 400 nm) irradiation.....	171
<b>Figure 5-19:</b> Absorbance spectra of Cy3-N3/ACN solution over time for (a) white light or (b) visible light (> 400 nm) irradiation.....	171
<b>Figure 5-20:</b> Absorbance spectra of Na-N3 films over time for (a) white light or (b) visible light (> 400 nm) irradiation. ....	171
<b>Figure 5-21:</b> Absorbance spectra of Cy3-N3 films over time for (a) white light, (b) visible light (> 400 nm) or (c) visible light (> 610 nm) irradiation. ....	172
<b>Figure 6-1:</b> Chemical structures of Cy-Poly, Cy-MES and PCBM.....	175
<b>Figure 6-2:</b> Schematic of device architecture for Cy-Poly/PCBM bilayer solar cells. ....	176
<b>Figure 6-3:</b> (a) Decrease of film absorption maxima after CB washing. (b) Absorption spectra of Cy5-Poly50 and Cy3-Poly50 films before (solid lines) and after (dotted lines) CB washing. ....	177
<b>Figure 6-4:</b> Effect of PCBM thickness on ITO/MoO <sub>3</sub> /Cy5-Poly20(15 nm)/PCBM/Al solar cells performance characteristics.....	179
<b>Figure 6-5:</b> (a) J-V characteristics of ITO/MoO <sub>3</sub> /Cy5-Poly50/PCBM(40 nm)/Al solar cells with different Cy5-Poly50 thicknesses. (b) Fill factor (FF) and short circuit current (J <sub>sc</sub> ) variation as function as Cy5-Poly50 thickness.....	179
<b>Figure 6-6:</b> White light (solid lines) and dark (dotted lines) J-V characteristics of (a) ITO/MoO <sub>3</sub> /Cy5-Poly/PCBM(40 nm)/Al and (b) ITO/MoO <sub>3</sub> /Cy3-Poly/PCBM(40 nm)/Al solar cells. ....	181
<b>Figure 6-7:</b> IPCE and absorption spectra for (a) ITO/MoO <sub>3</sub> /Cy5-Poly/PCBM(40 nm)/Al and (b) ITO/MoO <sub>3</sub> /Cy3-Poly/PCBM(40 nm)/Al solar cells. ....	181
<b>Figure 6-8:</b> White light (solid lines) and dark (dotted lines) J-V characteristics of (a) ITO/MoO <sub>3</sub> /Cy5-Poly(~5 nm)/PCBM(40 nm)/Ca (8 nm)/Al and (b) ITO/MoO <sub>3</sub> /Cy5-PEG50Poly50(~5-15 nm)/PCBM(40 nm)/Ca(8 nm)/Al solar cells. ....	182
<b>Figure 6-9:</b> Photo-current transients of Cy5-Poly/PCBM solar cells for different contents and voltage ramps. ....	183

**Figure 6-10:** Absorption spectra of a ~40 nm thick PCBM film on glass measured on a UV-Vis Cary 50 spectrometer or using an integrating sphere. We demonstrate the accuracy of the baseline in the integrating sphere in wavelength regions without absorption with the spectrum of an uncoated glass substrate. .... 189

**Figure 6-11:** (a) Dark-CELIV transients of Cy5-Poly/PCBM solar cells for different cyanine contents and voltage ramps. (b) Photo-CELIV transients taken before and after a measurement cycle. (c) J-V characteristics measured before and directly (less than 1 minute) after the CELIV experiments. Both measurements could be carried out on the commercial Paios system (Fluxim AG) without changing the electrical wiring. .... 190

**Figure 6-12:** J-V characteristics of ITO/MoO<sub>3</sub>/Cy5-Poly50/PCBM/Ca/Al solar cells as a function of bias voltage. .... 191

## List of Schemes

<b>Scheme 2-1:</b> Synthesis of Cy-Poly.....	57
<b>Scheme 2-2:</b> Synthesis of 4-azido-2,3,5,6-tetrafluorobenzoic acid.....	62
<b>Scheme 2-3:</b> Synthesis of Cy-FN3.....	62
<b>Scheme 2-4:</b> Synthesis of Cy-N3.....	63
<b>Scheme 2-5:</b> Synthesis of Cy-MES.....	65
<b>Scheme 2-6:</b> Synthesis of crosslinked cyanine polymers.....	65
<b>Scheme 2-7:</b> Synthesis of Cy-PF6.....	66

## List of Tables

<b>Table 2-1:</b> Repeating units and $M_n$ of copolymers. ....	58
<b>Table 2-2:</b> Weight loss in three degradation stages and residue fraction of copolymers.....	59
<b>Table 2-3:</b> Calculated weight fraction of copolymers. ....	60
<b>Table 2-4:</b> Glass transition temperature $T_g$ of copolymers.....	60
<b>Table 2-5:</b> Elemental analysis of Cy3-N3. ....	64
<b>Table 6-1:</b> Device performance of ITO/MoO <sub>3</sub> /Cy-Poly/PCBM(40 nm)/Al solar cells.....	180
<b>Table 6-2:</b> Device performance of ITO/MoO <sub>3</sub> /Cy5-Poly/PCBM(40 nm)/Ca (8 nm)/Al solar cells. .....	182
<b>Table 6-3:</b> Average mobility values for Cy5-Poly. ....	184

## Chapter 1: Introduction

### 1.1 Thesis Outline

The PhD project focused on the synthesis of novel cyanine dye counterions and the investigation of ionic junctions in cyanine based organic electronic devices. A particular goal was to fix the ionic junction in organic homojunction devices using cyanine dyes with an immobilizable anion. The fixation of ionic carriers in such devices leads to the establishment of a built-in potential and electric field across the intrinsic region, thereby attaining an efficient electroluminescence (EL) with a fast turn-on and a permanent photovoltaic response upon light illumination. To this end, special interest was given to an anionic phenyl azide which decomposes under UV light irradiation, leading to the formation of a highly reactive nitrene intermediate that rapidly reacts with adjacent covalent bonds. Therefore, the stabilization of such phenyl azide anions in place could be potentially achieved. The azido-perfluorobenzoate and non-fluorinated azido-benzoate anions were synthesized and introduced into cyanine dyes as immobilizable counter ions. However, we observed an efficient exciton quenching effect in an organic device employing cyanine dyes with azide functionalized anions (Cy-N3) as active components. This exciton quenching arose from the chemical degradation of cyanine chromophores induced by azide or benzoate group decomposition, which occurred already during device fabrication. Therefore, the attempt to fix the ionic junction in Cy-N3 films was not successful. The photodecomposition mechanism of phenyl azides and photorelaxation of cyanine dyes is discussed. We propose that a visible light induced azide photolysis via a triplet energy transfer from cyanine dye chromophores to the anions caused the observed pronounced instability of azides and consequently resulted in the failure of the concept.

Even though the fixation of ionic space charge turned out more challenging than expected, the effect of ionic charges on the optoelectronic properties were studied. For this purpose devices were poled to induce combined ionic and electronic effects. A particular concern of this project was to investigate the junction formation process in a cyanine dye light-emitting electrochemical cell (LEC). A method involving the combination of EL and photoluminescence (PL) measurements, photocurrent spectral response and optical modelling was proposed to

determine the position and width of the ionic junction during the LEC operation. The optimization of the ionic junction regarding its photovoltaic behavior was performed by altering the thickness of the active layer. To further improve the quantum efficiency of cyanine based LECs, new mono- (Cy1) and trimethine (Cy3) cyanines with hexafluorophosphate as a counter anion (Cy-PF6) were synthesized and the potential of their application in host-guest LECs was explored.

These studies were extended to pentamethine cyanine dyes which exhibit very poor luminescence as solid films. However, they present strong photocurrent generation which astonishingly does not depend significantly on poling. A section of this thesis is devoted to the photocurrent generation mechanism in ionic pentamethine (Cy5) cyanine films. Single layer devices using Cy5 with a hexafluorophosphate anion (Cy5-PF6) as active material were fabricated, which exhibited a linear current density-voltage (J-V) characteristic upon white light irradiation. The observed linear field dependence, which was independent on the electrode buffer layers or on poling, indicated an intrinsic generation of charge carriers in the bulk Cy5-PF6 films. Further evidence that supported a bulk charge generation was provided by incident photon-to-current conversion efficiency (IPCE) measurements performed on a semitransparent device. The values of photoconductivity in such cyanine films can be directly extracted from the linear slope of J-V curves and the possible mechanisms for the photo-induced generation of charge carriers are discussed.

Being able to form bilayers would add a further degree of freedom to move charges across the interface from one layer to another one. During this thesis it was therefore attempted to synthesize cyanine polyelectrolytes. The latter could be used as a base layer for the construction of a bilayer, e.g. by depositing an acceptor molecule or even another cyanine dye on top of it. In order to find an orthogonal solvent for the soluble fullerene derivative [6,6]-phenyl-C<sub>61</sub>-butyric acid methyl ester (PCBM) which does not remove or damage the underlying cyanine layer during the coating process, a special task of this project was to synthesize cyanine polyelectrolytes (Cy-Poly) that is not soluble in non-polar solvents. Different Cy-Poly copolymers consisting of a bulky polymer backbone as counter anions and cationic cyanine chromophores were synthesized. Absorbance spectra demonstrated a considerably reduced solubility of Cy-Poly films in chlorobenzene (CB) compared to cyanine small molecules. Thus, a second PCBM layer deposited from CB solutions onto Cy-Poly was



possible. The first bilayer solution-processed cyanine/PCBM organic solar cell (OSC) was fabricated and the optimization of cell performance was studied.

## **1.2 Organic Electronics**

### **1.2.1 Organic photovoltaic and electroluminescent devices**

Recently, organic electronics has drawn great attention of researchers from both academia and industry. The common goal points in the direction of developing efficient, inexpensive, flexible and portable organic electronic devices, including organic solar cells (OSCs), organic light-emitting diodes (OLEDs), light-emitting electrochemical cells (LECs), organic field-effect transistors (OFETs) and electrochromic displays. Compared to inorganic semiconductor technologies, the potential of low-cost fabrication for organic electronics originates from the light weight and solution processability of organic materials. Besides, the emerging concepts for plastic electronics of being flexible and transparent have been demonstrated, bringing about new benefits and extending the application in wider fields.<sup>1-4</sup>

Extensive research activities on organic semiconductor devices are addressing OSCs and OLEDs. Theoretically, reverse processes are taking place in OSCs and OLEDs. In an organic photovoltaic device, the energy of sunlight is converted to electrical current. In an electroluminescent device, the electrical energy is converted to light emission from the devices.

In both types of devices, the photoactive layer is sandwiched between two metal electrodes and at least one of them is transparent, typically indium tin oxide (ITO). Electron and hole transport layers are usually required in the device architecture, thereby facilitating the charge extraction in OSCs or injection in OLEDs.<sup>5,6</sup>

#### ***Operation principle of OSCs***

Historically, OSCs had a simple homojunction structure where dissociation of excitons takes place at the electrode interfaces (Schottky type) or relies on impurities or defects in the organic semiconductors.<sup>6,7</sup> This stems mainly from the fact that excitons cannot be easily splitted into free carriers due to the high exciton binding energy in most organic semiconductors.<sup>8</sup> Hence, the solar cell efficiencies were very low in such homojunction solar cells. Modern OSCs utilize a heterojunction structure consisting of two organic

semiconducting components with different electron affinities and ionization potentials. Exciton dissociation occurs predominately at the heterojunction interfaces. The electrons enter the region of the acceptor material with larger electron affinity and the holes travel through the donor material with lower ionization potential.<sup>6</sup> Two major types of donor-acceptor architectures have been demonstrated (**Figure 1-1**). Bilayer heterojunction devices contain two plane organic films on top of each other, forming a flat junction interface, while bulk heterojunction (BHJ) OSCs employ a blend of two admixed semiconductors as the photoactive layer material.<sup>9-11</sup>

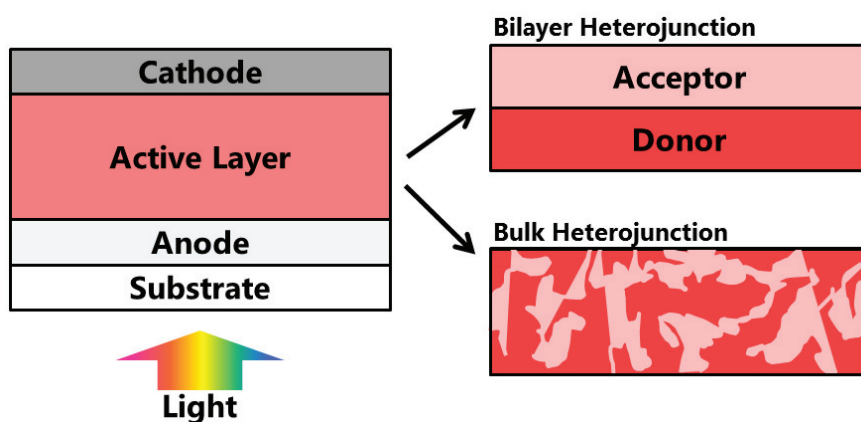


**Figure 1-1:** Schematic illustration of organic bilayer or BHJ devices.

Compared to bilayer heterojunction, BHJ devices considerably increase the interfacial area between the donor and acceptor materials. This arises from the interpenetrating network in BHJ, leading to an intimate contact between the two active components. Generally, the best BHJ devices exhibit well-controlled nanoscale morphology with a phase separation between both materials in the range of exciton diffusion lengths. Substantially improved solar cell efficiencies can be therefore achieved.<sup>11-14</sup>

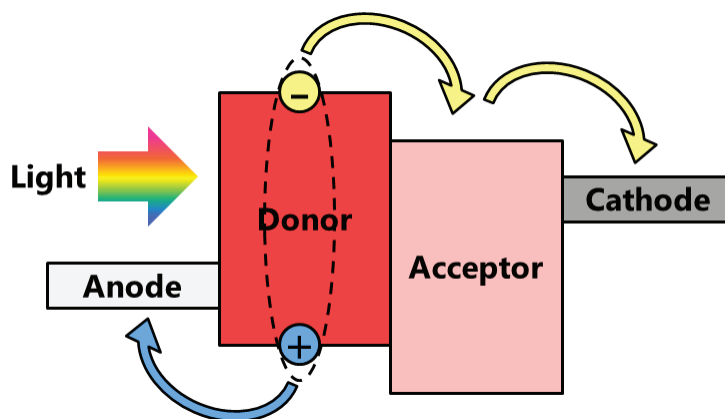


**Figure 1-2:** Schematic illustration of exciton dissociation process in a heterojunction solar cell.

The process of exciton dissociation is schematically depicted in **Figure 1-2**. Upon light illumination, the absorption of a photon in the donor material directly promotes an electron from the highest occupied molecular orbital (HOMO) to the lowest unoccupied molecular orbital (LUMO), leading to the formation of an exciton, namely a bound electron hole pair. The generated exciton diffuses to the heterojunction interfaces, followed by the dissociation of exciton into free charge carriers. Finally, free holes and electrons reach the respective electrodes, yielding electrical power.<sup>6,13</sup>

### **OLED and LEC**

Compared to OSCs, the reverse mechanism is present in OLEDs. Charge carriers are first injected from respective metal electrodes and recombine in the light-emitting layer, forming an exciton. Instead of dissociation, the exciton relaxes radiatively, causing luminescence. The emission of light is therefore observed.<sup>3,15</sup> Efficient charge carrier injection from electrodes for high performing OLEDs is crucial, which requires additional and unavoidable charge transport and injection buffer layers between the electrodes and the emissive layers. These layers also define the zone where charge carriers recombine and confine the charge carriers of opposite sign in order to increase the recombination probability. Therefore, state-of-the-art OLEDs utilize a multilayer architecture where air-sensitive electrodes with low work functions are typically applied to reach reasonably low operation voltages. Apart from the time-consuming and costly thermal sublimation processes required for the fabrication of OLEDs, another shortcoming associates with the rigorous encapsulation of the devices to prevent them from being exposed to oxygen and moisture.<sup>16,17</sup>

In 1995, Pei and coworkers demonstrated the first polymer based LEC employing a blend active layer containing an electroluminescent organic semiconductor, a salt and an ion-transporting polymer. Several promising advantages such as solution processability of the active layer, usage of air-stable electrodes, simple device geometry and low operating voltages make LECs an potentially cost-effective alternative to OLEDs.<sup>18,19,20</sup>

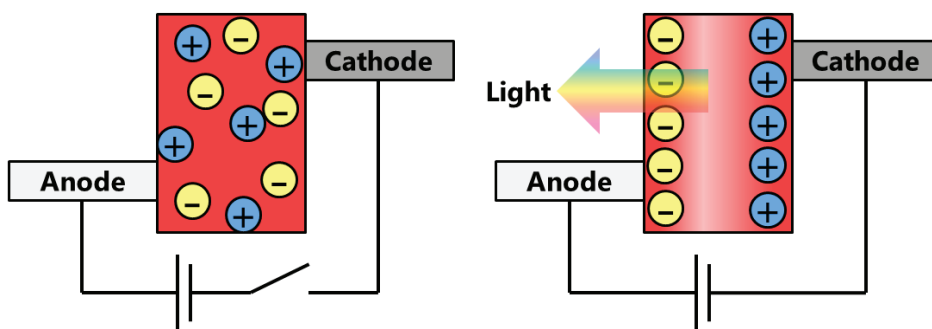


**Figure 1-3:** Schematic illustration of a LEC with or without an external voltage.

The operation mechanism of LECs has been intensively under debate. Recent studies show that the electrochemical doping model can best describe the working principle of LECs. This model involves the initial formation of electric double layers (EDLs) at electrode interfaces, which facilitates the charge injection by reducing the injection barriers. Subsequently, p- and n-type doped zones evolve within the active layer, leading to the formation of an intrinsic region where the emission of light takes place. The growing p- and n-doped regions result in a shrinking intrinsic layer, namely the p-i-n junction. In the end, the doped zones get very close or make contact, causing pronounced exciton quenching and eventually irreversible device degradation.<sup>16,17,21,22</sup>

### **Critical parameters**

A typical current density-voltage (J-V) characteristic curve of a solar cell is shown in **Figure 1-4**. Both dark and light curves from the J-V characteristics exhibit diode behaviors. The open circuit voltage ( $V_{oc}$ ) and short circuit current density ( $J_{sc}$ ) can be directly obtained from the curve. The maximum power output ( $P_{max}$ ) of a solar cell is the maximized product of voltage and current. At the point of  $P_{max}$ , the corresponding voltage and current density is  $V_{max}$  and  $J_{max}$ , respectively. The fill factor (FF) and the power conversion efficiency (PCE) of the solar cell is determined by the following equations (**Eq. 1-1** and **Eq. 1-2**):

$$FF = \frac{V_{max} J_{max}}{V_{oc} J_{sc}} \quad (\text{Eq. 1-1})$$

$$PCE = \frac{V_{max} J_{max}}{P_{in}} = \frac{V_{oc} J_{sc} FF}{P_{in}} \quad (\text{Eq. 1-2})$$

where  $P_{in}$  is the incident light power density.<sup>6,13,23</sup>

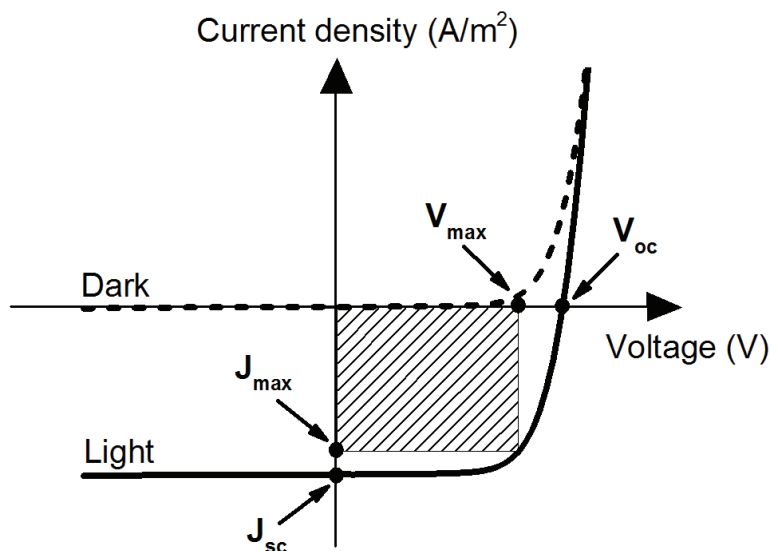


**Figure 1-4:** J-V characteristics of a solar cell under dark (dotted line) or white light illuminated conditions (solid line).

In an organic luminescent device, the internal EL quantum efficiency  $\eta_{int}$  is defined as the ratio of the amount of emitted photons to the amount of injected charge carriers. The evaluation of  $\eta_{int}$  is complicated since the collection of photons in the viewing direction is limited, hiding a possible loss of the emitted photons. Further, the small fraction of the total emitted light that is recorded by the viewer may vary with the operating voltage, viewing angle, and with the location and width of the emission zone.<sup>24</sup> Practically, the transient luminance ( $\text{cd m}^{-2}$ ) and current density ( $\text{mA cm}^{-2}$ ) is monitored during device operation. Thus, the switch-on time where light emission starts and the efficacy ( $\text{cd A}^{-1}$ ) of the device can be easily obtained.<sup>25-27</sup>

### **Fabrication techniques**

Solution processing such as spin coating and doctor blading are commonly used techniques for production of thin film organic electronic devices. Soluble organic semiconducting materials are dissolved in an organic solvent (or water), followed by deposition on the target surface at room temperature (RT) or elevated temperature. During evaporation of the solvent, homogeneous thin films can be obtained. An important prerequisite for solution processing is that the underlying material stays unaffected during the coating step. If orthogonal

solvents that do not dissolve the underlying layers are not available, posttreatment that induces polymerization or crosslinking reactions in the first layer via heating or ultraviolet (UV) light curing is usually required. Thus, the resulting films become insoluble in organic solvents, thereby making the further coating on top of them possible.<sup>13,28</sup>

Many organic semiconductors, especially small molecules, are not soluble in a wide variety of organic solvents. Hence, thermally stable small molecules and metal electrodes are usually deposited via vacuum evaporation technique. Compared to solution process, it takes much longer time to thermally sublime materials since high vacuum ( $< 10^{-5}$  mbar) needs to be reached before the deposition starts. One advantage of thermal evaporation process is that the remaining contaminants like oxygen or water can be potentially removed using the high vacuum. Polymers can decompose under excessive heat and have too large a mass for evaporation.<sup>3,28,29</sup> Side group modification of these polymers can be performed, which is capable of tuning their solubility substantially, yielding new soluble polymeric materials, e.g. polyelectrolytes. To achieve interpenetrating donor-acceptor networks or molecular doping, co-evaporation techniques are applied.<sup>13,30,31</sup>

It has been proposed that the use of eutectic gallium-indium (EGaIn) can conveniently substitute the evaporated metal electrodes, e.g. Al. EGaIn is a liquid at RT and has a work function at roughly 4.2 eV, which is quite close to Al (4.3 eV) and Ag (4.5 eV). Instead of the time-consuming evaporation step, direct deposition of the liquid metal alloy on top of the organic materials leads to an efficient contact between each other. Functional BHJ based OSCs using EGaIn as top electrode can be achieved.<sup>32</sup>

### 1.2.2 Synthesis and properties of organic semiconductors

In 1977, the first discovery of conductive polymers was demonstrated by Heeger and coworkers.<sup>33</sup> The electrical conductivity of a semiconducting polymer, polyacetylene, was substantially increased to several orders of magnitude after doping with iodine vapor. Later, numerous conductive polymers were reported including polyaniline (PANI), polyphenylene vinylene (PPV) and polythiophene (PT) (**Figure 1-5**).

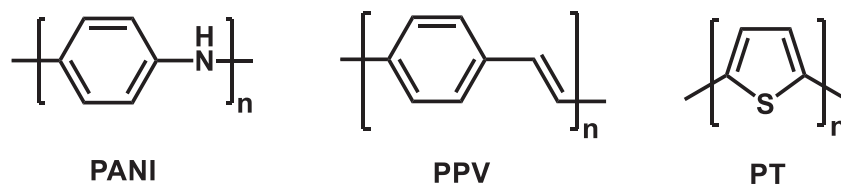


**Figure 1-5:** Chemical structures of conducting polymers PANI, PPV and PT.

In these polymers, the conjugated  $\pi$ -electrons are delocalized at the polymeric backbones containing alternating single and double bonds, resulting in a high electronic polarizability. By chemical synthesis and modification, the electrical, optical and mechanical properties of conjugated polymers can be largely modulated, thereby paving the way for applications in the field of organic optoelectronics and photovoltaics.<sup>4,28,34,35</sup> A special class of conducting polymers consisting of non-conjugated polymer backbones with pendant  $\pi$ -conjugated groups was proposed, for instance, vinyl and methacrylate polymers containing pendant oligothiophenes which may have unique properties of both the non-conjugated backbone and the conjugated oligomers.<sup>4,36,37</sup>

Small molecular weight organic semiconductors have also been intensively investigated for applications as photoactive components in organic electronic devices. Several commonly employed small molecule organic semiconductors such as metal phthalocyanine (MePc), pentacene, bathocuproine (BCP) and fullerene ( $C_{60}$ ) are shown in **Figure 1-6**.

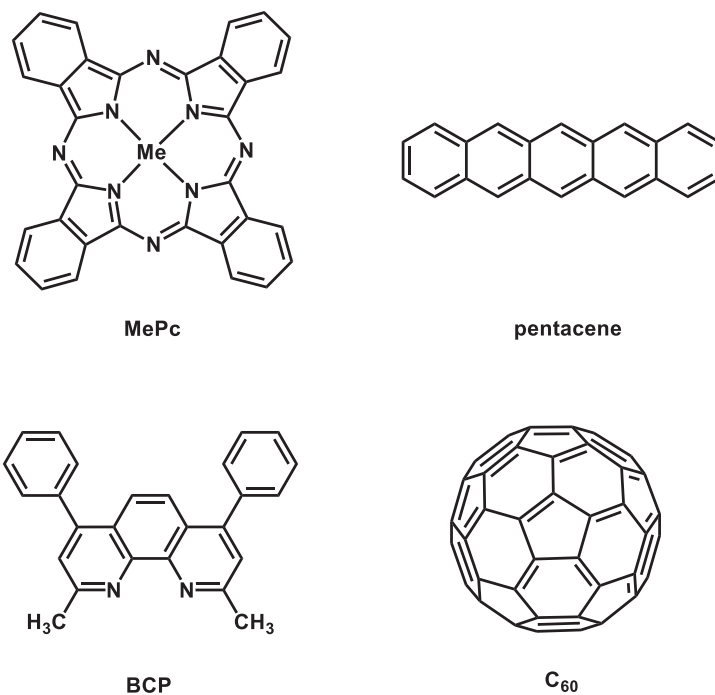


**Figure 1-6:** Chemical structures of small molecule organic semiconductors MePc, pentacene, BCP and C<sub>60</sub>.

Compared to conjugated polymers, several advantages of small molecule organic semiconductors have been proposed including ease of synthesis with simple purification process, high purity with well-defined molecular structure and molecular weight, possibility to be thermally evaporated, yielding closely packed homogeneous organic layers.<sup>9,23,28,38,39</sup>

### **Conjugated polyelectrolytes**

Conjugated polyelectrolytes (CPEs), as a novel class of conjugated polymers, contain an electronically delocalized  $\pi$ -electron system in the polymer backbone with pendant ionic functional groups. Their potential applications for optoelectronic and photovoltaic devices have attracted increasing attention from researchers. Generally CPEs can be classified into two types depending on the charges of the polymer backbone, which are cationic CPEs with positively charged backbones and anionic CPEs with negatively charged backbones (**Figure 1-7**).<sup>40-45</sup>



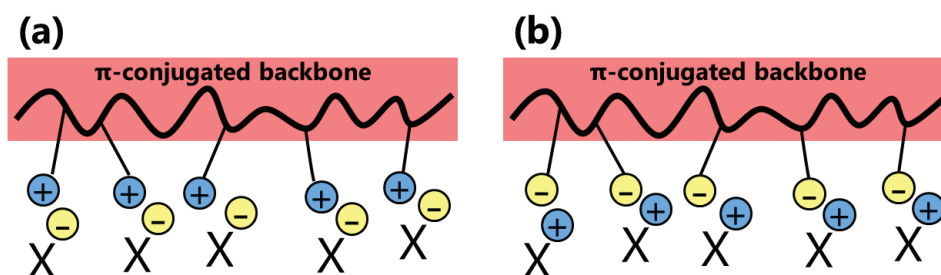


**Figure 1-7:** Schematic illustration of (a) cationic CPEs and (b) anionic CPEs.

CPEs exhibit superior optical and electronic properties, which are sensitively dependent on the hydrophobic polymeric backbones as well as the types of pendant ionic species. The unique characteristic of CPEs compared to neutral conjugated polymers associates with the high solubility in polar media, such as alcohol or water. This endows them with orthogonal solubility, allowing for the simple fabrication of multilayer structures by solution processing.<sup>40,44,46,47</sup>

A number of schemes for the synthesis of CPEs have been reported. The first CPEs based on PT as polymer backbones were introduced in 1987 by Wudl and coworkers.<sup>48</sup> The synthetic scheme involves an electropolymerization of a methyl sulfonate monomer, giving PT backbones with methyl sulfonate functional side groups, followed by the conversion into sodium salts. A more generalized synthetic scheme for CPEs was introduced by the synthesis of poly(p-phenylene) (PPP) based polyelectrolytes. Here, a neutral PPP precursor with tunable side groups was firstly obtained during polymerization, e.g. polycondensation. In a second step, the side groups were converted into ionic groups, e.g. by hydrolysis. Ionization of the pendant substitutes after polymerization leads to ease of characterization of the polymer precursors in common organic solvents before the solubility is dramatically varied in the final CPEs.<sup>40,41,49,50</sup>

### **Cyanine dyes**

Cyanine dyes are charged low band gap organic semiconducting materials consisting of a polymethine group as the  $\pi$ -conjugated system and an accompanying counter ion. Generically, cyanine dyes contain two nitrogen centers, linked with an odd number of methine groups. Cyanine dyes can be classified based on the length of polymethine chains, e.g. Cy3, Cy5 and heptamethine (Cy7) dyes. Typical absorbance spectra of Cy3, Cy5 and Cy7 films are shown in **Figure 1-8**. Different cyanines exhibit a diversity of physical, optical and

semiconducting properties, making them prominent candidates for different applications as photosensitizers, industrial paints, biological probes, electroluminescent organic semiconductors and active donor materials for OSCs.<sup>51-58</sup>

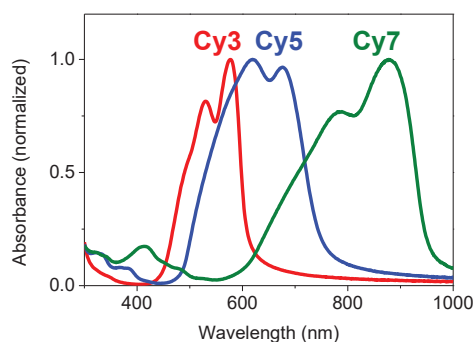


**Figure 1-8:** Typical absorbance spectra of Cy3, Cy5 and Cy7 thin films.

Cyanine dye chromophores can be readily achieved by organic synthesis, usually resulting in iodide or chloride as counter anions. To obtain a different anion, subsequent ion exchange reaction is required. A commonly applied strategy for counter anion conversion is demonstrated via a salt metathesis reaction, which leads to the precipitation of inorganic salts (e.g. silver halides) while leaving the dye chromophores with desired counter ions in the reaction media<sup>59</sup> or performs in the opposite manner, namely precipitation of the dye chromophores with introduced anions while leaving the other pair in solution<sup>60</sup>. Ion exchange of cyanine dyes via a solvent-solvent extraction or using ion exchange resins is also possible. (For further information, see Chapter 2)

Chemical modification on the polymethine group of cyanine dyes has been proposed. An activated chloro-substituted polymethinic linker on Cy7 dye chromophores was reacted with alkyl-thiols containing polyether or carboxylic functional groups. The efficient nucleophilic substitution provides possibilities to modify symmetric cyanine dyes with different nucleophiles, thereby introducing various possible functionalities.<sup>61</sup> It was reported that cyanine dyes can be polymerized by connecting the dye chromophores in a head-to-tail fashion. This polymeric cyanines exhibit distinct bathochromic shifts and absorb solely in the near infrared (NIR) region.<sup>62</sup>

## 1.3 Ionic Junctions

### 1.3.1 Mixed ionic/electronic conduction in organic materials

The incorporation of ionic carriers in conjugated organic semiconductors leads to a mixed ionic/electronic conduction character. Driven by an applied external voltage or other triggers, ions redistribute within the organic layer, resulting in intrinsic electrochemical oxidation and reduction of the organic materials. Several effects associated with the electrochemical doping process have been demonstrated including the increase of electronic conductivity and variation of color and volume of the organic semiconductors. Due to these interesting behaviors, the mixed ionic/electronic conductors are employed for many applications such as organic light-emitting and photovoltaic devices, electroactive actuators, electrochromic displays, organic sensors and transistors.<sup>63,64</sup>

#### ***Ion transport in solid organic materials***

Generally, state-of-the-art organic electronic devices employing the concept of mixed ionic/electronic conduction relies on additionally admixed ion-transporting polymer, e.g. poly(ethylene glycol) (PEG), to achieve fast ionic movement in solid organic films.<sup>18,65-67</sup> This is mainly attributed to the fact that most organic materials are poor ionic conductors. PEG is a semicrystalline material and is known to have a low glass transition temperature ( $T_g$ ) below 0 °C, which results in a soft and flexible polymer film with low rigidity and stiffness at RT.<sup>68</sup> Therefore, above  $T_g$  the high amplitude conformation fluctuations of the polymers can potentially enhance their ion-conducting capabilities.<sup>69</sup> With respect to the mechanism of ion transport, it has been proposed that the salts are dissolved in PEG films, generating polyether-salt complex electrolyte materials. The cation-containing complexes, formed due to cation coordination by the polyether oxygens, migrate in the solid films via a helical tunnel while the motion of anions, where the ions are less strongly solvated by the polymer, is realized due to the presence of anion-polymer van der Waals interaction by diffusing into regional free volumes caused by thermal fluctuations of the polymers.<sup>67,69-71</sup>

### 1.3.2 Dynamic junction in organic electronic devices

A commonly admixed ionic material in the polymer blends containing an active organic semiconductor and an ion-transporting PEG that enables the fast motion of ions is lithium

trifluoromethanesulfonate ( $\text{LiCF}_3\text{SO}_3$ ). The generated lithium-PEG electrolyte due to the strong coordination of  $\text{Li}^+$  cations to the electronegative polyether oxygens drifts to the cathode, while the anions drift to the anode when an external bias is applied.<sup>67,70</sup> Severe phase separation between the PEG and the active polymer in the blend is a known issue, which may result in poor film morphology and degraded device performance.<sup>63</sup> Improved morphology of the active layer was achieved by embedding the oligo(ethylene glycol) segments into the light-emitting polymers either as side groups<sup>72-77</sup> or in the main chains<sup>78-80</sup>, which potentially leads to a long-living light-emitting device without accelerated degradation of cell performance.

The coexistence of ionic and electronic conduction in organic materials can also be achieved with a single active component without additional incorporation of ionic carriers, e.g. ionic transition metal complexes (iTMCs).<sup>17,81</sup> Similar to iTMCs, cyanine dyes have also inherently both ionic and electronic charge conductivity. Therefore, in LECs using cyanines as active materials, no additional admixed salts are required.<sup>56</sup> The movement of ions in a cyanine film is enabled due to the presence of a small and mobile counter anion accompanied with the cationic cyanine chromophores. For organic electronic applications, cyanine dyes have attracted intensive attention, attributed to their prominent characteristics including high extinction coefficient, good solution processability with a wide variety of organic solvents, ease of chemical synthesis and purification and tunable absorption and emission.<sup>82-84</sup>

### ***p-i-n junction LECs***

The incorporation of ionic species in conjugated organic electroluminescent materials initiated the first demonstration of LECs.<sup>18</sup> With the assistance of ion-conducting polymer, ionic carriers in the photoactive layer redistribute upon the application of an external bias, leading to electrochemical oxidation and reduction to generate a p-doped region close to the anode and n-doped region close to the cathode. The doped regions are known to have a considerably enhanced electronic conductivity, thereby facilitating the charge carrier injection and transport from the respective metal electrodes. However, the electrochemical doping process is dynamic and reversible. Relaxation of ions occurs when the external voltage is no longer applied, resulting in an unstable p-i-n junction in organic LECs.<sup>16,21,85-87</sup>

The ion profiles in stacked LECs remain an interesting and crucial issue to achieve a better understanding of the functional principle during LEC operation. Different methods have been

carried out to investigate the evolution process of a p-i-n junction in an operating device. During the electrochemical doping upon an applied bias, the formation of the high-conductivity doped regions and the low-conductivity intrinsic region result in a clear increase of capacitance, observed by impedance spectroscopy measurements. A rough estimation of the junction width can be potentially obtained.<sup>88-91</sup> The depth profile of ionic species can also be probed by secondary ion mass spectrometry (SIMS) technique, which yields the element distribution of ions within the device.<sup>91-93</sup>

Direct visualization of the p-i-n junction in lateral structure LECs with a large interelectrode distance was obtained using optical microscopy and fluorescence imaging. The propagation of both p-type and n-type doped zones was monitored, demonstrating a clear image of junction formation process and a PL quenching behavior in the doped regions.<sup>65,94-97</sup> Furthermore, scanning Kelvin probe microscopy (SKPM) has been employed to study the potential profile of a functional LEC.<sup>65,98-100</sup> Results indicate that the doped regions exhibit a flat potential profile whereas a sharp potential drop is usually observed in the light-emission zone.<sup>65,98</sup> Nonetheless, direct imaging of a sandwiched LEC with a digital camera is not possible since the interelectrode space is usually very small ( $< 200$  nm).<sup>101-103</sup> Also, the electrochemical doping model cannot be simply translated from the lateral to the stacked LECs by scaling down the thickness of different zones since the intensity of the electric field in the device, which is sensitively depending on the thickness and the bias voltage, may consequently affect the field-dependent electron and hole mobilities.<sup>88,90,104,105</sup>

### ***Ionic space charge in cyanine photovoltaic devices***

The movement of the cyanine dye counter ions was found to be capable of modulating the photovoltaic behaviors of cyanine OSCs due to the effect of ionic space charge. In a cyanine/C<sub>60</sub> organic bilayer heterojunction solar cell, the anions redistribute within the cyanine layer upon the application of an external bias, establishing ionic interfacial space charges at the anode/cyanine and cyanine/C<sub>60</sub> interfaces due to accumulated ionic species. Clear changes in J-V characteristics were observed after biasing. The variation of V<sub>oc</sub> in such devices was well explained by the ionic motion which fine-tuned energy level of the donor and the donor-acceptor energy level offsets.<sup>106</sup>

Besides, it has been reported that the mobile counter ions, chloride (Cl<sup>-</sup>) or hexafluorophosphate (PF<sub>6</sub><sup>-</sup>), can diffuse into the adjacent organic layers, creating an ionic

profile across the heterojunction interface and a built-in electric field. This resulted in the shifts of electronic orbital energy levels of both organic materials and the control of electronic current flow in the devices. The spectral current response of the biased devices was dramatically altered, which indicated a change in the direction of electron transfer process between the donor and acceptor materials. The ionic space charge can therefore tremendously modulate the photovoltaic effect and solar cell performance in organic thin film devices.<sup>107</sup>

However, the above described ionic effect on photovoltaic behaviors is reversible and dynamic. Mobile ions can relax back upon removal of the external bias, which may take minutes to hours. Therefore, to achieve a permanent ionic distribution and internal built-in electric field, subsequent stabilization of the ionic carriers is required.

### ***Electrochromic displays***

The electrochromic effect of conjugated polymers is realized by the reversible electrochemical oxidation and reduction process originated from the ionic movement within the devices, which induces new absorption bands in the visible region of the materials. Electroactive polymers that exhibit a color change at different redox states are applied as the active components for electrochromic displays. Several promising advantages of polymer electrochromic materials have been demonstrated including ease of structure modification of the polymer backbone during synthesis, fast switching ability, multiple colors with the same material and high coloration efficiency.<sup>108-110</sup>

### ***Ionic electroactive actuators***

Associated with the electrochemical doping process, the ion transport induced volume change of conjugated polymers allows for the potential application for electroactive actuators and artificial muscles. Swelling and shrinking of the active polymers can be achieved due to the redistribution of the mobile ionic carriers in the devices upon an external voltage. Generally, the ingress and egress of ionic species (along with intercalating solvating species) in the conjugated polymers directly yields the expansion and contraction of the regional volume of the materials. A bending of the polymer thin film is therefore observed as a function of device charging.<sup>111-114</sup>

### 1.3.3 Attempts towards a fixed ionic junction

Several attempts to achieve a fixation of ionic carriers have been performed in different organic electronic devices. As discussed above, the redistribution of ionic species driven by an external voltage is not stable since relaxation of ions takes place upon the removal of the bias. The established ionic junction with the desired ionic profiles and internal built-in electric field disappears gradually. A number of benefits can be obtained after the stabilization of ions including fast response of electroluminescence, permanent photovoltaic behavior, high rectification and well-controlled electronic current flow. For example, the initial ionic motion towards respective electrodes in LECs under a constant voltage is usually very slow, which considerably limits the switch-on time and the potential applications. Once the ionic carriers are fixed in place, the desirable ionic distribution and the doped zones are stabilized even during device idling. Therefore, an instantaneous light emission can be expected once the voltage is applied to the device with fixed ions. The proposed methods for stabilization of ionic junctions can be mainly categorized into four types: (1) reducing the ionic mobility by lowering the temperature, (2) generating immobile ionic species by chemical reactions, e.g. polymerization, (3) reducing the ionic conductivity by curing the ionic conductors, (4) bilayer devices containing oppositely charged mobile ions that are removed via solvent-soaking or diffuse into the other layer.

#### ***Temperature-controlled stabilization of ions***

Initially, the stabilization of ions in LECs was demonstrated by physically immobilizing the ionic carriers at low temperature (Figure 1-9).<sup>115-124</sup>

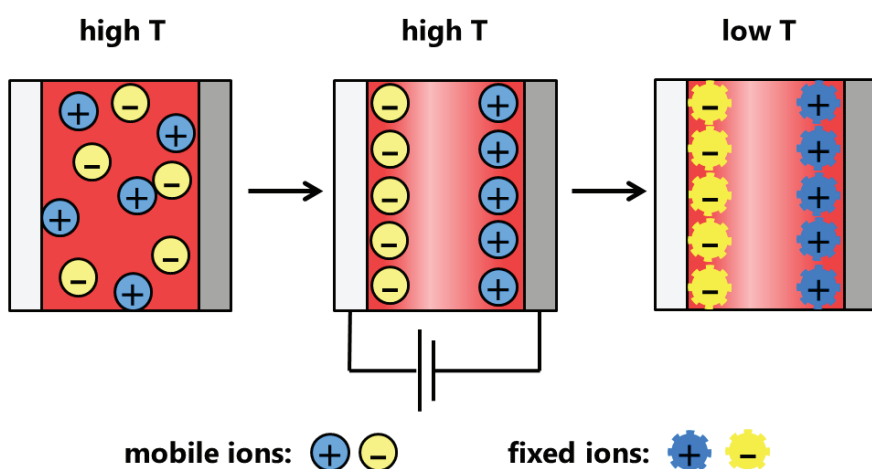


**Figure 1-9:** Schematic illustration of stabilization of ions by lowering the temperature.

Here, the devices were firstly operated under a constant bias at RT, which is above the  $T_g$  of the ion conductive PEG, to achieve the desired ion distribution and doping profiles in the active layer. In a second step, the generated p-i-n junction was frozen by reducing the temperature below the  $T_g$  of PEG (e.g. < 200 K). By lowering the temperature of PEG films below  $T_g$ , the segmental motion of the polymer chain was considerably restricted, which largely reduced the possible movement of ionic species in the PEG films and therefore achieved the immobilization of ions.<sup>68,69,120</sup> Finally, devices with frozen junctions were characterized at cryogenic temperatures with respect to their electroluminescent behaviors. It was reported that the fixed p-i-n junction LECs exhibit several OLED characteristics including high diode rectification ratio, instantaneous response of the light emission and unipolar emission at low voltages.<sup>116-118</sup>

It is well known that the electrochemical doping results in PL quenching in the both p-type and n-type doped zones.<sup>85,94,95,125,126</sup> Therefore, the excessive presence of doped species in the doped regions leads to severe exciton quenching process, which eventually deteriorates the EL efficiency and the device performance especially when the doped zones get close to each other. It was found that the relaxation of ions in an established p-i-n junction initiates from the widening of intrinsic region, leading to narrowing doped regions from the intrinsic layer toward the metal electrodes. Thus, it can be concluded that the relaxation of a p-i-n junction initially leads to significantly less PL quenching effect due to the reduction of dopants without immediately affecting the Ohmic contact characteristics induced by the doped zones. Under a controlled doping relaxation, Gao and coworkers demonstrated that the quantum efficiency of EL in polymer LECs was considerably improved by elevating the temperature for a well-controlled period after a frozen p-i-n junction was achieved at low temperatures. The PL quenching phenomenon in the emission zone due to the excessive electrochemical doping was thus alleviated.<sup>124</sup> Photovoltaic effects have been observed in stabilized p-i-n junction LECs, indicating that the established ionic profile and built-in electric field can potentially assist the splitting of excitons upon light illumination and the frozen junction devices can also be operated as solar cells.<sup>119,121,123,127</sup>

Practically, the operation of LECs under reduced temperatures may be inconvenient, which considerably limits the potential application for lightening purposes. Several strategies have demonstrated the possibilities to immobilize the ionic motion at RT.<sup>128-131</sup> LEC devices containing crown ether and Li salt as solid electrolyte materials and electroluminescent



polymer blends were fabricated. The utilized crown ether/Li salt complexes exhibited a high ionic mobility at elevated temperatures (60 °C – 80 °C) but a very low ionic conductivity at RT. A dynamic p-i-n junction is firstly achieved upon the application of an external bias on the LECs at high temperatures which enabled the motion of ionic charge carriers. Subsequently, the junction with desired doping profiles was cooled to RT, thereby stabilizing the ionic distribution in the active layer. Very high performing LECs with high external EL quantum efficiencies were obtained, which demonstrated prominent electrical and optical characteristics similar to those of OLEDs, including unipolar J-V dependence, light emission in forward bias only, and instantaneous light emission upon biasing.<sup>128</sup>

Random copolymers consisting of a methyl methacrylate backbone with oligo PEG as pedant groups were designed, aiming at increasing the  $T_g$  of ionic transporting polymer above RT. Results demonstrated that the  $T_g$  of the copolymers increases clearly by diluting the PEG content with methyl methacrylate repeating units. Hence, stabilizing the mobile ions at RT by utilizing PEG based copolymers with high  $T_g$  as ion-transport material was achieved via a similar method as it was performed in Ref. [128] involving generating a p-i-n junction at elevated temperatures, followed by cooling to RT.<sup>129</sup> A similar approach using an ionic liquid, imidazolium salt, as electrolyte has also been reported for the fixation of a p-i-n junction in LECs.<sup>130</sup>

### ***Polymerization of ionic species***

Leger and coworkers demonstrated another approach to achieve the stabilization of ions in organic homojunction or heterojunction devices by chemically fixing the ionic species in situ. This method involved polymerization of the functional ionic monomers, generating immobile and bulky polyelectrolytes in the active layer, which exhibited a largely reduced ionic mobility.<sup>132-134</sup> Schematic illustration of this approach is shown in **Figure 1-10**.

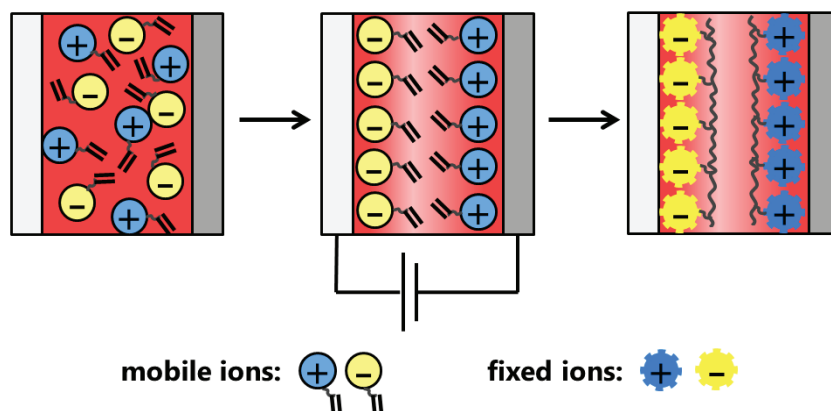


**Figure 1-10:** Schematic illustration of stabilization of ions by polymerizing the ionic monomers.

Instead of using the typical lithium salt in the matrix of the active layer, polymerizable ionic monomer pairs were employed as electrolyte materials for LECs application. During the device operation under a constant voltage, the mobile ion pairs drifted to the electrodes similar as Li salts. Subsequently, the vinyl-functionalized monomer species underwent a polymerization reaction initiated by the electrochemical generation of radicals in the conjugated polymers. This led to the covalent bonding via the vinylic groups of the ionic carriers, forming immobile ionic polymers in position. The immobilization of ions and fixation of the homojunction with desired electrochemical doping profiles were therefore achieved. The fixed junction was demonstrated to be stable under a wide range of operating voltages at RT. The resulting devices exhibited diode characteristics with high rectification, unipolar emission and a photovoltaic behavior.<sup>132</sup> The concept of fixing the ionic carriers was also applied for the homojunction or donor/acceptor heterojunction photovoltaic devices, a high  $V_{oc}$  was achieved and a significant improvement of  $J_{sc}$  was obtained owing to the improved charge carrier collection efficiency induced by the electrochemical doping processes.<sup>133</sup>

It was found that the phase compatibility between the ionic monomers and conjugated polymers is very low, thereby resulting in poor film morphology in the device. This issue was addressed by replacing the polymerizable ionic monomers with ionic liquids, which exhibit a much better miscibility with the emissive polymers. These ionic liquids were functionalized with vinyl or allyl groups during synthesis via a salt metathesis reaction, which allowed for the following polymerization step. Significantly improved device performance was achieved including high brightness, excellent rectification and fast switch-on time.<sup>134</sup>

### **Curable ionic conductors**

It has been proposed that the small molecules containing acrylate or methacrylate groups can dissolve certain amount of lithium salts. This arises from the polar nature of the (meth)acrylate moieties and endows them with reasonable ionic charge conductivities in solid films. However, the ion conduction channels will be cut off if polymerization or crosslinking reaction of (meth)acrylate groups takes place, which considerably decreases the ionic transporting ability. Based on this behavior, Pei and coworkers demonstrated an approach to fix the mobile ions by curing the polymerizable ionic conductors.<sup>135,136</sup> Schematic illustration of this approach is shown in **Figure 1-11**.

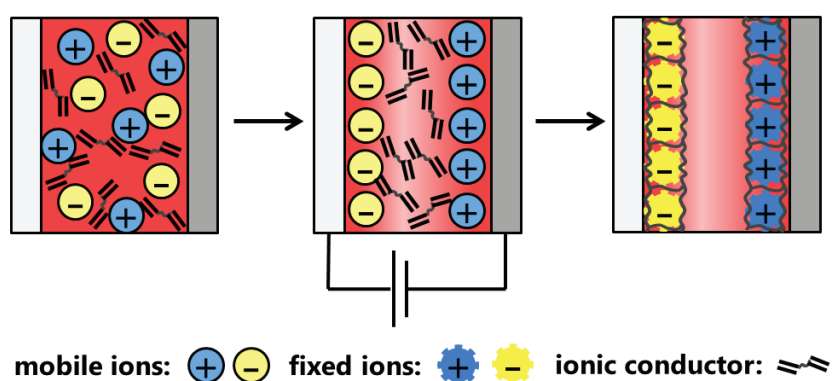


**Figure 1-11:** Schematic illustration of stabilization of ions by curing the ionic conductors.

In this approach, the (meth)acrylate functionalized ionic conducting materials were employed in the active layer containing an electroluminescent polymer and a typical lithium salt as electrolyte. During device charging, the crosslinking of acrylate or methacrylate groups occurred, which was initiated by the heat from device operation particularly at high current density or by the ionic radicals generated from electrochemical doping. A significantly decreased ionic conductivity of the cured polymer was obtained, resulting in the fixation of ionic carriers. This device exhibited a very fast switch-on below 5 ms, showing an instant light emission upon application of an external voltage. A stable photovoltaic response in fixed p-i-n junction LECs was achieved, demonstrating a high  $V_{oc}$  and an increase of  $J_{sc}$  without decay after device idling for 16 hours.<sup>135</sup> A further attempt focused on combining the advantages of both (meth)acrylate and the ion-transporting PEG. A low molecular weight methacrylate group terminated PEG oligomer was applied as curable ionic conductor for the junction fixation in LECs. After curing, the devices exhibited a high maximum current efficacy up to  $11.9 \text{ cd A}^{-1}$ , a long lifetime up to 27000 hours before decaying to 75% of the peak brightness and a pronounced enhancement of the uniformity and stability of the junction.<sup>136</sup>

Further, the benefits of both polymerizable ionic monomers and crosslinkable ionic conductors are combined. Edman and coworkers reported that the best device performance in LECs regarding their rectification ratio and long-term stability was achieved by polymerizing the ionic monomer pairs together with the curable ionic transporting materials with PEG segments.<sup>137,138</sup> An additional admixed radical initiator in the blend films brought about new advantages. For example, the utilization of a photo initiator enabled the junction stabilization process to be well-controlled. Upon a short term UV exposure at RT, the immediate formation of photo induced radicals initiated the curing reaction between the ionic species and the functionalized PEG units, yielding a rapid fixation of the p-i-n junction in the LECs with fast switch-on and high rectification ratio that did not dissipate after 24 hours storage.<sup>138</sup>

### **Other methods**

The fixed ionic distribution has also applied for bilayer devices, achieving a stabilized p-n junction (**Figure 1-12**).

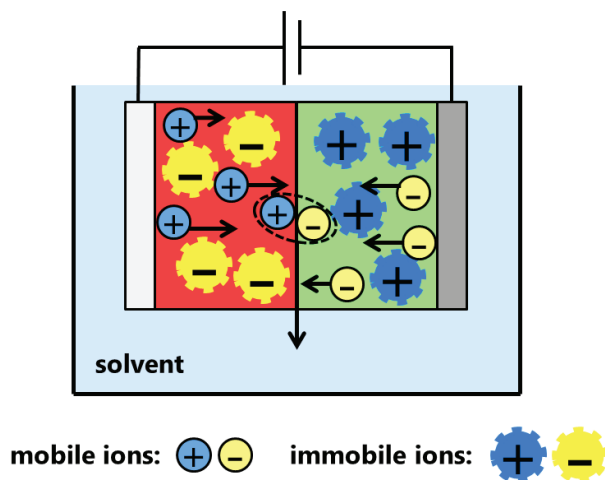


**Figure 1-12:** Schematic illustration of stabilization of ions by solvent-soaking under device charging.

Conjugated polyacetylenes with oppositely charged pendant groups and mobile ions were sequentially spin casted and sandwiched between two gold electrodes. The solvent used for the coating of second layer did not dissolve the first underlying polymer film, thereby resulting in a neat bilayer structure. Subsequently, the device was charged under an applied bias while immersed in a solvent, which dissolved the liberated salts. The liberation of the mobile cations and anions was attributed to the electrochemical doping process where the

injected charge carriers were stabilized by the pendant ionic species linked to the conjugated polymer backbones. Therefore, a p-n junction with fixed intrinsic ion profiles was obtained in the devices, which exhibited a diode behavior in the J-V characteristics with moderate rectification.<sup>139</sup>

A novel approach for fixing the ionic junctions was demonstrated by Bernards and coworkers using a soft-contact lamination technique (**Figure 1-13**).

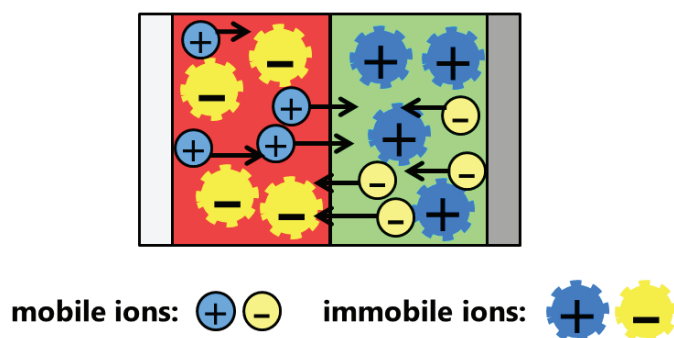


**Figure 1-13:** Schematic illustration of stabilization of ions by ion diffusion after lamination.

Bilayer devices containing two organic semiconducting materials with either mobile anions or cations were fabricated. Due to the gradients in concentrations, both mobile cations and anions diffused into the other layer. This resulted in the establishment of built-in potential and modification of the energy levels of organic semiconductors. The resulting devices with fixed ionic junctions demonstrated a very high rectification, which allowed the electronic current to flow preferentially in one direction. Photovoltaic response was obtained in such devices when illuminated by white light.<sup>140</sup> A similar work was carried out using the lamination technique, demonstrating a fixed ionic junction between aqueous gels containing polyelectrolytes with oppositely charged mobile ions.<sup>141</sup>

A chemically fixed p-n heterojunction via a B-F covalent bond formation process was established. In this method, two polymer films were solution casted sequentially from orthogonal solvents. The first and second layer consisted of a neutral polymer with an anion-trapping functional group and a cationic polymer with mobile fluoride anions, respectively. Upon device charging, the fluoride anions drifted into the neutral polymer layer, which induced the B-F covalent bond formation. The ions were thus stabilized, leading to the electrochemical doping of the materials. The fixed p-n junction electronic devices showed an instantaneous EL emission and high current rectification.<sup>142</sup>

Theoretically, apart from the methods described above, other chemical reactions which enable a chemical linkage of functionalized mobile ionic groups in position upon an external trigger are also possible to be potentially employed for the fixation of ionic junctions.

## 1.4 Phenyl Azides

### 1.4.1 Photo-induced decomposition and reaction

Organic azides, as a unique class of organic functional groups, have been investigated over several decades. It has been reported that azides can decompose by various triggers including temperature, light and acid or transition metal catalysts.<sup>143,144</sup> Phenyl azides, as the simplest compound among all aromatic azides, decompose thermally or photochemically, leading to a wide variety of products. The complex photochemistry of phenyl azides and derivatives enables them to be excellent candidates as precursors for nanomaterial synthesis, photoaffinity labelling (PAL) agents, light-sensitive photoresists and surface engineering reagents.<sup>145-151</sup>

Photo-induced decomposition of phenyl azides results in the cleavage of the nitrogen – nitrogen covalent bond in the azide groups, yielding very reactive phenyl nitrene intermediates by releasing dinitrogen gas. Different types of nitrenes (singlet and triplet) can be produced via photolysis of phenyl azides, which sensitively depends on the reaction conditions and mechanisms, such as the kind of photosensitizers used. Nitrenes are electron-deficient molecular fragments with six electrons in the valence shell on the nitrogen atom. Singlet nitrenes have two electron pairs and an empty orbital whereas triplet nitrenes have one pair of electrons and two electrons with parallel spins (**Figure 1-14**).<sup>152-155</sup>

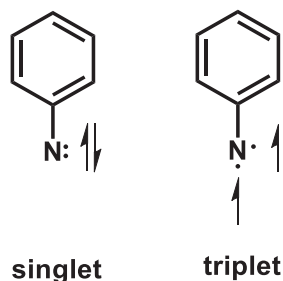


**Figure 1-14:** Schematic illustration of singlet and triplet phenyl nitrenes.

Both singlet and triplet nitrene intermediates can undergo various chemical reactions including intra- or intermolecular cycloaddition, C-H insertion and H-abstraction. Differences between the singlet and triplet phenyl nitrenes were also drawn with regard to their preferred reactions and the resulting products.<sup>144,156-159</sup>

### **Direct photogeneration of phenyl nitrenes**

Phenyl nitrenes can be obtained from aryl azides precursors upon light illumination. Phenyl azides absorb UV light, generating photoexcited azides which subsequently dissociate by expelling  $N_2$  and thereby yielding singlet nitrenes. On the other hand, intersystem crossing (ISC) process may take place, which leads to the formation of triplet excited azides, followed by decomposition to give triplet nitrenes. ISC from the singlet to the triplet nitrene may also exist, which was confirmed to be a barrier-less process. The rate of ISC can be significantly enhanced by heavy atoms or alcohols.<sup>146,161</sup> A simplified scheme is shown in **Figure 1-15**.<sup>143,145,146,156,160,162</sup>

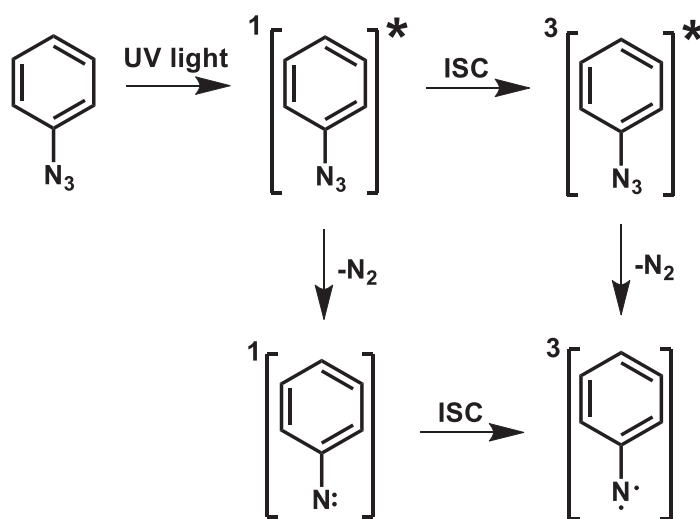


**Figure 1-15:** Schematic illustration for direct photogeneration of phenyl nitrenes upon UV light irradiation.

To figure out which pathway is involved in producing triplet nitrenes, a triplet quencher can be artificially added into the reaction system. If the triplet aryl nitrenes are generated via singlet nitrenes, the addition of a triplet quencher would not affect the original photochemical process. Therefore, the products that arise from either singlet or triplet nitrenes can still be obtained. Since the presence of a triplet quencher can potentially block the pathway of triplet nitrenes generation from triplet azides in the excited state, the

products that result preferentially from triplet nitrenes would be considerably decreased or disappear.<sup>143,145</sup> For the direct photolysis of alkyl azides using UV light irradiation, it was reported that the addition of triplet sensitizer did not affect the product distribution. This experiment suggests that the decomposition of a directly photoexcited alkyl azide to yield a singlet nitrene is the prevailing reaction. As the competitive process, ISC to a triplet azide may proceed in a negligible manner.<sup>143,163</sup>

### **Triplet sensitized photolysis of azides**

Alternatively, an efficient way to produce triplet nitrenes is via sensitized photolysis of organic azides in the presence of a triplet sensitizer. Here, the irradiated light is firstly absorbed by a triplet sensitizer, followed by an energy transfer process from the photoexcited sensitizer to the azides. This process directly populates the triplet state of the organic azides, which lose  $N_2$  and therefore result in the formation of triplet nitrenes. A simplified scheme for producing triplet phenyl nitrenes is shown in **Figure 1-16**.<sup>156,157,162-167</sup>

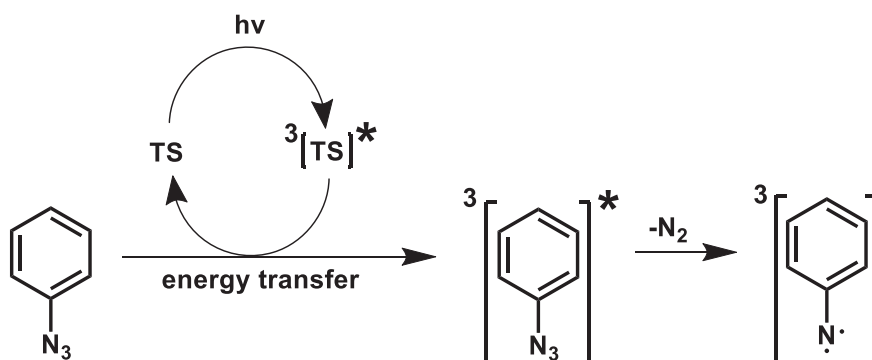


**Figure 1-16:** Schematic illustration for triplet sensitized photolysis of phenyl azides, (TS: triplet sensitizer).

As described above, direct photolysis of organic azides yields both singlet and triplet nitrenes, suggesting that the products originating from both nitrene intermediates can be obtained in a different ratio. For triplet sensitized photolysis, the products that arise from triplet nitrenes are predominately yielded. However, it was reported that the addition of a singlet sensitizer, which promotes the formation of singlet nitrenes, does not affect the product distribution, which remains the same as the case from the direct light illumination. It was therefore concluded that the generation of triplet nitrenes via triplet sensitization process stem solely from the dissociation of excited triplet azides and no ISC of singlet nitrenes are involved in the photochemical process.<sup>143,168,169</sup>



Normally, organic azides absorb UV light below 290 nm and the maximum absorption signals of phenyl azides are situated in the range of 250 nm to 280 nm.<sup>145,149,162</sup> Typical triplet sensitizers for photodecomposition of azides are aromatic ketones, e.g. acetophenone and benzophenone, which exhibit an absorption band between 300 nm and 400 nm.<sup>164,165,170</sup> Therefore, low-pressure or medium-pressure mercury lamps, which irradiate predominately in the UV region, are commonly employed as light sources for the photolysis of organic azides. However, it has been proposed that extensive irradiation using high-energy UV light may introduce photodecomposition of organic compounds due to their poor functional group tolerance.<sup>171,172</sup>

Recently, visible light induced sensitization for the photolysis of organic azides has been demonstrated using ruthenium or iridium complexes as triplet sensitizers. Upon absorption of visible light, these photoexcited sensitizers undergo efficient ISC, yielding stable and long-lived excited species in the triplet states. Subsequently, triplet – triplet energy transfer process from the triplet species of the sensitizers to the organic azides takes place, leading to the production of triplet nitrenes. The visible light sensitized azide photolysis is very attractive and useful in organic synthesis. With the addition of the transition metal complexes as photosensitive catalysts, organic chemical reactions that rely on triplet nitrenes may proceed under much milder conditions without using UV lamps as light sources.<sup>171,173,174</sup>

Pronounced visible light sensitization using a ruthenium complex was achieved for the photolysis of vinyl or acyl azides. In these cases, the employed complex  $\text{Ru}(\text{bpy})_3^{2+}$  has a triplet energy of 46 kcal/mol, while the triplet level of vinyl and acyl azides were calculated to be 45.4 kcal/mol and 41 kcal/mol, respectively. Clearly, the efficient photosensitization can be attributed to the perfect matching of the triplet energy levels between the sensitizer and the organic azides.<sup>171,173</sup> For phenyl azides, the triplet energy was estimated to be in the range of 68 – 75 kcal/mol, which is much higher than the energy of visible light sensitizers. Generally, triplet – triplet energy transfer proceeds with a diffusion-controlled rate when the triplet level of sensitizers is higher than that of the acceptors. However, for the sensitized photodecomposition of phenyl azides, measurable sensitization behaviors were obtained using sensitizers with triplet energy of 50 kcal/mol or less. This indicates that sensitizers with lower triplet energies are considerably more effective than expected for a classical endothermic energy transfer. To explain this phenomenon, it has been suggested that a non-classical energy transfer process is involved, which occurs between the phenyl azides and

triplet sensitizers. It is known that the ground state of azide groups exhibit a linear configuration. Nonetheless, the photoexcitation of phenyl azides is accompanied by a strong bending of the N-N-N bond in the azide groups, resulting in a non-spectroscopic triplet state. This state cannot be detected by spectroscopic methods, but can be reached by energy transfer process. Therefore, it can be concluded that much less energy is required for a vertical excitation from thermally populated bent azides in the ground state to the excited triplet azides with the same bent configurations. Hence, efficient triplet sensitizers with low triplet energies can be expected for the photodecomposition of organic azides.<sup>170,175,176</sup>

### ***Matrix isolation technique***

Due to the high reactivity of nitrenes, it is not possible to capture these intermediates at RT since they rapidly react with the surrounding species, undertaking different chemical reactions and thereby yielding various products. At low temperatures, the reactivity of nitrene intermediates is significantly reduced. The matrix isolation technique enables the characterization of reactive species that are dispersed in an inert matrix material at cryogenic temperatures. Initially, the reactive nitrenes were successfully detected by freezing the organic material as matrix, e.g. organic solvents, to 77 K and measuring electron paramagnetic resonance (EPR) or absorption spectra.<sup>156,166,177-179</sup>

However, the frozen solvents at 77 K may also have some interactions with the target reactive intermediates, which may potentially affect the resulting spectra and lead to ambiguities. Besides, frozen solvents are very often not transparent in the IR or UV spectral range. Therefore, inert noble gases, e.g. argon and neon, are considered as better matrix materials and a much lower temperature is typically required, which is at ~10 K.<sup>180-182</sup> Triplet phenyl nitrenes were successfully trapped in an argon matrix and their IR absorption spectra were clearly identified, which exhibited strong and characteristic absorption signals at 747 cm<sup>-1</sup> and 655 cm<sup>-1</sup>.<sup>183-185</sup>

### ***Typical reactions of phenyl nitrenes***

The reactive nitrene intermediates undergo numerous chemical reactions once generated thermally or photochemically. They can insert into adjacent C-H or N-H covalent single bonds, react with alkenes via intermolecular cycloaddition to give aziridines, abstract hydrogen atoms from surrounding media such as organic solvents and undergo reversible or

irreversible rearrangements.<sup>151,153</sup> A generalized reaction scheme for singlet and triplet phenyl nitrenes is shown in **Figure 1-17**.

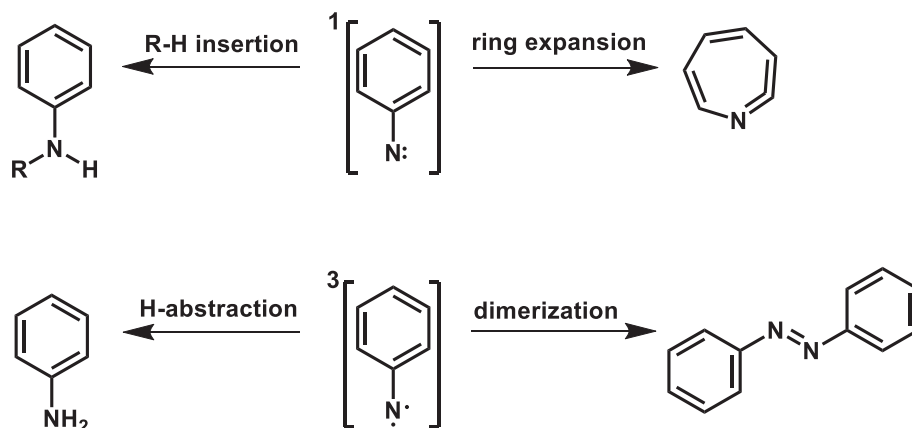


**Figure 1-17:** Simplified schemes for typical reactions of singlet and triplet phenyl nitrenes.

An important reaction that takes place for singlet phenyl nitrenes is C-H insertion to yield secondary amines. This reaction can be both intra- or intermolecular and insertion to both C(sp<sup>2</sup>)-H and C(sp<sup>3</sup>)-H single bonds is possible. It has been suggested that the selectivity of insertion into sp<sup>3</sup> C-H bonds decreases from tertiary, to secondary and to primary species.<sup>151,186</sup> Besides, addition reactions to C=C double bonds were also reported for singlet nitrenes. Alternatively, ring expansion to a corresponding seven-membered azepine was detected, which was induced by structural rearrangement.<sup>187</sup> It was found that the halogen atom substituents on the aromatic rings can substantially suppress the ring expansion of the singlet phenyl nitrenes and the insertion reactions are thus more favorable for fluorinated phenyl nitrenes.<sup>146,188-191</sup>

Compared to singlet nitrenes which favor C-H insertion reactions, the triplet species of phenyl nitrenes demonstrate a strong preference to abstract hydrogen atoms to yield anilines or dimerize to generate azo compounds. For a reaction system without triplet sensitizers where the triplet nitrenes arise exclusively from singlet azides or nitrenes via ISC, it was suggested that nitro group functionalized phenyl azides largely increased the yield of anilines, indicating that the quantum yield of ISC was enhanced and the triplet products were promoted.<sup>145,146,162,192,193</sup>

It should be noted that the above discussed chemical reactions for phenyl nitrenes are basically performed in solutions. The diffusion of reactive species is relatively free in the

solvents and the chance to undergo hydrogen abstraction or dimerization is reasonably high particularly for triplet nitrenes. However, if the motion of nitrenes is hindered such as in solid states, insertion reactions into the nearby covalent bonds would play a dominant role. Therefore, triplet phenyl nitrenes that favorably result in anilines or azo compounds as major products in solutions can also react in a very non-selective manner in the solid state, which enables the potential applications for thin film technologies.<sup>145,194</sup>

#### **1.4.2 Application for nanostructure modification**

Phenyl azides and derivatives have been widely employed as PAL agents, which consist of a biological ligand functionalized with a photoactive group. Upon light illumination, C-H insertion reaction by nitrene intermediates takes place, forming a stable covalent bond between the labelling agent and a target biopolymer, e.g. protein. The binding site structure of the labeled biomolecule will be characterized and determined.<sup>146,151,195-199</sup> However, as described above, singlet phenyl nitrenes may undergo rapid ring expansion instead of insertion reaction, which results in poor PAL efficiencies. Therefore, perfluorophenyl azides (PFPAs) are demonstrated to be among the most popular PAL agents since the undesired ring expansion is not present. Besides, PFPAs exhibit many advantages including high reaction efficiencies, superior stability during storage in the dark and ease of preparation during synthesis.<sup>145,146</sup>

##### ***Surface functionalization***

Recently, PFPAs have been applied as excellent coupling agents for surface functionalization techniques. *p*-substituted tetrafluorophenyl azides are among the best candidates as coupling agents since they are heterobifunctional with two reactive centers. During chemical synthesis, different organic groups with new functionalities can be designed and then introduced into the PFPAs bearing already a light sensitive azide group at the para position. Therefore, the successful binding between the azide and the target surface directly leads to the surface modification with the introduced functionalities. This strategy applies to the substrate surfaces that possess sufficient C-H, N-H and C=C covalent bonds, e.g. polymers or biomolecules, which serve as the target groups for the potential insertion and cycloaddition reactions.<sup>146,147,200-202</sup> A schematic illustration is shown in **Figure 1-18**.

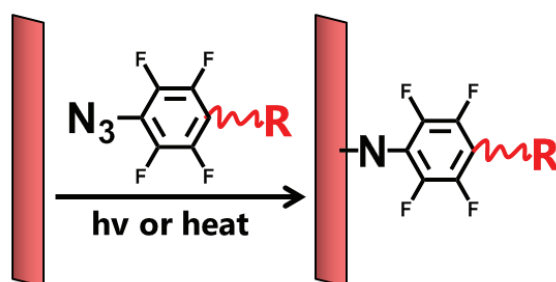


**Figure 1-18:** Simplified scheme for surface functionalization via direct binding of PFPAs.

With regard to the substrates such as metal oxides, silicon oxides and metal films that cannot be efficiently bonded by PFPAs via nitrene chemistry, a two-step approach is typically employed. Here, PFPAs with organic groups that enable an efficient binding to such substrates are firstly synthesized, e.g. silane-substituted PFPAs for metal oxides surfaces or thiol-functionalized PFPAs for gold films. These chemically modified PFPAs are then utilized to functionalize the corresponding substrates, yielding photoactive phenyl azides on the surface. Subsequently, the target molecules such as polymers are attached to the substrates via the azide coupling chemistry triggered by UV light or elevated temperatures.<sup>146,203-209</sup> A schematic illustration of this two-step approach is shown in **Figure 1-19**.

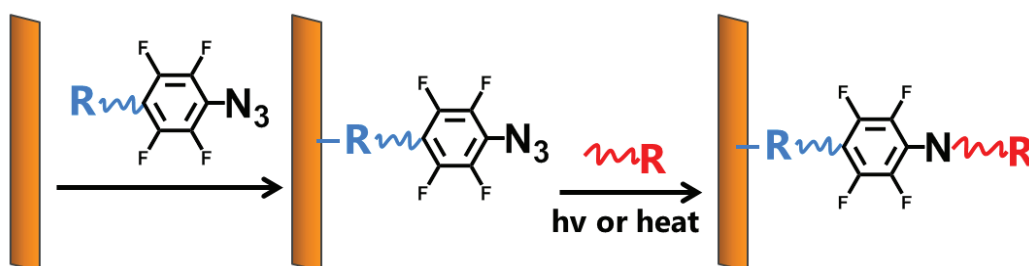


**Figure 1-19:** Simplified schemes for surface functionalization with PFPAs by a two-step approach.

### **Morphology control**

One application of organic azides for organic electronics is to stabilize the heterostructure and film morphology of the active layer in BHJ organic solar cells. Generally, a certain phase separation between the donor and acceptor is required for the optimal solar cell performance. However, this specific morphology is thermodynamically not stable over time and degradation of cell performances is usually observed in an aged device. Here, the thermo- and photosensitive azides act as crosslinkers, which establish crosslinked nanostructures via nitrene chemistry in the photovoltaic devices.<sup>210-212</sup>

Bis-azides bearing two reactive nitrene precursors were used as small molecule additives in the BHJ blend layer. Upon UV light illumination, the photogenerated nitrene species reacted rapidly with the matrix materials, leading to crosslinking of the different components in the film and thus the stabilization of the desired bulk interpenetrating heterostructure. Some possible bis-azides photocrosslinkers are shown in **Figure 1-20**, including bis(perfluorophenyl) azide (bis(PFBA)), sterically hindered fluoro-phenyl-azides (sFPA), 4,4'-bis(azidomethyl)-1,1'-biphenyl (BABP) and 1,6-diazidohexane (DAZH).<sup>213-217</sup>

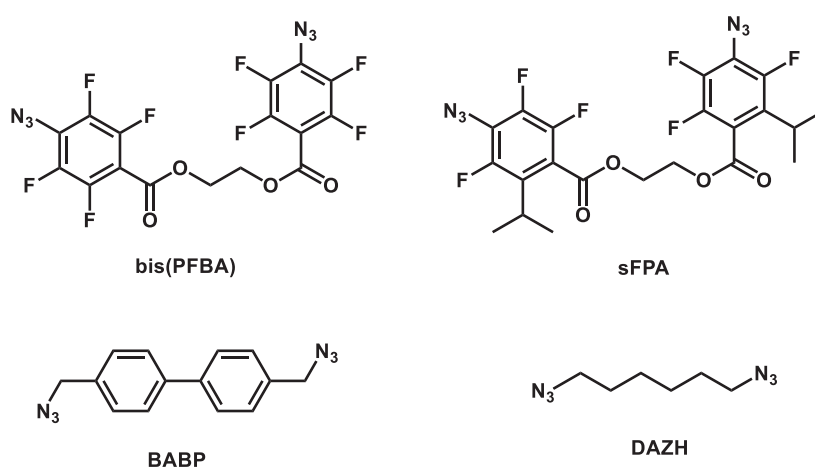


**Figure 1-20:** Chemical structures of photocrosslinkers bis(PFBA), sFPA, BABP and DAZH.

The dual-functional sFPA crosslinkers demonstrated an excellent crosslinking capability. A few weight percent of this additive admixed into the blend resulted in stabilization of bulk morphology with high crosslinking densities. An enhancement of photovoltaic lifetime for BHJ organic solar cells was therefore achieved. Besides, it was suggested that the photocrosslinking reactions occurred predominantly between the side chains of the polymers. Thus, the crosslinking step did not affect the  $\pi$ -conjugated systems at the polymer backbones as well as optical and semiconducting properties of the active materials.<sup>214,215,217</sup>

Azide-functionalized conjugated polymers are also applied for the stabilization of bulk morphology in OSCs.<sup>218-221</sup> The azide functional groups are generally incorporated into the side chains of the polymer donor materials. The content of azide moiety in the system can be designed during the synthesis of the copolymers by conveniently tuning the feed ratio of azide-containing monomer units. Upon UV light exposure, the crosslinkable azides decompose, yielding reactive nitrene intermediates which rapidly react with the donor, the conjugated polymer, and the acceptor, typically fullerene and its derivatives, with little

selectivity. This results in stabilized domains with both donor – donor and donor – acceptor networks. On the other hand, it was found that the thermally induced nitrenes can selectively react with the fullerenes via addition reactions, leading to the stabilization of nanomorphology with pure donor – acceptor crosslinks. In this case, no reactions between the azides and the donor materials were observed.<sup>212,218,222</sup>

## 1.5 References

- [1] A. Facchetti,  $\pi$ -conjugated polymers for organic electronics and photovoltaic cell applications, *Chem. Mater.* **2011**, 23, 733-758.
- [2] T. W. Kelley, P. F. Baude, C. Gerlach, D. E. Ender, D. Muires, M. A. Haase, D. E. Vogel, S. D. Theiss, recent progress in organic electronics: materials, devices, and processes, *Chem. Mater.* **2004**, 16, 4413-4422.
- [3] L. S. Hung, C. H. Chen, recent progress of molecular organic electroluminescent materials and devices, *Mater. Sci. Eng. R-Rep.* **2002**, 39, 143-222.
- [4] Y. Shirota, organic materials for electronic and optoelectronic devices, *J. Mater. Chem.* **2000**, 10, 1-25.
- [5] K. Walzer, B. Maennig, M. Pfeiffer, K. Leo, highly efficient organic devices based on electrically doped transport layers, *Chem. Rev.* **2007**, 107, 1233-1271.
- [6] H. Spanggaard, F. C. Krebs, a brief history of the development of organic and polymeric photovoltaics, *Sol. Energy Mater. Sol. Cells* **2004**, 83, 125-146.
- [7] G. A. Chamberlain, organic solar cells: a review, *Solar Cells* **1983**, 8, 47-83.
- [8] M. Knupfer, exciton binding energies in organic semiconductors, *Appl. Phys. A* **2003**, 77, 623-626.
- [9] Y. Lin, Y. Li, X. Zhan, small molecule semiconductors for high-efficiency organic photovoltaics, *Chem. Soc. Rev.* **2012**, 41, 4245-4272.
- [10] C. W. Tang, two-layer organic photovoltaic cell, *Appl. Phys. Lett.* **1986**, 48, 183.
- [11] G. Yu, J. Gao, J. C. Hummelen, F. Wudl, A. J. Heeger, polymer photovoltaic cells: enhanced efficiencies via a network of internal donor-acceptor heterojunctions, *Science* **1995**, 270, 1789.
- [12] K. M. Coakley, M. D. McGehee, conjugated polymer photovoltaic cells, *Chem. Mater.* **2004**, 16, 4533-4542.

- [13] S. Günes, H. Neugebauer, N. S. Sariciftci, conjugated polymer-based organic solar cells, *Chem. Rev.* **2007**, 107, 1324-1338.
- [14] W. Ma, C. Yang, X. Gong, K. Lee, A. J. Heeger, thermally stable, efficient polymer solar cells with nanoscale control of the interpenetrating network morphology, *Adv. Funct. Mater.* **2005**, 15, 1617-1622.
- [15] J. L. Segura, the chemistry of electroluminescent organic materials, *Acta Polym.* **1998**, 49, 319-344.
- [16] S. Toshner, J. Leger, chapter 7: ionic carriers in polymer light-emitting and photovoltaic devices, *Organic Electronics: Emerging Concepts and Technologies* **2013**.
- [17] R. D. Costa, E. Ortí, H. J. Bolink, F. Monti, G. Accorsi, N. Armaroli, luminescent ionic transition-metal complexes for light-emitting electrochemical cells, *Angew. Chem. Int. Ed.* **2012**, 51, 8178-8211.
- [18] Q. Pei, G. Yu, C. Zhang, Y. Yang, A. J. Heeger, polymer light-emitting electrochemical cells, *Science* **1995**, 269, 1086-1088.
- [19] R. H. Friend, R. W. Gymer, A. B. Holmes, J. H. Burroughes, R. N. Marks, C. Taliani, D. D. C. Bradley, D. A. Dos Santos, J. L. Brédas, M. Lögdlund, W. R. Salaneck, electroluminescence in conjugated polymers, *Nature* **1999**, 397, 121-128.
- [20] N. C. Greenham, S. C. Moratti, D. D. C. Bradley, R. H. Friend, A. B. Holmes, efficient light-emitting diodes based on polymers with high electron affinities, *Nature* **1993**, 365, 628-630.
- [21] S. B. Meier, D. Tordera, A. Pertegás, C. Roldán-Carmona, E. Ortí, H. J. Bolink, light-emitting electrochemical cells: recent progress and future prospects, *Mater. Today* **2014**, 17, 217-223.
- [22] S. van Reenen, P. Matyba, A. Dzwilewski, R. A. J. Janssen, L. Edman, M. Kemerink, a unifying model for the operation of light-emitting electrochemical cells, *J. Am. Chem. Soc.* **2010**, 132, 13776-13781.
- [23] B. P. Rand, J. Genoe, P. Heremans, J. Poortmans, solar cells utilizing small molecular weight organic semiconductors, *Prog. Photovolt: Res. Appl.* **2007**, 15, 659-676.
- [24] S. R. Forrest, D. D. C. Bradley, M. E. Thompson, measuring the efficiency of organic light-emitting devices, *Adv. Mater.* **2003**, 15, 1043-1048.
- [25] D. Dini, electrochemiluminescence from organic emitters, *Chem. Mater.* **2005**, 17, 1933-1945.



- [26] U. Mitschke, P. Bäuerle, the electroluminescence of organic materials, *J. Mater. Chem.* **2000**, 10, 1471-1507.
- [27] S. van Reenen, T. Akatsuka, D. Tordera, M. Kemerink, H. J. Bolink, universal transients in polymer and ionic transition metal complex light-emitting electrochemical cells, *J. Am. Chem. Soc.* **2013**, 135, 886-891.
- [28] H. Hoppe, N. S. Sariciftci, organic solar cells: an overview, *J. Mater. Res.* 2004, 19, 1924-1945.
- [29] M. Baldo, M. Deutsch, P. Burrows, H. Gossenberger, M. Gerstenberg, V. Ban, S. Forrest, organic vapor phase deposition, *Adv. Mater.* **1998**, 10, 1505-1514.
- [30] M. Hiramoto, H. Fujiwara, M. Yokoyama, three-layered organic solar cell with a photoactive interlayer of codeposited pigments, *Appl. Phys. Lett.* **1991**, 58, 1062.
- [31] W. Geens, T. Aernouts, J. Poortmans, G. Hadziioannou, organic co-evaporated films of a PPV-pentamer and C<sub>60</sub>: model systems for donor/acceptor polymer blends, *Thin Solid Films* **2002**, 403-404, 438-443.
- [32] A. D. Pasquier, S. Miller, M. Chhowalla, on the use of Ga-In eutectic and halogen light source for testing P3HT-PCBM organic solar cells, *Sol. Energy Mater. Sol. Cells* **2006**, 90, 1828-1839.
- [33] H. Shirakawa, E. J. Louis, A. G. MacDiarmid, C. K. Chiang, A. J. Heeger, synthesis of electrically conducting organic polymers: halogen derivatives of polyacetylene, (CH)<sub>x</sub>, *J. Chem. Soc. Chem. Commun.* **1977**, 16, 578-580.
- [34] M. A. Rahman, P. Kumar, D. Park, Y. Shim, electrochemical sensors based on organic conjugated polymers, *Sensors* **2008**, 8, 118-141.
- [35] K. M. Molapo, P. M. Ndangili, R. F. Ajayi, G. Mbambisa, S. M. Mailu, electronics of conjugated polymers (I): polyaniline, *Int. J. Electrochem. Sci.* **2012**, 7, 11859-11875.
- [36] K. Nawa, K. Miyawaki, I. Imae, N. Noma, Y. Shirota, polymers containing pendant oligothiophenes as a novel class of electrochromic materials, *J. Mater. Chem.* **1993**, 3, 113-114.
- [37] I. Imae, K. Nawa, Y. Ohseido, N. Noma, Y. Shirota, synthesis of a novel family of electrochemically-doped vinyl polymers containing pendant oligothiophenes and their electrical and electrochromic properties, *Macromolecules* **1997**, 30, 380-386.

- [38] V. Coropceanu, J. Cornil, D. A. da S. Filho, Y. Olivier, R. Silbey, J. Brédas, charge transport in organic semiconductors, *Chem. Rev.* **2007**, 107, 926-952.
- [39] P. Peumans, A. Yakimov, S. R. Forrest, small molecular weight organic thin-film photodetectors and solar cells, *J. Appl. Phys.* **2003**, 93, 3693.
- [40] W. Lee, J. H. Seo, H. Y. Woo, conjugated polyelectrolytes: a new class of semiconducting material for organic electronic devices, *Polymer* **2013**, 54, 5104-5121.
- [41] H. Jiang, P. Taranekekar, J. R. Reynolds, K. S. Schanze, conjugated polyelectrolytes: synthesis, photophysics, and applications, *Angew. Chem. Int. Ed.* **2009**, 48, 4300-4316.
- [42] M. R. Pinto, K. S. Schanze, conjugated polyelectrolytes: synthesis and applications, *Synthesis Stuttgart* **2002**, 9, 1293-1309.
- [43] C. V. Hoven, A. Garcia, G. C. Bazan, T. Nguyen, recent applications of conjugated polyelectrolytes in optoelectronic devices, *Adv. Mater.* **2008**, 20, 3793-3810.
- [44] A. Duarte, K. Pu, B. Liu, G. C. Bazan, recent advances in conjugated polyelectrolytes for emerging optoelectronic applications, *Chem. Mater.* **2011**, 23, 501-515.
- [45] U. Scherf, counterion pinning in conjugated polyelectrolytes for applications in organic electronics, *Angew. Chem. Int. Ed.* **2011**, 50, 5016-5017.
- [46] W. Ma, P. K. Iyer, X. Gong, B. Liu, D. Moses, G. C. Bazan, A. J. Heeger, water/methanol-soluble conjugated copolymer as an electron-transport layer in polymer light-emitting diodes, *Adv. Mater.* **2005**, 17, 274-277.
- [47] J. H. Seo, E. B. Namdas, A. Gutacker, A. J. Heeger, G. C. Bazan, conjugated polyelectrolytes for organic light emitting transistors, *Appl. Phys. Lett.* **2010**, 97, 043303.
- [48] A. O. Patil, Y. Ikenoue, F. Wudl, A. J. Heeger, water-soluble conducting polymers, *J. Am. Chem. Soc.* **1987**, 109, 1858-1859.
- [49] R. Rulkens, M. Schulze, G. Wegner, rigid-rod polyelectrolytes: synthesis of sulfonated poly(p-phenylene)s, *Macromol. Rapid. Commun.* **1994**, 15, 669-676.
- [50] I. U. Rau, M. Rehahn, rigid-rod polyelectrolytes: carboxylated poly(para-phenylene)s via a novel precursor route, *Polymer* **1993**, 34, 2889-2893.
- [51] A. Mishra, R. K. Behera, P. K. Behera, B. K. Mishra, G. B. Behera, cyanines during the 1990s: a review, *Chem. Rev.* **2000**, 100, 1973-2011.

- [52] R. M. A. El-Aal, synthesis and characterization of new photosensitizer bridgehead cyanine dyes, *Proc. Indian Acad. Sci. (Chem. Sci.)* **1999**, 111, 343-352.
- [53] P. F. Santos, L. V. Reis, P. Almeida, A. S. Oliveira, L. F. V. Ferreira, singlet oxygen generation ability of squarylium cyanine dyes, *J. Photochem. Photobiol. A* **2003**, 160, 159-161.
- [54] J. Kulbacka, A. Pola, D. Mosiadz, A. Choromanska, P. Nowak, M. Kotulska, M. Majkowski, A. Hryniewicz-Jankowska, L. Purzyc, J. Saczko, cyanines as efficient photosensitizers in photodynamic reaction: photophysical properties and in vitro photodynamic activity, *Biochemistry (Moscow)* **2011**, 76, 473-479.
- [55] S. A. Soper, Q. L. Mattingly, steady-state and picosecond laser fluorescence studies of nonradiative pathways in tricyanocyanine dyes: implications to the design of near-IR fluorochromes with high fluorescence efficiencies, *J. Am. Chem. Soc.* **1994**, 116, 3744-3752.
- [56] A. Pertegás, D. Tordera, J. J. Serrano-Pérez, E. Ortí, H. J. Bolink, light-emitting electrochemical cells using cyanine dyes as the active components, *J. Am. Chem. Soc.* **2013**, 135, 18008-18011.
- [57] B. Fan, F. A. de Castro, J. Heier, R. Hany, F. Nüesch, high performing doped cyanine bilayer solar cell, *Org. Electron.* **2010**, 11, 583-588.
- [58] G. Wicht, S. Bücheler, M. Dietrich, T. Jäger, F. Nüesch, T. Offermans, J. Tisserant, L. Wang, H. Zhang, R. Hany, stability of bilayer trimethine cyanine dye/fullerene organic solar cells, *Sol. Energy Mater. Sol. Cells* **2013**, 117, 585-591.
- [59] G. Shanker, G. Hegde, C. Rodriguez-Abreu, self-assembly of thiacyanine dyes in water for the synthesis of active hybrid nanofibers, *Liq. Cryst.* **2016**, 43, 473-483.
- [60] A. C. Véron, H. Zhang, A. Linden, F. Nüesch, J. Heier, R. Hany, T. Geiger, NIR-absorbing heptamethine dyes with tailor-made counterions for application in light to energy conversion, *Org. Lett.* **2014**, 16, 1044-1047.
- [61] S. A. Hilderbrand, K. A. Kelly, R. Weissleder, C. Tung, monofunctional near-infrared fluorochromes for imaging applications, *Bioconjugate Chem.* **2005**, 16, 1275-1281.
- [62] T. Geiger, H. Benmansour, B. Fan, R. Hany, F. Nüesch, low-band gap polymeric cyanine dyes absorbing in the NIR region, *Macromol. Rapid. Commun.* **2008**, 29, 651-658.
- [63] J. M. Leger, organic electronics: the ions have it, *Adv. Mater.* **2008**, 20, 837-841.

- [64] S. E. Feicht, G. D. Degen, A. S. Khair, moving ion fronts in mixed ionic-electronic conducting polymer films, *AIChE J.* **2015**, 61, 1447-1454.
- [65] P. Matyba, K. Maturova, M. Kemerink, N. D. Robinson, L. Edman, the dynamic organic p-n junction, *Nature Mater.* **2009**, 8, 672-676.
- [66] L. Edman, bringing light to solid-state electrolytes: the polymer light-emitting electrochemical cell, *Electrochim. Acta* **2005**, 50, 3878-3885.
- [67] S. Tang, L. Edman, quest for an appropriate electrolyte for high-performance light-emitting electrochemical cells, *J. Phys. Chem. Lett.* **2010**, 1, 2727-2732.
- [68] J. A. Faucher, J. V. Koleske, E. R. Santee Jr. J. J. Stratte, C. W. Wilson III, glass transitions of ethylene oxide polymers, *J. Appl. Phys.* **1966**, 37, 3962-3964.
- [69] L. C. Hardy, D. F. Shriver, preparation and electrical response of solid polymer electrolytes with only one mobile species, *J. Am. Chem. Soc.* **1985**, 107, 3823-3828.
- [70] M. A. Ratner, D. F. Shriver, ion transport in solvent-free polymers, *Chem. Rev.* **1988**, 88, 109-124.
- [71] B. L. Papke, M. A. Ratner, D. F. Shriver, conformation and ion-transport models for the structure and ionic conductivity in complexes of polyethers with alkali metal salts, *J. Electrochem. Soc.* **1982**, 129, 1694-1701.
- [72] Q. Sun, Y. Li, Q. Pei, polymer light-emitting electrochemical cells for high-efficiency low-voltage electroluminescent devices, *J. Display. Technol.* **2007**, 3, 211-224.
- [73] Q. Pei, Y. Yang, efficient photoluminescence and electroluminescence from a soluble polyfluorene, *J. Am. Chem. Soc.* **1996**, 118, 7416-7417.
- [74] Y. Yang, Q. Pei, efficient blue-green and white light-emitting electrochemical cells based on poly[9,9-bis(3,6-dioxaheptyl)-fluorene-2,7-diyl], *J. Appl. Phys.* **1997**, 81, 3294-3298.
- [75] J. Morgado, R. H. Friend, F. Cacialli, B. S. Chuah, S. C. Moratti, A. B. Holmes, light-emitting devices based on a poly(p-phenylene vinylene) derivative with ion-coordinating side groups, *J. Appl. Phys.* **1999**, 86, 6392-6395.
- [76] C. Huang, W. Huang, J. Guo, C. Yang, E. Kang, a novel rigid-rod alternating poly(p-phenylenevinylene) derivative with oligo(ethylene oxide) side chains, *Polymer* **2001**, 42, 3929-3938.

- [77] J. Morgado, R. H. Friend, F. Cacialli, B. S. Chuah, H. Rost, S. C. Moratti, A. B. Holmes, light-emitting electrochemical cells based on poly(p-phenylene vinylene) copolymers with ion-transporting side groups, *Synth. Met.* **2001**, 122, 111-113.
- [78] C. Yang, G. He, R. Wang, Y. Li, luminescent block copolymer containing PEO-like segments for polymer light-emitting devices, *Mol. Cryst. Liq. Cryst.* **1999**, 337, 473-476.
- [79] Q. Sun, H. Wang, C. Yang, G. He, Y. Li, blue-green light-emission LECs based on block copolymers containing di( $\alpha$ -naphthalene vinylene)benzene chromophores and tri(ethylene oxide) spacers, *Synth. Met.* **2002**, 128, 161-165.
- [80] Q. Sun, H. Wang, C. Yang, Y. Li, synthesis and electroluminescence of novel copolymers containing crown ether spacers, *J. Mater. Chem.* **2003**, 13, 800-806.
- [81] R. D. Costa, E. Ortí, H. J. Bolink, S. Graber, C. E. Housecroft, E. C. Constable, efficient and long-living light-emitting electrochemical cells, *Adv. Funct. Mater.* **2010**, 20, 1511-1520.
- [82] R. Hany, B. Fan, F. A. de Castro, J. Heier, W. Kylberg, F. Nüesch, strategies to improve cyanine dye multi layer organic solar cells, *Prog. Photovolt: Res. Appl.* **2011**, 19, 851-857.
- [83] H. Zhang, G. Wicht, C. Gretener, M. Nagel, F. Nüesch, Y. Romanyuk, J. Tisserant, R. Hany, semitransparent organic photovoltaics using a near-infrared absorbing cyanine dye, *Sol. Energy Mater. Sol. Cells* **2013**, 118, 157-164.
- [84] O. Malinkiewicz, T. Grancha, A. Molina-Ontoria, A. Soriano, H. Brine, H. J. Bolink, efficient, cyanine dye based bilayer solar cells, *Adv. Energy Mater.* **2013**, 3, 472-477.
- [85] P. Pachler, F. P. Wenzl, U. Scherf, G. Leising, the efficiency of light-emitting electrochemical cells, *J. Phys. Chem. B* **2005**, 109, 6020-6024.
- [86] Y. Kervella, M. Armand, O. Stéphan, organic light-emitting electrochemical cells based on polyfluorene investigation of the failure modes, *J. Electrochem. Soc.* **2001**, 148, H155-H160.
- [87] F. AlTal, J. Gao, long-term testing of polymer light-emitting electrochemical cells: reversible doping and black spots, *Org. Electron.* **2015**, 18, 1-7.
- [88] S. van Reenen, R. A. J. Janssen, M. Kemerink, dynamic processes in sandwich polymer light-emitting electrochemical cells, *Adv. Funct. Mater.* **2012**, 22, 4547-4556.
- [89] A. Munar, A. Sandström, S. Tang, L. Edman, shedding light on the operation of polymer light-emitting electrochemical cells using impedance spectroscopy, *Adv. Funct. Mater.* **2012**, 22, 1511-1517.

- [90] I. H. Campbell, D. L. Smith, C. J. Neef, J. P. Ferraris, capacitance measurements of junction formation and structure in polymer light-emitting electrochemical cells, *Appl. Phys. Lett.* **1998**, 72, 2565-2567.
- [91] L. Holzer, F. P. Wenzl, R. Sotgiu, M. Gritsch, S. Tasch, H. Hutter, M. Sampietro, G. Leising, charge distribution in light emitting electrochemical cells, *Synth. Met.* **1999**, 102, 1022-1023.
- [92] S. B. Toshner, Z. Zhu, I. V. Kosilkin, J. M. Leger, characterization of ion profiles in light-emitting electrochemical cells by secondary ion mass spectroscopy, *ACS Appl. Mater. Interfaces* **2012**, 4, 1149-1153.
- [93] M. Gritsch, H. Hutter, L. Holzer, S. Tasch, local ions distribution inhomogeneities in polymer based light emitting cells, *Mikrochim. Acta* **2000**, 135, 131-137.
- [94] J. Gao, J. Dane, visualization of electrochemical doping and light-emitting junction formation in conjugated polymer films, *Appl. Phys. Lett.* **2004**, 84, 2778-2780.
- [95] J. Gao, J. Dane, planar polymer light-emitting electrochemical cells with extremely large interelectrode spacing, *Appl. Phys. Lett.* **2003**, 83, 3027-3029.
- [96] Y. Hu, J. Gao, direct imaging and probing of the p-n junction in a planar polymer light-emitting electrochemical cell, *J. Am. Chem. Soc.* **2011**, 133, 2227-2231.
- [97] D. J. Dick, A. J. Heeger, Y. Yang, Q. Pei, imaging the structure of the p-n junction in polymer light-emitting electrochemical cells, *Adv. Mater.* **1996**, 8, 985-987.
- [98] S. van Reenen, P. Matyba, A. Dzwilewski, R. A. J. Janssen, L. Edman, M. Kemerink, salt concentration effects in planar light-emitting electrochemical cells, *Adv. Funct. Mater.* **2011**, 21, 1795-1802.
- [99] D. B. Rodovsky, O. G. Reid, L. S. C. Pingree, D. S. Ginger, concerted emission and local potentiometry of light-emitting electrochemical cells, *ACS Nano* **2010**, 4, 2673-2680.
- [100] J. D. Slinker, J. A. Defranco, M. J. Jaquith, W. R. Silveira, Y. Zhong, J. M. Moran-Mirabal, H. G. Craighead, H. D. Abruña, J. A. Marohn, G. G. Malliaras, direct measurement of the electric-field distribution in a light-emitting electrochemical cell, *Nature Mater.* **2007**, 6, 894-899.
- [101] H. J. Bolink, E. Coronado, R. D. Costa, E. Ortí, M. Sessolo, S. Graber, K. Doyle, M. Neuburger, C. E. Housecroft, E. C. Constable, long-living light-emitting electrochemical cells – control through supramolecular interactions, *Adv. Mater.* **2008**, 20, 3910-3913.

- [102] R. D. Costa, E. Ortí, H. J. Bolink, S. Graber, C. E. Housecroft, E. C. Constable, intramolecular  $\pi$ -stacking in a phenylpyrazole-based iridium complex and its use in light-emitting electrochemical cells, *J. Am. Chem. Soc.* **2010**, 132, 5978-5980.
- [103] M. Lenes, G. Garcia-Belmonte, D. Tordera, A. Pertegás, J. Bisquert, H. J. Bolink, operating modes of sandwiched light-emitting electrochemical cells, *Adv. Funct. Mater.* **2011**, 21, 1581-1586.
- [104] C. Liao, H. Chen, H. Su, K. Wong, tailoring carrier injection efficiency to improve the carrier balance of solid-state light-emitting electrochemical cells, *Phys. Chem. Chem. Phys.* **2012**, 14, 9774-9784.
- [105] J. C. deMello, N. Tessler, S. C. Graham, R. H. Friend, ionic space-charge effects in polymer light-emitting diodes, *Phys. Rev. B* **1998**, 57, 12951-12963.
- [106] M. Lenes, H. J. Bolink, ionic space-charge effects in solid state organic photovoltaics, *ACS Appl. Mater. Interfaces* **2010**, 2, 3664-3668.
- [107] H. Benmansour, F. A. Castro, M. Nagel, J. Heier, R. Hany, F. Nüesch, ionic space charge driven organic photovoltaic devices, *Chimia* **2007**, 61, 787-791.
- [108] R. J. Mortimer, A. L. Dyer, J. R. Reynolds, electrochromic organic and polymeric materials for display applications, *Displays* **2006**, 27, 2-18.
- [109] G. Sonmez, polymeric electrochromics, *Chem. Commun.* **2005**, 5251-5259.
- [110] R. J. Mortimer, organic electrochromic materials, *Electrochim. Acta* **1999**, 44, 2971-2981.
- [111] R. H. Baughman, conducting polymer artificial muscles, *Synth. Met.* **1996**, 78, 339-353.
- [112] S. Ashley, artificial muscles, *Sci. Am.* **2003**, 289, 53-59.
- [113] E. Smela, conjugated polymer actuators for biomedical applications, *Adv. Mater.* **2003**, 15, 481-494.
- [114] T. Mirfakhrai, J. D. W. Madden, R. H. Baughman, polymer artificial muscles, *Mater. Today* **2007**, 10, 30-38.
- [115] J. Liang, Z. Yu, L. Li, H. Gao, Q. Pei, chapter 4: stable junction polymer light-emitting electrochemical cells, *Organic Nanophotonics* **2015**, page 87-117.
- [116] J. Gao, G. Yu, A. J. Heeger, polymer light-emitting electrochemical cells with frozen p-i-n junction, *Appl. Phys. Lett.* **1997**, 71, 1293-1295.

- [117] J. Gao, Y. Li, G. Yu, A. J. Heeger, polymer light-emitting electrochemical cells with frozen junctions, *J. Appl. Phys.* **1999**, 86, 4594-4599.
- [118] Y. Li, J. Gao, D. Wang, G. Yu, Y. Cao, A. J. Heeger, a.c. impedance of frozen junction polymer light-emitting electrochemical cells, *Synth. Met.* **1998**, 97, 191-194.
- [119] J. Gao, G. Yu, A. J. Heeger, polymer p-i-n junction photovoltaic cells, *Adv. Mater.* **1998**, 10, 692-695.
- [120] J. Dane, C. Tracy, J. Gao, direct observation of a frozen junction in polymer light-emitting electrochemical cells, *Appl. Phys. Lett.* **2005**, 86, 153509.
- [121] A. AlTal, J. Gao, scanning photocurrent and PL imaging of a frozen polymer p-i-n junction, *Phys. Status Solidi RRL* **2015**, 9, 77-81.
- [122] J. Shin, S. Xiao, Å. Fransson, L. Edman, polymer light-emitting electrochemical cells: frozen-junction operation of an "ionic liquid" device, *Appl. Phys. Lett.* **2005**, 87, 043506.
- [123] A. Inayeh, B. Dorin, J. Gao, scanning photocurrent and photoluminescence imaging of a frozen polymer p-n junction, *Appl. Phys. Lett.* **2012**, 101, 253305.
- [124] Y. Zhang, Y. Hu, J. Gao, improving the efficiency of polymer light-emitting electrochemical cells by controlled doping relaxation, *Appl. Phys. Lett.* **2006**, 88, 163507.
- [125] S. van Reenen, M. V. Vitorino, S. C. Meskers, R. A. J. Janssen, M. Kemerink, photoluminescence quenching in films of conjugated polymers by electrochemical doping, *Phys. Rev. B* **2014**, 89, 205206.
- [126] S. B. Meier, D. Hartmann, D. Tordera, H. J. Bolink, A. Winnacker, W. Sarfert, dynamic doping and degradation in sandwich-type light-emitting electrochemical cells, *Phys. Chem. Chem. Phys.* **2012**, 14, 10886-10890.
- [127] Y. Zhang, Y. Hu, J. Gao, photovoltaic response of a polymer p-i-n junction, *Appl. Phys. Lett.* **2007**, 91, 233509.
- [128] G. Yu, Y. Cao, M. Andersson, J. Gao, A. J. Heeger, polymer light-emitting electrochemical cells with frozen p-i-n junction at room temperature, *Adv. Mater.* 1998, 10, 385-388.
- [129] G. Wantz, B. Gautier, F. Dumur, T. N. T. Phan, D. Gigmes, L. Hirsch, J. Gao, towards frozen organic PN junctions at room temperature using high- $T_g$  polymeric electrolytes, *Org. Electron.* **2012**, 13, 1859-1864.



- [130] C. Yang, Q. Sun, J. Qiao, Y. Li, ionic liquid doped polymer light-emitting electrochemical cells, *J. Phys. Chem. B* **2003**, 107, 12981-12988.
- [131] L. Edman, M. A. Summers, S. K. Buratto, A. J. Heeger, polymer light-emitting electrochemical cells: doping, luminescence, and mobility, *Phys. Rev. B* **2004**, 70, 115212.
- [132] J. M. Leger, D. B. Rodovsky, G. P. Bartholomew, self-assembled, chemically fixed homojunctions in semiconducting polymers, *Adv. Mater.* **2006**, 18m 3130-3134.
- [133] J. M. Leger, D. G. Patel, D. B. Rodovsky, G. P. Bartholomew, polymer photovoltaic devices employing a chemically fixed p-i-n junction, *Adv. Funct. Mater.* **2008**, 18, 1212-1219.
- [134] I. V. Kosilkin, M. S. Martens, M. P. Murphy, J. M. Leger, polymerizable ionic liquids for fixed-junction polymer light-emitting electrochemical cells, *Chem. Mater.* **2010**, 22, 4838-4840.
- [135] Z. Yu, M. Sun, Q. Pei, electrochemical formation of stable p-i-n junction in conjugated polymer thin films, *J. Phys. Chem. B* **2009**, 113, 8481-8486.
- [136] Z. Yu, M. Wang, G. Lei, J. Liu, L. Li, Q. Pei, stabilizing the dynamic p-i-n junction in polymer light-emitting electrochemical cells, *J. Phys. Chem. Lett.* **2011**, 2, 367-372.
- [137] S. Tang, K. Irgum, L. Edman, chemical stabilization of doping in conjugated polymers, *Org. Electron.* **2010**, 11, 1079-1087.
- [138] S. Tang, L. Edman, on-demand photochemical stabilization of doping in light-emitting electrochemical cells, *Electrochim. Acta* **2011**, 56, 10473-10478.
- [139] C. H. W. Cheng, M. C. Lonergan, a conjugated polymer pn junction, *J. Am. Chem. Soc.* **2004**, 126, 10536-10537.
- [140] D. A. Bernards, S. Flores-Torres, H. D. Abruña, G. G. Malliaras, observation of electroluminescence and photovoltaic response in ionic junctions, *Science* **2006**, 313, 1416-1419.
- [141] O. J. Cayre, S. T. Chang, O. D. Velev, polyelectrolyte diode: nonlinear current response of a junction between aqueous ionic gels, *J. Am. Chem. Soc.* **2007**, 129, 10801-10806.
- [142] C. V. Hoven, H. Wang, M. Elbing, L. Garner, D. Winkelhaus, G. C. Bazan, chemically fixed p-n heterojunctions for polymer electronics by means of covalent B-F bond formation, *Nature Mater.* **2010**, 9, 249-252.

- [143] R. A. Abramovitch, E. P. Kyba, chapter 5: decomposition of organic azides, *The Azido Group* **1971**, John Wiley & Sons, Ltd.
- [144] G. L'abbe, decomposition and addition reactions of organic azides, *Chem. Rev.* **1969**, 69, 345-363.
- [145] J. F. W. Keana, S. X. Cai, new reagents for photoaffinity labeling: synthesis and photolysis of functionalized perfluorophenyl azides, *J. Org. Chem.* **1990**, 55, 3640-3647.
- [146] L. H. Liu, M. Yan, perfluorophenyl azides: new applications in surface functionalization and nanomaterial synthesis, *Acc. Chem. Res.* **2010**, 43, 1434-1443.
- [147] O. Norberg, L. Deng, M. Yan, O. Ramström, photo-click immobilization of carbohydrates on polymeric surfaces-a quick method to functionalize surfaces for biomolecular recognition studies, *Bioconjugate Chem.* **2009**, 20, 2364-2370.
- [148] K. R. Gee, E. A. Archer, H. C. Kang, 4-sulfotetrafluorophenyl (STP) esters: new water-soluble amine-reactive reagents for labeling biomolecules, *Tetrahedron Lett.* **1999**, 40, 1471-1474.
- [149] J. F. W. Keana, S. X. Cai, functionalized perfluorophenyl azides: new reagents for photoaffinity labeling, *J. Fluorine Chem.* **1983**, 43, 151-154.
- [150] L. R. Odell, N. Chau, A. Mariana, M. E. Graham, P. J. Robinson, A. McCluskey, azido and diazarinyl analogues of bis-tyrphostin as asymmetrical inhibitors of dynamin GTPase, *ChemMedChem* **2009**, 4, 1182-1188.
- [151] S. Bräse, G. Gil, K. Knepper, V. Zimmermann, organic azides: an exploding diversity of a unique class of compounds, *Angew. Chem. Int. Ed.* **2005**, 44, 5188-5240.
- [152] W. H. Pearson, P. S. Ramamoorthy, H. Y. Lo, phenyl azide, *e-EROS Encyclopedia of Reagents for Organic Synthesis* **2008**.
- [153] R. Belloli, nitrenes, *J. Chem. Educ.* **1971**, 48, 422-426.
- [154] R. A. Abramovitch, B. A. Davis, preparation and properties of imido intermediates (imidogens), *Chem. Rev.* **1964**, 64, 149-185.
- [155] L. Horner, A. Christmann, nitrenes, *Angew. Chem. Int. Ed.* **1963**, 2, 599-608.
- [156] E. Leyva, M. S. Platz, G. Persy, J. Wirz, photochemistry of phenyl azide: the role of singlet and triplet phenylnitrene as transient intermediates, *J. Am. Chem. Soc.* **1986**, 108, 3783-3790.

- [157] A. K. Schrock, G. B. Schuster, photochemistry of phenyl azide: chemical properties of the transient intermediates, *J. Am. Chem. Soc.* **1984**, 106, 5228-5234.
- [158] E. F. C. Scriven, K. Turnbull, azides: their preparation and synthetic uses, *Chem. Rev.* **1988**, 88, 297-368.
- [159] M. F. Budyka, M. M. Kantor, M. V. Alfimov, the photochemistry of phenyl azide, *Russ. Chem. Rev.* **1992**, 61, 25-39.
- [160] N. Gritsan, M. Platz, chapter 11: photochemistry of azides: the azide/nitrene interface, *organic azides: syntheses and application* **2010**.
- [161] R. Poe, J. Grayzar, M. J. T. Young, E. Leyva, K. A. Schnapp, M. S. Platz, remarkable catalysis of intersystem crossing of singlet (pentafluorophenyl)nitrene, *J. Am. Chem. Soc.* **1991**, 113, 3209-3211.
- [162] H. Dürr, H. Kober, triplet states from azides, *Top. Curr. Chem.* **1976**, 66, 89-114.
- [163] F. D. Lewis, W. H. Saunders Jr., the intermediates in direct photolysis of alkyl azides, *J. Am. Chem. Soc.* **1968**, 90, 7031-7033.
- [164] R. F. Klima, A. D. Gudmundsdóttir, intermolecular triplet-sensitized photolysis of alkyl azides trapping of triplet alkyl nitrenes, *J. Photochem. Photobiol. A* **2004**, 162, 239-247.
- [165] A. Reiser, L. J. Leyshon, spin state of photogenerated phenylnitrene, *J. Am. Chem. Soc.* **1971**, 93, 4051-4052.
- [166] L. Barash, E. Wasserman, W. A. Yager, generation of methylenes from germinal diazides via excited nitrenes, *J. Am. Chem. Soc.* **1967**, 89, 3931-3932.
- [167] M. Tsuda, S. Oikawa, triplet states of photosensitive aromatic azides, *ACS Symp. Ser.* **1976**, 25, 423-445.
- [168] J. S. Swenton, T. J. Ikeler, B. H. Williams, interaction of aromatic hydrocarbon excited singlet states with 2-azidobiphenyl, *J. Chem. Soc. D* **1969**, 1263-1264.
- [169] J. S. Swenton, T. J. Ikeler, B. H. Williams, the photochemistry of singlet and triplet azide excited states, *J. Am. Chem. Soc.* **1970**, 92, 3103-3109.
- [170] L. J. Leyshon, A. Reiser, sensitized photodecomposition of phenyl azide and  $\alpha$ -naphthyl azide, *J. Chem. Soc. Faraday Trans. 2*, **1972**, 68, 1918.
- [171] E. P. Farney, T. P. Yoon, visible-light sensitization of vinyl azides by transition-metal photocatalysis, *Angew. Chem. Int. Ed.* **2014**, 53, 793-797.

- [172] A. Marcinek, E. Leyva, D. Whitt, M. S. Platz, evidence for stepwise nitrogen extrusion and ring expansion upon photolysis of phenyl azide, *J. Am. Chem. Soc.* **1993**, 115, 8609-8612.
- [173] E. Brachet, T. Ghosh, I. Ghosh, B. König, visible light C-H amidation of heteroarenes with benzoyl azides, *Chem. Sci.* **2015**, 6, 987-992.
- [174] C. K. Prier, D. A. Rankic, D. W. C. MacMillan, visible light photoredox catalysis with transition metal complexes: applications in organic synthesis, *Chem. Rev.* **2013**, 113, 5322-5363.
- [175] F. D. Lewis, W. H. Saunders, sensitized photolysis of organic azides. possible case of nonclassical energy transfer, *J. Am. Chem. Soc.* **1968**, 90, 7033-7038.
- [176] A. Treinin, chapter 1: general and theoretical aspects, *The Azido Group* **1971**, John Wiley & Sons, Ltd.
- [177] G. Smolinsky, E. Wasserman, W. A. Yager, the E.P.R. of ground state triplet nitrenes, *J. Am. Chem. Soc.* **1962**, 84, 3220-3221.
- [178] A. Reiser, G. Bowes, R. J. Horne, photolysis of aromatic azides. part 1. – electronic spectra of aromatic nitrenes and their parent azides, *Trans. Faraday Soc.* **1966**, 62, 3162-3169.
- [179] A. Reiser, V. Frazer, ultra-violet absorption spectra of aromatic nitrenes and dinitrenes, *Nature* **1965**, 208, 682-683.
- [180] S. Rajam, A. V. Jadhav, Q. Li, S. K. Sarkar, P. N. D. Singh, A. Rohr, T. C. S. Pace, R. Li, J. A. Krause, C. Bohne, B. S. Ault, A. D. Gudmundsdottir, triplet sensitized photolysis of a vinyl azide: direct detection of a triplet vinyl azide and nitrene, *J. Org. Chem.* **2014**, 79, 9325-9334.
- [181] N. P. Gritsan, I. Likhovvorik, Z. Zhu, M. S. Platz, observation of perfluoromethylnitrene in cryogenic matrixes, *J. Phys. Chem. A* **2001**, 105, 3039-3041.
- [182] T. Bally, chapter 17: matrix isolation, *Reactive Intermediate Chemistry* **2003**, John Wiley & Sons.
- [183] O. L. Chapman, J. P. Le Roux, 1-aza-1,2,4,6-cycloheptatetraene, *J. Am. Chem. Soc.* **1978**, 100, 282-285.
- [184] J. C. Hayes, R. S. Sheridan, infrared spectrum of triplet phenylnitrene. On the origin of dihydroazepine in low-temperature matrices, *J. Am. Chem. Soc.* **1990**, 112, 5879-5881.
- [185] J. Mieres-Pérez, E. Mendez-Vega, K. Velappan, W. Sander, reaction of triplet phenylnitrene with molecular oxygen, *J. Org. Chem.* **2015**, 80, 11926-11931.

- [186] W. Lwowski, T. J. Maricich, carbethoxynitrene. Selectivity of the C-H insertion, *J. Am. Chem. Soc.* **1964**, 86, 3164-3165.
- [187] C. J. Shields, D. R. Chrisope, G. B. Schuster, A. J. Dixon, M. Poliakoff, J. J. Turner, photochemistry of aryl azides: detection and characterization of a dehydroazepine by time-resolved infrared spectroscopy and flash photolysis at room temperature, *J. Am. Chem. Soc.* **1987**, 109, 4723-4726.
- [188] I. R. Dunkin, P. C. P. Thomson, pentafluorophenyl nitrene: a matrix isolated aryl nitrene that does not undergo ring expansion, *J. Chem. Soc. Chem. Commun.* 1982, 1192-1193.
- [189] W. T. Borden, N. P. Gritsan, C. M. Hadad, W. L. Karney, C. R. kemnitz, M. S. Platz, the interplay of theory and experiment in the study of phenylnitrene, *Acc. Chem. Res.* **2000**, 33, 765-771.
- [190] M. S. Platz, comparison of phenylcarbene and phenylnitrene, *Acc. Chem. Res.* **1995**, 28, 487-492.
- [191] R. E. Banks, G. R. Sparkes, studies in azide chemistry. part V. synthesis of 4-azido-2,3,5,6-tetrafluoro-, 4-azido-3-chloro-2,5,6-trifluoro-, and 4-azido-3,5-dichloro-2,6-difluoro-pyridine, and some thermal reactions of the tetrafluoro-compound, *J. Chem. Soc. Perkin Trans.* **1972**, 1, 2964-2970.
- [192] Y. Z. Li, J. P. Kirby, M. W. George, M. Poliakoff, G. B. Schuster, 1,2-didehydroazepines from the photolysis of substituted aryl azides: analysis of their chemical and physical properties by time-resolved spectroscopic methods, *J. Am. Chem. Soc.* **1988**, 110, 8092-8098.
- [193] T. Y. Liang, G. B. Schuster, photochemistry of 3- and 4-nitrophenyl azide: detection and characterization of reactive intermediates, *J. Am. Chem. Soc.* **1987**, 109, 7803-7810.
- [194] E. Leyva, M. J. T. Young, M. S. Platz, high yields of formal CH insertion products in the reactions of polyfluorinated aromatic nitrenes, *J. Am. Chem. Soc.* **1986**, 108, 8307-8309.
- [195] G. W. J. Fleet, R. R. Porter, J. R. Knowles, affinity labelling of antibodies with aryl nitrene as reactive group, *Nature* **1969**, 224, 511-512.
- [196] K. A. Schnapp, R. Poe, E. Leyva, N. Soundararajan, M. S. Platz, expository photochemistry of fluorinated aryl azides. implications for the design of photoaffinity labeling reagents, *Bioconjugate Chem.* **1993**, 4, 172-177.
- [197] H. Bayley, J. R. Knowles, photogenerated reagents for membrane labeling. 1. phenylnitrene formed within the lipid bilayer, *Biochemistry* **1978**, 17, 2414-2419.

- [198] J. R. Knowles, photogenerated reagents for biological receptor-site labeling, *Acc. Chem. Res.* **1972**, 5, 155-160.
- [199] E. Okada, Y. Komazawa, M. Kurihara, H. Inoue, N. Miyata, H. Okuda, T. Tsuchiya, Y. Yamakoshi, synthesis of C<sub>60</sub> derivatives for photoaffinity labeling, *Tetrahedron Lett.* **2004**, 45, 527-529.
- [200] M. Yan, S. Cai, M. N. Wybourne, J. F. W. Keana, photochemical functionalization of polymer surfaces and the production of biomolecule-carrying micrometer-scale structures by deep-UV lithography using 4-substituted perfluorophenyl azides, *J. Am. Chem. Soc.* **1993**, 115, 814-816.
- [201] M. Yan, S. Cai, M. N. Wybourne, J. F. W. Keana, N-hydroxysuccinimide ester functionalized perfluorophenyl azides as novel photoactive heterobifunctional cross-linking reagents. the covalent immobilization of biomolecules to polymer surfaces, *Bioconjugate Chem.* **1994**, 5, 151-157.
- [202] S. J. Pastine, D. Okawa, B. Kessler, M. Rolandi, M. Llorente, A. Zettl, J. M. J. Fréchet, a facile and patternable method for the surface modification of carbon nanotube forests using perfluoroarylazides, *J. Am. Chem. Soc.* **2008**, 130, 4238-4239.
- [203] X. Pei, H. Yu, Z. Pei, M. Theurer, C. Ammer, S. André, H. Gabius, M. Yan, O. Ramström, photoderivatized polymer thin films at quartz crystal microbalance surfaces: sensors for carbohydrate – protein interactions, *Anal. Chem.* **2007**, 79, 6897-6902.
- [204] L. Liu, M. H. Engelhard, M. Yan, surface and interface control on photochemically initiated immobilization, *J. Am. Chem. Soc.* **2006**, 128, 14067-14072.
- [205] M. Yan, J. Ren, covalent immobilization of ultrathin polymer films by thermal activation of perfluorophenyl azide, *Chem. Mater.* **2004**, 16, 1627-1632.
- [206] M. Yan, J. Ren, covalent immobilization of polypropylene thin films, *J. Mater. Chem.* **2005**, 15, 523-527.
- [207] X. Wang, O. Ramström, M. Yan, a photochemically initiated chemistry for coupling underivatized carbohydrates to gold nanoparticles, *J. Mater. Chem.* **2009**, 19, 8944-8949.
- [208] D. Joester, E. Klein, E. Geiger, L. Addadi, temperature-sensitive micrometer-thick layers of hyaluronan grafted on microspheres, *J. Am. Chem. Soc.* **2006**, 128, 1119-1124.
- [209] M. A. Bartlett, M. Yan, fabrication of polymer thin films and arrays with spatial and topographical controls, *Adv. Mater.* **2001**, 13, 1449-1451.

- [210] J. W. Rumer, I. McCulloch, organic photovoltaics: crosslinking for optimal morphology and stability, *Mater. Today* **2015**, 18, 425-435.
- [211] A. Guerrero, G. Garcia-Belmonte, recent advances to understand morphology stability of organic photovoltaics, *Nano-Micro Lett.* **2017**, 9: 10.
- [212] G. Wantz, L. Derue, O. Dautel, A. Rivaton, P. Hudhomme, C. Dagron-Lartigau, stabilizing polymer-based bulk heterojunction solar cells via crosslinking, *Polym. Int.* **2014**, 63, 1346-1361.
- [213] J. W. Rumer, R. S. Ashraf, N. D. Eisenmenger, Z. Huang, I. Meager, C. B. Nielsen, B. C. Schroeder, M. L. Chabinyc, I. McCulloch, dual function additives: a small molecule crosslinker for enhanced efficiency and stability in organic solar cells, *Adv. Energy Mater.* **2015**, 5, 1401426.
- [214] R. Png, P. Chia, J. Tang, B. Liu, S. Sivaramakrishnan, M. Zhou, S. Khong, H. S. O. Chan, J. H. Burroughes, L. Chua, R. H. Friend, P. K. H. Ho, high-performance polymer semiconducting heterostructure devices by nitrene-mediated photocrosslinking of alkyl side chains, *Nat. Mater.* **2010**, 9, 152-158.
- [215] B. Liu, R. Png, L. Zhao, L. Chua, R. H. Friend, P. K. H. Ho, high internal quantum efficiency in fullerene solar cells based on crosslinked polymer donor networks, *Nat. Commun.* **2012**, 3, 1321.
- [216] N. Cho, H. Yip, J. A. Davies, P. D. Kazarinoff, D. F. Zeigler, M. M. Durban, Y. Segawa, K. M. O'Malley, C. K. Luscombe, A. K. Y. Jen, in-situ crosslinking and n-doping of semiconducting polymers and their application as efficient electron-transporting materials in inverted polymer cells, *Adv. Energy Mater.* **2011**, 1, 1148-1153.
- [217] L. Derue, O. Dautel, A. Tournebize, M. Drees, H. Pan, S. Berthumeyrie, B. Pavageau, E. Cloutet, S. Chambon, L. Hirsch, A. Rivaton, P. Hudhomme, A. Facchetti, G. Wantz, thermal stabilisation of polymer-fullerene bulk heterojunction morphology for efficient photovoltaic solar cells, *Adv. Mater.* **2014**, 26, 5831-5838.
- [218] B. Gholamkhash, S. Holdcroft, toward stabilization of domains in polymer bulk heterojunction films, *Chem. Mater.* **2010**, 22, 5371-5376.
- [219] C. Nam, Y. Qin, Y. S. Park, H. Hlaing, X. Lu, B. M. Ocko, C. T. Black, R. B. Grubbs, photo-cross-linkable azide-functionalized polythiophene for thermally stable bulk heterojunction solar cells, *Macromolecules* **2012**, 45, 2338-2347.

[220] H. J. Kim, A. Han, C. Cho, H. Kang, H. Cho, M. Y. Lee, J. M. J. Fréchet, J. H. Oh, B. J. Kim, solvent-resistant organic transistors and thermally stable organic photovoltaics based on cross-linkable conjugated polymers, *Chem. Mater.* **2012**, 24, 215-221.

[221] K. A. Murray, A. B. Holmes, S. C. Moratti, G. Rumbles, conformational changes in regioregular polythiophenes due to thermal crosslinking, *J. Mater. Chem.* **1999**, 9, 2109-2115.

[222] M. Prato, Q. C. Li, F. Wudl, V. Lucchini, addition of azides to fullerene C<sub>60</sub>: synthesis of azafulleroids, *J. Am. Chem. Soc.* 1993, 115, 1148-1150.



## Chapter 2: Synthesis of Cyanine Dyes and Polyelectrolytes

### 2.1 Introduction

Generic cyanine dyes contain two nitrogen centers, one of which is positively charged.<sup>1</sup> To maintain charge neutrality, cyanine dyes are accompanied by a counter anion. Iodide or chloride usually results from the dye synthesis. In a subsequent step, exchange with a different anion is possible.

Here, I present different strategies to alter the cyanine counter ion, generating new cyanine small molecules with a desired small anion or cyanine polyelectrolytes (Cy-Poly) with a large anionic polymer backbone. The aim of synthesizing such new cyanine dyes and their application in organic devices will be individually described in the following chapters.

In this chapter, part of the data for Cy-Poly are taken from the following publication: "Cyanine dye polyelectrolytes for organic bilayer solar cells" by Lei Wang, Christian Hinderling, Sandra Jenatsch, Frank Nüesch, Daniel Rentsch, Roland Steim, Hui Zhang, Roland Hany, *Polymer*, **2014**, 55, 3195-3201. All synthesis was performed by the author. NMR measurements and spectra analysis were carried out by the author and Daniel Rentsch (Empa).

### 2.2 Experimental

#### 2.2.1 Materials and methods

Unless stated otherwise, all chemicals and solvents were used without further purification. Methyl methacrylate (MMA, distilled before use, Aldrich), 2-sulfoethyl methacrylate (H-MES, ABCR), ethylene glycol dimethacrylate (EDMA, Aldrich), poly(ethylene glycol) methyl ether methacrylate (PEGMA, filtered through a plug of basic alumina before use, Aldrich), 2,2'-azobis(2-methylpropionitrile) (AIBN, recrystallized from diethyl ether before use, Fluka), silver(I) oxide (Ag<sub>2</sub>O, Sigma-Aldrich), thin layer chromatography (TLC) silica gel (Merck), 1,3,3-trimethyl-2-[5-(1,3,3-trimethyl-1,3-dihydro-indol-2-ylidene)-penta-1,3-dienyl]-3H-indolium chloride (Cy5-Cl, FEW Chemicals), 1-ethyl-2[3-(1-ethyl-3,3-dimethyl-1,3-dihydro-indol-2-ylidene)-propenyl]-3,3-dimethyl-3H-indolium iodide (Cy3-I, FEW Chemicals), 2-[2-[2-chloro-3-[2-(1,3-dihydro-1,1,3-trimethyl-2H-benzo[e]-indol-2-ylidene)-ethylidene]-1-cyclohexen-1-

yl]-ethenyl]-1,1,3-trimethyl-1H-benzo[e]indolium chloride (Cy7-Cl, FEW Chemicals), 3-ethyl-2-[3-(3-ethyl-3H-benzoxazol-2-ylidene)-propenyl]-benzoxazolium iodide (bCy3-I, FEW Chemicals), 3-ethyl-2-(2-((3-ethylbenzo[d]oxazol-2(3H)-ylidene)methyl)but-1-enyl)benzo[d]oxazol-3-ium ethylsulfate (STCy3-ES, Synthon Chemicals), 3,3'-diethylthiacyanine iodide (Cy1-I, Sigma-Aldrich), methyl pentafluorobenzoate (Aldrich), 4-azidobenzoic acid (TCI America), sodium azide ( $\text{NaN}_3$ , Sigma-Aldrich), sodium hydroxide ( $\text{NaOH}$ , Sigma-Aldrich), sodium bicarbonate ( $\text{NaHCO}_3$ , Sigma), sodium sulfate ( $\text{Na}_2\text{SO}_4$ , Sigma-Aldrich), sodium hexafluorophosphate ( $\text{NaPF}_6$ , Aldrich), hydrochloric acid ( $\text{HCl}$ , Sigma-Aldrich), silver nitrate ( $\text{AgNO}_3$ , Sigma-Aldrich), Amberlite IRA-400 chloride form (Aldrich), methanol ( $\text{MeOH}$ , Sigma-Aldrich), ethanol ( $\text{EtOH}$ , Sigma-Aldrich), 2-propanol (Sigma-Aldrich), dichloromethane (DCM, Sigma-Aldrich), chloroform ( $\text{CHCl}_3$ , Sigma-Aldrich), tetrahydrofuran (THF, Merck), diethyl ether (Sigma-Aldrich), acetone (Sigma-Aldrich), 2,2,3,3-tetrafluoro-1-propanol (TFP, Aldrich), dimethyl sulfoxide (DMSO, Carl Roth).

Nuclear magnetic resonance (NMR) spectra were recorded on Bruker 300 MHz, 400 MHz and 500 MHz spectrometers. Thermogravimetric analysis (TGA) was carried out on a Netzsch TG 209 F1. X-ray fluorescence (XRF) spectra were measured on an ARL Advant XP. Differential scanning calorimetry (DSC) analysis was carried out on a Perkin Elmer DSC 8000. Elemental analysis was carried out by the micro-laboratory of ETH Zürich. Ion chromatography analysis was carried out on a Metrohm 883 Basic IC plus. Electrospray ionization mass spectroscopy (ESI-MS) was carried out on a Waters Xevo TQD. Gel permeation chromatography (GPC) analysis was carried out on an Agilent Serie 1100.

### 2.2.2 Synthesis of Cy-Poly

#### *Synthesis of Poly20*

The synthesis of Poly20 is described as a representative example. Copolymers Poly30, Poly50, PEG25Poly50 and PEG50Poly50 were prepared accordingly. MMA (1 mL, 9.35 mmol) and H-MES (454 mg, 2.34 mmol) were dissolved in anhydrous THF (12 mL) under stirring. AIBN (9.7 mg, 0.059 mmol) was then added to the solution under nitrogen flow and the reaction flask was heated to 70 °C under reflux for 20 h. The solution was then cooled to room temperature, poured into diethyl ether (90 mL) and agitated for 5 min. The precipitate was collected by

filtration and purified by washing twice with diethyl ether. Poly20 was then dried at 40 °C in vacuum (936 mg, yield 67%).

#### ***Synthesis of Poly30***

MMA (1 mL, 9.35 mmol), H-MES (779 mg, 4.01 mmol), AIBN (11.0 mg, 0.067 mmol) and THF (14 mL) gave 1350 mg Poly30 (78%).

#### ***Synthesis of Poly50***

MMA (0.63 mL, 5.89 mmol), H-MES (1.14 g, 5.87 mmol), AIBN (11.0 mg, 0.067 mmol) and THF (20 mL) gave 1233 mg Poly50 (71%).

#### ***Synthesis of PEG25Poly50***

MMA (209 mL, 2.08 mmol), H-MES (812 mg, 4.18 mmol), PEGMA (632 mg, 2.11 mmol), AIBN (7.2 mg, 0.044 mmol) and THF (20 mL) gave 1160 mg PEG25Poly50 (70%).

#### ***Synthesis of PEG50Poly50***

PEGMA (1.21 g, 4.02 mmol), H-MES (782 mg, 4.03 mmol), AIBN (6.8 mg, 0.041 mmol) and THF (20 mL) gave 361 mg PEG50Poly50 (18%).

#### ***Synthesis of Cy5-Poly20***

The synthesis of Cy5-Poly20 is described as a representative example. Other Cy-Poly were prepared accordingly. Poly20 (200 mg containing 0.336 mmol sulfonic acid groups) and Ag<sub>2</sub>O (117 mg, 0.505 mmol) were mixed in MeOH (15 mL). The reaction flask was covered with aluminum foil to prevent exposure to light and was then stirred at 60 °C for 6 h. excessive Ag<sub>2</sub>O was completely removed via a filtration-centrifugation-filtration cycle. Cy5-Cl (148 mg, 0.353 mmol) dissolved in MeOH (5 mL) was then added drop wise to the flask and the reaction mixture was stirred overnight. Subsequently, MeOH was added for dilution, the solution was centrifuged and AgCl was filtered. MeOH was then evaporated under reduced pressure and unreacted Cy5-Cl was removed by washing with EtOH for several times. EtOH was removed under reduced pressure and Cy5-Poly20 was dried under vacuum at 40 °C (170 mg, 52%).

#### ***Synthesis of Cy5-Poly30***

Poly30 (200 mg containing 0.468 mmol sulfonic acid groups), Ag<sub>2</sub>O (163 mg, 0.703 mmol), MeOH (20 mL) and Cy5-Cl (206 mg, 0.492 mmol) gave 179 mg Cy5-Poly30 (47%).

#### ***Synthesis of Cy5-Poly50***

Poly50 (200 mg containing 0.68 mmol sulfonic acid groups), Ag<sub>2</sub>O (236 mg, 1.02 mmol), MeOH (30 mL) and Cy5-Cl (299 mg, 0.714 mmol) gave 190 mg Cy5-Poly50 (28%).

#### ***Synthesis of Cy5-PEG25Poly50***

PEG25Poly50 (200 mg containing 0.51 mmol sulfonic acid groups), Ag<sub>2</sub>O (162 mg, 0.70 mmol), MeOH (30 mL), and Cy5-Cl (226 mg, 0.54 mmol) gave 123 mg Cy5-PEG25Poly50 (43%).

#### ***Synthesis of Cy5-PEG50Poly50***

PEG50Poly50 (287 mg containing 0.58 mmol sulfonic acid groups), Ag<sub>2</sub>O (191 mg, 0.83 mmol), MeOH (35 mL), and Cy5-Cl (266 mg, 0.63 mmol) gave 308 mg Cy5-PEG50Poly50 (60%).

#### ***Synthesis of Cy3-Poly20***

Poly20 (200 mg containing 0.336 mmol sulfonic acid groups), Ag<sub>2</sub>O (117 mg, 0.505 mmol), MeOH (15 mL) and Cy3-I (181 mg, 0.353 mmol) gave 171 mg Cy3-Poly20 (52%). For Cy3-Poly20, Cy3-Poly30 and Cy3-Poly50, unreacted Cy3-I was removed by washing thoroughly with 2-propanol instead of EtOH.

#### ***Synthesis of Cy3-Poly30***

Poly30 (200 mg containing 0.468 mmol sulfonic acid groups), Ag<sub>2</sub>O (163 mg, 0.703 mmol), MeOH (20 mL) and Cy3-I (252 mg, 0.492 mmol) gave 170 mg Cy3-Poly30 (45%).

#### ***Synthesis of Cy3-Poly50***

Poly50 (200 mg containing 0.68 mmol sulfonic acid groups), Ag<sub>2</sub>O (236 mg, 1.02 mmol), MeOH (30 mL) and Cy3-I (366 mg, 0.714 mmol) gave 172 mg Cy3-Poly50 (37%).

### **2.2.3 Synthesis of Cy-FN3**

#### ***Synthesis of methyl 4-azido-2,3,5,6-tetrafluorobenzoate (2)***

A mixture of methyl pentafluorobenzoate (**1**) (2 mL, 13.56 mmol) and NaN<sub>3</sub> (1.15 g, 17.69 mmol) was dissolved in a mixture of acetone (20 mL) and water (10 mL). The reaction flask was heated to 70 °C under reflux for 8 h. After cooling to room temperature, the solution was diluted with water (60 mL) and extracted by diethyl ether (3 X 60 mL). The extract was dried with Na<sub>2</sub>SO<sub>4</sub> and the solvent was evaporated under reduced pressure to give **2** (3.02 g, 90%).

#### ***Synthesis of 4-azido-2,3,5,6-tetrafluorobenzoic acid (3)***

Methyl 4-azido-2,3,5,6-tetrafluorobenzoate (**2**) (2.81 g, 11.29 mmol) was dissolved in a mixture of water (12 mL) and MeOH (60 mL). Aqueous NaOH solution (20%, w/w, 6 mL) was

added drop wise to the flask and the mixture was then stirred for 3 h at room temperature. Subsequently, the solution was slowly acidified by 1 M aqueous HCl to pH = 1 and extracted with DCM (3 X 60 mL). The extract was dried with Na<sub>2</sub>SO<sub>4</sub> and the solvent was evaporated under reduced pressure to give **3** (2.54 g, 96%).

### **Synthesis of Cy5-FN3**

The synthesis of Cy5-FN3 is described as a representative example. Cy7-FN3 was prepared accordingly. 4-azido-2,3,5,6-tetrafluorobenzoic acid (**3**) (250 mg, 1.06 mmol) was dissolved in NaHCO<sub>3</sub> aqueous solution (33 mL). The mixture was stirred for 30 min (pH = 8), diluted with 20 mL water and extracted with DCM solution (50 mL) containing Cy5-Cl (419 mg, 1 mmol). The organic phase was further extracted with water (2 X 50 mL), dried with Na<sub>2</sub>SO<sub>4</sub> and the solvent was evaporated under reduced pressure at room temperature to give Cy5-FN3 (458 mg, 74%).

### **Synthesis of Cy7-FN3**

4-azido-2,3,5,6-tetrafluorobenzoic acid (**3**) (47 mg, 0.2 mmol), NaHCO<sub>3</sub> aqueous solution (35 mL) and Cy7-Cl (97 mg, 0.16 mmol)/CHCl<sub>3</sub> (40 mL) solution gave Cy7-FN3 (51 mg, 40%).

### **Synthesis of Cy3-FN3**

Cy3-I (800 mg, 1.56 mmol) was dissolved in MeOH and the solution was then mixed with AgNO<sub>3</sub> (462 mg, 2.72 mmol) aqueous solution (50 mL), stirred for 30 min and filtered to remove precipitates. After evaporation of solvents, the solids were re-dissolved in CHCl<sub>3</sub> (50 mL) and unreacted AgNO<sub>3</sub> was removed by filtration. 4-azido-2,3,5,6-tetrafluorobenzoic acid (**3**) (500 mg, 2.12 mmol) was dissolved in NaHCO<sub>3</sub> aqueous solution (33 mL). The mixture was kept stirring for 30 min (pH = 8), diluted with 20 mL water and extracted with the previously prepared Cy3-NO<sub>3</sub>/CHCl<sub>3</sub> solution. The organic phase was further extracted with water (2 X 50 mL), dried with Na<sub>2</sub>SO<sub>4</sub> and the solvent was evaporated under reduced pressure at room temperature to give Cy3-FN3 (528 mg, 54%).

## **2.2.4 Synthesis of Cy-N3**

### **Synthesis of Cy5-N3**

4-azidobenzoic acid (**5**) (491 mg, 3.01 mmol) was dissolved in NaOH aqueous solution (30 mL). The mixture was kept stirring for 4 h (pH = 9), diluted with 30 mL water and extracted with CHCl<sub>3</sub> (60 mL) solution containing Cy5-Cl (339 mg, 0.81 mmol). The organic phase was

further extracted with water (2 X 50 mL), dried with Na<sub>2</sub>SO<sub>4</sub> and the solvent was evaporated under reduced pressure at room temperature to give Cy5-N3 (302 mg, 68%).

### ***Synthesis of Cy3-N3***

Cy3-I (419 mg, 0.82 mmol) was dissolved in MeOH (50 mL) and the solution was then passed through Amberlite IRA-400 chloride form anion exchange resin to give Cy3-Cl/MeOH solution. After evaporation of MeOH, the Cy3-Cl solid was dissolved in CHCl<sub>3</sub> (70 mL). 4-azidobenzoic acid (**5**) (617 mg, 3.78 mmol) was dissolved in NaOH aqueous solution (50 mL). The mixture was kept stirring for 4 h (pH = 9), diluted with 20 mL water and extracted with the previously prepared Cy3-Cl/CHCl<sub>3</sub> solution. The organic phase was further extracted with water (2 X 50 mL), dried with Na<sub>2</sub>SO<sub>4</sub> and the solvent was evaporated under reduced pressure at room temperature. The product was obtained by recrystallization from water to give Cy3-N3 (234 mg, 52%).

## **2.2.5 Synthesis of Cy-MES**

### ***Synthesis of Cy5-MES***

The synthesis of Cy5-MES is described as a representative example. Cy3-MES was prepared accordingly. H-MES (300 mg, 1.55 mmol) and Ag<sub>2</sub>O (500 mg, 2.16 mmol) were mixed in EtOH for 6 h. After cooling, the mixture was diluted with 20 mL EtOH. Excessive Ag<sub>2</sub>O was removed via a filtration-centrifugation-filtration cycle. 5 mL EtOH solution containing Cy5-Cl (616 mg, 1.47 mmol) was then added drop wise and the mixture was stirred for 30 min at room temperature. The solution was then centrifuged and AgCl was removed by filtration. EtOH was evaporated and the products re-dissolved in DCM. Unreacted Ag-MES was three times extracted with water. The organic phase was dried with anhydrous Na<sub>2</sub>SO<sub>4</sub>, DCM was removed by evaporation and Cy5-MES was dried at 40 °C under vacuum (739 mg, 87%).

### ***Synthesis of Cy3-MES***

H-MES (300 mg, 1.55 mmol), Ag<sub>2</sub>O (500 mg, 2.16 mmol), EtOH (31 mL) and Cy3-I (705 mg, 1.47 mmol) gave Cy3-MES (705 mg, 83%).

## **2.2.6 Synthesis of Cy-PF6**

### ***Synthesis of bCy3-PF6***

The synthesis of bCy3-PF6 is described as a representative example. STCy3-PF6 and Cy1PF6 were prepared accordingly. bCy3-I (809 mg, 1.76 mmol) was dissolved in MeOH (80 mL) and then added drop wise into a MeOH (50 mL) solution containing NaPF<sub>6</sub> (1590 mg, 9.46 mmol). The mixture was stirred for 2 h. The precipitates were collected by filtration and purified three times by re-dissolution in DMSO and precipitation in MeOH to give bCy3-PF6 (309 mg, 37%).

### Synthesis of STCy3-PF6

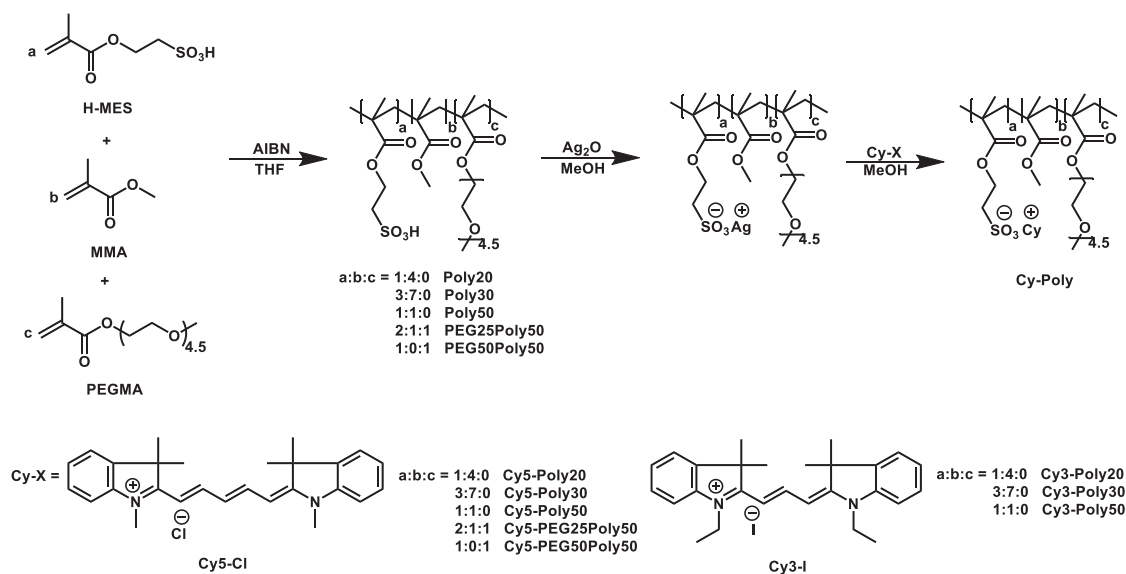
STCy3-ES (501 mg, 0.78 mmol) and NaPF<sub>6</sub> (669 mg, 3.98 mmol) gave STCy3-PF6 (341 mg, 67%).

### Synthesis of Cy1-PF6

Cy1-I (513 mg, 1.1 mmol) and NaPF<sub>6</sub> (2095 mg, 12.47 mmol) gave Cy1-PF6 (234 mg, 44%).

## 2.3 Results and Discussion

### 2.3.1 Synthesis and characterization of Cy-Poly



**Scheme 2-1:** Synthesis of Cy-Poly.

The Cy-Poly were synthesized according to **Scheme 2-1**. The synthetic route involved the thermal radical copolymerization initiated by AIBN. Next, the sulfonic acid side groups were deprotonated by reacting with Ag<sub>2</sub>O. Cyanine cations were then incorporated into the copolymers via a salt metathesis reaction with elimination of silver halides.

All copolymers were fully characterized by NMR spectroscopy (see 2.6 Supporting Information). The compositions were obtained by integration of monomer signals and were in good agreement with the feed ratio a:b:c of H-MES, MMA and PEGMA. For example, a feed ratio a:b:c of 1:4:0 yielded the copolymer Poly20 containing exactly 20% H-MES and 80% MMA monomer repeating units. This suggests that the monomer reactivity is very similar. A similar reactivity between H-MES and MMA was reported previously.<sup>2</sup> Thereby, the content of cyanine dyes in the final polyelectrolytes could be conveniently tuned in advance by varying the feed ratio.

GPC analysis was performed to determine the molecular weight of Poly20. However, due to the presence of sulfonic acid groups, the copolymer did not pass through the columns with THF as the eluent. Apparently, the sulfonic acid moieties cause an undesired interaction between the GPC column and the copolymer, thereby resulting in a longer retention of the polymer on the column and an erroneously low molecular weight. Therefore, the molecular weight of copolymers could not be determined by GPC.<sup>2</sup>

The number of repeating units for the copolymers was obtained from <sup>1</sup>H NMR spectra. Two methyl groups ( $\delta^1\text{H}$  1.14 ppm,  $\delta^{13}\text{C}$  25.8 ppm;  $\delta^1\text{H}$  1.29 ppm,  $\delta^{13}\text{C}$  29.3 ppm, recorded in DMSO-d<sub>6</sub>) with equal and small intensities were observed. Both groups showed an HMBC cross-correlation signal to a –CN group at 125.1 ppm. This indicates that these signals are due to the methyl groups of the (CH<sub>3</sub>)<sub>2</sub>CN-C- initiator fragment, located at the beginning of the chain.<sup>3</sup> With the help of diffusion-edited <sup>1</sup>H NMR experiments we further proved that this group was indeed attached to the polymer chain and does not stem from small molecular weight impurities.

Integration of the methyl protons of the terminal groups and the monomer units in the middle of polymer chains gave the approximate number of repeating units. Accordingly, number average molecular weights  $M_n$  could be readily calculated (**Table 2-1**).

**Table 2-1:** Repeating units and  $M_n$  of copolymers.

<b>Copolymer</b>	<b>Repeating units</b>	<b><math>M_n</math> (g/mol)</b>
Poly20	324	38510
Poly30	316	40530



Poly50	297	43706
PEG25Poly50	274	54007
PEG50Poly50	201	49662

It should be noted that these  $M_n$  values are minimum molecular weights because polymer chains that terminate via recombination contain two terminal initiator fragments. For the polymerization of pure MMA it has been shown that polymers terminate predominately via disproportionation.<sup>3</sup> Olefinic resonances in the  $^1\text{H}$  NMR spectra were detected at  $\sim 5.6$  ppm and  $\sim 6.1$  ppm with intensities  $< 1/3$  of the initiator methyl groups. This confirms that polymer formation by disproportionation also dominates here, but signal intensities were too small for a quantitative analysis.

TGA of different copolymers was carried out and the results are shown in **Table 2-2**.

**Table 2-2:** Weight loss in three degradation stages and residue fraction of copolymers.

Copolymer	Weight loss and residue fraction (%)			
	100-220 °C	220-380 °C	380-500 °C	Residue (> 800 °C)
Poly20	9.4	30.5	49.7	5.2
Poly30	4.8	46.3	35.3	9.8
Poly50	3.9	59.9	18.7	15.4
PEG25Poly50	15.7	46.8	20.6	12.9
PEG50Poly50	24.1	37.5	15.8	12.3

Thermal degradation of all copolymers proceeds in a three-stage process. For copolymers without PEGMA as monomer units (Poly20, Poly30 and Poly50), the predominant degradation occurs at the second stage between 220 °C to 380 °C and the third stage between 380 °C to 500 °C. As observed similarly in Ref. [3], the residue fraction at temperature above 800 °C, 5.2% for Poly20, 9.8% for Poly30, 15.4% for Poly50, increases with the increase of H-MES content in the polymers. Besides, it was found that the first weight loss between 100 °C to 220 °C becomes more dominant with the increase of PEGMA content in

the copolymers. This indicates that the PEGMA is thermally more labile compared to H-MES and MMA monomer units.

**Table 2-3:** Calculated weight fraction of copolymers.

Copolymer	Calculated weight fraction (%)		
	H-MES	MMA	PEGMA
Poly20	32.7	67.3	0
Poly30	45.4	54.6	0
Poly50	66.0	34.0	0
PEG25Poly50	49.3	12.7	38.0
PEG50Poly50	39.3	0	60.7

Further, the second weight loss (220-380 °C) values for Poly20 (30.5%), Poly30 (46.3%), Poly50 (59.9%), PEG25Poly50 (46.8%) and PEG50Poly50 (37.5%) were in good agreement with the calculated weight fraction of H-MES content (**Table 2-3**) in Poly20 (32.7%), Poly30 (45.4%), Poly50 (66.0%), PEG25Poly50 (49.3%) and PEG50Poly50 (39.3%), suggesting that the second weight loss process is due to the degradation of H-MES moieties, which are thermally more labile than MMA.

**Table 2-4:** Glass transition temperature  $T_g$  of copolymers.

Copolymer	Glass transition temperature $T_g$ (°C)
Poly50	49.5
PEG25Poly50	5.7
PEG50Poly50	-26.1

$T_g$  of Poly50, PEG25Poly50 and PEG50Poly50 was determined by DSC measurements (shown in **Table 2-4**). PEG is known to have a low  $T_g$ , which sensitively depends on the molecular weight.<sup>4</sup> The increase of PEG units in the copolymers reduced  $T_g$  significantly, from 49.5 °C to

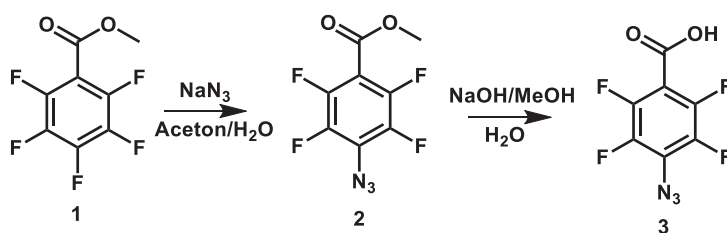
-26.1 °C. This result resembles the finding reported previously<sup>5,6</sup>, where it was found that  $T_g$  of copolymers could be altered by simply modifying the ratio of monomer units.

The cyanine content in all Cy-Poly was confirmed by NMR measurements (see 2.6 Supporting Information). Integration of NMR signals for protons belonging to cyanine dye chromophores and MES matched, signifying the complete conversion of sulfonic acid groups. No residual Ag could be detected with XRF in Cy5-Poly20 and Cy3-Poly20 within the detection limit of ~50 ppm. The reason for the successful salt metathesis reaction between the intermediate silver salt and the cyanine is the presence of the halide anions that drives the pairing by precipitation of AgCl or AgI.

The synthesis of Cy-Poly containing more than 50% H-MES monomer units was not possible. The copolymers with higher H-MES content (> 50%) could be synthesized and the intermediate silver salt could be prepared. Subsequently, the incorporation of cyanine dyes led to an instant precipitation of both silver halides and partially formed Cy-Poly. The precipitates were not soluble in a wide variety of solvents and the Cy-Poly could therefore not be isolated from the silver halides. Apparently, the Cy-Poly solubility is sensitively dependent on the dye fraction and cyanine contents above 50% led to insoluble products. The unsuccessful synthesis of such Cy-Poly might be due to steric reasons. Since the bulky cyanine cations must arrange in close proximity to the sulfonate anions, this close arrangement of dye cations could become very difficult with the increasing density of anions present in the polymer backbone.

### 2.3.2 Synthesis of perfluorophenyl azides

The synthesis of 4-azido-2,3,5,6-tetrafluorobenzoic acid (**3**) was reported in the literature.<sup>7,8</sup> The fluorine at para position of methyl pentafluorobenzoate (**1**) was firstly substituted by an azide to give methyl 4-azido-2,3,5,6-tetrafluorobenzoate (**2**), followed by hydrolysis of the methyl benzoate group under basic conditions (**Scheme 2-2**).

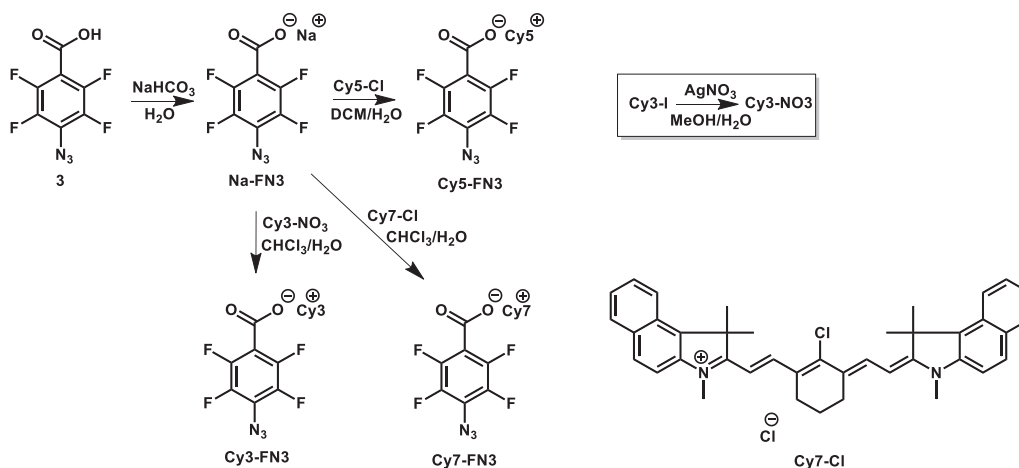


**Scheme 2-2:** Synthesis of 4-azido-2,3,5,6-tetrafluorobenzoic acid.

The synthesis was successful with high yields and all products were characterized by NMR spectroscopy and the  $^1\text{H}$ ,  $^{19}\text{F}$  and  $^{13}\text{C}$  NMR chemical shifts were assigned (see 2.6 Supporting Information).

### 2.3.3 Anion exchange of cyanine dyes

Cyanine dyes with 4-azido-2,3,5,6-tetrafluorobenzoate counter anions (Cy-FN3) were synthesized according to **Scheme 2-3**. 4-azido-2,3,5,6-tetrafluorobenzoic acid (**3**) was deprotonated with  $\text{NaHCO}_3$  to give Na-FN3, followed by solvent extraction with DCM or  $\text{CHCl}_3$ . NMR spectra with chemical assignments for all Cy-FN3 dyes are compiled in 2.6 Supporting Information.



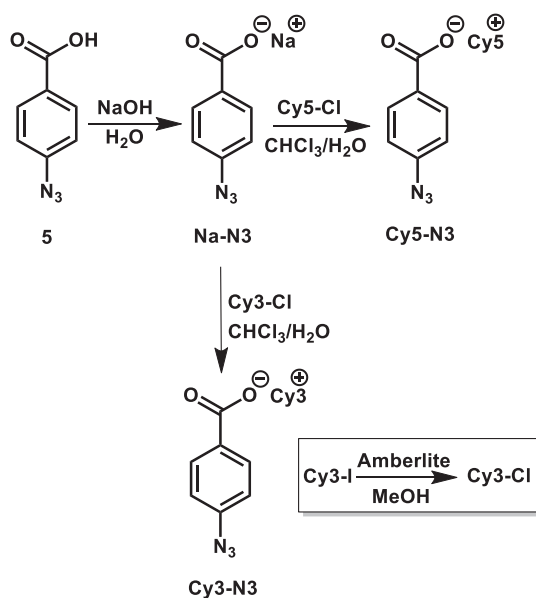
**Scheme 2-3:** Synthesis of Cy-FN3.

The liquid-liquid extraction process efficiently separated the cyanine dyes with new counter ions from sodium chloride, yielding Cy5-FN3 and Cy7-FN3 with complete anion exchange dissolved in the organic phase. However, due to solubility problems, the direct solvent

extraction was not successful with the starting material Cy3-I, which gave only 30% to 65% ion exchange. Hence, the iodide in Cy3-I was firstly exchanged with nitrate, generating Cy3-NO<sub>3</sub>, followed by solvent extraction to give Cy3-FN3.

The anion exchange efficiency was quantified by NMR. A reference solvent TFP that contains both H and F atoms was added as an external standard to the NMR sample. By measuring <sup>1</sup>H NMR and <sup>19</sup>F NMR spectra and comparing H and F intensities between the dyes and the standard, the exchange ratio could be conveniently calculated.

As observed from <sup>19</sup>F NMR spectra, the 4-azido-2,3,5,6-tetrafluorobenzoate anions degraded in the range of 1% to 5% already during synthesis and storage at 4 °C. This observation was attributed to the decarboxylation of perfluorophenyl benzoate ions, as will be explained in Chapter 4.



**Scheme 2-4:** Synthesis of Cy-N3.

The synthesis of Cy-N3 was carried out according to **Scheme 2-4** (for NMR data, see 2.6 Supporting Information). Similar to the synthesis of Cy-FN3, 4-azidobenzoic acid (**5**) was deprotonated with NaOH to give Na-N3, followed by a solvent extraction to exchange the 4-azidobenzoate anions. As found before, iodide could not be completely removed via solvent extraction. Here, Cy3-I was firstly passed through an Amberlite anion exchange resin, giving

Cy3-Cl. The following extraction process was performed with Cy3-Cl chloroform solution and Na-N3 aqueous solution.

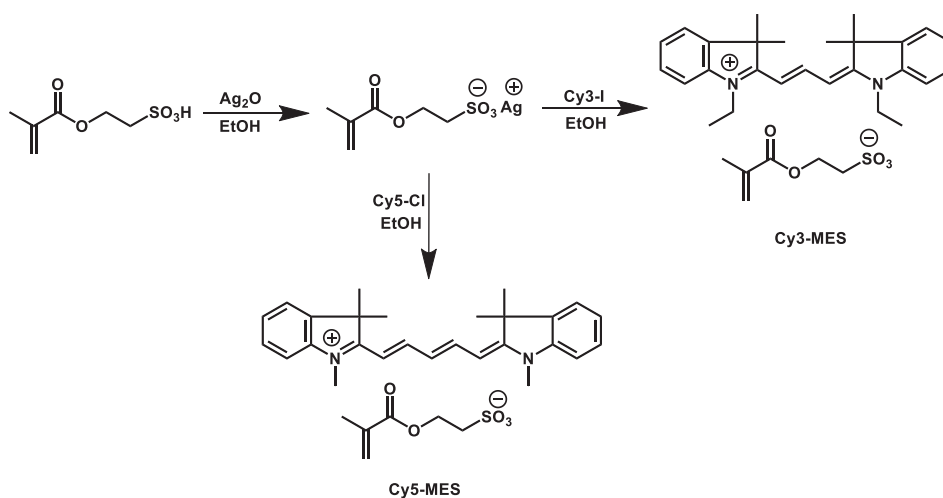
NaOH instead of NaHCO<sub>3</sub> aqueous solution was used to deprotonate 4-azidobenzoic acid (**5**) since complete deprotonation with NaHCO<sub>3</sub> was not successful. The pKa values of the structurally closely related benzoic acid and pentafluorobenzoic acid are 4.204 and 1.48 respectively,<sup>9,10</sup> which indicates that 4-azidobenzoic acid (**5**) is a much weaker acid than 4-azido-2,3,5,6-tetrafluorobenzoic acid (**3**). Cy7-N3 could not be prepared by this synthetic route. It was found that the long heptamethine cyanine was more labile under basic conditions compared to trimethine or pentamethine dye, NMR (see 2.6 Supporting Information) showed that the Cy7 chromophores were destroyed during washing with pH = 9 aqueous solution.

Ion chromatography analysis confirmed that there were no residual chloride ions in Cy3-N3. ESI-MS spectra of Cy3-N3 showed a strong signal at m/z ~162, indicating the existence of 4-azidobenzoate ions. Besides, no iodide signals were found in ESI-MS spectra.

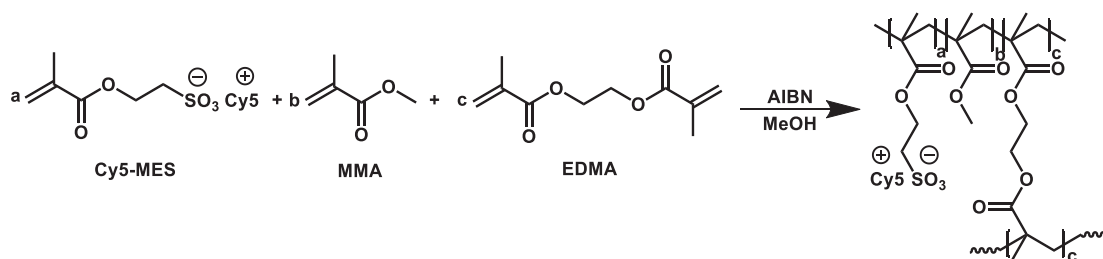
**Table 2-5:** Elemental analysis of Cy3-N3.

Element weight fraction	[C]%	[H]%	[N]%	[O]%
Measured values	70.15	6.87	11.48	10.16
	70.14	6.75	11.63	10.31
Calculated values (Cy3-N3)	74.56	6.81	12.79	5.84
Calculated values (Cy3-N3 · 1.9 H <sub>2</sub> O)	70.18	7.05	12.03	10.72

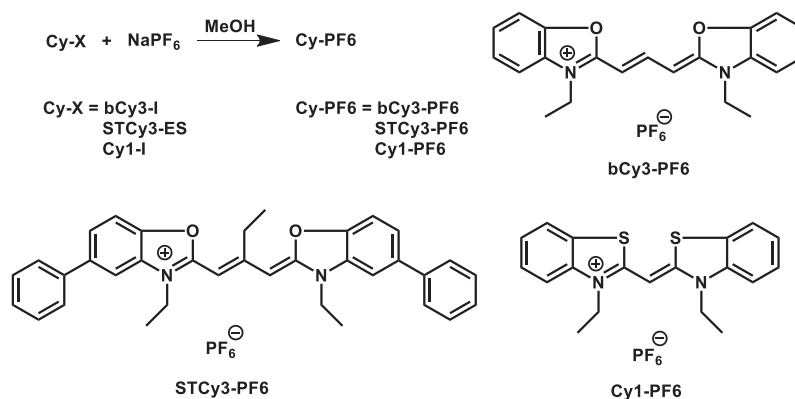
According to elemental analysis (**Table 2-5**), Cy3-N3 contained ~5.9% water which originated from the recrystallization process. Water could not be removed by drying (10<sup>-3</sup> mbar) at room temperature for ~16 h. Drying at elevated temperatures resulted in dye decomposition.



Similar to the synthesis of Cy-Poly, Cy-MES was prepared via salt metathesis reaction by elimination of silver halides (**Scheme 2-5**). Products were fully characterized by NMR spectroscopy and the results are shown in 2.6 Supporting Information. Using XRF analysis, no residual silver was found in both Cy3-MES and Cy5-MES within a detection limit of 50 ppm.



**Scheme 2-6** shows an alternative attempt to synthesize crosslinked cyanine polymers where Cy5-MES was directly polymerized with MMA as spacer and EDMA as crosslinker. However, this approach was not successful. The polymerization of MES anions strongly polarized the polymer backbone during the reaction. The increasing electrostatic repulsion hindered the further linking of MES. This resulted in a chain growth that highly favored MMA and EDMA over MES and consequently a limited number of MES could be polymerized. We also speculate that the AIBN initiator attacks the cyanine dye chromophores, causing an undesired consumption of the initiator and the loss of dye functionality.



**Scheme 2-7:** Synthesis of Cy-PF<sub>6</sub>.

All Cy-PF<sub>6</sub> were synthesized according to **Scheme 2-7** via salt metathesis reactions. NMR results are shown in 2.6 Supporting Information. Due to the solubility difference between the starting materials (bCy3-I, STCy3-ES and Cy1-I) and the products, Cy-PF<sub>6</sub> precipitates immediately in MeOH, which helped to isolate the products. The complete anion exchange was confirmed by <sup>1</sup>H NMR and <sup>19</sup>F NMR spectroscopy, using TFP as external reference compound. TLC analysis confirmed that there were no residual starting materials in final STCy3-PF<sub>6</sub> and Cy1-PF<sub>6</sub>. No residual iodide in bCy3-PF<sub>6</sub> and Cy1-PF<sub>6</sub> was detected by XRF, further confirming that the anion exchange was complete and the products were pure.

## 2.4 Conclusions

Cy-Poly were synthesized via a versatile synthetic route involving an initial copolymerization of H-MES, MMA and PEGMA, followed by deprotonation of the pendant sulfonic acid groups and incorporation of cyanine dyes with elimination of silver halides. The composition of copolymers was confirmed by TGA and NMR spectroscopy. With the help of diffusion-edited NMR measurements and the assignment of the terminal groups, the number of repeat units (~250) and  $M_n$  (~45 kg/mol) for the polymers could be calculated. As revealed by DSC measurements, incorporated PEG segments in the polymer backbone considerably decreased the  $T_g$  (from 49.5 °C to -26.1 °C). Two different cyanine cations Cy3 and Cy5 were introduced into the copolymers, yielding Cy3-Poly and Cy5-Poly with tunable cyanine contents ranging from 20% to 50%. Cy-Poly with cyanine contents larger than 50% could not be prepared due to steric reasons.



Anion exchange reactions for different cyanine dyes were carried out. 4-azido-2,3,5,6-tetrafluorobenzoate or 4-azidobenzoate anions were introduced as counter anions to give Cy-FN3 or Cy-N3, respectively. The reaction scheme involved the deprotonation of the corresponding benzoic acids by a base (NaHCO<sub>3</sub> or NaOH), followed by a solvent extraction process to isolate the cyanine dye with new counter anions in the organic phase from the reaction mixture. Cy-MES and Cy-PF6 were prepared via salt metathesis reactions either by precipitating silver halide as side product and leaving Cy-MES in the solution, or by precipitating directly Cy-PF6 as main product. Both approaches could nicely separate the desired ion pairs, thereby yielding Cy-MES and Cy-PF6 with high purity, confirmed by NMR, XRF and TLC analysis.

## 2.5 References

- [1] A. Mishra, R. K. Behera, P. K. Behera, B. K. Mishra, G. B. Behera, cyanines during the 1990s: a review, *Chem. Rev.* **2000**, 100, 1973-2011.
- [2] Steven L. Hurley, Martin L. Mittleman, Charles A. Wilkie, preparation and thermal degradation of copolymers of 2-sulfoethyl methacrylate and methyl methacrylate, *Polymer Degradation and Stability* **1993**, 39, 345-354.
- [3] K. Hatada, T. Kitayama, E. Masuda, studies on the radical polymerization of methyl methacrylate in bulk and in benzene using totally deuterated monomer technique, *Polymer Journal*, **1986**, 18, 395-402.
- [4] J. A. Faucher, J. V. Koleske, E. R. Santee Jr. J. J. Stratte, C. W. Wilson III, glass transitions of ethylene oxide polymers, *J. Appl. Phys.* **1966**, 37, 3962-3964.
- [5] S. Zhou, X. Deng, H. Yang, biodegradable poly( $\epsilon$ -caprolactone)-poly(ethylene glycol) block copolymers: characterization and their use as drug carriers for a controlled delivery system, *Biomaterials* **2003**, 24, 3563-3570.
- [6] H. Fukuzaki, M. Yoshida, M. Asano, M. Kumakura, synthesis of low-molecular-weight copoly(L-lactic acid/ $\epsilon$ -caprolactone) by direct copolycondensation in the absence of catalysts, and enzymatic degradation of the polymers, *Polymer*, **1990**, 31, 2006-2014.
- [7] J. F. W. Keana, S. X. Cai, new reagents for photoaffinity labeling: synthesis and photolysis of functionalized perfluorophenyl azides, *J. Org. Chem.* **1990**, 55, 3640-3647.

[8] O. Norberg, L. Deng, M. Yan, O. Ramström, photo-click immobilization of carbohydrates on polymeric surfaces-a quick method to functionalize surfaces for biomolecular recognition studies, *Bioconjugate Chem.* **2009**, 20, 2364-2370.

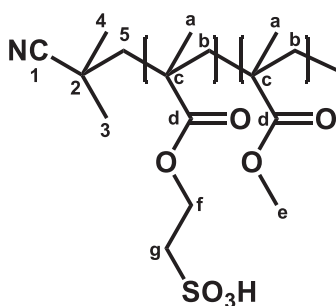
[9] G. K. S. Prakash, J. Hu, pentafluorobenzoic acid, *e-EROS Encyclopedia of Reagents for Organic Synthesis*, 2006.

[10] W. M. Haynes, *CRC Handbook of Chemistry and Physics*, 96<sup>th</sup> Edition, 2015-2016, page 5-99.

## 2.6 Supporting Information

<sup>1</sup>H NMR, <sup>19</sup>F NMR and <sup>13</sup>C NMR spectra were recorded at 298 K on Bruker 300 MHz, 400 MHz and 500 MHz NMR spectrometers. Chemical shifts ( $\delta$ ) in ppm were calibrated to residual solvent peaks, DMSO-d<sub>6</sub>:  $\delta$  = 2.49 and 39.5 ppm, methanol-d<sub>4</sub>:  $\delta$  = 3.31 and 49.0 ppm, chloroform-d:  $\delta$  = 7.26 and 77.2 ppm, for <sup>1</sup>H NMR and <sup>13</sup>C NMR respectively. No internal solvent calibration was performed for <sup>19</sup>F NMR spectra. For <sup>1</sup>H NMR and <sup>19</sup>F NMR data coupling patterns are described as s = singlet, d = doublet, t = triplet, q = quartet, m = multiplet, br = broad and coupling constants J are reported in Hz. For <sup>13</sup>C NMR data multiplicities of carbons are mentioned as s = quaternary, d = CH, t = CH<sub>2</sub>, and q = CH<sub>3</sub>. For 1D and 2D NMR experiments standard Bruker pulse programs and measuring parameters were applied. Double quantum filtered homonuclear correlation spectroscopy (DQF-COSY), gradient selected heteronuclear single quantum coherence (gHSQC) and heteronuclear multiple bond coherence (gHMBC) were used for <sup>1</sup>H and <sup>13</sup>C NMR chemical shift assignments (w = weak correlation peak). The resonances belonging to low molecular weight impurities were identified by recording diffusion-edited <sup>1</sup>H NMR spectra.

### 2.6.1 NMR characterization for Cy-Poly



**Identification of polymer part for Poly20, Poly30 and Poly50**

$^1\text{H}$  NMR (DMSO- $d_6$ , 400.13 MHz):  $\delta$  4.10 (m, 2H, H-f); 3.52 (s, 3H, H-e1); 3.50 (s, 3H, H-e2); 2.80 (m, 2H, H-g); 1.80 (m, 2H, H-b2); 1.72 (m, 2H, H-b1); 0.89 (s, 3H, H-a2); 0.72 (s, 3H, H-a1).

$^{13}\text{C}$  NMR (DMSO- $d_6$ , 100.61 MHz):  $\delta$  177.3 (s, C-d1); 176.5 (s, C-d2); 61.2 (t, C-f); 53.6 (t, C-b1); 53.4 (t, C-b2); 51.8 (q, C-e2); 51.8 (q, C-e1); 49.6 (t, C-g); 44.4 (s, C-c2); 44.1 (s, C-c1); 18.6 (q, C-a2); 16.4 (q, C-a1).

HMBC correlations: H-a1  $\rightarrow$  C-(b1, c1, d1); H-a2  $\rightarrow$  C-(b2, c2, d2); H-b1  $\rightarrow$  C-(d1); H-e1  $\rightarrow$  C-(d1); H-e2  $\rightarrow$  C-(d2); H-g  $\rightarrow$  C-(f).

Two sets of resonances are observed for the polymer part. From the correlations of the methoxy protons "e" to at least two carboxyl carbons at 177.3 and 176.5 ppm in the HMBC NMR spectrum we concluded that the doubling of resonances observed in the polymer part must origin from its tacticity. For the NMR resonances assignable to the polymer part of all compounds at least two sets of resonances were observed.

**Identification of terminal group for Poly20, Poly30 and Poly50**

$^1\text{H}$  NMR (DMSO- $d_6$ , 400.1 MHz):  $\delta$  1.85 (m, 2H, H-5); 1.29 (s, 3H, H-4); 1.14 (s, 3H, H-3).

$^{13}\text{C}$  NMR (DMSO- $d_6$ , 100.6 MHz):  $\delta$  125.1 (s, C-1); 50.6 (t, C-5); 29.8 (s, C-2); 29.3 (q, C-4); 25.8 (q, C-3).

HMBC correlations: H-3  $\rightarrow$  C-(1, 2, 4, 5); H-4  $\rightarrow$  C-(1, 2, 3, 5); H-5  $\rightarrow$  C-(1w).

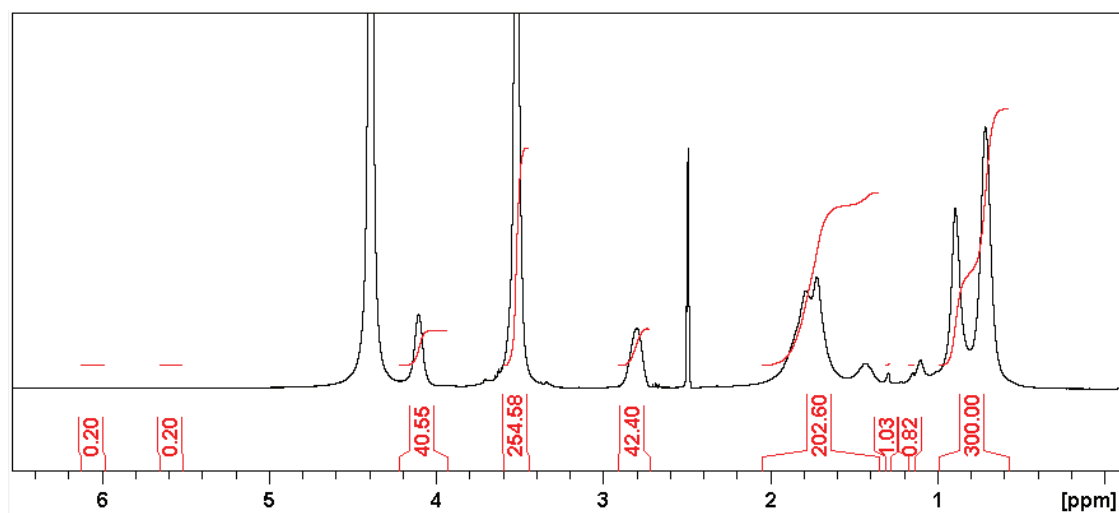


Figure 2-1:  $^1\text{H}$  NMR spectrum of Poly20 (DMSO- $d_6$ ).

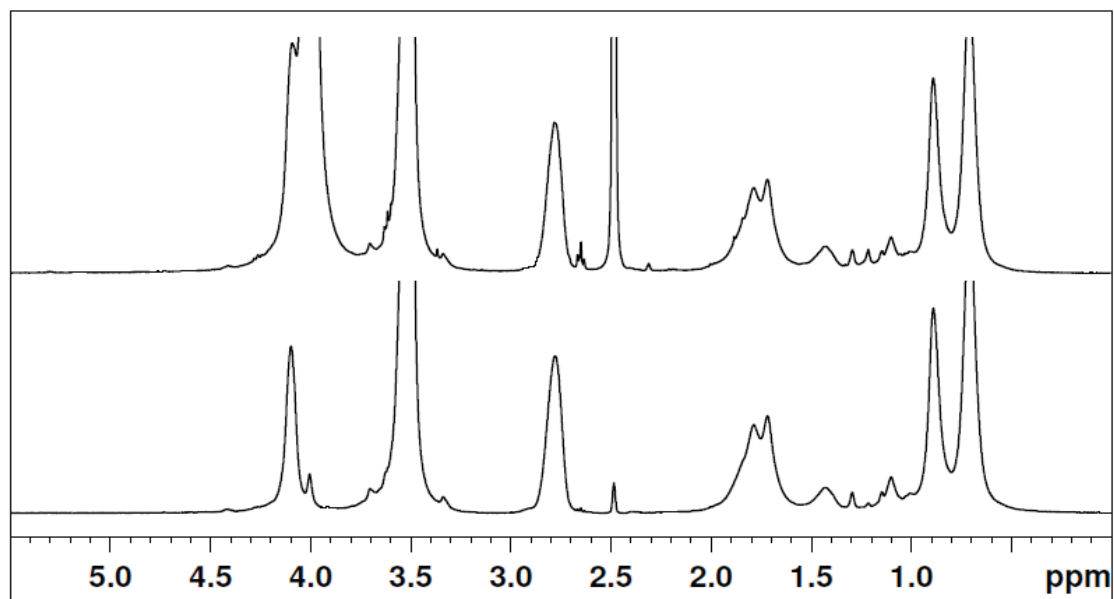


Figure 2-2:  $^1\text{H}$  diffusion-edited NMR spectra of Poly20 ( $\text{DMSO-d}_6$ ).

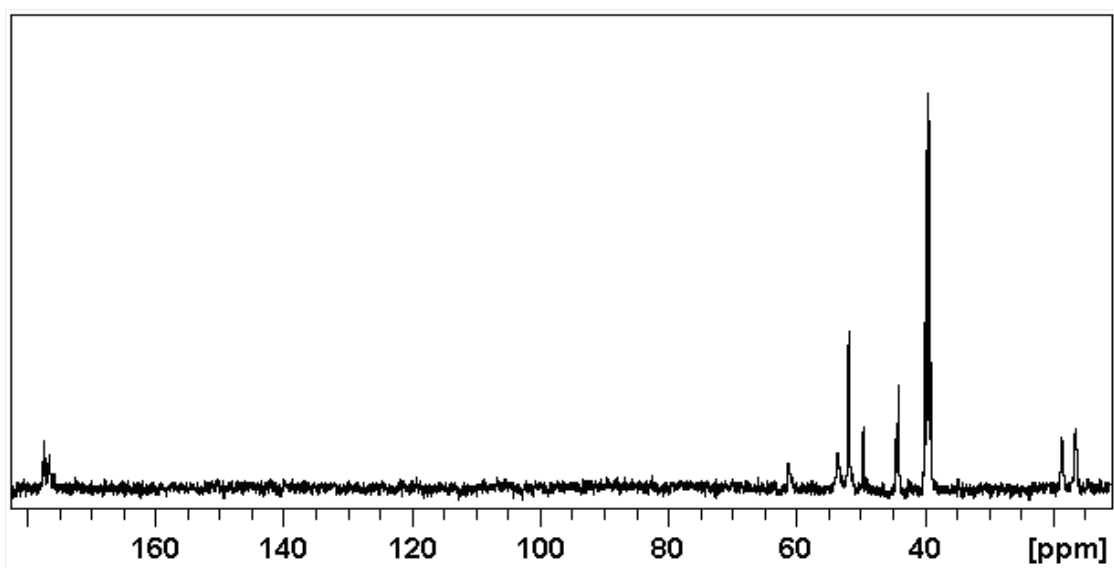


Figure 2-3:  $^{13}\text{C}\{^1\text{H}\}$  NMR spectrum of Poly20 ( $\text{DMSO-d}_6$ ).

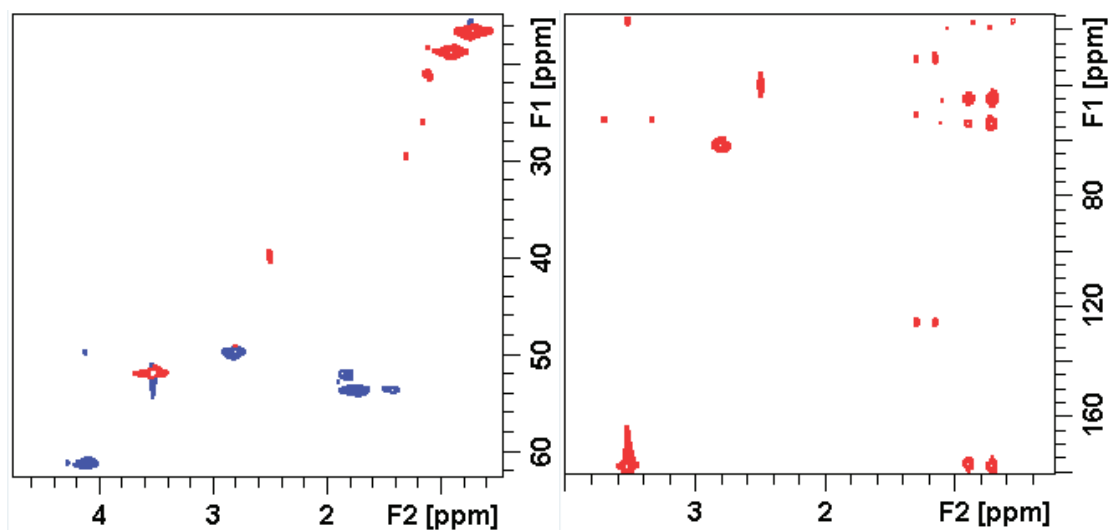


Figure 2-4: HSQC and HMBC NMR spectra of Poly20 (DMSO-d<sub>6</sub>).

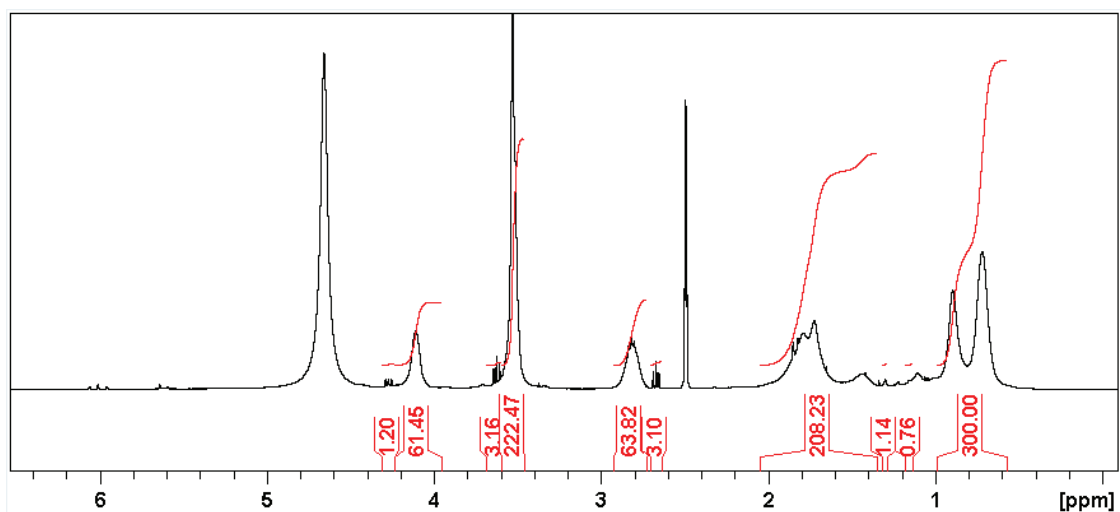


Figure 2-5: <sup>1</sup>H NMR spectrum of Poly30 (DMSO-d<sub>6</sub>).

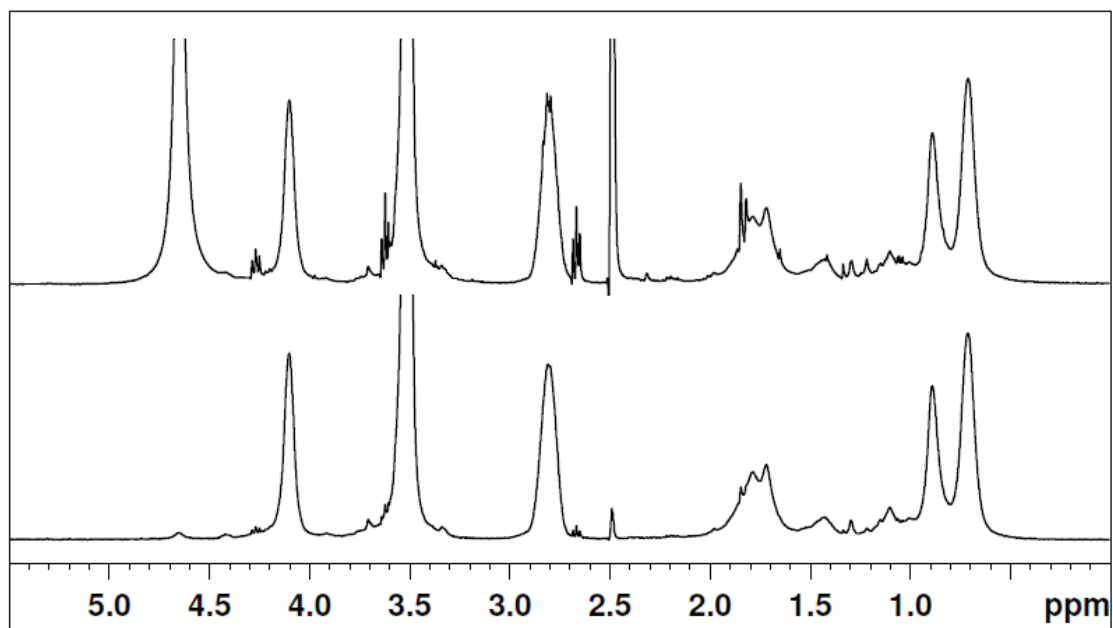


Figure 2-6:  $^1\text{H}$  diffusion-edited NMR spectra of Poly30 ( $\text{DMSO-d}_6$ ).

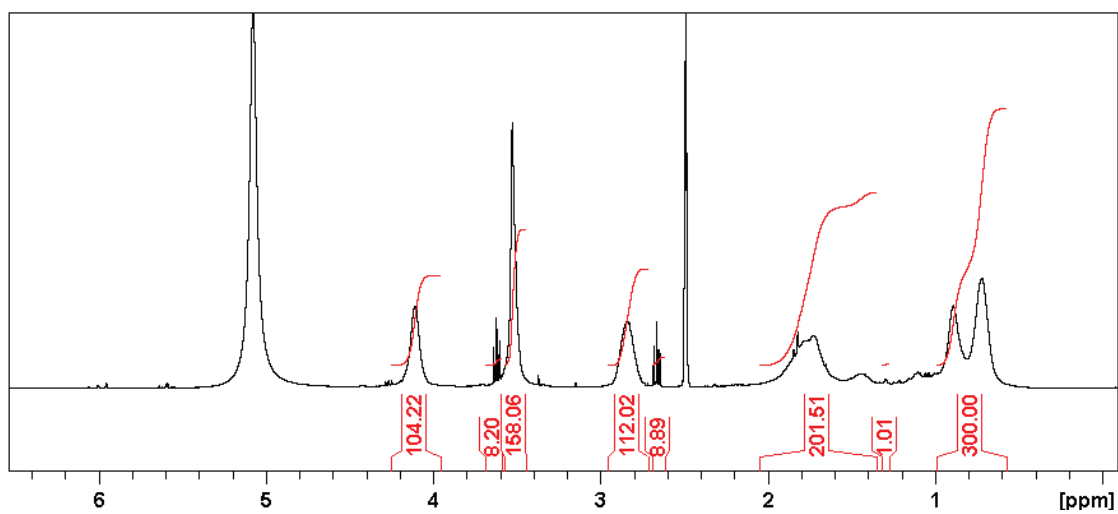


Figure 2-7:  $^1\text{H}$  NMR spectrum of Poly50 ( $\text{DMSO-d}_6$ ).

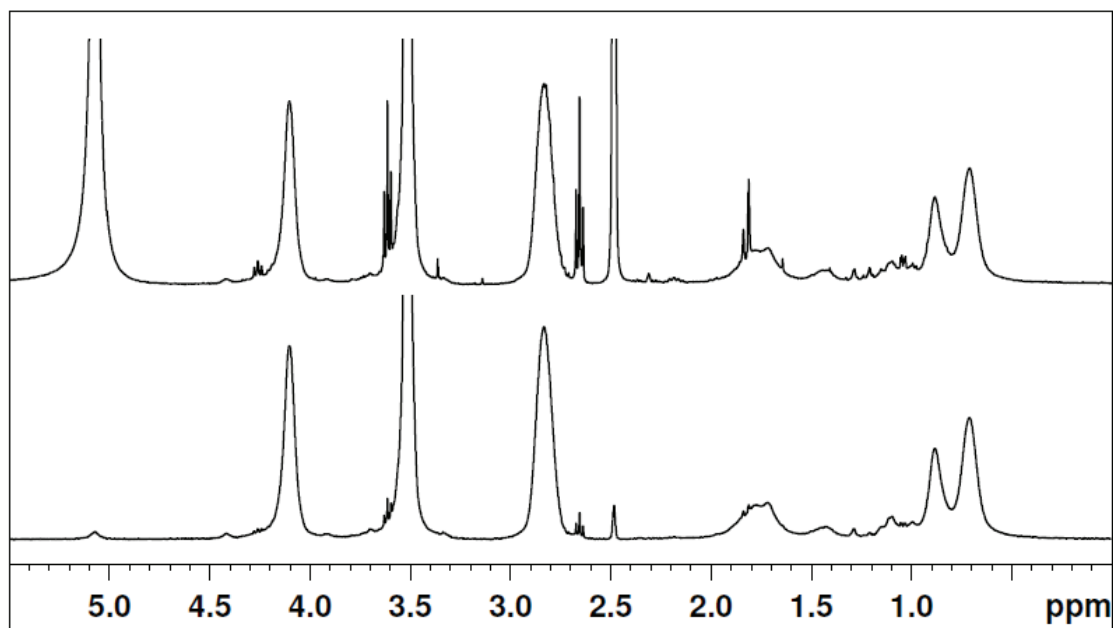
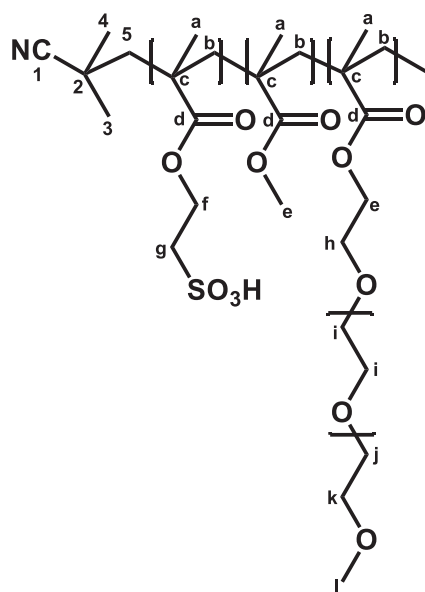


Figure 2-8:  $^1\text{H}$  diffusion-edited NMR spectra of Poly50 ( $\text{DMSO-d}_6$ ).



**Identification of polymer part for PEG25Poly50 and PEG50Poly50**

$^1\text{H}$  NMR (methanol- $\text{d}_4$ , 400.13 MHz):  $\delta$  4.33 (m, 2H, H-f); 4.12 (m, 2H, H-e); 3.74 (m, 2H, H-h); 3.68 (m, H-i); 3.65 (m, 2H, H-j); 3.58 (m, 2H, H-k); 3.38 (s, 3H, H-l); 3.24 (m, 2H, H-g); 2.00 (m, 2H, H-b2); 1.89&1.55 (m, 2H, H-b1); 1.09 (s, 3H, H-a2); 0.94 (s, 3H, H-a1).

$^{13}\text{C}$  NMR (methanol- $d_4$ , 100.61 MHz):  $\delta$  179.0 (s, C-d1); 178.1 (s, C-d2); 73 (t, C-k); 71.6 (t, C-i); 71.4 (t, C-j); 69.7 (t, C-h); 65.5 (t, C-e); 61.6 (t, C-f); 59.2 (q, C-l); 55.4 (t, C-b2); 55.3 (t, C-b1); 50.9 (t, C-g); 46.4 (s, C-c2); 46.1 (s, C-c1); 19.7 (q, C-a2); 17.9 (q, C-a1).

HMBC correlations: H-a1  $\rightarrow$  C-(b1, c1, d1); H-a2  $\rightarrow$  C-(b2, c2, d2); H-b1  $\rightarrow$  C-(d1); H-i  $\rightarrow$  C-(h, i, j); H-j  $\rightarrow$  C-(k); H-k  $\rightarrow$  C-(j); H-l  $\rightarrow$  C-(k); H-f  $\rightarrow$  C-(d1, g); H-g  $\rightarrow$  C-(f).

**Identification of terminal group for PEG25Poly50 and PEG50Poly50**

$^1\text{H}$  NMR (methanol- $d_4$ , 400.13 MHz):  $\delta$  1.38 (s, 3H, H-3); 1.28 (s, 3H, H-4).

$^{13}\text{C}$  NMR (methanol- $d_4$ , 100.61 MHz):  $\delta$  126.4 (s, C-1); 31.6 (s, C-2); 30.6 (q, C-4); 26.9 (q, C-3).

HMBC correlations: H-3  $\rightarrow$  C-(1, 2, 4); H-4  $\rightarrow$  C-(1, 2).

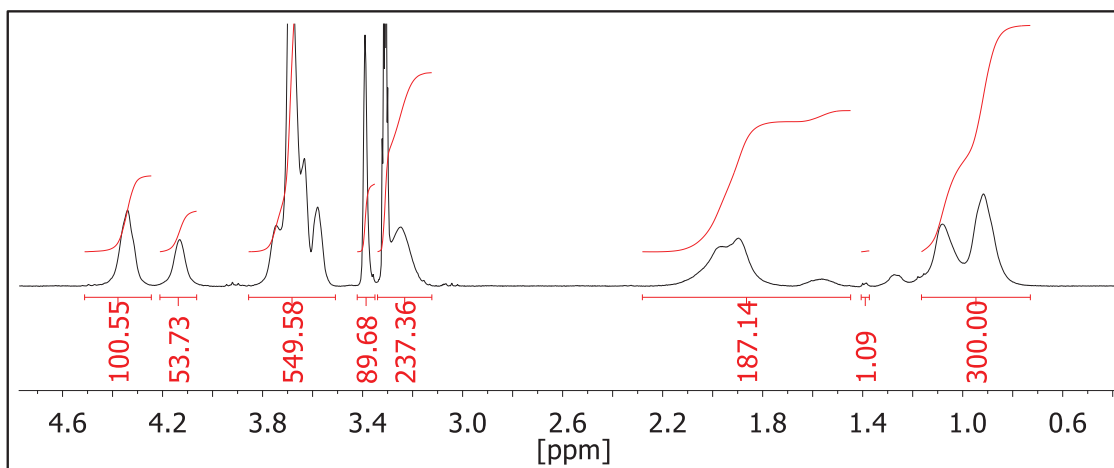


Figure 2-9:  $^1\text{H}$  NMR spectrum of PEG25Poly50 (methanol- $d_4$ ).

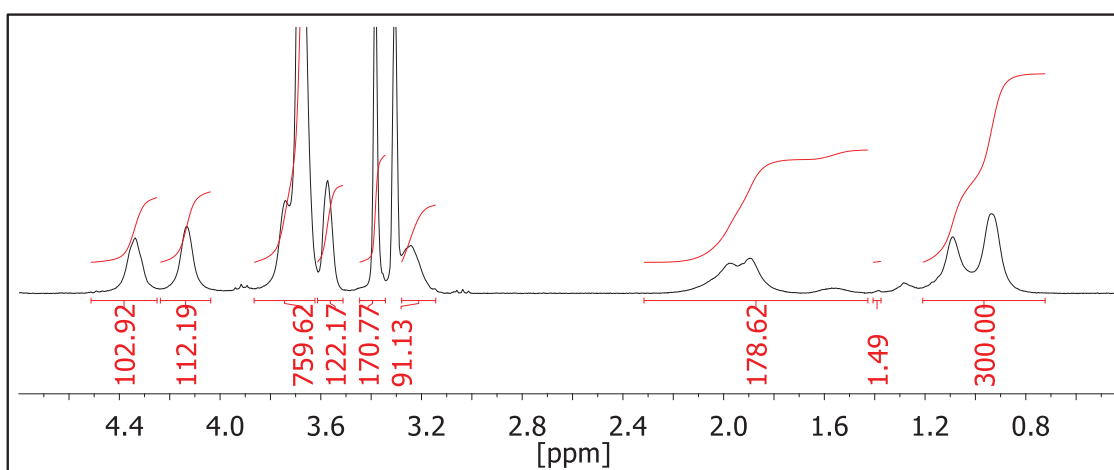


Figure 2-10:  $^1\text{H}$  NMR spectrum of PEG50Poly50 (methanol- $d_4$ ).



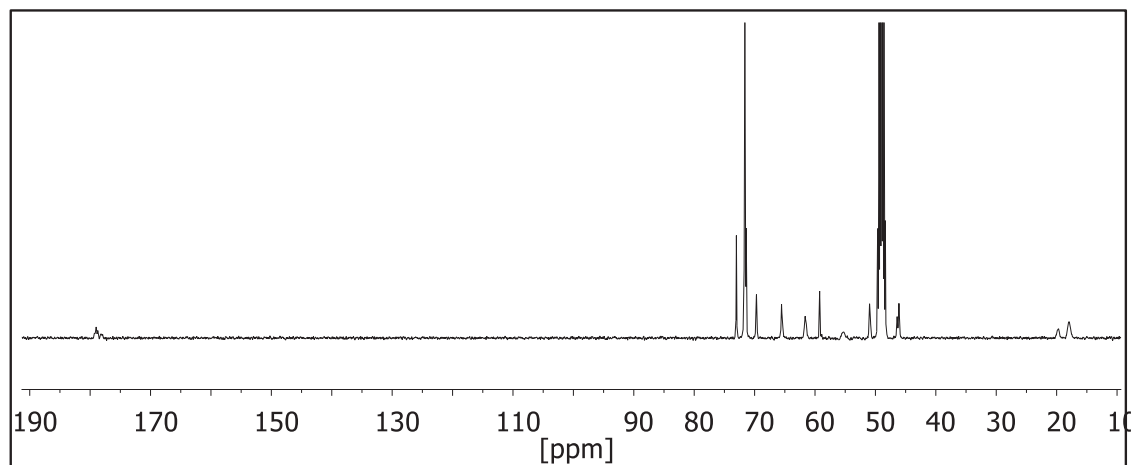
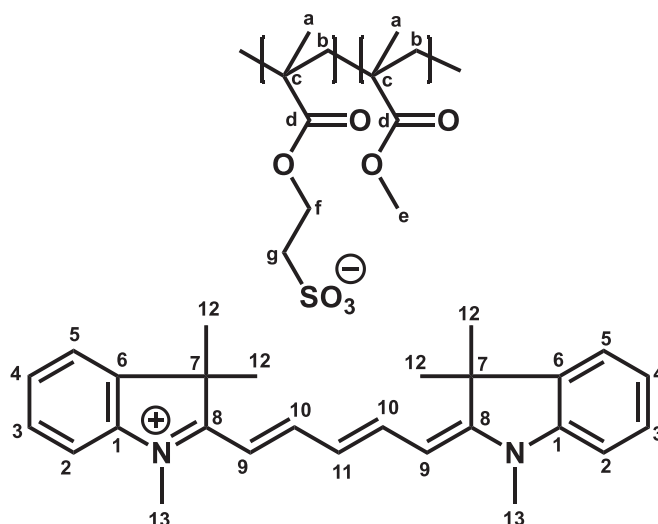


Figure 2-11:  $^{13}\text{C}\{^1\text{H}\}$  NMR spectrum of PEG50Poly50 (methanol- $\text{d}_4$ ).



#### Identification of dye part for Cy5-Poly20, Cy5-Poly30 and Cy5-Poly50

$^1\text{H}$  NMR (methanol- $\text{d}_4$ , 400.13 MHz):  $\delta$  8.21 (dd,  $J = 13.7, 12.4$ , 2H, H-10); 7.48 (m, 2H, H-5); 7.40 (m, 2H, H-3); 7.31 (m, 2H, H-2); 7.24 (m, 2H, H-4); 6.63 (t,  $J = 12.4$ , 1H, H-11); 6.27 (d,  $J = 13.7$ , 2H, H-9); 3.65 (s, 6H, H-13); 1.70 (s, 12H, H-12).

$^{13}\text{C}$  NMR (methanol- $\text{d}_4$ , 100.61 MHz):  $\delta$  175.1 (s, C-8); 155.4 (d, C-10); 144.2 (s, C-1); 142.4 (s, C-6); 129.6 (d, C-3); 126.4 (d, C-11); 126.1 (d, C-4); 123.2 (d, C-5); 111.8 (d, C-2); 104.4 (d, C-9); 50.4 (s, C-7); 31.7 (q, C-13); 27.9 (q, C-12).

HMBC correlations: H-2  $\rightarrow$  C-(4, 6); H-3  $\rightarrow$  C-(1, 5); H-4  $\rightarrow$  C-(2, 5w, 6); H-5  $\rightarrow$  C-(1, 3, 7); H-9  $\rightarrow$  C-(7, 11); H-10  $\rightarrow$  C-(8, 10); H-11  $\rightarrow$  C-(9, 10w); H-12  $\rightarrow$  C-(5, 7, 8, 12); H-13  $\rightarrow$  C-(1, 8).

#### Identification of polymer part for Cy5-Poly20, Cy5-Poly30 and Cy5-Poly50

$^1\text{H}$  NMR (methanol- $d_4$ , 400.13 MHz):  $\delta$  4.35 (m, 2H, H-f); 3.59 (s, 3H, H-e); 3.14 (m, 2H, H-g); 1.92 (m, 2H, H-b2); 1.85 (m, 2H, H-b1); 1.01 (s, 3H, H-a2); 0.83 (s, 3H, H-a1).

$^{13}\text{C}$  NMR (methanol- $d_4$ , 100.61 MHz):  $\delta$  179.3 (s, C-d1); 178.5 (s, C-d2); 62.0 (t, C-f); 55.5 (t, C-b1); 54.0 (t, C-b2); 52.4 (q, C-e); 50.8 (t, C-g); 46.0 (s, C-c2); 45.7 (s, C-c1); 19.7 (q, C-a2); 17.4 (q, C-a1).

HMBC correlations: H-a1  $\rightarrow$  C-(b1, c1, d1); H-a2  $\rightarrow$  C-(c2, d2); H-b1  $\rightarrow$  C-(d1w); H-e  $\rightarrow$  C-(d1, d2); H-g  $\rightarrow$  C-(f).

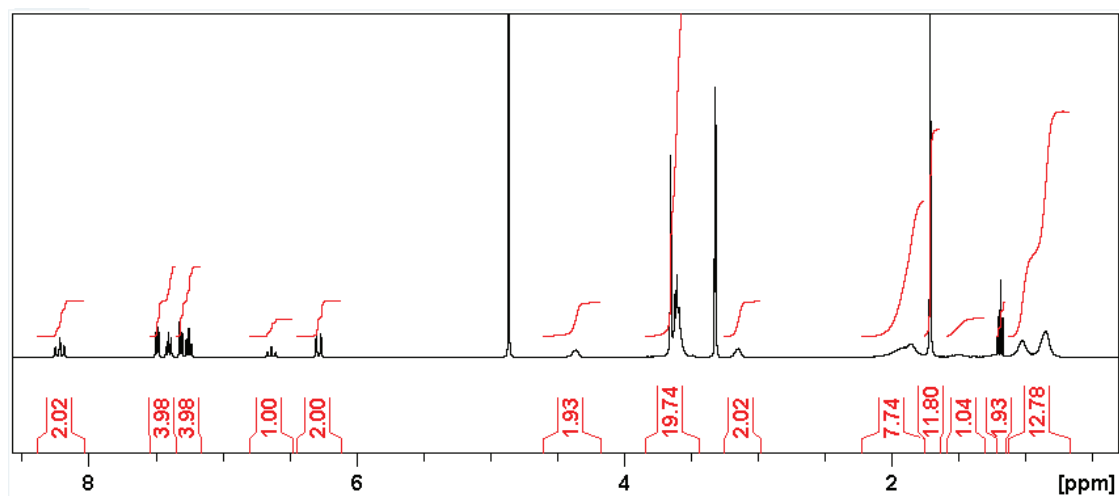


Figure 2-12:  $^1\text{H}$  NMR spectrum of Cy5-Poly20 (methanol- $d_4$ ).

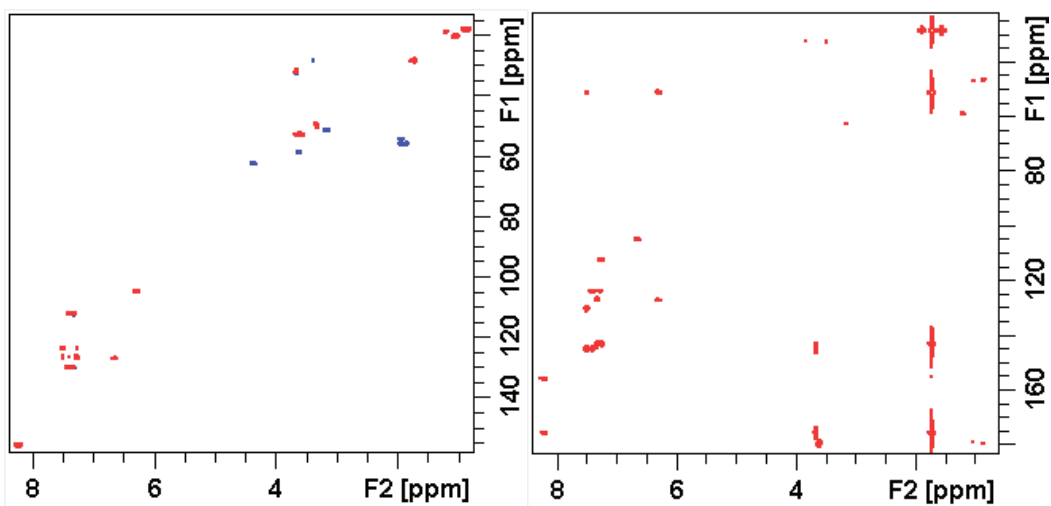


Figure 2-13: HSQC and HMBC spectra of Cy5-Poly20 (methanol- $d_4$ ).

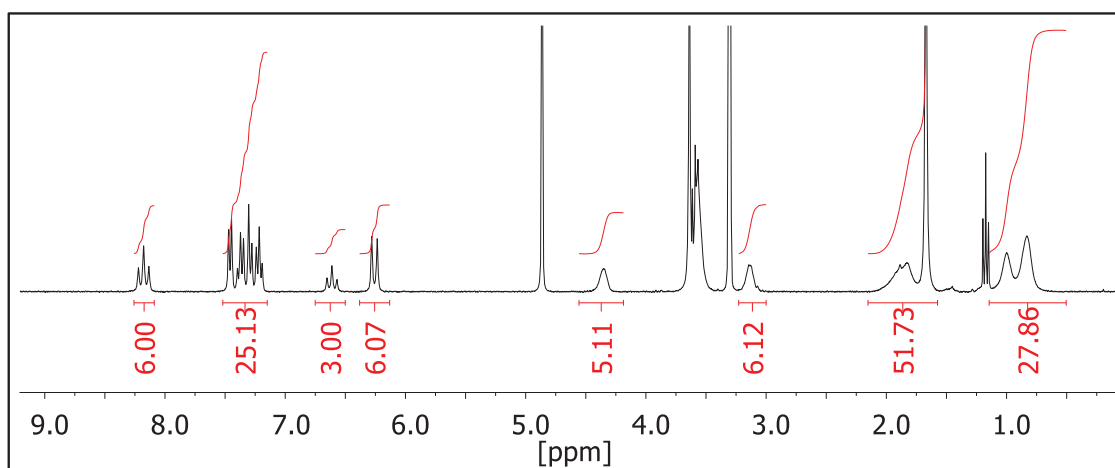


Figure 2-14: <sup>1</sup>H NMR spectrum of Cy5-Poly30 (methanol-d<sub>4</sub>).

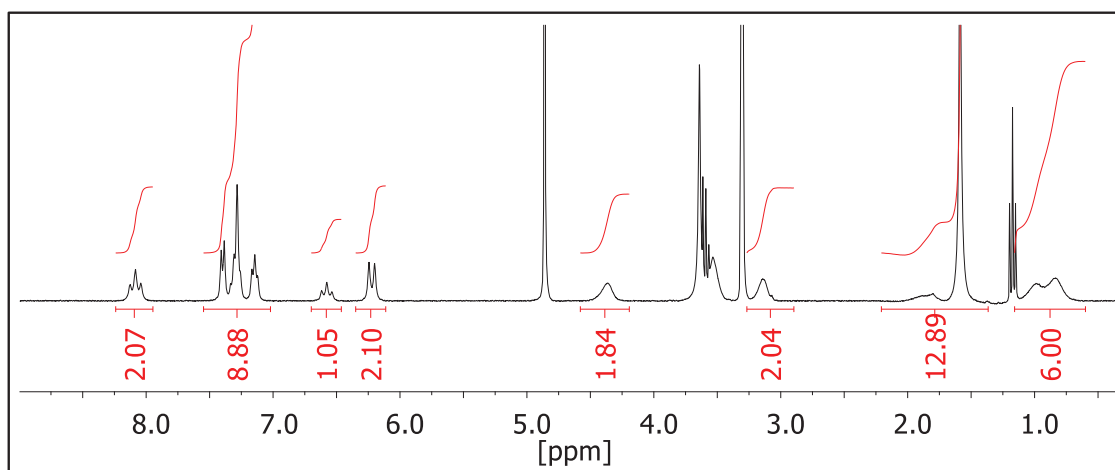
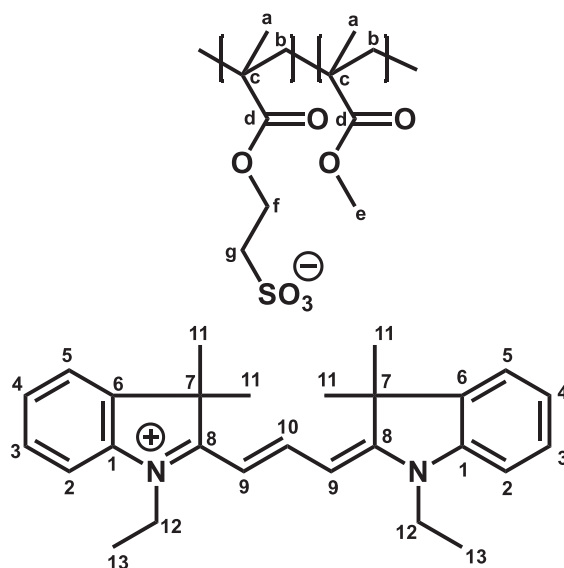


Figure 2-15: <sup>1</sup>H NMR spectrum of Cy5-Poly50 (methanol-d<sub>4</sub>).



#### **Identification of dye part for Cy3-Poly20, Cy3-Poly30 and Cy3-Poly50**

$^1\text{H}$  NMR (methanol- $d_4$ , 400.13 MHz):  $\delta$  8.56 (t,  $J = 13.5$ , 1H, H-10); 7.56 (m, 2H, H-5); 7.46 (m, 2H, H-3); 7.37 (m, 2H, H-2); 7.32 (m, 2H, H-4); 6.49 (d,  $J = 13.5$ , 2H, H-9); 4.23 (q,  $J = 7.3$ , 4H, H-12); 1.77 (s, 12H, H-11); 1.43 (t,  $J = 7.3$ , 6H, H-13).

$^{13}\text{C}$  NMR (methanol- $d_4$ , 100.61 MHz):  $\delta$  175.6 (s, C-8); 152.3 (d, C-10); 143.0 (s, C-1); 142.4 (s, C-6); 130.1 (d, C-3); 126.8 (d, C-4); 123.6 (d, C-5); 112.2 (d, C-2); 103.4 (d, C-9); 50.7 (s, C-7); 40.3 (t, C-12); 28.3 (q, C-11); 12.7 (q, C-13).

HMBC correlations: H-2  $\rightarrow$  C-(4, 6); H-3  $\rightarrow$  C-(1, 5); H-4  $\rightarrow$  C-(2, 5, 6, 7w); H-5  $\rightarrow$  C-(1, 2w, 3, 7); H-9  $\rightarrow$  C-(6w, 7, 8w, 9, 10w, 11w); H-10  $\rightarrow$  C-(8, 9w); H-11  $\rightarrow$  C-(6, 7, 8, 11); H-12  $\rightarrow$  C-(1, 8, 13); H-13  $\rightarrow$  C-(12).

DQF-COSY correlations: H-2  $\rightarrow$  H-(3); H-3  $\rightarrow$  H-(2, 4); H-4  $\rightarrow$  H-(3, 5); H-5  $\rightarrow$  H-(4); H-9  $\rightarrow$  H-(10); H-10  $\rightarrow$  H-(9); H-12  $\rightarrow$  H-(13); H-13  $\rightarrow$  H-(12).

#### **Identification of polymer part for Cy3-Poly20, Cy3-Poly30 and Cy3-Poly50**

$^1\text{H}$  NMR (methanol- $d_4$ , 400.13 MHz):  $\delta$  4.34 (m, 2H, H-f); 3.59 (s, 3H, H-e); 3.13 (m, 2H, H-g); 1.92 (m, 2H, H-b2); 1.85 (m, 2H, H-b1); 1.01 (s, 3H, H-a2); 0.84 (s, 3H, H-a1).

$^{13}\text{C}$  NMR (methanol- $d_4$ , 100.61 MHz):  $\delta$  179.5 (s, C-d1); 178.5 (s, C-d2); 62.1 (t, C-f); 55.5 (t, C-b1); 54.0 (t, C-b2); 52.5 (q, C-e); 50.8 (t, C-g); 46.2 (s, C-c2); 45.8 (s, C-c1); 19.8 (q, C-a2); 17.5 (q, C-a1).

HMBC correlations: H-a1  $\rightarrow$  C-(b1, c1, d1); H-a2  $\rightarrow$  C-(c2, d2); H-b1  $\rightarrow$  C-(c1, d1); H-b2  $\rightarrow$  C-(c2); H-e  $\rightarrow$  C-(d1, d2); H-f  $\rightarrow$  C-(g); H-g  $\rightarrow$  C-(f).

DQF-COSY correlations: H-f  $\rightarrow$  H-(g); H-g  $\rightarrow$  H-(f).

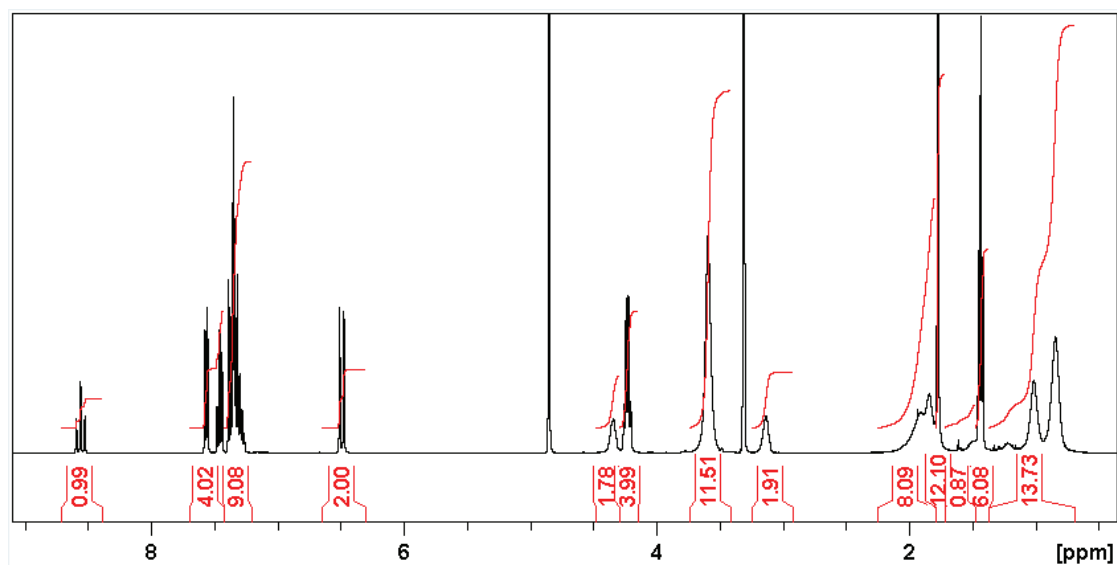


Figure 2-16: <sup>1</sup>H NMR spectrum of Cy3-Poly20 (methanol-d<sub>4</sub>).

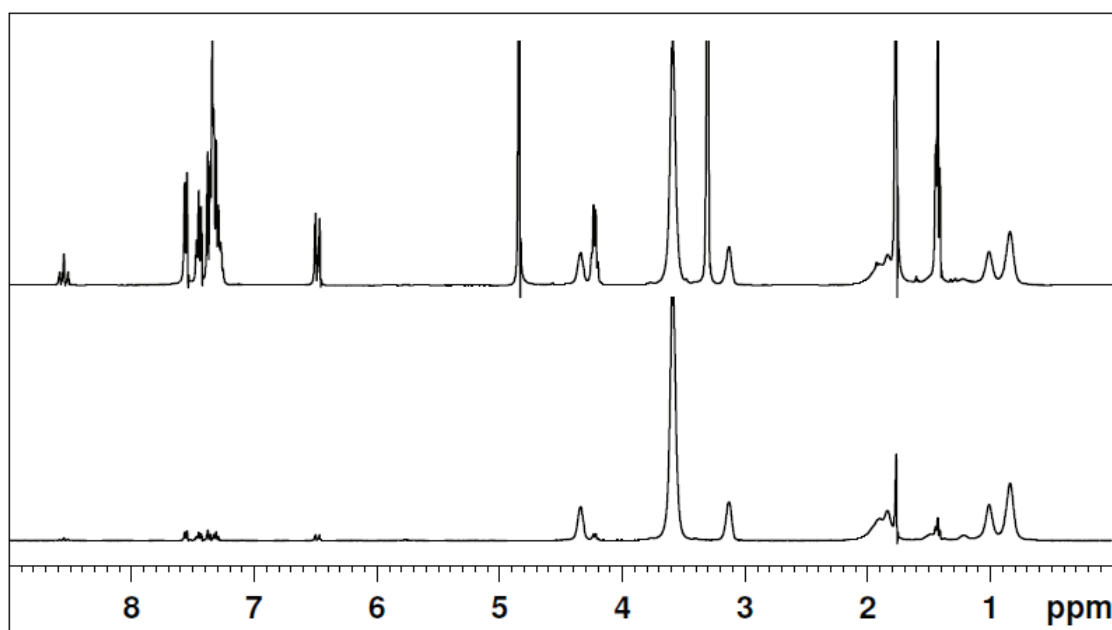


Figure 2-17: <sup>1</sup>H diffusion-edited NMR spectra of Cy3-Poly20 (methanol-d<sub>4</sub>).

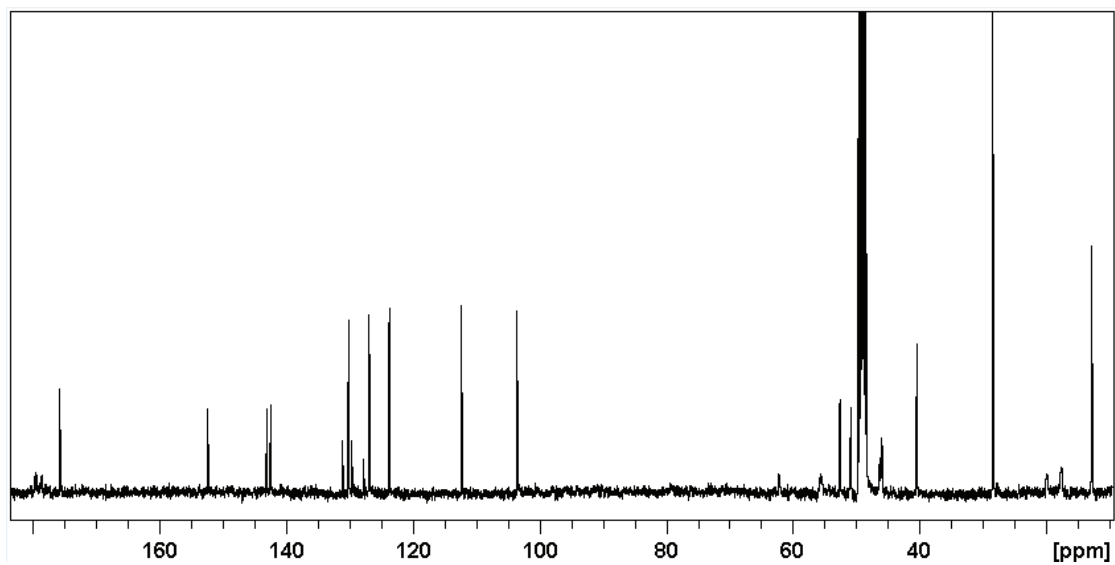


Figure 2-18:  $^{13}\text{C}\{^1\text{H}\}$  NMR spectrum of Cy3-Poly20 (methanol- $\text{d}_4$ ).

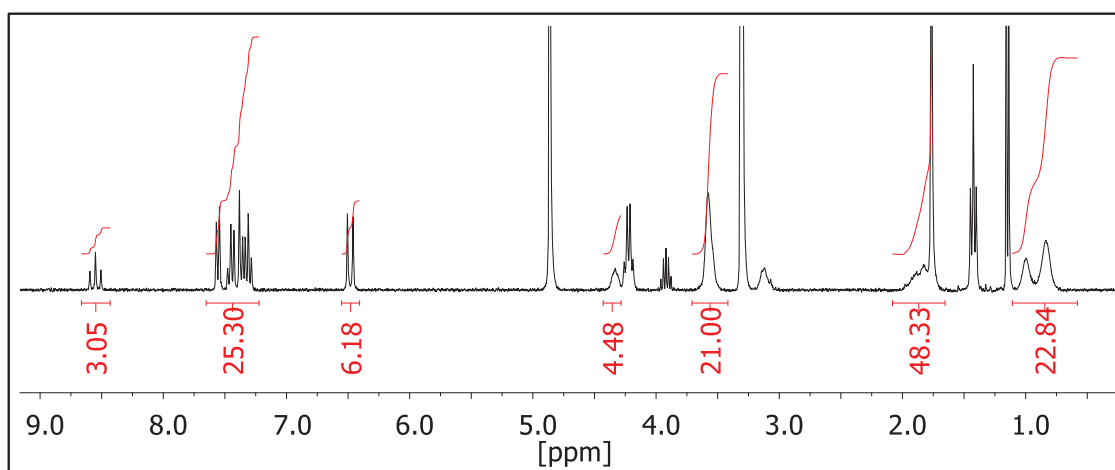


Figure 2-19:  $^1\text{H}$  NMR spectrum of Cy3-Poly30 (methanol- $\text{d}_4$ ).

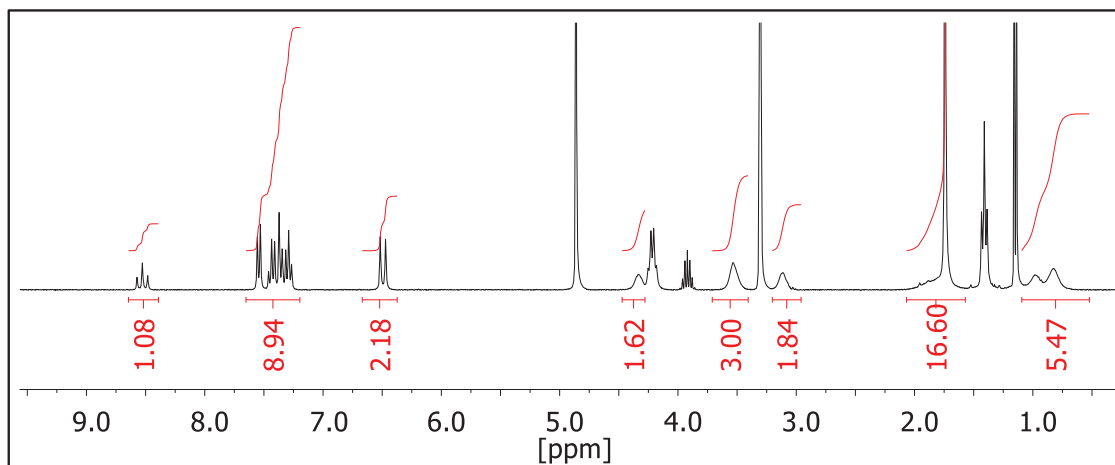
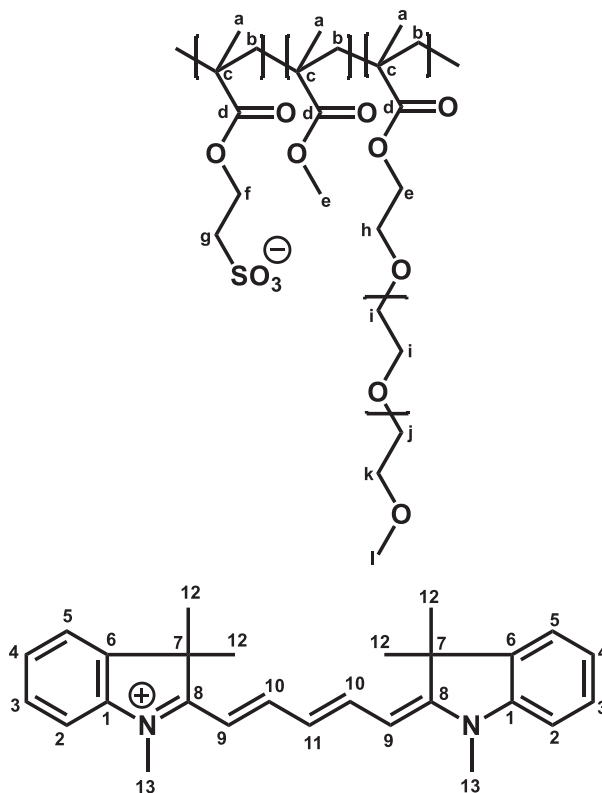


Figure 2-20:  $^1\text{H}$  NMR spectrum of Cy3-Poly50 (methanol- $\text{d}_4$ ).



**Identification of dye part for Cy5-PEG25Poly50 and Cy5-PEG50Poly50**

$^1\text{H}$  NMR (methanol- $\text{d}_4$ , 400.13 MHz):  $\delta$  8.16 (dd,  $J = 13.7, 12.4$ , 2H, H-10); 7.44 (m, 2H, H-5); 7.36 (m, 2H, H-3); 7.31 (m, 2H, H-2); 7.21 (m, 2H, H-4); 6.62 (t,  $J = 12.4$ , 1H, H-11); 6.28 (d,  $J = 13.7$ , 2H, H-9); 3.65 (s, 6H, H-13); 1.65 (s, 12H, H-12).

**Identification of polymer part for Cy5-PEG25Poly50 and Cy5-PEG50Poly50**

$^1\text{H}$  NMR (methanol- $d_4$ , 400.13 MHz):  $\delta$  4.37 (m, 2H, H-f); 4.08 (m, 2H, H-e); 3.63&3.62&3.60&3.52 (m, H-h, i, j, k); 3.35 (s, 3H, H-l); 3.15 (m, 2H, H-g); 1.81&1.49 (m, 2H, H-b); 1.05 (s, 3H, H-a2); 0.91 (s, 3H, H-a1).

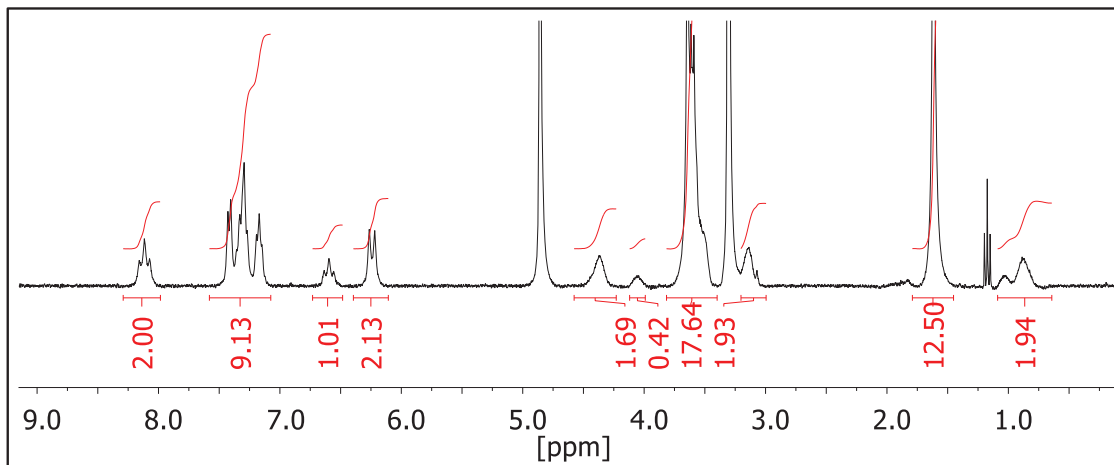


Figure 2-21:  $^1\text{H}$  NMR spectrum of Cy5-PEG25Poly50 (methanol- $d_4$ ).

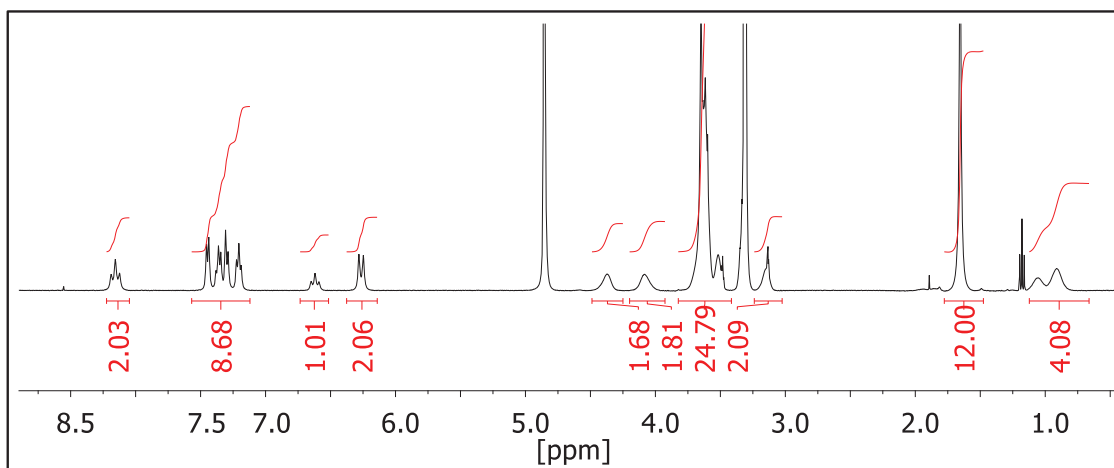
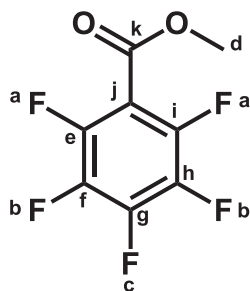


Figure 2-22:  $^1\text{H}$  NMR spectrum of Cy5-PEG50Poly50 (methanol- $d_4$ ).

### 2.6.2 NMR characterization for Cy-FN3





$^1\text{H}$  NMR (chloroform-d, 300.13 MHz):  $\delta$  3.98 (s, 3H, H-d).

$^{19}\text{F}$  NMR (chloroform-d, 376.50 MHz):  $\delta$  -138.11 (m, 2F, F-a); -148.49 (m, 1F, F-c); -160.34 (m, 2F, F-b).

$^{13}\text{C}$  NMR (chloroform-d, 75.48 MHz):  $\delta$  159.49 (C-k); 147.06 – 136.07 (C-e, f, g, h, i); 108.10 (C-j); 53.36 (C-d).

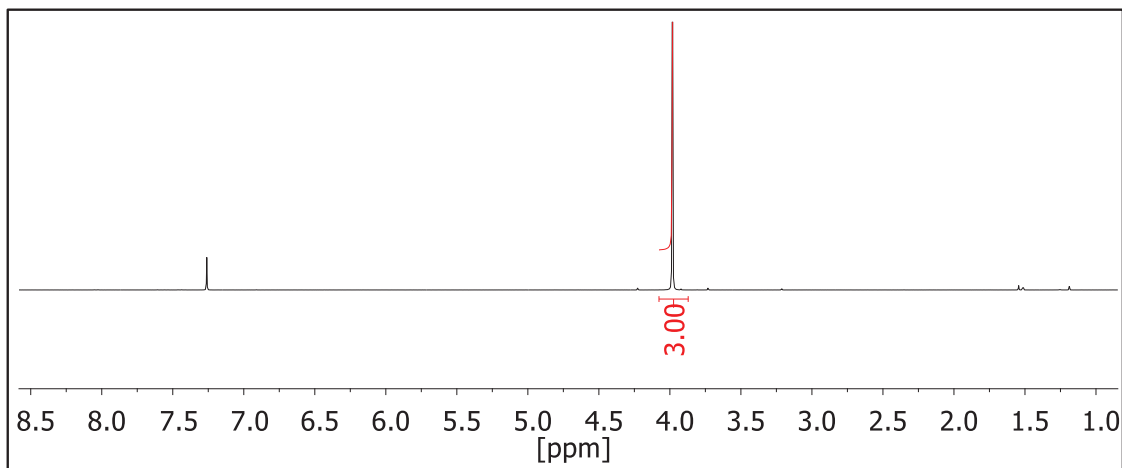


**Figure 2-23:**  $^1\text{H}$  NMR spectrum of methyl pentafluorobenzoate (1) (chloroform-d).

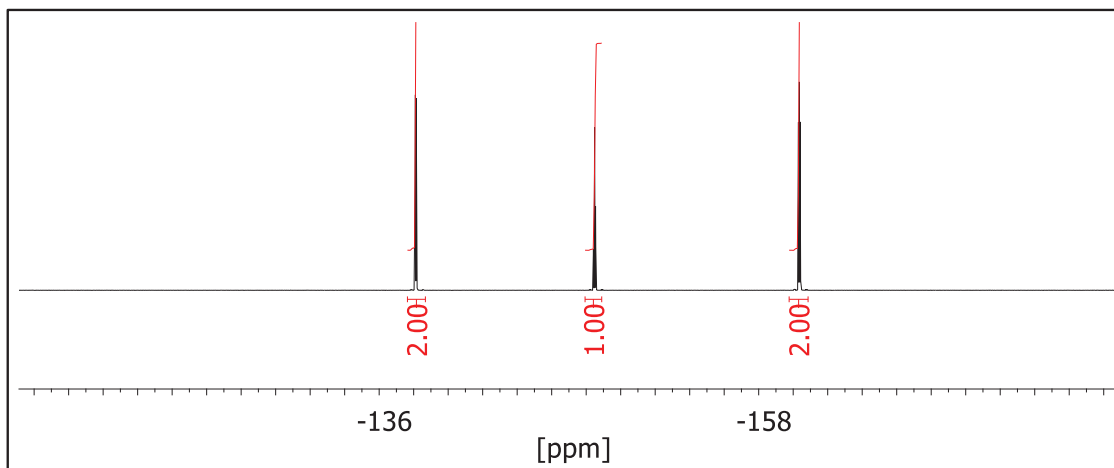


**Figure 2-24:**  $^{19}\text{F}$  NMR spectrum of methyl pentafluorobenzoate (1) (chloroform-d).

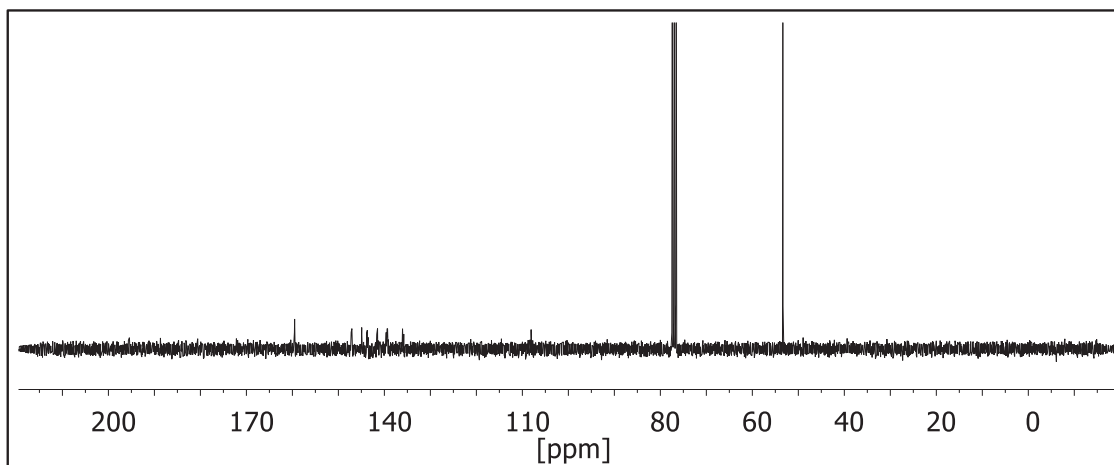
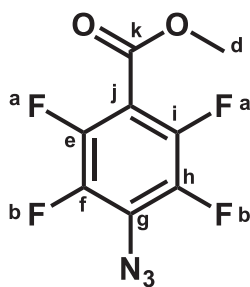


**Figure 2-25:**  $^{13}\text{C}$  NMR spectrum of methyl pentafluorobenzoate (1) (chloroform-d).



$^1\text{H}$  NMR (chloroform-d, 300.13 MHz):  $\delta$  3.97 (s, 3H, H-d).

$^{19}\text{F}$  NMR (chloroform-d, 376.50 MHz):  $\delta$  -138.62 (m, 2F, F-a); -150.89 (m, 2F, F-b).

$^{13}\text{C}$  NMR (chloroform-d, 75.48 MHz):  $\delta$  159.77 (C-k); 147.03 – 138.69 (C-e, f, h, i); 123.37 (C-g); 107.61 (C-j); 53.20 (C-d).

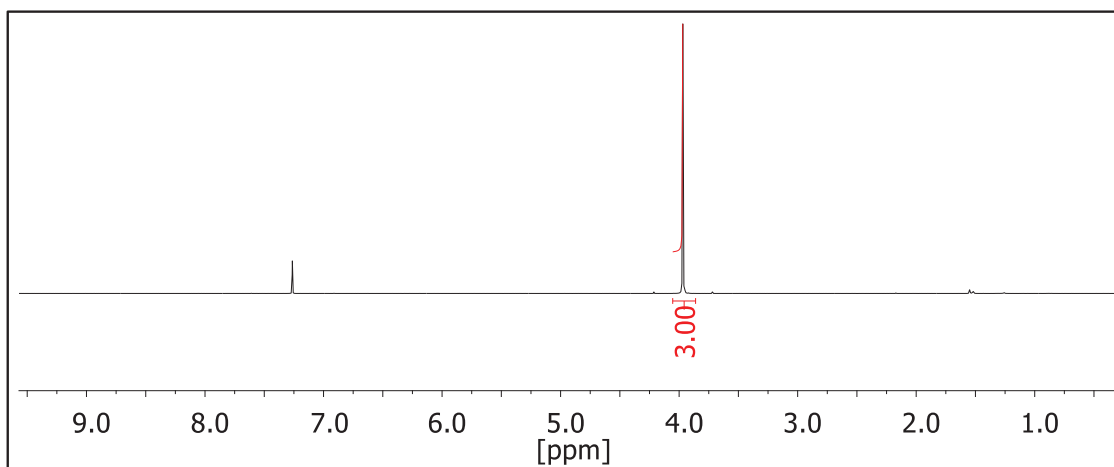


**Figure 2-26:**  $^1\text{H}$  NMR spectrum of methyl 4-azido-2,3,5,6-tetrafluorobenzoate (2) (chloroform-d).

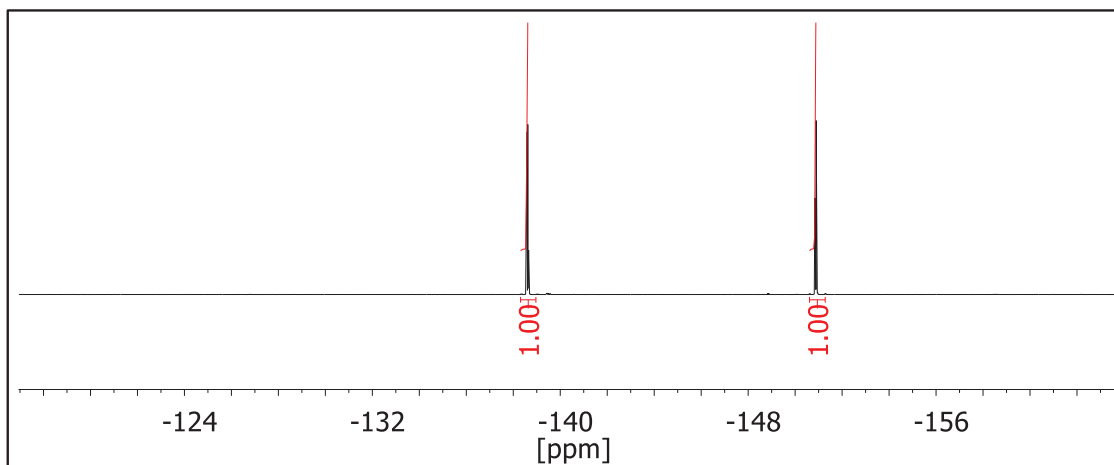


**Figure 2-27:**  $^{19}\text{F}$  NMR spectrum of methyl 4-azido-2,3,5,6-tetrafluorobenzoate (2) (chloroform-d).

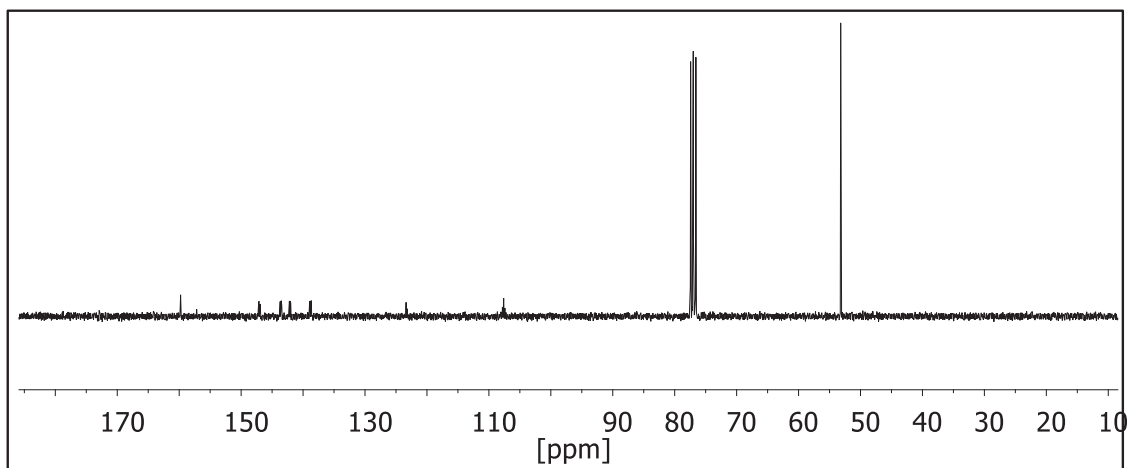
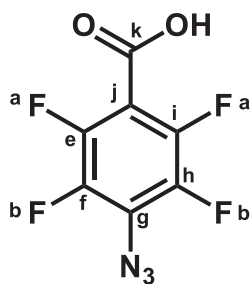


**Figure 2-28:**  $^{13}\text{C}$  NMR spectrum of methyl 4-azido-2,3,5,6-tetrafluorobenzoate (2) (chloroform-d).



$^{19}\text{F}$  NMR (DMSO- $d_6$ , 282.40 MHz):  $\delta$  -141.38 (m, 2F, F-a); -151.60 (m, 2F, F-b).

$^{13}\text{C}$  NMR (DMSO- $d_6$ , 75.48 MHz):  $\delta$  160.46 (C-k); 146.31 – 139.10 (C-e, f, h, i); 123.03 (C-g); 108.96 (C-j).

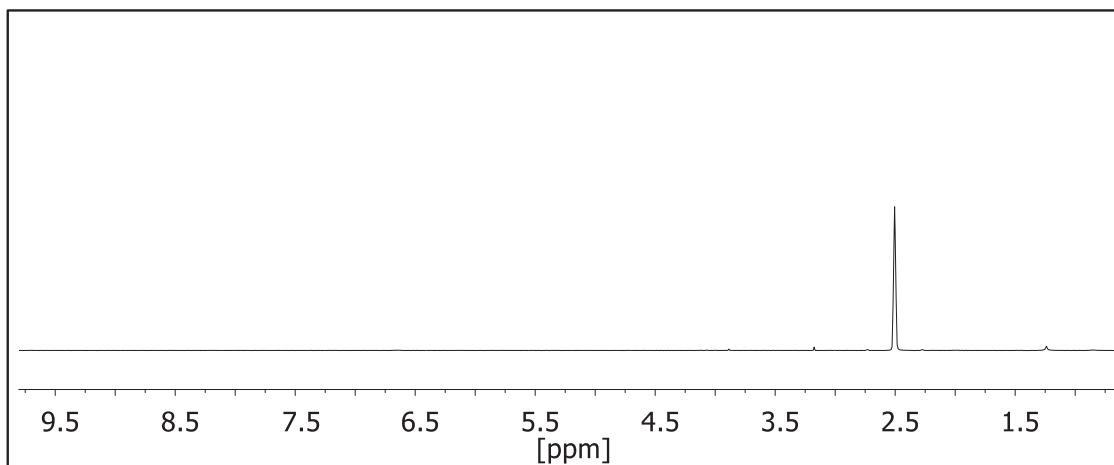


**Figure 2-29:** <sup>1</sup>H NMR spectrum of methyl 4-azido-2,3,5,6-tetrafluorobenzoic acid (3) (DMSO-d<sub>6</sub>).

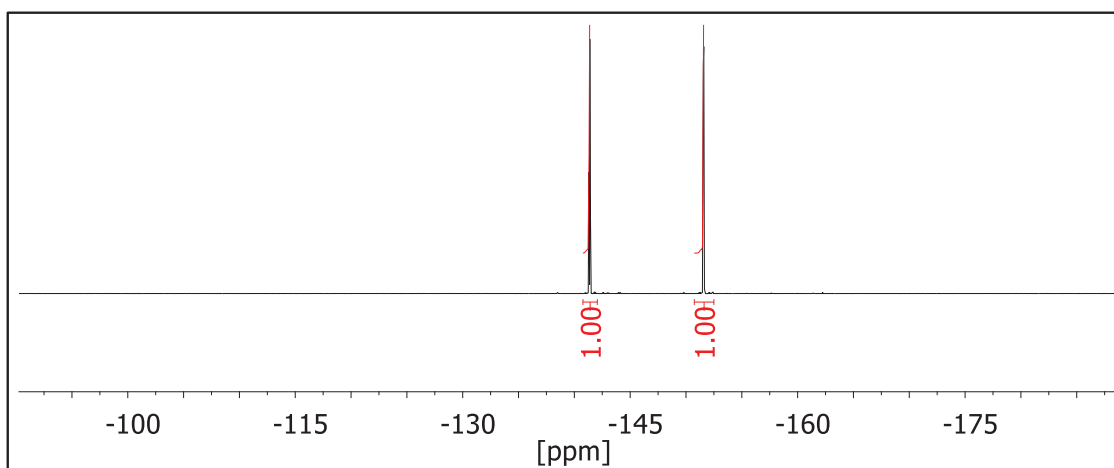


**Figure 2-30:** <sup>19</sup>F NMR spectrum of methyl 4-azido-2,3,5,6-tetrafluorobenzoic acid (3) (DMSO-d<sub>6</sub>).

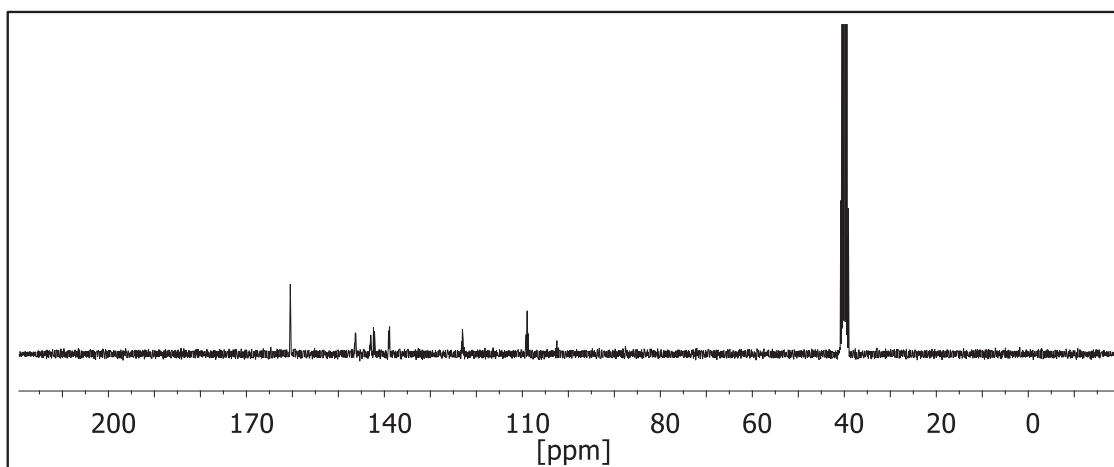
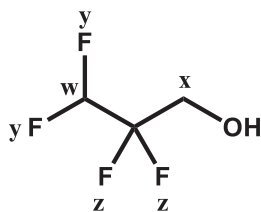


**Figure 2-31:** <sup>13</sup>C NMR spectrum of methyl 4-azido-2,3,5,6-tetrafluorobenzoic acid (3) (DMSO-d<sub>6</sub>).



$^1\text{H}$  NMR (methanol- $d_4$ , 400.13 MHz):  $\delta$  6.13 (1H, H-w); 3.85 (2H, H-x).

$^{19}\text{F}$  NMR (methanol- $d_4$ , 376.50 MHz):  $\delta$  -129.57 (tt, 2F, F-z); -141.93 (tt, 2F, F-y).

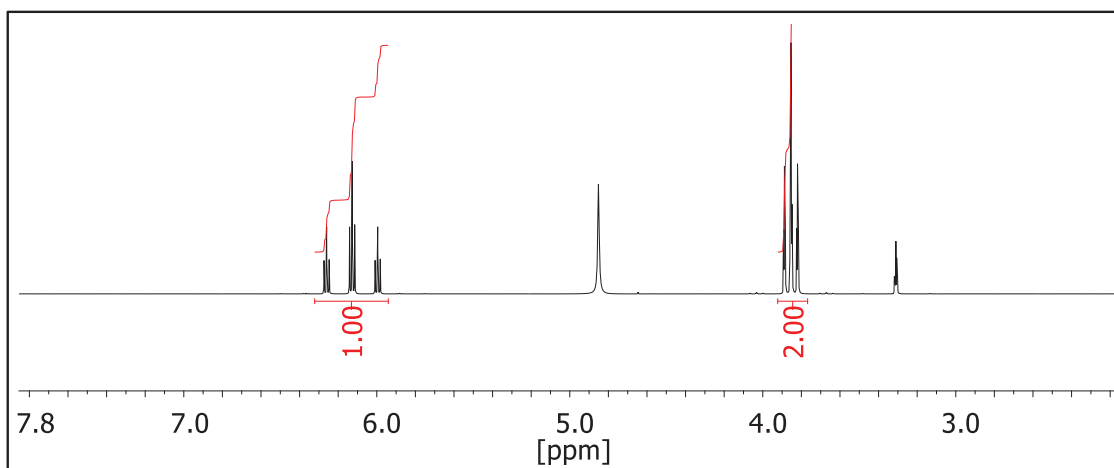


Figure 2-32:  $^1\text{H}$  NMR spectrum of TFP (methanol- $d_4$ ).

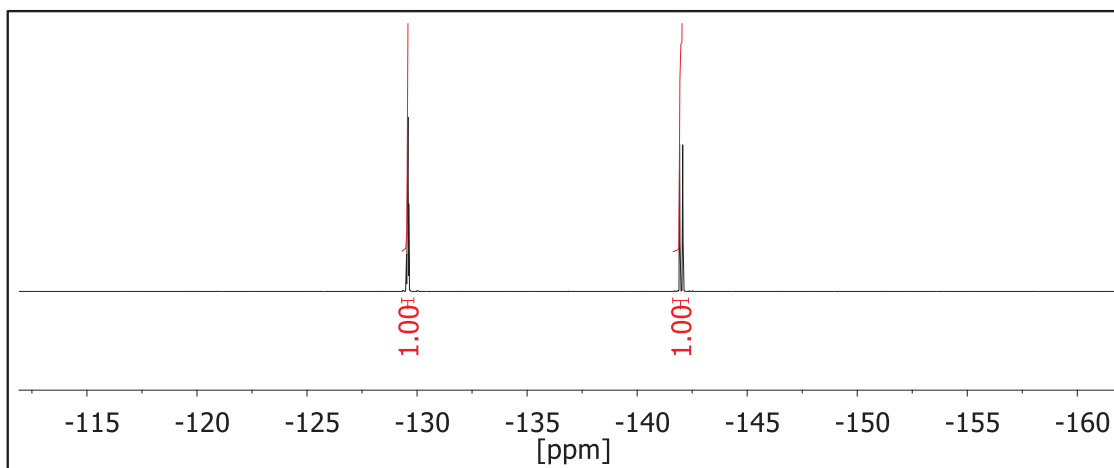
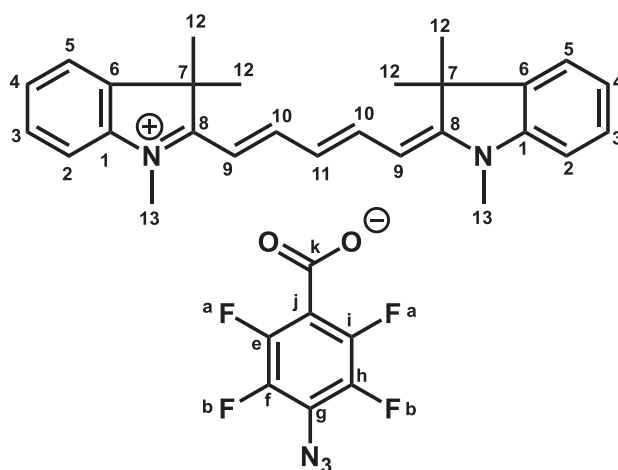


Figure 2-33:  $^{19}\text{F}$  NMR spectrum of TFP (methanol- $d_4$ ).



$^1\text{H}$  NMR (methanol- $d_4$ , 400.18 MHz):  $\delta$  8.26 (dd, 2H, H-10); 7.50 (m, 2H, H-5); 7.44 (m, 2H, H-3); 7.32 (m, 2H, H-2); 7.29 (m, 2H, H-4); 6.64 (t, 1H, H-11); 6.30 (d, 2H, H-9); 3.62 (s, 6H, H-13); 1.71 (s, 12H, H-12).

$^{19}\text{F}$  NMR (methanol- $d_4$ , 376.54 MHz):  $\delta$  -145.72 (m, 2F, F-a); -154.59 (m, 2F, F-b).

$^{13}\text{C}$  NMR (methanol- $d_4$ , 125.76 MHz):  $\delta$  173.87 (s, C-8); 154.06 (d, C-10); 142.84 (s, C-1); 141.09 (s, C-6); 128.29 (d, C-3); 125.17 (d, C-11); 124.81 (d, C-4); 121.85 (d, C-5); 110.38 (d, C-2); 102.91 (d, C-9); 49.06 (s, C-7); 30.09 (q, C-13); 26.41 (q, C-12).

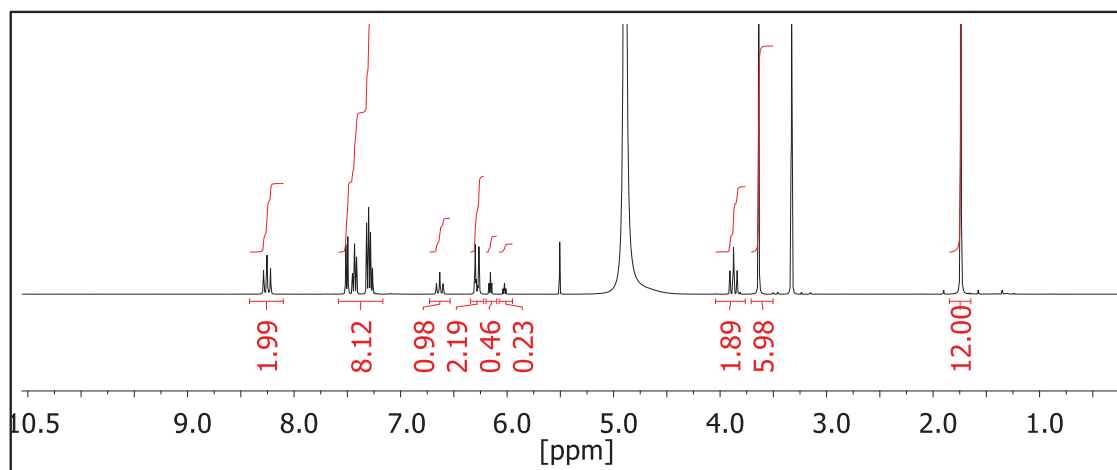


**Figure 2-34:**  $^1\text{H}$  NMR spectrum of Cy5-FN3 (with TFP) (methanol- $d_4$ ).

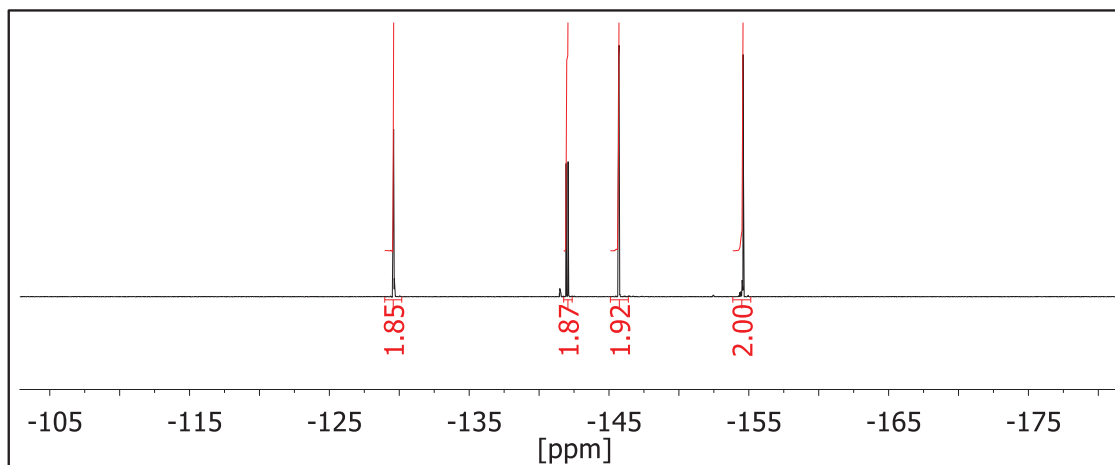


Figure 2-35:  $^{19}\text{F}$  NMR spectrum of Cy5-FN3 (with TFP) (methanol- $\text{d}_4$ ).

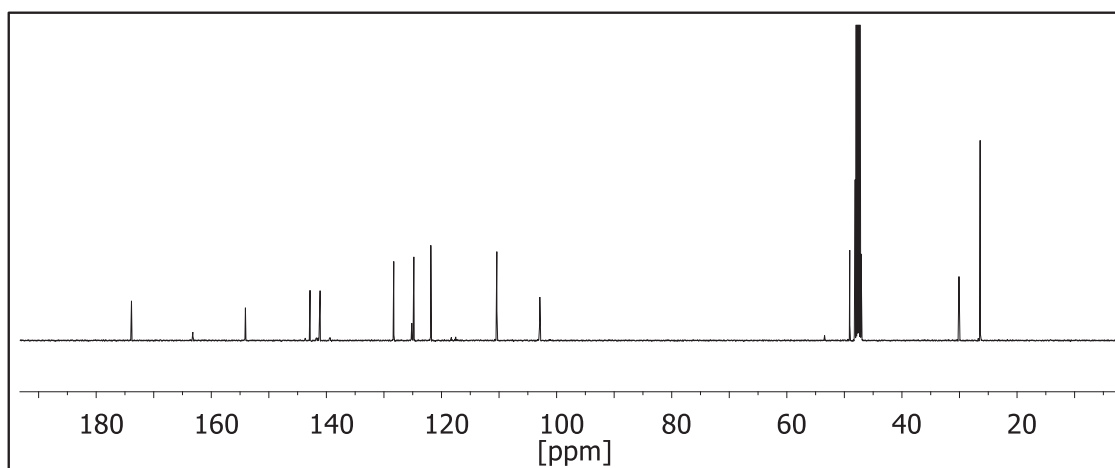
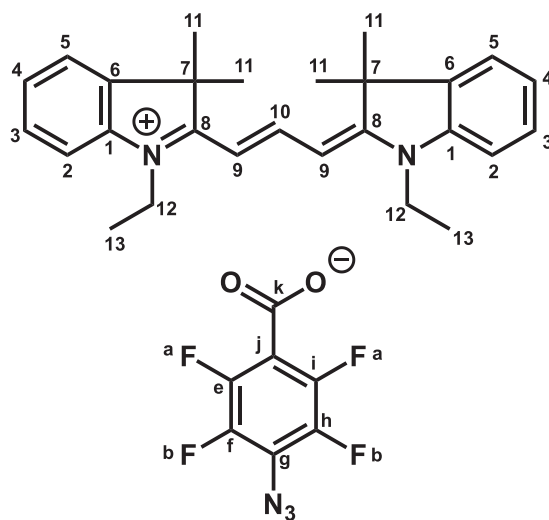


Figure 2-36:  $^{13}\text{C}$  NMR spectrum of Cy5-FN3 (methanol- $\text{d}_4$ ).



$^1\text{H}$  NMR (methanol- $d_4$ , 500.13 MHz):  $\delta$  8.56 (t, 1H, H-10); 7.55 (m, 2H, H-5); 7.46 (m, 2H, H-3); 7.37 (m, 2H, H-2); 7.32 (m, 2H, H-4); 6.46 (d, 2H, H-9); 4.22 (q, 4H, H-12); 1.77 (s, 12H, H-11); 1.43 (t, 6H, H-13).

$^{19}\text{F}$  NMR (methanol- $d_4$ , 470.59 MHz):  $\delta$  -145.78 (m, 2F, F-a); -154.66 (m, 2F, F-b).

$^{13}\text{C}$  NMR (methanol- $d_4$ , 125.76 MHz):  $\delta$  174.15 (s, C-8); 150.83 (d, C-10); 141.50 (s, C-1); 140.90 (s, C-6); 128.65 (d, C-3); 125.37 (d, C-4); 122.19 (d, C-5); 110.83 (d, C-2); 102.05 (d, C-9); 49.26 (s, C-7); 38.94 (t, C-12); 26.90 (q, C-11); 11.34 (q, C-13).

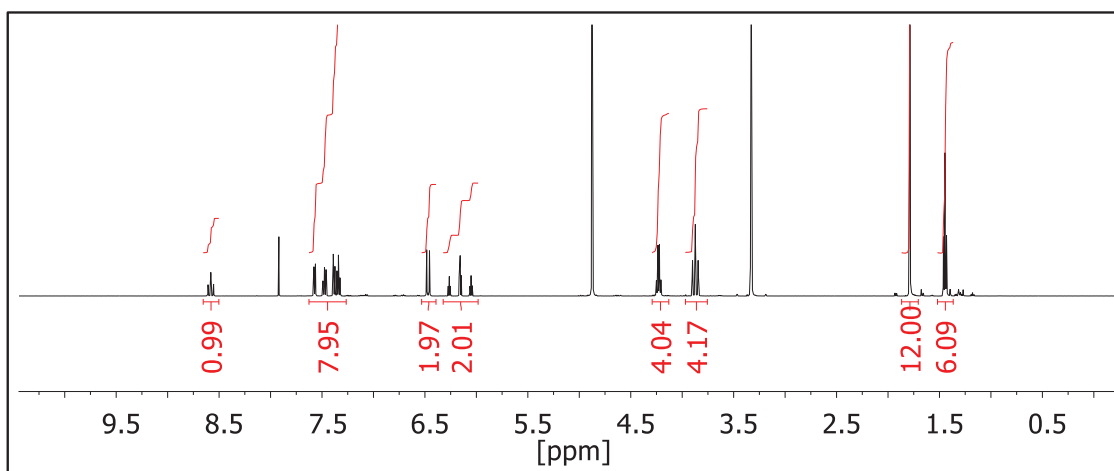


Figure 2-37:  $^1\text{H}$  NMR spectrum of Cy3-FN3 (with TFP) (methanol- $d_4$ ).

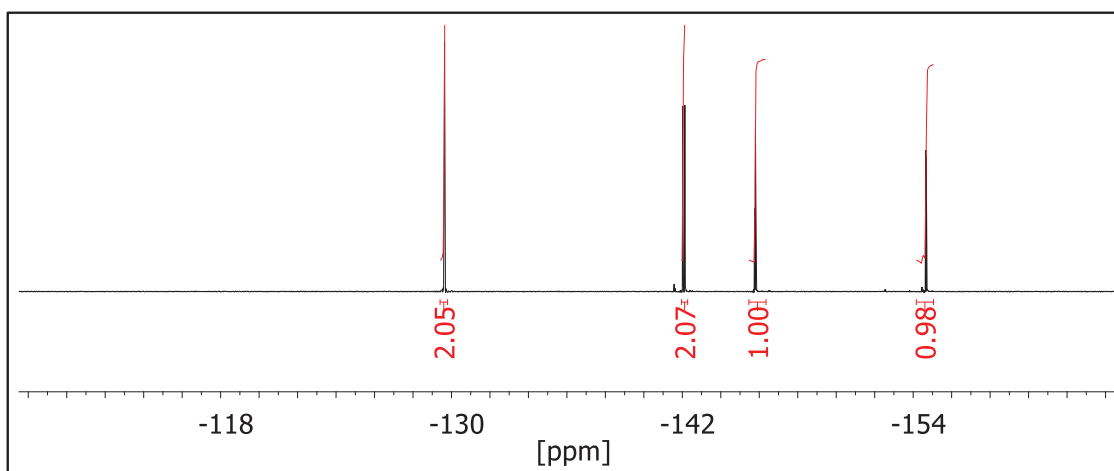


Figure 2-38:  $^{19}\text{F}$  NMR spectrum of Cy3-FN3 (with TFP) (methanol- $d_4$ ).



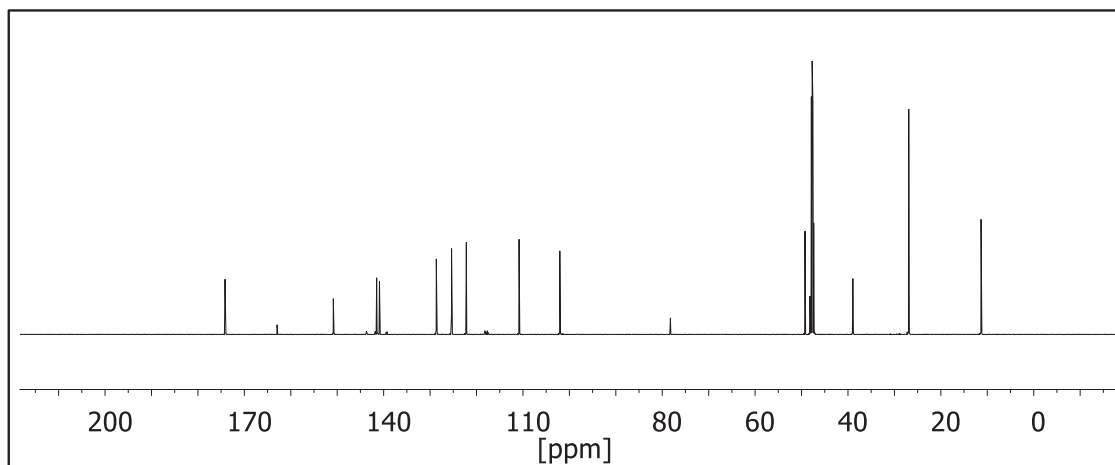
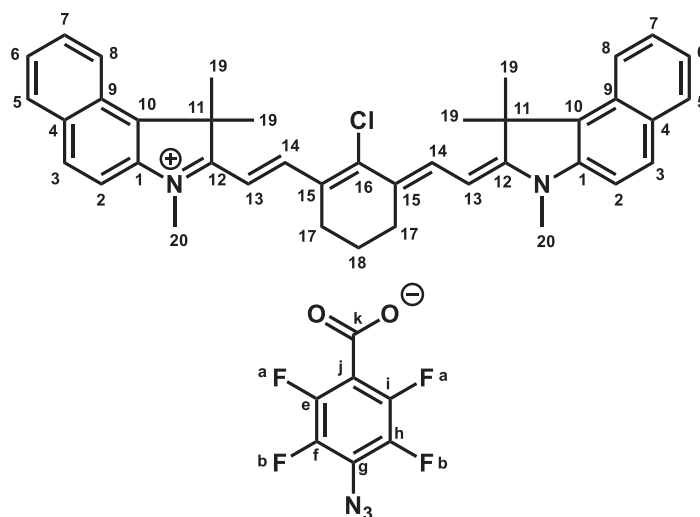


Figure 2-39:  $^{13}\text{C}$  NMR spectrum of Cy3-FN3 (methanol- $d_4$ ).



$^1\text{H}$  NMR (methanol- $d_4$ , 500.13 MHz):  $\delta$  8.55 (d, 2H, H-14); 8.27&8.03&7.64&7.50 (H-2, 3, 5, 6, 7, 8); 6.30 (d, 2H, H-13); 3.80 (s, 6H, H-20); 2.79 (t, 4H, H-17); 2.04 (s, 12H, H-19); 2.00 (t, 2H, H-18).

$^{19}\text{F}$  NMR (methanol- $d_4$ , 470.59 MHz):  $\delta$  -145.79 (m, 2F, F-a); -154.65 (m, 2F, F-b).

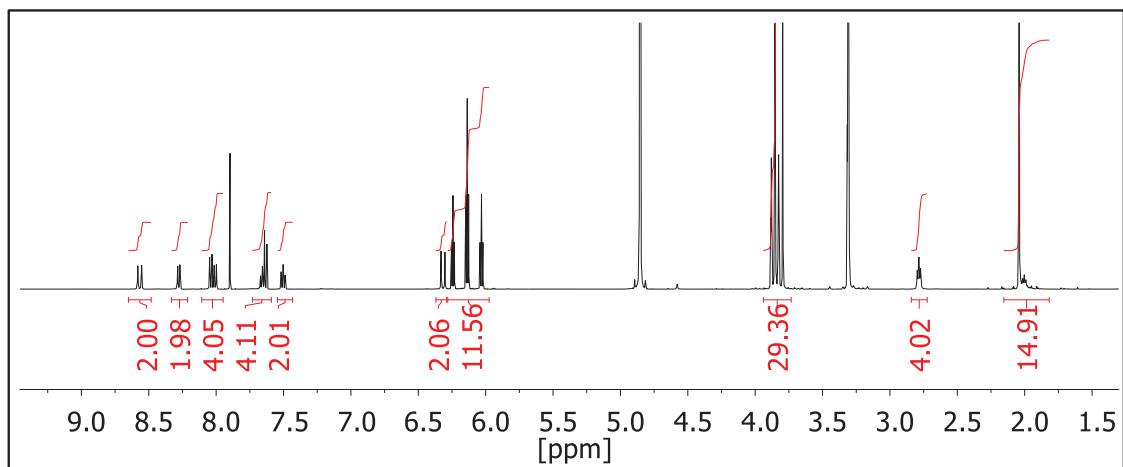


Figure 2-40:  $^1\text{H}$  NMR spectrum of Cy7-FN3 (with TFP) (methanol- $\text{d}_4$ ).

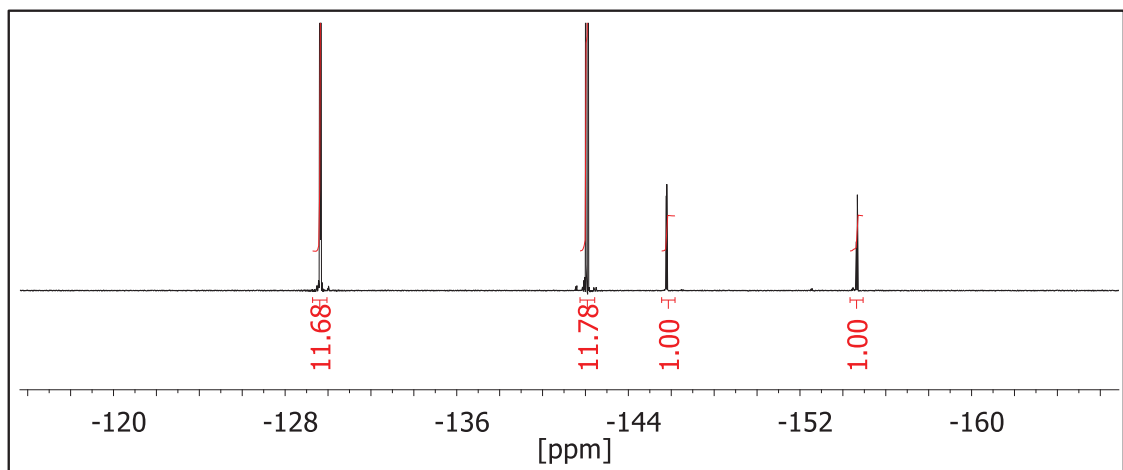
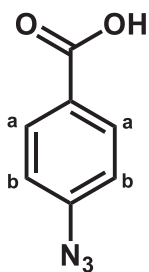
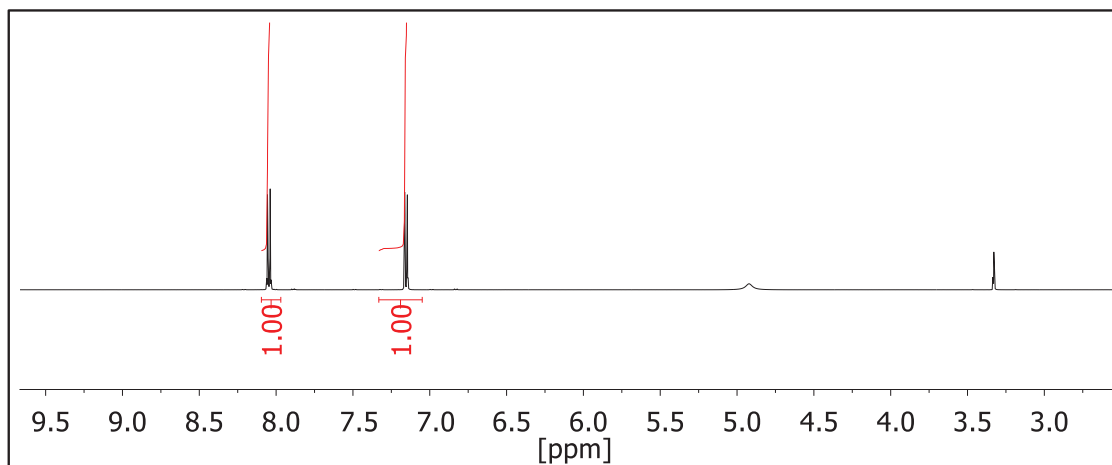


Figure 2-41:  $^{19}\text{F}$  NMR spectrum of Cy7-FN3 (with TFP) (methanol- $\text{d}_4$ ).

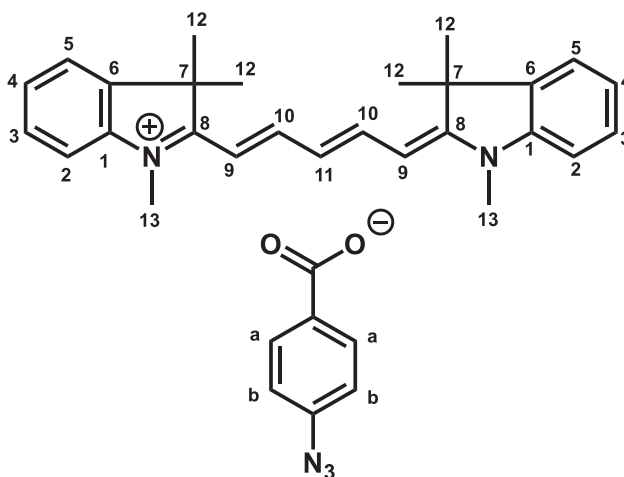
### 2.6.3 NMR characterization for Cy-N3



$^1\text{H}$  NMR (methanol- $\text{d}_4$ , 500.13 MHz):  $\delta$  8.06 (2H, H-a); 7.16 (2H, H-b).



**Figure 2-42:**  $^1\text{H}$  NMR spectrum of 4-azido benzoic acid (5) (methanol- $\text{d}_4$ ).



$^1\text{H}$  NMR (methanol- $\text{d}_4$ , 400.13 MHz):  $\delta$  8.26 (dd,  $J = 13.8, 12.4$ , 2H, H-10); 7.97 (2H, H-a); 7.50 (m, 2H, H-5); 7.43 (m, 2H, H-3); 7.32 (m, 2H, H-2); 7.27 (m, 2H, H-4); 7.04 (2H, H-b); 6.63 (t,  $J = 12.4$ , 1H, H-11); 6.30 (d,  $J = 13.8$ , 2H, H-9); 3.64 (s, 6H, H-13); 1.74 (s, 12H, H-12).

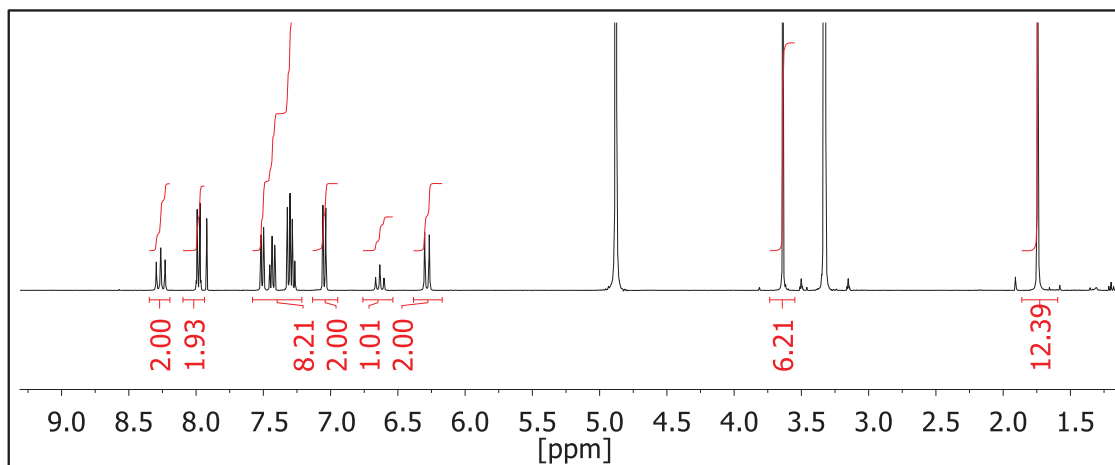
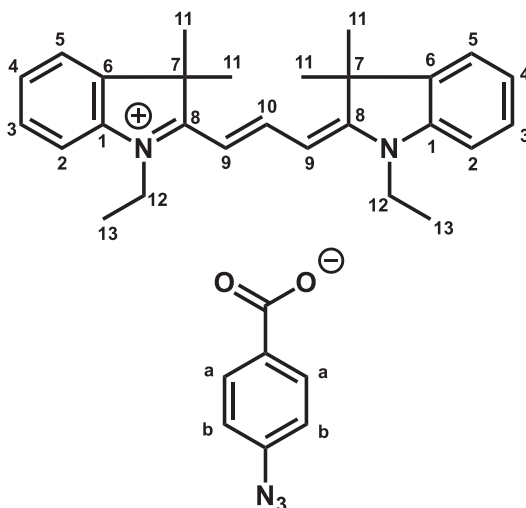
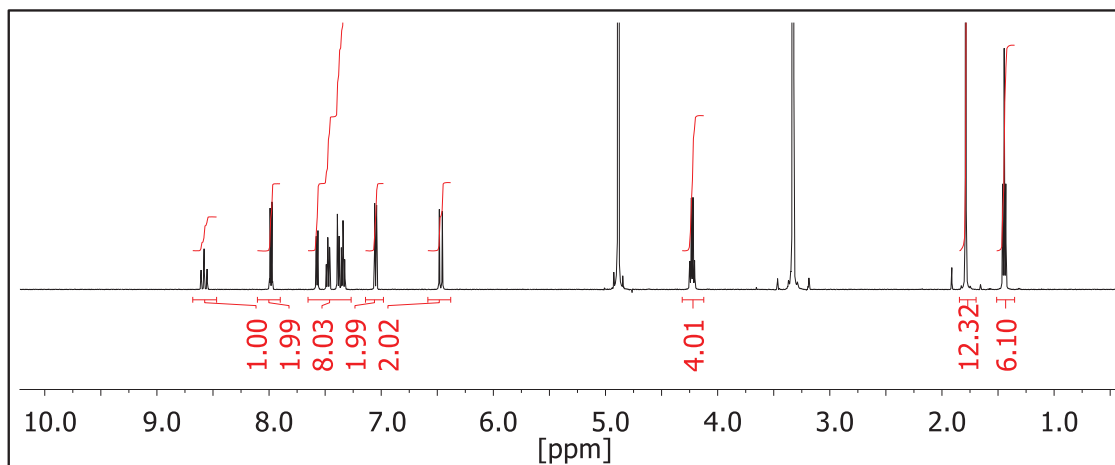


Figure 2-43:  $^1\text{H}$  NMR spectrum of Cy5-N3 (methanol- $d_4$ ).



$^1\text{H}$  NMR (methanol- $d_4$ , 400.13 MHz):  $\delta$  8.58 (t,  $J = 13.5$ , 1H, H-10); 7.97 (2H, H-a); 7.57 (m, 2H, H-5); 7.47 (m, 2H, H-3); 7.39 (m, 2H, H-2); 7.34 (m, 2H, H-4); 7.05 (2H, H-b); 6.48 (d,  $J = 13.5$ , 2H, H-9); 4.22 (q,  $J = 7.3$ , 4H, H-12); 1.79 (s, 12H, H-11); 1.45 (t,  $J = 7.3$ , 6H, H-13).



**Figure 2-44:** <sup>1</sup>H NMR spectrum of Cy3-N3 (methanol-d<sub>4</sub>).

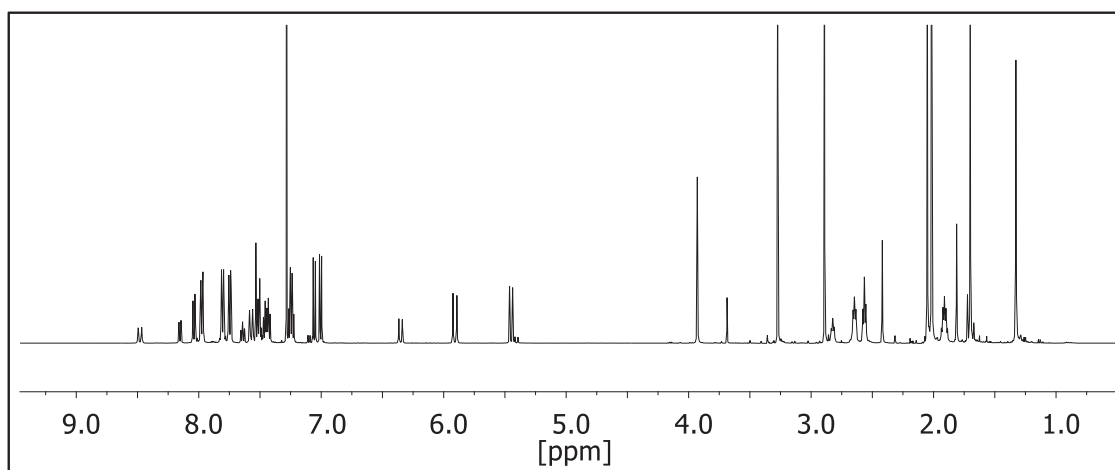
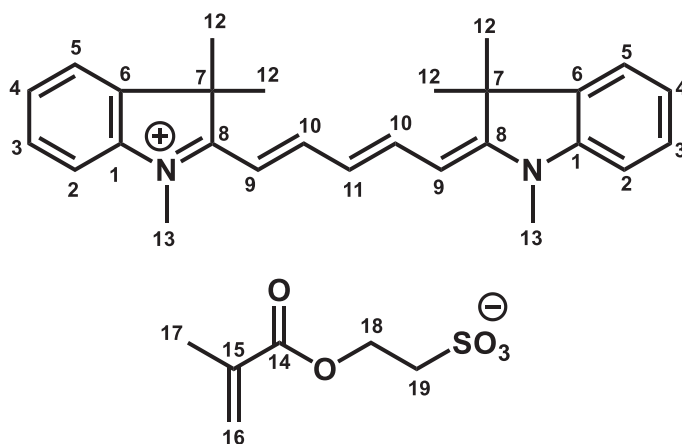


**Figure 2-45:** <sup>1</sup>H NMR spectrum of Cy7-Cl (methanol-d<sub>4</sub>) extracted after washing with NaOH aqueous solution (pH = 9).

## 2.6.4 NMR characterization for Cy-MES



$^1\text{H}$  NMR (methanol- $d_4$ , 400.13 MHz):  $\delta$  8.22 (dd,  $J = 13.8, 12.4$ , 2H, H-10); 7.48 (m, 2H, H-5); 7.40 (m, 2H, H-3); 7.29 (m, 2H, H-2); 7.25 (m, 2H, H-4); 6.62 (t,  $J = 12.4$ , 1H, H-11); 6.27 (d,  $J = 13.8$ , 2H, H-9); 6.12&5.60 (m, 2H, H-16); 4.49 (t,  $J = 7.1$ , 2H, H-18); 3.62 (s, 6H, H-13); 3.17 (t,  $J = 7.1$ , 2H, H-19); 1.92 (m, 3H, H-17); 1.71 (s, 12H, H-12).

$^{13}\text{C}$  NMR (methanol- $d_4$ , 100.61 MHz):  $\delta$  175.3 (s, C-8); 168.6 (s, C-14); 155.5 (d, C-10); 144.3 (s, C-1); 142.5 (s, C-6); 137.6 (s, C-15); 129.7 (d, C-3); 126.6 (d, C-11); 126.5 (t, C-16); 126.2 (d, C-4); 123.3 (d, C-5); 111.8 (d, C-2); 104.3 (d, C-9); 61.7 (t, C-18); 51.2 (t, C-19); 50.4 (s, C-7); 31.5 (q, C-13); 27.8 (q, C-12); 18.4 (q, C-17).

HMBC correlations: H-2  $\rightarrow$  C-(4, 6); H-3  $\rightarrow$  C-(1, 2w, 5); H-4  $\rightarrow$  C-(2, 6); H-5  $\rightarrow$  C-(1, 3, 7); H-9  $\rightarrow$  C-(7, 8w, 10w, 11, 12w); H-10  $\rightarrow$  C-(8, 9, 10); H-11  $\rightarrow$  C-(9, 10); H-12  $\rightarrow$  C-(5, 7, 8, 12); H-13  $\rightarrow$  C-(1, 8); H-16  $\rightarrow$  C-(14, 15, 17); H-17  $\rightarrow$  C-(14, 15, 16); H-18  $\rightarrow$  C-(14, 19); H-19  $\rightarrow$  C-(18).

DQF-COSY correlations: H-2  $\rightarrow$  H-(3); H-3  $\rightarrow$  H-(2, 4); H-4  $\rightarrow$  H-(3, 5); H-5  $\rightarrow$  H-(4); H-9  $\rightarrow$  H-(10); H-10  $\rightarrow$  H-(9, 11); H-11  $\rightarrow$  H-(10); H-16  $\rightarrow$  H-(17); H-17  $\rightarrow$  H-(16); H-18  $\rightarrow$  H-(19); H-19  $\rightarrow$  H-(18).

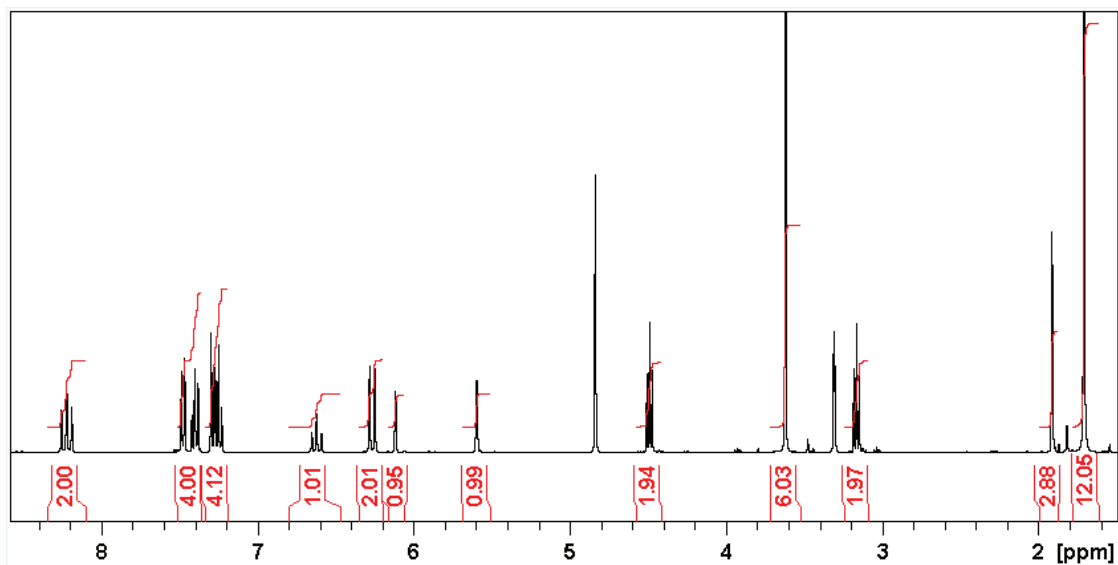


Figure 2-46: <sup>1</sup>H NMR spectrum of Cy5-MES (methanol-d<sub>4</sub>).

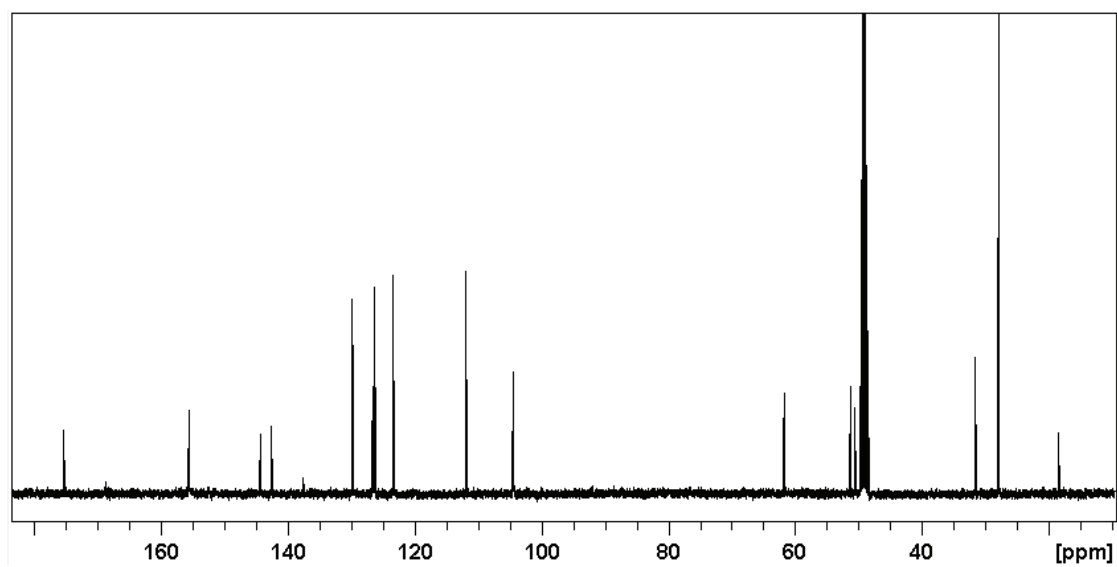


Figure 2-47: <sup>13</sup>C{<sup>1</sup>H} NMR spectrum of Cy5-MES (methanol-d<sub>4</sub>).

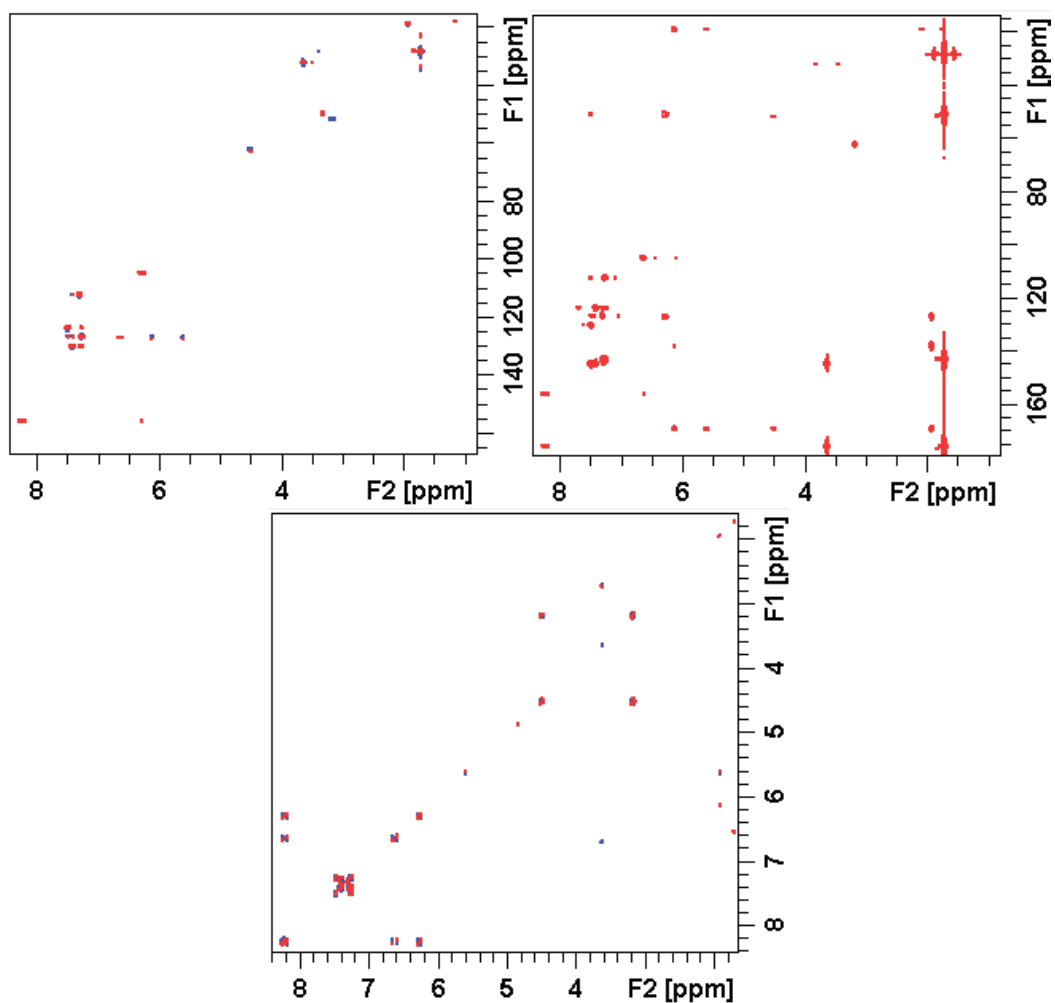
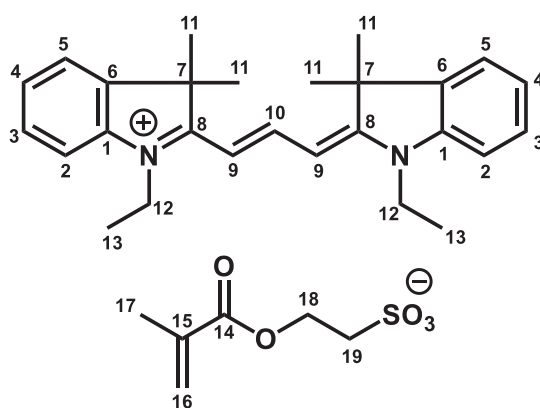


Figure 2-48: HSQC, HMBC and DQF-COSY NMR spectra of Cy5-MES (methanol- $d_4$ ).



$^1\text{H}$  NMR (methanol- $d_4$ , 400.13 MHz):  $\delta$  8.55 (t,  $J = 13.5$ , 1H, H-10); 7.55 (m, 2H, H-5); 7.45 (m, 2H, H-3); 7.36 (m, 2H, H-2); 7.31 (m, 2H, H-4); 6.48 (d,  $J = 13.5$ , 2H, H-9); 6.11&5.60 (m, 2H, H-



16); 4.49 (t,  $J = 7.1$ , 2H, H-18); 4.22 (q,  $J = 7.3$ , 4H, H-12); 3.17 (t,  $J = 7.1$ , 2H, H-19); 1.92 (m, 3H, H-17); 1.77 (s, 12H, H-11); 1.42 (t,  $J = 7.3$ , 6H, H-13).

$^{13}\text{C}$  NMR (methanol- $d_4$ , 100.61 MHz):  $\delta$  175.3 (s, C-8); 168.5 (s, C-14); 152.3 (d, C-10); 142.9 (s, C-1); 142.3 (s, C-6); 137.5 (s, C-15); 130.0 (d, C-3); 126.7 (d, C-4); 126.5 (t, C-16); 123.6 (d, C-5); 112.2 (d, C-2); 103.4 (d, C-9); 61.7 (t, C-18); 51.2 (t, C-19); 50.6 (s, C-7); 40.3 (t, C-12); 28.2 (q, C-11); 18.4 (q, C-17); 12.6 (q, C-13).

HMBC correlations: H-2  $\rightarrow$  C-(4, 6); H-3  $\rightarrow$  C-(1, 5); H-4  $\rightarrow$  C-(2, 5, 6); H-5  $\rightarrow$  C-(1, 3, 7); H-9  $\rightarrow$  C-(7, 8w, 9, 10w, 11w); H-10  $\rightarrow$  C-(8, 9w); H-11  $\rightarrow$  C-(6, 7, 8, 11); H-12  $\rightarrow$  C-(1, 8, 13); H-13  $\rightarrow$  C-(12); H-16  $\rightarrow$  C-(14, 15, 17); H-17  $\rightarrow$  C-(14, 15, 16); H-18  $\rightarrow$  C-(14, 19); H-19  $\rightarrow$  C-(18).

DQF-COSY correlations: H-2  $\rightarrow$  H-(3); H-3  $\rightarrow$  H-(2, 4); H-4  $\rightarrow$  H-(3, 5); H-5  $\rightarrow$  H-(4); H-9  $\rightarrow$  H-(10); H-10  $\rightarrow$  H-(9); H-12  $\rightarrow$  H-(13); H-13  $\rightarrow$  H-(12); H-16  $\rightarrow$  H-(17); H-17  $\rightarrow$  H-(16); H-18  $\rightarrow$  H-(19); H-19  $\rightarrow$  H-(18).

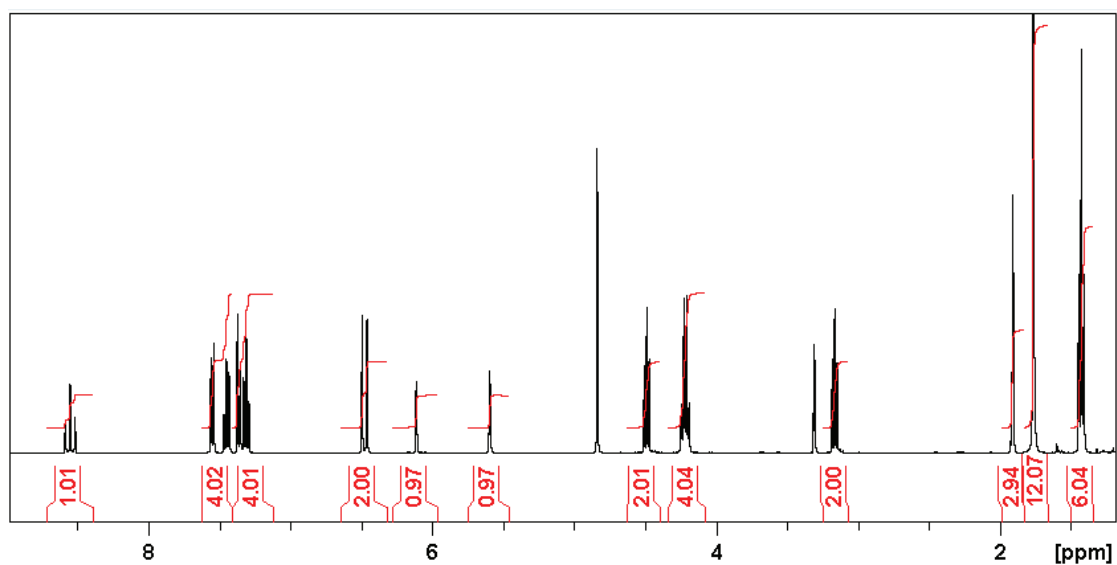


Figure 2-49:  $^1\text{H}$  NMR spectrum of Cy3-MES (methanol- $d_4$ ).

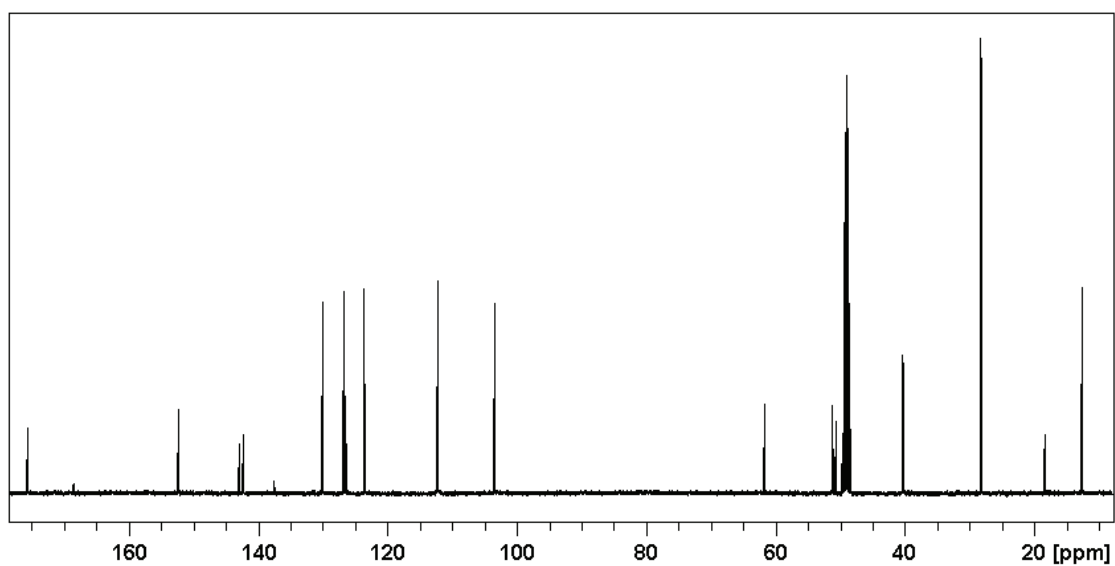


Figure 2-50:  $^{13}\text{C}\{^1\text{H}\}$  NMR spectrum of Cy3-MES (methanol- $\text{d}_4$ ).

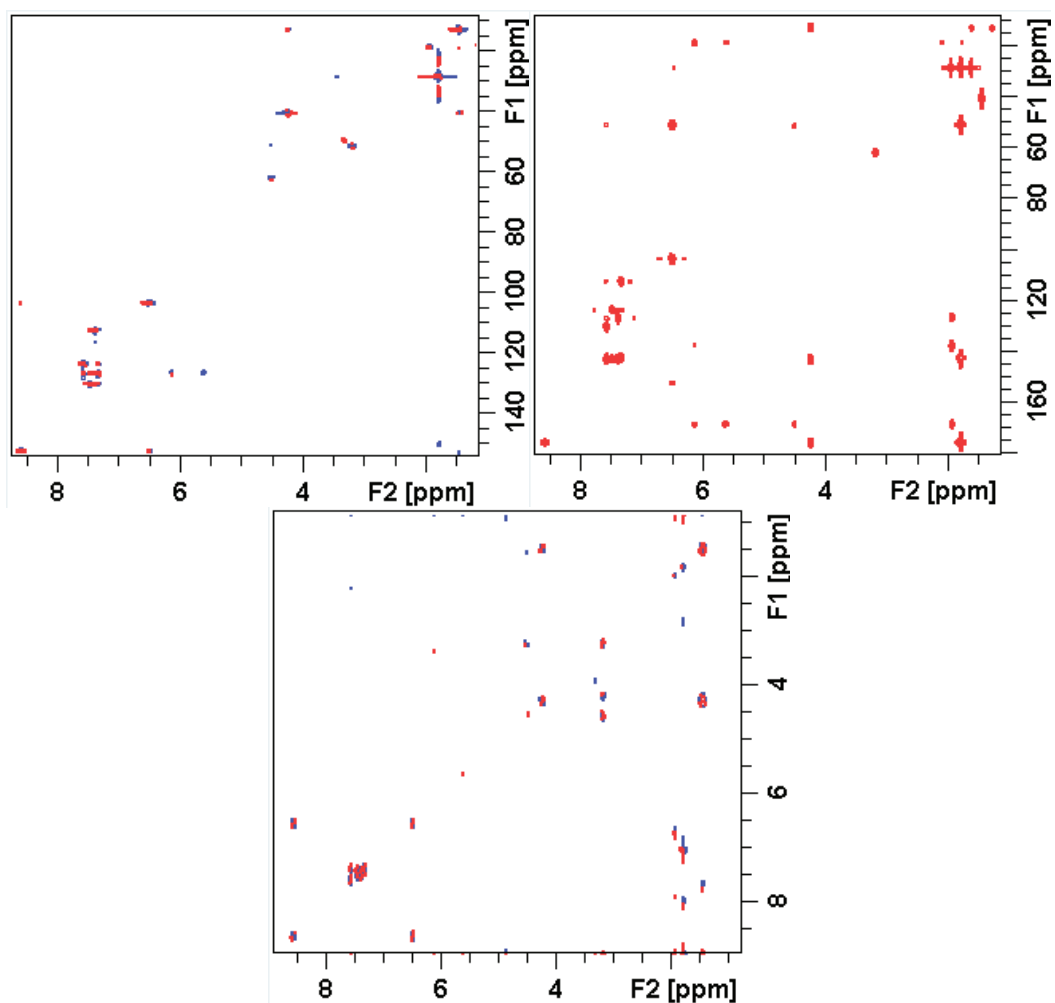
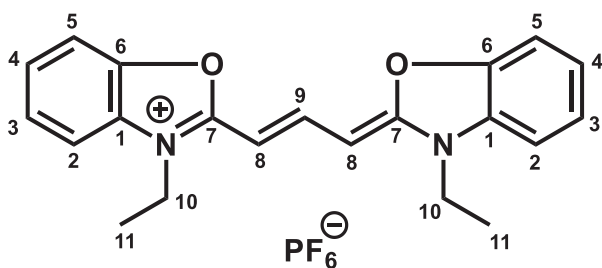


Figure 2-51: HSQC, HMBC and DQF-COSY NMR spectra of Cy3-MES (methanol- $\text{d}_4$ ).

## 2.6.5 NMR characterization for Cy-PF6

**Identification of dye part for bCy3-PF6**

$^1\text{H}$  NMR (DMSO- $d_6$ , 400.13 MHz):  $\delta$  8.30 (t,  $J = 13.3$ , 1H, H-9); 7.75 (m, 2H, H-5); 7.68 (m, 2H, H-3); 7.46 (m, 2H, H-2); 7.40 (m, 2H, H-4); 6.06 (d,  $J = 13.3$ , 2H, H-8); 4.25 (q,  $J = 7.2$ , 4H, H-10); 1.36 (t,  $J = 7.2$ , 6H, H-11).

$^{19}\text{F}$  NMR (DMSO- $d_6$ , 376.54 MHz):  $\delta$  -69.40 & -70.91 (6F, F- $\text{PF}_6$ ).

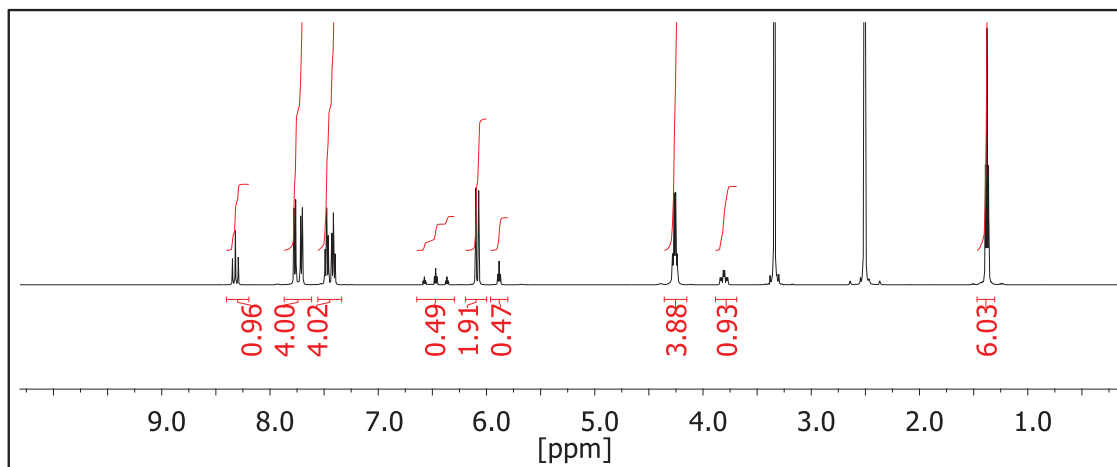


**Figure 2-52:**  $^1\text{H}$  NMR spectrum of bCy3-PF6 (with TFP) (DMSO- $d_6$ ).

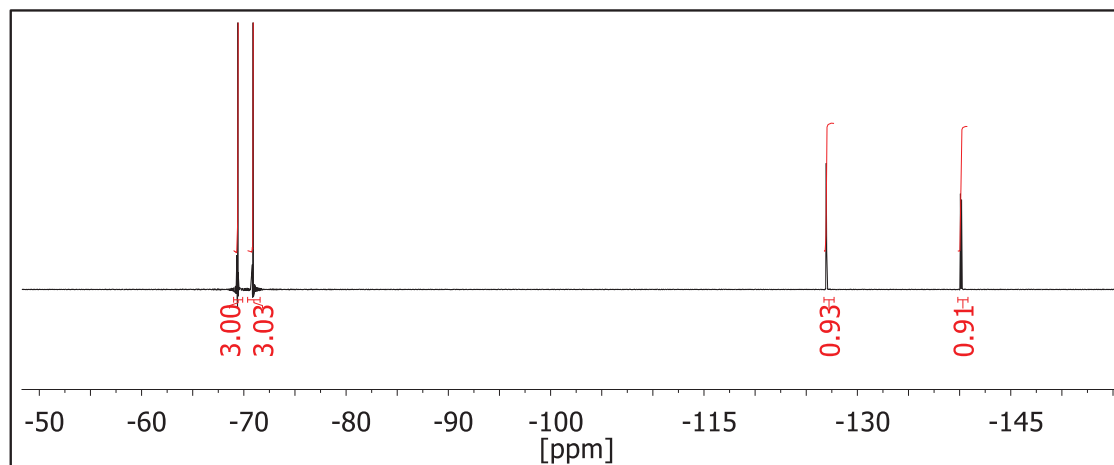
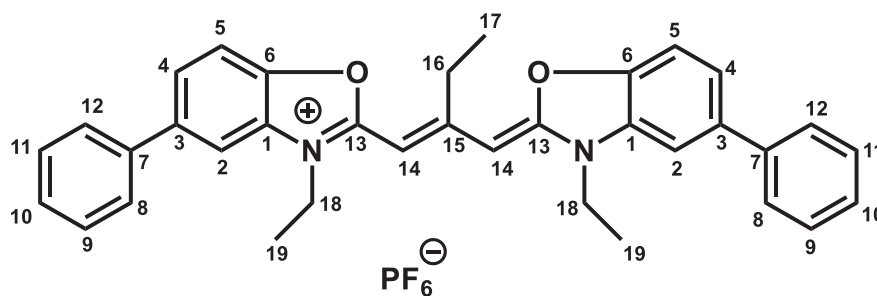


Figure 2-53:  $^{19}\text{F}$  NMR spectrum of bCy3-PF6 (with TFP) (DMSO- $d_6$ ).



#### Identification of dye part for STCy3-PF6

$^1\text{H}$  NMR (DMSO- $d_6$ , 400.13 MHz):  $\delta$  8.04&7.85&7.78&7.70&7.52&7.43 (H-2, 4, 5, 8, 9, 10, 11, 12); 5.87 (t, 2H, H-14); 4.39 (br, 4H, H-18); 2.98 (br, 2H, H-16); 1.44 (br, 6H, H-19); 1.36 (t, 3H, H-17).

$^{19}\text{F}$  NMR (DMSO- $d_6$ , 376.54 MHz):  $\delta$  -69.20&-71.09 (6F, F-PF $_6$ ).

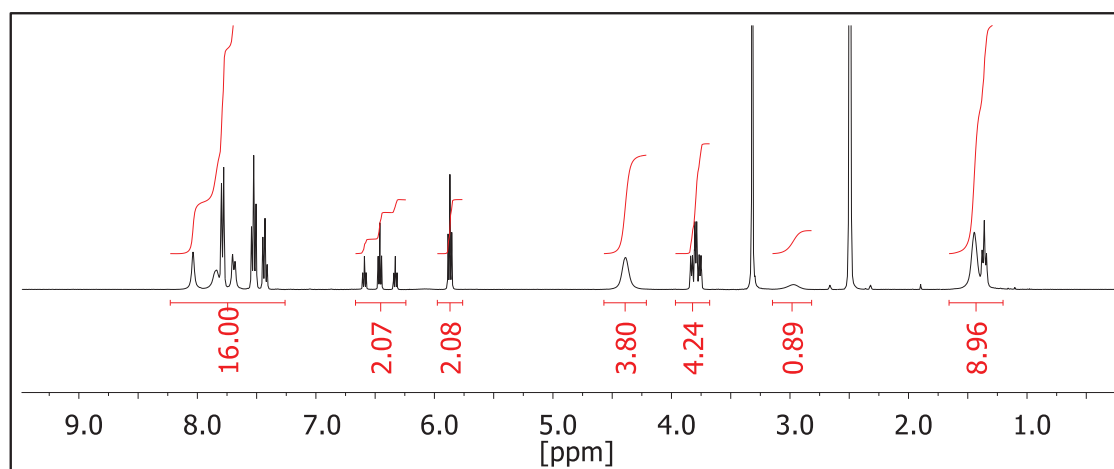


Figure 2-54:  $^1\text{H}$  NMR spectrum of STCy3-PF6 (with TFP) (DMSO- $d_6$ ).

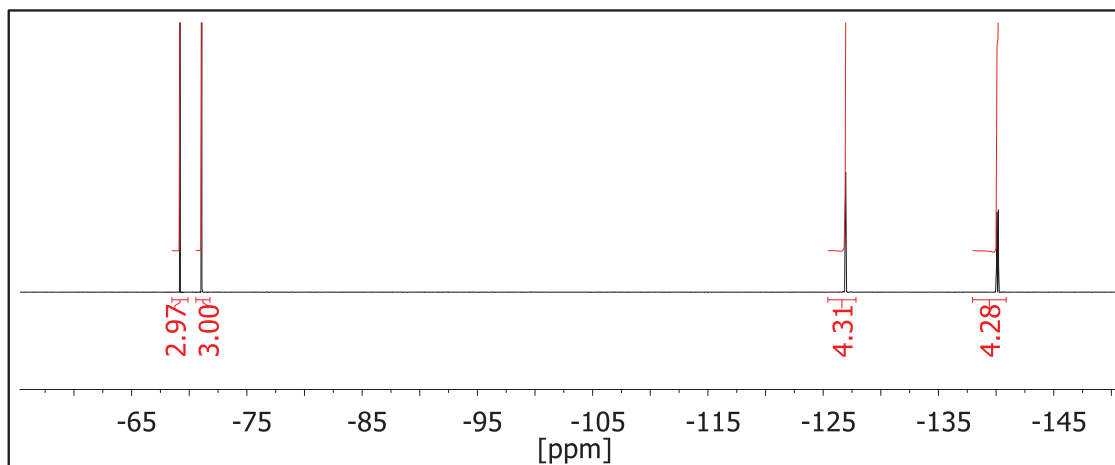
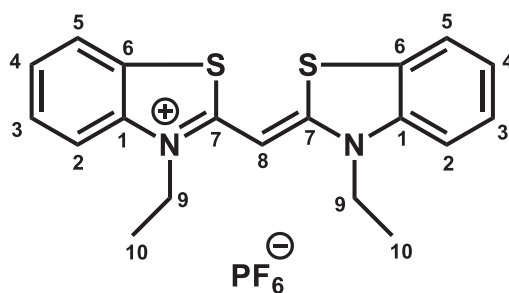


Figure 2-55:  $^{19}\text{F}$  NMR spectrum of STCy3-PF6 (with TFP) (DMSO- $d_6$ ).



#### Identification of dye part for Cy1-PF6

$^1\text{H}$  NMR (DMSO- $d_6$ , 400.13 MHz):  $\delta$  8.22 (m, 2H, H-5); 7.90 (m, 2H, H-3); 7.70 (m, 2H, H-2); 7.51 (m, 2H, H-3); 6.75 (s, 1H, H-8); 4.71 (q,  $J = 7.1$ , 4H, H-9); 1.38 (t,  $J = 7.1$ , 6H, H-10).

$^{19}\text{F}$  NMR (DMSO- $d_6$ , 376.54 MHz):  $\delta$  -69.20 & -71.09 (6F, F-PF $_6$ ).

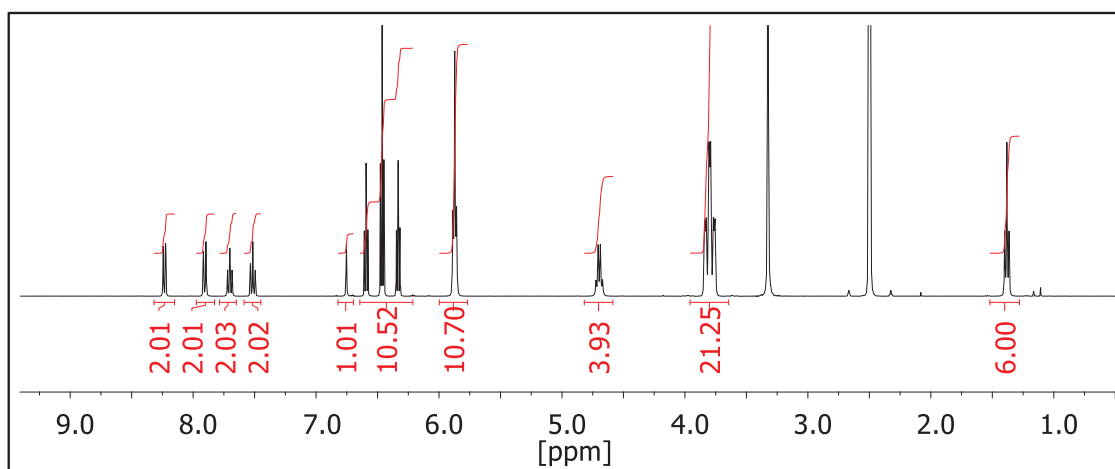
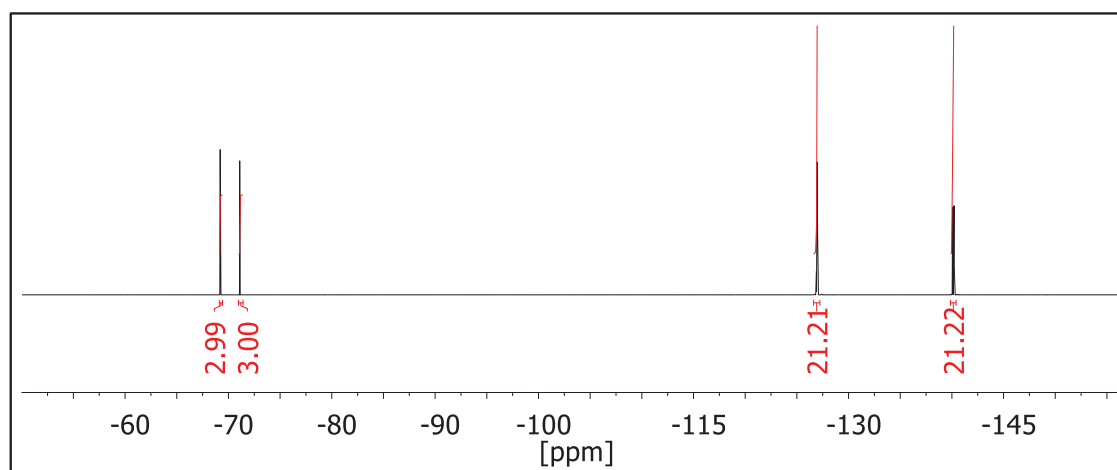


Figure 2-56:  $^1\text{H}$  NMR spectrum of Cy1-PF6 (with TFP) (DMSO- $d_6$ ).



**Figure 2-57:**  $^{19}\text{F}$  NMR spectrum of Cy1-PF6 (with TFP) ( $\text{DMSO-d}_6$ ).

## Chapter 3: Cyanine Dye Light-emitting Electrochemical Cells

### 3.1 Introduction

In 1995, Pei and coworkers introduced the concept of polymer light-emitting electrochemical cells (LECs).<sup>1</sup> The simple device architecture of such LECs consists of two metal electrodes in between an active layer based on a luminescent conjugated polymer, a salt and an ion-transporting poly(ethylene glycol) (PEG) is sandwiched. The addition of a salt considerably modified the properties of organic light-emitting diodes (OLEDs) that are based on a multi-stack geometry. The mobile ions redistribute within the active layer upon an external bias, facilitating the charge injection from respective electrodes by lowering the injection barriers. Therefore, the use of additional charge injection and transport layers and air-sensitive electrodes is not required for fabrication of LECs. A rigorous encapsulation after fabrication can be potentially eliminated. Compared to OLEDs, more advantages of LECs have been demonstrated including low operation voltage, solution processability of the emissive layer, insensitivity to the active layer thickness, etc.<sup>2-8</sup>

The operating mechanism of LECs has been intensively under debate. Recently, the electrochemical doping model was found to best describe the working principle of LECs. This model involves the initial formation of electric double layers (EDLs) at the electrodes, followed by the growth of p-type and n-type doping regions adjacent to the electrodes, consequently leading to a shrinking intrinsic layer where the emission of light takes place.<sup>2,3,9</sup> During the operation of LECs, an ionic junction is established due to the redistribution of the mobile ions, thereby inducing a potential energy shift and an internal electric field across the intrinsic region. This built-in potential allows for the control of electronic current flow preferentially in one direction, thereby resulting in a high rectification and diode characteristics. Photovoltaic response can also be achieved in such ionic junctions upon exposure to light.<sup>10,11</sup>

Cyanine dyes are charged organic semiconducting salts with inherently built-in ionic and electronic charge conductivity. Typically, cationic cyanine chromophores are accompanied by a mobile counter anion such as perchlorate or hexafluorophosphate. Therefore, no

additionally admixed salts are required for cyanine dye based LECs. Besides, cyanine dyes are soluble in a wide variety of organic solvents, yielding homogeneous films via solution process. Tunable absorption/emission spectra and energy bandgap can be achieved by modifying the polymethine chain and other functional groups during synthesis. All these interesting properties of cyanines make them promising candidates as active components for LECs. However, it was demonstrated that cyanines exhibit a self-quenching mechanism of their fluorescence.<sup>12</sup> A low PL quantum yield of < 1% in solid films was determined, resulting in a poor-performing LEC with an external quantum efficiency of only 0.001%.<sup>13</sup> Considerably improved LECs employing a host-guest system were proposed by dispersing a cyanine emitter with smaller bandgap into a matrix material.<sup>13,14</sup>

Here, we demonstrate a method to determine the junction position and width in an operated LEC using a trimethine cyanine/hexafluorophosphate as active material. This method involves a combination of electroluminescence (EL), photoluminescence (PL), incident photo-to-current conversion efficiency (IPCE) and optical simulation. At the point of maximum current during operation of the LEC, the intrinsic region was determined to have a width of ~19.8 nm and to be situated at ~37% of the total active layer thickness away from the anode. LEC devices containing cyanine dyes with different thickness were investigated and optimization of such LECs in terms of their photovoltaic effects during the operation is presented. Preliminary attempts of host-guest LECs based on cyanine binary blends were also studied and the results are discussed.

In this chapter, part of the data for determination of junction position and width in cyanine dye LECs are taken from the following publication: "Doping evolution and junction formation in stacked cyanine dye light-emitting electrochemical cells" by Sandra Jenatsch, Lei Wang, Matia Bulloni, Anna C. Véron, Beat Ruhstaller, Stéphane Altazin, Frank Nüesch, Roland Hany, *ACS Appl. Mater. Interfaces* **2016**, 8, 6554-6562. Fabrication of all devices and characterization regarding transient current and luminance measurements, absorbance spectra, PL spectra for Cy3-PF6 films, IPCE and J-V characteristics were performed by the author. PL measurements for host-guest blend films and optical modelling were carried out by Sandra Jenatsch (Empa).



## 3.2 Experimental

### 3.2.1 Materials and methods

STCy3-PF6, Cy1-PF6 and bCy3-PF6 were synthesized in our laboratory (**Figure 3-1**, for synthesis, see Chapter 2), 1-ethyl-2[3-(1-ethyl-3,3-dimethyl-1,3-dihydro-indol-2-ylidene)-propenyl]-3,3-dimethyl-3H-indolium hexafluorophosphate (Cy3-PF6, FEW Chemicals), silver (Ag, Cerac), poly(3,4-ethylenedioxythiophene):poly(styrene sulfonate) (PEDOT, Clevis P VP Al 4083), tris-(8-hydroxyquinoline)aluminum (Alq<sub>3</sub>, Aldrich), molybdenum (VI) oxide (MoO<sub>3</sub>, Aldrich), acetonitrile (ACN, Sigma-Aldrich).

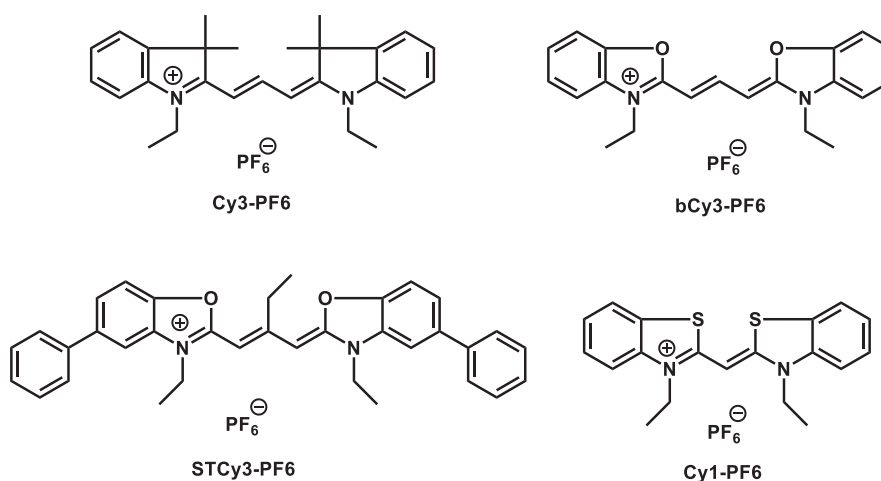


**Figure 3-1:** Chemical structures of Cy-PF6.

Absorbance spectra were measured on a Varian Cary 50 UV-Vis spectrophotometer. Film thicknesses were measured by profilometry (Ambios XP1). The thickness of very thin cyanine film (below 50 nm) was calculated by comparing with the maximum absorbance of thick films with a known thickness. Optical simulations were carried out using the commercially available simulation software SETFOS, version 4.1 (Fluxim).

### 3.2.2 Device fabrication and characterization

ITO coated glass substrates were successively cleaned by sonication in acetone, ethanol, detergent and de-ionized water. PEDOT films (~80 nm) were spin-coated and heated at 120 °C for 15 min before further use. The hole transporting layer MoO<sub>3</sub> (10 nm) and cathode

buffer layer Alq<sub>3</sub> (2 nm) was deposited by thermal evaporation at a pressure below  $5 \cdot 10^{-6}$  mbar. Cyanine films (~30 – 155 nm) were spin coated from ACN solutions with different concentrations inside a nitrogen-filled glove box (< 1 ppm H<sub>2</sub>O, < 6 ppm O<sub>2</sub>). Devices were completed by evaporating Ag (80 nm or 12 nm) through a shadow mask to define eight cells on each substrate with areas of 0.031 cm<sup>2</sup> or 0.071 cm<sup>2</sup>.

Light-emitting electrochemical cells (LECs) and solar cells were mounted under N<sub>2</sub> into an air-tight homemade transfer box and operated or measured outside the glovebox. LEC were operated under a constant voltage driven by a Keithley 2400. Transient luminance and current were monitored using a Konica Minolta luminance meter LS-110 equipped with a close-up lens No. 110 and the Keithley 2400, respectively. IPCE was measured using a 300 W Xe light source equipped with an AM1.5G filter and a monochromator. The light intensity was determined using a calibrated Si diode. PL spectra for biased devices were measured on a Horiba Jobin Yvon Fluorolog spectrometer. For these measurements, the voltage was switched off during the scan of PL spectra and re-applied immediately afterwards. Current-voltage (J-V) characteristics were measured using 100 mW cm<sup>-2</sup> simulated AM1.5G solar irradiation on a calibrated solar simulator from spectra Nova.

### 3.3 Results and Discussion

#### 3.3.1 Determination of junction position and width

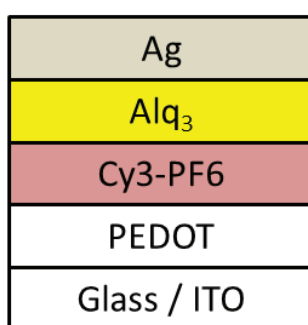


**Figure 3-2:** Schematic of device architecture for Cy3-PF6 LECs.

LECs with Cy3-PF6 as active component were fabricated, employing PEDOT and Alq<sub>3</sub> as anode and cathode buffer layer, respectively (**Figure 3-2**). The thickness of Cy3-PF6 film is ~30 nm.

The LEC was operated under constant voltage at 3 V. A characteristic transient current and luminance behavior of an operating Cy3-PF6 LEC is shown in **Figure 3-3a**, it can be clearly seen that the current decreased during the initial ~10 min and no detectable luminance was observed. In this stage, the ions redistribute within the active layer and drift to the respective electrode interfaces, leading to the formation of EDLs. These layers facilitate the hole and electron injection from the electrodes, allowing for the subsequent electrochemical oxidation and reduction to generate p-type doped region adjacent to the anode and n-type doped region adjacent to the cathode, respectively.<sup>1-3,9,15,16</sup>

After ~10 min operation, both current and luminance increased with time, yielding a switch-on of the LEC at ~20 min. We define the switch-on time of the LECs when the detected luminance reaches 0.1 cd m<sup>-2</sup>. Here, the doped zones propagate toward each other, generating a narrowing intrinsic region where light emission takes place. The growing doped zones result in the formation of highly conductive regions adjacent to both electrodes, thereby transporting electronic charge carriers that recombine in the intrinsic region. The formed excitons relax radiatively and the emission of light is detected. As the doped zones widen and the intrinsic zone shrinks over time, more and more holes and electrons are injected into the device and meet in the narrowing intrinsic region with an increasing potential drop. Consequently, an increase of both current and luminance are observed during the operation of the LEC.<sup>1-3</sup>

The luminance reached a maximum value of ~20 cd m<sup>-2</sup> after ~3 h and then started to drop. It has been demonstrated that the doping quenches the PL in both p-type and n-type zones.<sup>16-20</sup> Here, the drop of luminance indicates that excitons start to be quenched by approaching the doped species, leading to more non-radiative relaxation and a substantial reduction of exciton-to-photon conversion efficiency. Extensive doping results in a narrow junction, thereby allowing for an efficient quenching of excitons due to their close proximity to the doped zones.

Eventually, current density of the LEC reduced as well after reaching a maximal value of  $\sim 500$   $\text{mA cm}^{-2}$ . This suggests that permanent device degradation occurs in this stage, induced by irreversible chemical changes in the active layer and at electrode/active layer interfaces.<sup>19,21</sup>

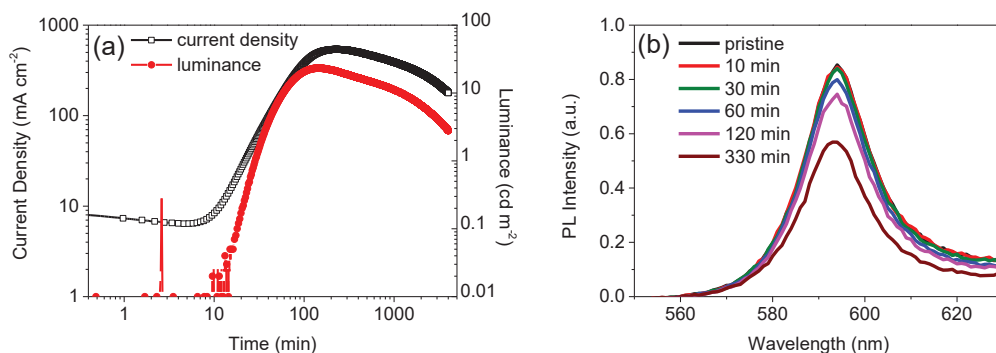


**Figure 3-3:** (a) Transient current density (open squares) and luminance (filled circles) in ITO/PEDOT/Cy3-PF6(30 nm)/Alq<sub>3</sub>/Ag LECs operated under constant bias at 3 V, (b) PL spectra recorded after biasing for different time.

As discussed above, dynamic doping evolution takes place in an operating LEC, leading to the formation of a p-i-n junction. Generally, both p- and n-doped regions grow with time, while leaving a shrinking intrinsic region. Therefore, it is of interest to investigate the junction formation process in terms of its width and position during the LEC operation. Many attempts have been performed for planar LECs based on a direct visualization of the junction using optical microscopy and fluorescence imaging.<sup>15-17,22,23</sup> However, stacked LECs possess a much higher potential for practical applications compared with planar LECs. Direct imaging of the junction with a digital camera is not possible for a stacked LEC since the interelectrode distance is typically very small ( $< 200$  nm).<sup>24-26</sup> Further, due to the large difference of active layer thicknesses, the electrochemical doping model cannot be simply translated from the lateral to the sandwiched structured LECs by scaling down the thickness of different zones.<sup>27,28</sup> It was found that the transient current response and junction width is sensitively dependent on the applied bias. Therefore, LECs with large difference of thickness cannot be directly compared in terms of their electrochemical doping and ionic junction formation process since the intensity of the electric field, depending on the thickness and the bias voltage, may consequently affect the field-dependent electron and hole mobilities.<sup>27,29,30</sup>

Here, we monitored the PL spectra of the active layer in a stacked Cy3-PF6 LEC during constant voltage operation. As can be seen in **Figure 3-3b**, PL intensities at  $\sim 594$  nm

decreased continuously for an operation period of 330 min except for the initial 30 min where no PL quenching was observed. This implies that doping-induced PL quenching is present in the device. Since EL and PL spectra of the Cy3-PF6 LEC overlap, PL measurements were carried out when the external bias was switched off. This resulted in a partial relaxation and redistribution of the ions and eventually a longer time (~5.5 h) was required to drive the LEC to the point of maximum current.<sup>21,31,32</sup> We assume that the remaining PL signals stem solely from the undoped intrinsic region and the PL in both p- and n-doped zones is completely quenched. Then the ratio between the remaining and the initial PL intensity directly indicates the width of the junction. For instance, at maximum current (330 min), 66% PL intensities remained, suggesting that the width of the intrinsic region is 66% of the total active layer and 34% of the layer was doped.

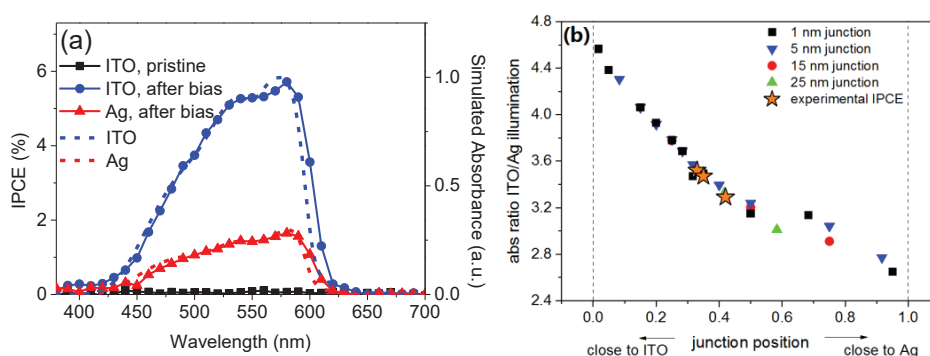


**Figure 3-4:** (a) Experimental IPCE spectra for pristine (black squares) and biased device at maximum current under light irradiated through ITO (blue circles) or Ag (red triangles) and simulated intrinsic layer absorbance spectra for light irradiated through ITO (blue dotted) or Ag (red dotted), (b) simulated ratio of the absorbance for light irradiated through ITO and Ag for different junction thicknesses and positions, the vertical lines indicate the active layer thickness, experimental results of three different cells are marked by orange stars.

Migration of the ions affects the internal electric field and the potential drops primarily across the intrinsic region. It was demonstrated that the high electric field across the ionic junction assists the splitting of excitons into free charge carriers.<sup>10,11</sup> Therefore, when illuminated with light, a LEC device with an established p-i-n junction can also be operated as a solar cell. A permanent photovoltaic response can be obtained if the ionic junctions are stabilized by immobilizing the ions.<sup>33,34</sup>

Semitransparent LECs were fabricated by depositing 12 nm Ag layer as top electrode, which allowed for the illumination of light through both ITO and Ag contacts. The photovoltaic

response of such LECs was investigated by IPCE measurements. For a pristine device without bias, almost no current generation was observed since no p-i-n junction that facilitates charge separation was present (**Figure 3-4a**). For devices biased to the maximum current, different IPCE spectra were obtained upon light illumination through ITO or Ag electrode. It can be clearly seen that both IPCE spectra of biased devices follow the simulated absorbance of the intrinsic layer (**Figure 3-4a**, dotted lines), suggesting that the charge generation takes place within the Cy3-PF6 layer. Further, the charge extraction efficiency of a biased and illuminated LEC from different directions is proportional to the light that is absorbed in the intrinsic region. Therefore, the IPCE values sensitively depend on the junction position within the active layer. Optical modelling was performed by considering the full cell stack and dividing the active layer into three regions (p-i-n) with a constant total thickness. Results demonstrate that the ratio of absorbance of the junction when light is illuminated from ITO or Ag is sensitively dependent on the junction position but independent on the junction width (**Figure 3-4b**). The experimental ratios of the IPCE intensity at the point of maximum absorbance ( $\sim 580$  nm) for three individual cells were 3.52, 3.29 and 3.47. From simulated results, these values are situated at  $37 \pm 5\%$  of the total active layer thickness away from the ITO, thereby indicating the position of the junction.

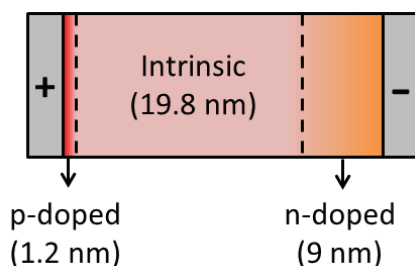


**Figure 3-5:** Schematic of p-doped, intrinsic and n-doped zones of active layer in a Cy3-PF6 LEC at maximum current situation.

Taking the PL measurements into account, which estimated the junction width to be  $\sim 66\%$  at the point of maximum current, a picture of the whole active layer regarding three different zones can be depicted (**Figure 3-5**), yielding the thicknesses of p-doped, intrinsic and n-doped regions for 1.2 nm, 19.8 nm and 9 nm, respectively.

### 3.3.2 Photovoltaic effect of the p-i-n junction

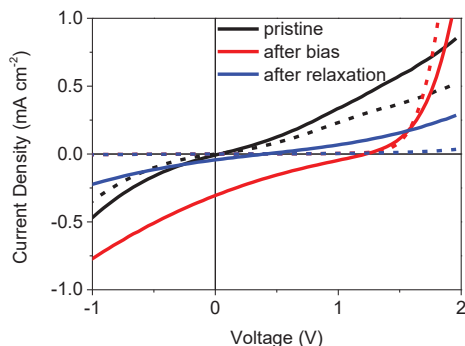


**Figure 3-6:** White light (solid lines) and dark (dotted lines) J-V characteristics of ITO/PEDOT/Cy3-PF6(30 nm)/Alq<sub>3</sub>/Ag devices measured before bias (pristine), after bias at 3 V for ~3 h to the maximum current and relaxation for 17 h after the bias is switched off.

In a pristine Cy3-PF6 LEC, J-V characteristics showed that no photovoltaic performance was obtained. No current was generated upon illumination with white light, which is in agreement with the IPCE measurements. In a second step, an external voltage of 3 V was applied to the device and the maximum current was reached after ~3 h. The bias was then switched off and J-V curves were measured immediately afterwards. As can be seen from **Figure 3-6**, the device demonstrates high rectification and diode-like dark current behavior, resulting from the p-i-n junction in the active layer, which controls the flow of electronic current.<sup>34</sup> A high open-circuit voltage ( $V_{oc}$ ) of ~1.2 V and a short-circuit current density ( $J_{sc}$ ) of ~0.3 mA cm<sup>-2</sup> were achieved. However, the junction established in such LECs was not stable, both diode feature in the dark and photovoltaic effect upon light irradiation disappeared after device idling for 17 h (**Figure 3-6**). This is attributed to the dynamic and reversible electrochemical doping process, leading to redistribution and relaxation of ions when the external bias is no longer applied.<sup>4,20,33,35-37</sup>

Notably, the pristine Cy3-PF6 LEC before bias exhibited a high dark current, which permanently disappeared after bias. For instance, a high current density of ~0.3 mA cm<sup>-2</sup> was present at -1 V in the pristine device, which substantially decreased to < 0.005 mA cm<sup>-2</sup> after bias for ~3 h. The pristine dark current was largely reduced if thicker cyanine films ( $\geq 90$  nm) were used in LECs (see **Figure 3-7** and 3.6 Supporting Information). Besides, the use of MoO<sub>3</sub> instead of PEDOT as anode buffer layer leads to much less pristine current in the dark J-V

characteristics (see 3.6 Supporting Information). We speculate that the Cy3-PF6 layers deposited on PEDOT yield poor film morphology with pinholes. This results in numerous microshunts in the active layer and the apparent leakage current in the dark. It was reported that postproduction thermal and electrical annealing leads to morphology modification and burning of shunts, which considerably improves the efficiency of organic light-emitting diodes and solar cells.<sup>38-40</sup> It is therefore anticipated that the microshunts in the Cy3-PF6 LEC were mostly burned during the external bias, thereby presenting a pronounced reduction of dark current. In **Figure 3-6**, after relaxation of 17 h, the dark current is low, this is good because it can be expected that the microshunts – when they are burned – remained burned. If the pristine dark current resulted from a hole-only current, the situation would be different.

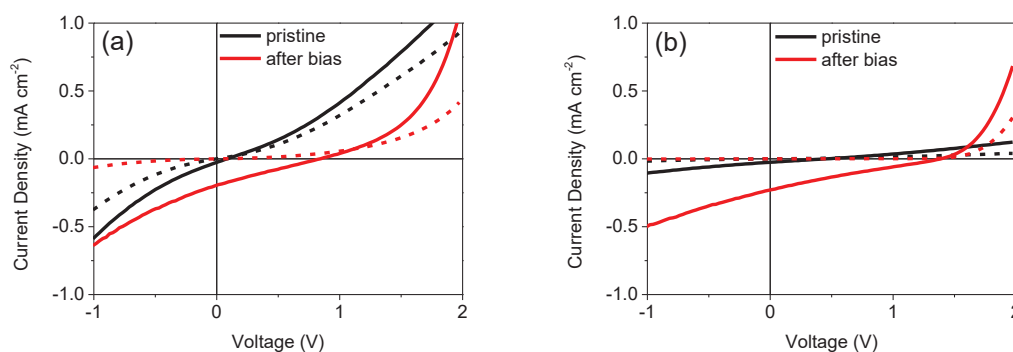


**Figure 3-7:** White light (solid lines) and dark (dotted lines) J-V characteristics of ITO/PEDOT/Cy3-PF6((a) 30 nm, (b) 90 nm)/Alq<sub>3</sub>/Ag devices measured before bias (pristine), after bias at (a) 4 V, (b) 6 V for 10 – 20 min to the maximum current.

Photovoltaic performance of LECs after bias was optimized by varying the thickness of Cy3-PF6 films (see 3.6 Supporting Information). Devices were biased at different voltages to the point of maximum current. From **Figure 3-7a**, we found that a  $V_{oc}$  of only  $\sim 0.8$  V was obtained and the leakage current in the dark after bias at 4 V for 10 – 20 min was still partially present. This may result from the insufficient biasing time that did not enable a complete removal of microshunts by electrical annealing. It is known from the literature that shunts in the device can largely deteriorate the solar cell performance, leading to poor rectification and a lowered  $V_{oc}$ .<sup>40</sup> This observation further supports our speculation that burning of shunts takes place during bias, occurring simultaneously with the junction establishment.



Obviously, the device employing 90 nm Cy3-PF6 as active layer performed the best after bias to the maximum current, giving a high  $V_{oc}$  of  $\sim 1.4$  V (**Figure 3-7b** and 3.6 Supporting Information). Similar fill factor (FF) of  $\sim 23\%$  was obtained for all devices with a Cy3-PF6 layer of different thicknesses. LECs with thinner Cy3-PF6 films ( $\leq 60$  nm) exhibited a higher pristine current in the dark J-V curves. In addition, low  $J_{sc}$  values ( $< 0.2$  mA cm $^{-2}$ ) were obtained in the device with thicker Cy3-PF6 films ( $\geq 130$  nm), which consequently led to a low power conversion efficiency (PCE). This may be attributed to the extensive absorption of light in the p-type doped region in such thick cyanine films, which largely reduces the amount of photons that can reach the p-i-n junction. Generally, the active layer of LECs has a thickness between 100 nm and 200 nm.<sup>1,2,41</sup> Cyanine based LECs with a light-emitting layer of  $\sim 80$  nm was reported.<sup>13</sup> Besides, we found that devices with a Cy3-PF6 film below 60 nm did not work if MoO $_3$  was deposited as buffer layer. Very thin active layers resulted in direct contact between the anode and cathode and therefore only short-circuited devices were obtained in such LECs. Thus, we conclude that the optimized thickness of active layer in the Cy3-PF6 device is determined to be  $\sim 90$  nm where an optimal photovoltaic performance after bias is obtained.

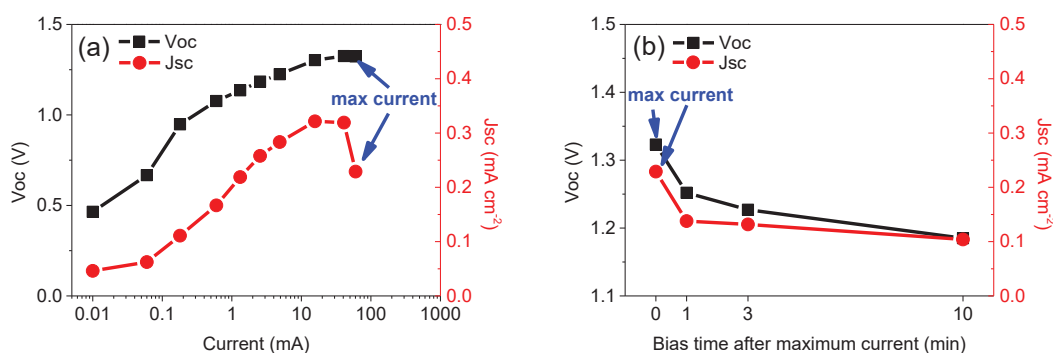


**Figure 3-8:** Evolution of  $V_{oc}$  and  $J_{sc}$  in ITO/PEDOT/Cy3-PF6(90 nm)/Alq $_3$ /Ag device after biasing at 5 V (a) to different current or (b) for different time after maximum current is reached.

To investigate the evolution of photovoltaic performance in the LEC during operation, a device employing a Cy3-PF6 film with the optimized thickness of 90 nm was fabricated and biased with a constant external voltage at 5 V. J-V characteristics under light were recorded after the device was biased to different current (**Figure 3-8a**). It can be seen that higher currents resulted in a higher  $V_{oc}$ , which increased from  $\sim 0.5$  V to  $\sim 1.3$  V at the point of maximum current. Similar behavior was found for the increase of  $J_{sc}$ . Differently, the maximal

$J_{sc}$  value was achieved before the maximum current was reached in the device and a drop of  $J_{sc}$  was observed at the point of maximum current. As shown in **Figure 3-3a**, the transient luminance in an operated LEC already starts to decay after reaching a maximum value before the maximum current is reached, indicating that a remarkable exciton quenching effect is present due to overdoping at the maximum current situation. We therefore speculate that the best photovoltaic performance may correspond to the point at which the maximum luminance is situated. Continuous bias was applied to the device after the maximum current. From **Figure 3-8b**, we observe that both  $V_{oc}$  and  $J_{sc}$  drop substantially, which is attributed to the permanent device degradation due to excessive electrochemical doping processes.<sup>20,37,42</sup>

A reverse electrochemical doping was also achieved when a negative bias was applied to the LECs (see 3.6 Supporting Information). Namely, p-type doping occurs adjacent to the Ag and n-type doping to the ITO electrode. Light emission was observed when the device was operated under a constant bias of -5 V. J-V characteristics of a Cy3-PF6 LEC biased at -6.5 V for ~20 min demonstrated a minus  $V_{oc}$ , suggesting that a reverse p-i-n junction was established in the active layer.<sup>43</sup>

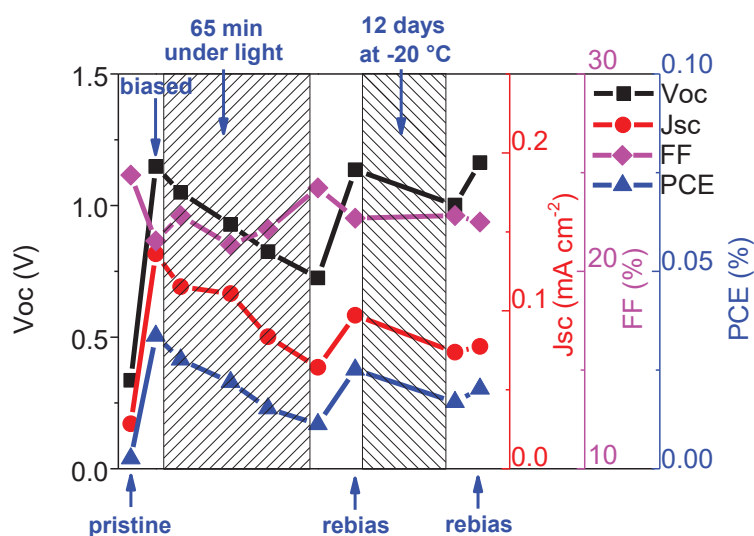


**Figure 3-9:** Photovoltaic performance of ITO/PEDOT/Cy3-PF6(90 nm)/Alq<sub>3</sub>/Ag LECs before bias (pristine) and after bias at 5 V to the maximum current, after white light illumination for 65 min and storage at -20 °C for 12 days.

Due to the reversible electrochemical process as discussed above, the photovoltaic behavior of a biased LEC is also not stable (**Figure 3-9**). Cell performance decreased rapidly upon exposure to white light. 65 min illumination of light resulted in a drop of ~40% for  $V_{oc}$  and  $J_{sc}$ .

FF stayed unchanged at ~24%. Furthermore, it can be observed that the relaxation of ions was considerably slowed down by storing a biased device at -20 °C, leading to a decrease of only ~10% for  $V_{oc}$  and ~20% for  $J_{sc}$  after storage for 12 days. It was proposed that the p-i-n junction in polymer LECs can be frozen at 100 K or at RT, yielding a stable diode rectification and light emission with a fast response.<sup>11,42</sup> To redistribute the ions and rebuild the p-i-n junction, partially relaxed devices after light illumination or storage at -20 °C were rebiased at 5 V to the maximum current point and photovoltaic parameters, particularly  $V_{oc}$  (~1.2 V), were restored.

### 3.3.3 Host-guest light-emitting electrochemical cells

Three different cyanine dyes were successfully synthesized and were used for the investigation of host-guest cyanine LECs. The host-guest approach has been successfully employed in OLEDs and LECs to improve the quantum efficiency of electroluminescence.<sup>13,14,44-48</sup> This approach involves the addition of a dye emitter into an organic semiconductor matrix, yielding a homogeneous binary blend film. In this film, the emitting dye is present in a small content and well-dispersed within a host material. During device operation, the guest emitter is excited via either Förster energy transfer from singlet excitons generated in the host, or sequential capture of electrons and holes transferred from the host. Therefore, the charge carrier transport and the light emission processes are separated into different materials, which potentially prevent the self-quenching behavior of the emitter and lead to high quantum efficiency in the organic electroluminescent devices.

Cyanine dyes are promising organic semiconducting molecules with strong electroluminescence. However, it is known that cyanines suffer from a severe self-quenching effect in solid films, which considerably limits the PL quantum yield (typically < 1%). LECs using cyanine dyes as guest emitting materials in a host-guest system were demonstrated.<sup>13,14</sup> In such devices, emission of light arises solely from the cyanines, exhibiting a significantly enhanced external quantum efficiency compared to the single-component LECs.

Here, we study the potential application of the synthesized cyanine dyes as either matrix material or emitter in host-guest LECs. Firstly, the thermal stability of bCy3-PF6 and STCy3-PF6 films was investigated. We observed that bCy3-PF6 films were unstable when stored in

the dark in  $N_2$  atmosphere at RT (**Figure 3-10**). This indicates that this dye is thermodynamically unstable when coated as thin films. The freshly deposited films showed two clear absorbance signals corresponding to the monomer and dimer species of the dye. Within the first day storage, remarkable change of the absorbance spectra was observed, showing a decrease in dimer absorption and a pronounced increase in monomer absorption. No further change in the absorbance spectra occurred after 1 day storage. Comparatively, STCy3-PF6 thin films were stable during storage under the same conditions. No variation in the absorbance spectra was found within 6 days.

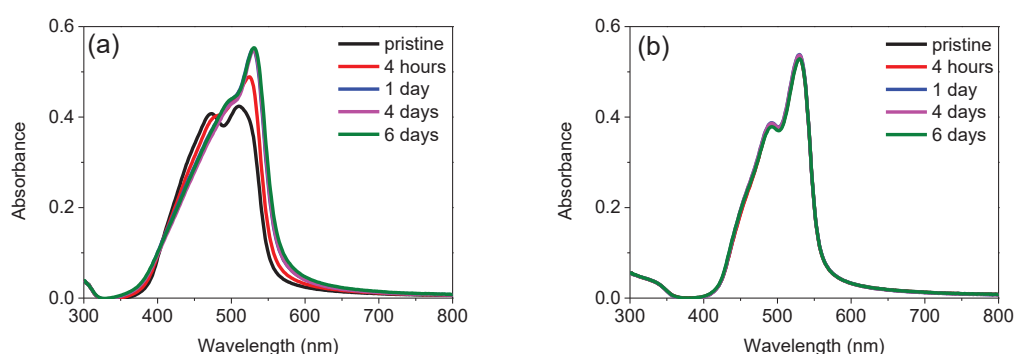


**Figure 3-10:** Variation of absorbance spectra of (a) bCy3-PF6 and (b) STCy3-PF6 thin films during storage in the dark in  $N_2$  at RT.

Next, a binary cyanine blend employing the monomethine cyanine dye Cy1-PF6 as matrix material and the stable STCy3-PF6 as emitter was studied. It was found that the PL intensity of pure Cy1-PF6 films is very low, suggesting that an extensive self-quenching effect is present in the thin films and therefore a low fluorescence quantum yield is obtained. By adding different amount of STCy3-PF6 into the blends, considerable change in the PL spectra was observed. The emission signal of Cy1-PF6 almost disappeared and the emission of STCy3-PF6 at  $\sim 540$  nm with a much stronger signal appeared. The optimal content of STCy3-PF6 admixed in the blend was determined to be 1%, which exhibited the highest PL intensity (**Figure 3-11**). This experiment confirmed the preliminary concept of improving quantum efficiencies with LECs bearing a host-guest system.

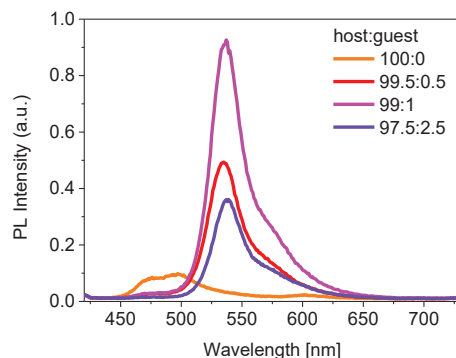


**Figure 3-11:** PL spectra of host-guest blend films in different ratio.

### 3.4 Conclusions

LECs using cyanine dyes as active materials were studied. To better understand the functional principle of LECs, we proposed a method based on the combination of EL and PL measurements, which were performed during the operation under a constant external bias. This method enabled a rough estimation of the junction width at every transient situation during the operation. The junction position at the point of maximum current was determined by measuring photocurrent spectral response in a semitransparent LEC and optical simulation. Hence, a clear picture of the p-i-n junction regarding the three zones in a working LEC was obtained. In a second step, the photovoltaic effect of a biased device was investigated and optimized by altering the thickness of active layer. Results demonstrate that a LEC with a ~90 nm thick Cy3-PF6 film yields the best photovoltaic performance after bias. Besides, microshunts that result in leakage dark current were eliminated and reversely established p-i-n junction was achieved in such optimized LECs. Photovoltaic performance was recorded by measuring white light J-V characteristics during the operation. It was speculated that the best photovoltaic behavior appears at the point where the maximum luminance is situated. Due to the dynamic electrochemical doping process, light illumination on a biased device led to a rapid decrease of photovoltaic parameters. This decrease can be largely slowed down by freezing the ion motion at -20 °C. Rebiasing the partially relaxed devices allowed for a restoration of photovoltaic performance. Host-guest system was established with Cy1-PF6 as host material and STCy3-PF6 as guest material. Pronounced improvements of PL in the blend films were achieved, demonstrating the potential of being employed in host-guest LECs with high quantum efficiencies.

### 3.5 References

- [1] Q. Pei, G. Yu, C. Zhang, Y. Yang, A. J. Heeger, polymer light-emitting electrochemical cells, *Science* **1995**, 269, 1086-1088.
- [2] R. D. Costa, E. Ortí, H. J. Bolink, F. Monti, G. Accorsi, N. Armaroli, luminescent ionic transition-metal complexes for light-emitting electrochemical cells, *Angew. Chem. Int. Ed.* **2012**, 51, 8178-8211.
- [3] S. B. Meier, D. Tordera, A. Pertegás, C. Roldán-Carmona, E. Ortí, H. J. Bolink, light-emitting electrochemical cells: recent progress and future prospects, *Mater. Today* **2014**, 17, 217-223.
- [4] S. Toshner, J. Leger, chapter 7: ionic carriers in polymer light-emitting and photovoltaic devices, *Organic Electronics: Emerging Concepts and Technologies* **2013**.
- [5] X. Gong, D. Moses, A. J. Heeger, chapter 4: polymer-based light-emitting diodes (PLEDs) and displays fabricated from arrays of PLEDs, *Organic Light Emitting Devices: Synthesis, Properties, and Applications*, Wiley-VCH Verlag GmbH & Co. kGaA, **2006**.
- [6] Q. Pei, Y. Yang, G. Yu, C. Zhang, A. J. Heeger, polymer light-emitting electrochemical cells: in situ formation of a light-emitting p-n junction, *J. Am. Chem. Soc.* **1996**, 118, 3922-3929.
- [7] C. W. Tang, S. A. VanSlyke, organic electroluminescent diodes, *Appl. Phys. Lett.* **1987**, 51, 913-915.
- [8] J. H. Burroughes, D. D. C. Bradley, A. R. Brown, R. N. Marks, K. Mackay, R. H. Friend, P. L. Burns, A. B. Holmes, light-emitting diodes based on conjugated polymers, *Nature* **1990**, 347, 539-541.
- [9] S. van Reenen, P. Matyba, A. Dzwilewski, R. A. J. Janssen, L. Edman, M. Kemerink, a unifying model for the operation of light-emitting electrochemical cells, *J. Am. Chem. Soc.* **2010**, 132, 13776-13781.
- [10] D. A. Bernard, S. Flores-Torres, H. D. Abruña, G. G. Malliaras, observation of electroluminescence and photovoltaic response in ionic junctions, *Science* **2006**, 313, 1416-1419.
- [11] J. Gao, G. Yu, A. J. Heeger, polymer light-emitting electrochemical cells with frozen p-i-n junction, *Appl. Phys. Lett.* **1997**, 71, 1293-1295.

- [12] F. A. Castro, H. Benmansour, J. Moser, C. F. O. Graeff, F. Nüesch, R. Hany, photoinduced hole-transfer in semiconducting polymer/low-bandgap cyanine dye blends: evidence for unit charge separation quantum yield, *Phys. Chem. Chem. Phys.* **2009**, *11*, 8886-8894.
- [13] A. Pertegás, D. Tordera, J. J. Serrano-Pérez, E. Ortí, H. J. Bolink, light-emitting electrochemical cells using cyanine dyes as the active components, *J. Am. Chem. Soc.* **2013**, *135*, 18008-18011.
- [14] A. Pertegás, M. Y. Wong, M. Sessolo, E. Zysman-Colman, H. J. Bolink, efficient light-emitting electrochemical cells using small molecular weight, ionic, host-guest systems, *ECS J. Solid State Sci. Technol.* **2016**, *5*, R3160-R3163.
- [15] P. Matyba, K. Maturova, M. Kemerink, N. D. Robinson, L. Edman, the dynamic organic p-n junction, *Nat. Mater.* **2009**, *8*, 672-676.
- [16] J. Gao, J. Dane, visualization of electrochemical doping and light-emitting junction formation in conjugated polymer films, *Appl. Phys. Lett.* **2004**, *84*, 2778-2780.
- [17] J. Gao, J. Dane, planar polymer light-emitting electrochemical cells with extremely large interelectrode spacing, *Appl. Phys. Lett.* **2003**, *83*, 3027-3029.
- [18] S. van Reenen, M. V. Vitorino, S. C. Meskers, R. A. J. Janssen, M. Kemerink, photoluminescence quenching in films of conjugated polymers by electrochemical doping, *Phys. Rev. B* **2014**, *89*, 205206.
- [19] S. B. Meier, D. Hartmann, D. Tordera, H. J. Bolink, A. Winnacker, W. Sarfert, dynamic doping and degradation in sandwich-type light-emitting electrochemical cells, *Phys. Chem. Chem. Phys.* **2012**, *14*, 10886-10890.
- [20] P. Pachler, F. P. Wenzl, U. Scherf, G. Leising, the efficiency of light-emitting electrochemical cells, *J. Phys. Chem. B* **2005**, *109*, 6020-6024.
- [21] F. AlTal, J. Gao, long-term testing of polymer light-emitting electrochemical cells: reversible doping and black spots, *Org. Electron.* **2015**, *18*, 1-7.
- [22] Y. Hu, J. Gao, direct imaging and probing of the p-n junction in a planar polymer light-emitting electrochemical cell, *J. Am. Chem. Soc.* **2011**, *133*, 2227-2231.
- [23] D. J. Dick, A. J. Heeger, Y. Yang, Q. Pei, imaging the structure of the p-n junction in polymer light-emitting electrochemical cells, *Adv. Mater.* **1996**, *8*, 985-987.

- [24] H. J. Bolink, E. Coronado, R. D. Costa, E. Ortí, M. Sessolo, S. Graber, K. Doyle, M. Neuburger, C. E. Housecroft, E. C. Constable, long-living light-emitting electrochemical cells – control through supramolecular interactions, *Adv. Mater.* **2008**, 20, 3910-3913.
- [25] R. D. Costa, E. Ortí, H. J. Bolink, S. Graber, C. E. Housecroft, E. C. Constable, intramolecular  $\pi$ -stacking in a phenylpyrazole-based iridium complex and its use in light-emitting electrochemical cells, *J. Am. Chem. Soc.* **2010**, 132, 5978-5980.
- [26] M. Lenes, G. Garcia-Belmonte, D. Tordera, A. Pertegás, J. Bisquert, H. J. Bolink, operating modes of sandwiched light-emitting electrochemical cells, *Adv. Funct. Mater.* **2011**, 21, 1581-1586.
- [27] C. Liao, H. Chen, H. Su, K. Wong, tailoring carrier injection efficiency to improve the carrier balance of solid-state light-emitting electrochemical cells, *Phys. Chem. Chem. Phys.* **2012**, 14, 9774-9784.
- [28] S. van Reenen, R. A. J. Janssen, M. Kemerink, dynamic processes in sandwich polymer light-emitting electrochemical cells, *Adv. Funct. Mater.* **2012**, 22, 4547-4556.
- [29] I. H. Campbell, D. L. Smith, C. J. Neef, J. P. Ferraris, capacitance measurements of junction formation and structure in polymer light-emitting electrochemical cells, *Appl. Phys. Lett.* **1998**, 72, 2565-2567.
- [30] J. C. deMello, N. Tessler, S. C. Graham, R. H. Friend, ionic space-charge effects in polymer light-emitting diodes, *Phys. Rev. B* **1998**, 57, 12951-12963.
- [31] X. Li, J. Gao, G. Liu, reversible luminance decay in polymer light-emitting electrochemical cells, *Appl. Phys. Lett.* **2013**, 102, 223303.
- [32] X. Li, F. AlTal, G. Liu, J. Gao, long-term, intermittent testing of sandwich polymer light-emitting electrochemical cells, *Appl. Phys. Lett.* **2013**, 103, 243304.
- [33] Z. Yu, M. Sun, Q. Pei, electrochemical formation of stable p-i-n junction in conjugated polymer thin films, *J. Phys. Chem. B* **2009**, 113, 8481-8486.
- [34] J. M. Leger, D. G. Patel, D. B. Rodovsky, G. P. Bartholomew, polymer photovoltaic devices employing a chemically fixed p-i-n junction, *Adv. Funct. Mater.* **2008**, 18, 1212-1219.
- [35] J. Liang, Z. Yu, L. Li, H. Gao, Q. Pei, chapter 4: stable junction polymer light-emitting electrochemical cells, *Organic Nanophotonics* **2015**, page 87-117.



- [36] L. Edman, D. Moses, A. J. Heeger, influence of the anion on the kinetics and stability of a light-emitting electrochemical cell, *Synth. Met.* **2003**, 138, 441-446.
- [37] Y. Kervella, M. Armand, O. Stéphan, organic light-emitting electrochemical cells based on polyfluorene investigation of the failure modes, *J. Electrochem. Soc.* **2001**, 148, H155-H160.
- [38] W. Ma, C. Yang, X. Gong, K. Lee, A. J. Heeger, thermally stable, efficient polymer solar cells with nanoscale control of the interpenetrating network morphology, *Adv. Funct. Mater.* **2005**, 15, 1617-1622.
- [39] T. Lee, O. O. Park, effect of electrical annealing on the luminous efficiency of thermally annealed polymer light-emitting diodes, *Appl. Phys. Lett.* **2000**, 77, 3334-3336.
- [40] F. Padinger, R. S. Rittberger, N. S. Sariciftci, effects of postproduction treatment on plastic solar cells, *Adv. Funct. Mater.* **2003**, 13, 85-88.
- [41] S. Tang, L. Edman, quest for an appropriate electrolyte for high-performance light-emitting electrochemical cells, *J. Phys. Chem. Lett.* **2010**, 1, 2727-2732.
- [42] G. Yu, Y. Cao, M. Andersson, J. Gao, A. J. Heeger, polymer light-emitting electrochemical cells with frozen p-i-n junction at room temperature, *Adv. Mater.* **1998**, 10, 385-388.
- [43] H. Benmansour, F. A. Castro, M. Nagel, J. Heier, R. Hany, F. Nüesch, ionic space charge driven organic photovoltaic devices, *Chimia* **2007**, 61, 787-791.
- [44] D. F. O'Brien, M. A. Baldo, M. E. Thompson, S. R. Forrest, improved energy transfer in electrophosphorescent devices, *Appl. Phys. Lett.* **1999**, 74, 442-444.
- [45] V. Cleave, G. Yahioğlu, P. L. Barny, R. H. Friend, N. Tessler, harvesting singlet and triplet energy in polymer LEDs, *Adv. Mater.* **1999**, 11, 285-288.
- [46] H. Su, C. Wu, F. Fang, K. Wong, efficient solid-state host-guest light-emitting electrochemical cells based on cationic transition metal complexes, *Appl. Phys. Lett.* **2006**, 89, 261118.
- [47] A. R. Hosseini, C. Y. Koh, J. D. Slinker, S. Flores-Torres, H. D. Abruña, G. G. Malliaras, addition of a phosphorescent dopant in electroluminescent devices from ionic transition metal complexes, *Chem. Mater.* **2005**, 17, 6114-6116.
- [48] X. Gong, J. C. Ostrowski, G. C. Bazan, D. Moses, A. J. Heeger, M. S. Liu, A. K. -Y. Jen, electrophosphorescence from a conjugated copolymer doped with an iridium complex: high brightness and improved operational stability, *Adv. Mater.* **2003**, 15, 45-49.

## 3.6 Supporting Information

### 3.6.1 LECs with different Cy3-PF6 film thickness

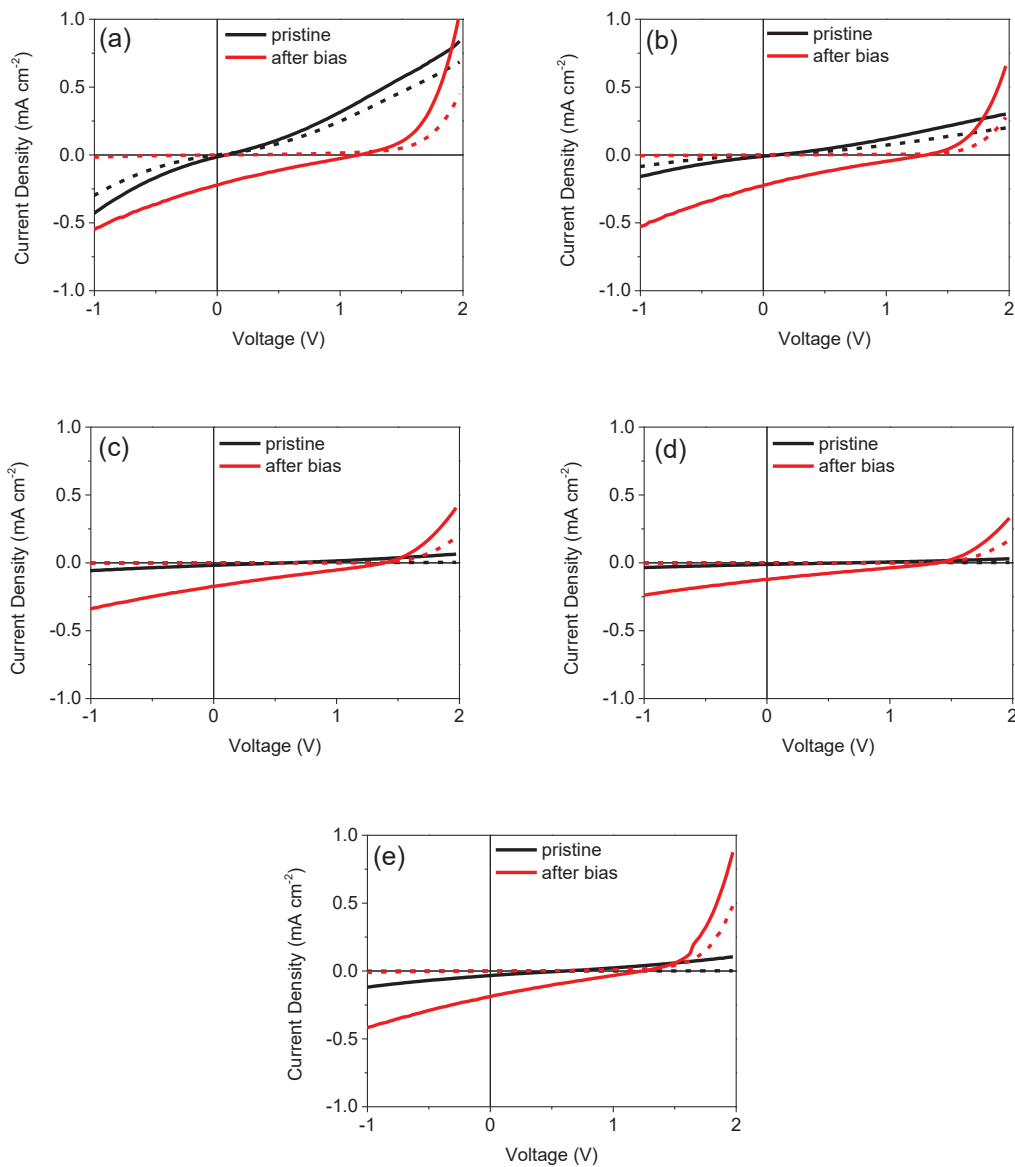


**Figure 3-12:** White light (solid lines) and dark (dotted lines) J-V characteristics of ITO/PEDOT/Cy3-PF6((a) 45 nm, (b) 60 nm, (c) 130 nm, (d) 155 nm)/Alq<sub>3</sub>/Ag and (e) ITO/MoO<sub>3</sub>/Cy3-PF6(60 nm)/Alq<sub>3</sub>/Ag devices measured before bias (pristine) and after bias at (a) 4 V, (b) 5 V, (c) 9 V, (d) 10 V, (e) 6 V for 10 – 20 min to the maximum current.

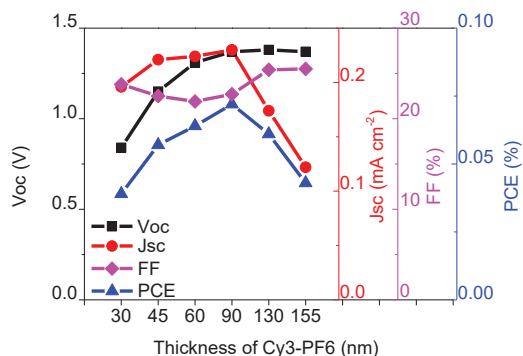


**Figure 3-13:** Photovoltaic performance of ITO/PEDOT/Cy3-PF6/Alq<sub>3</sub>/Ag LECs with different Cy3-PF6 thickness after biasing to the maximum current.

### 3.6.2 Reversely biased Cy3-PF6 LECs

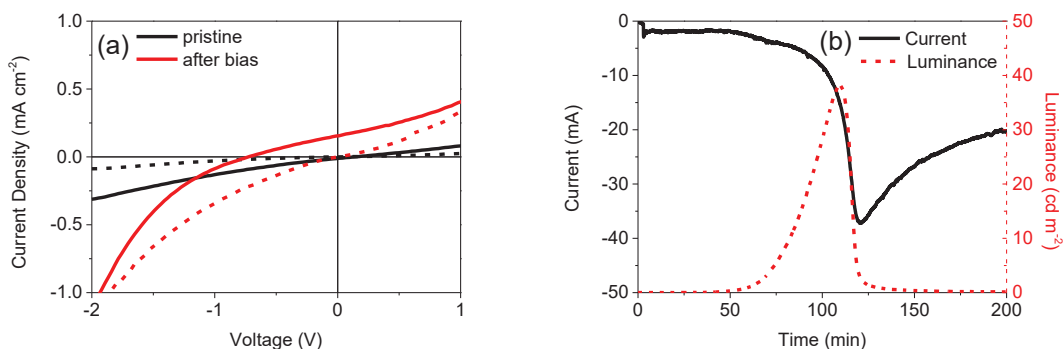


**Figure 3-14:** (a) White light (solid lines) and dark (dotted lines) J-V characteristics of ITO/PEDOT/Cy3-PF6(90 nm)/Alq<sub>3</sub>/Ag LECs before and after bias at -6.5 V for ~20 min, (b) transient current and luminance in ITO/PEDOT/Cy3-PF6(90 nm)/Alq<sub>3</sub>/Ag LECs operated under constant bias at -5 V.

## Chapter 4: Photoconductivity in Ionic Cyanine Films

### 4.1 Introduction

Since the early 1950, production of carrier pairs in organic semiconductors has been very thoroughly studied in single crystals of polyacene.<sup>1</sup> High energy radiation ionization, thermal production, single and multi-photon processes as well as reactions between excitons have been shown to operate in charge generation. The photoconductivity of thin organic films triggered a lot of interest due to its application in xerographic photoreceptors.<sup>2</sup> More recently, photogeneration of charge carriers, also known as photoconductivity, has been addressed in organic thin film diodes. Here one particular interest is to use low energy photons close to the absorption band edge of the organic semiconductor to produce charge carriers. Quite different mechanisms for photo-induced charge carriers have been proposed which can grossly be classified by the way they operate. The first mechanism relies on lowering the charge injection barrier at the electrodes, which can be achieved by trapping charges of opposite sign to the bias applied at the electrode. This strategy generally leads to exponential dependence of photoconductivity on light intensity and produces photo multiplication factors of up to  $10^3$ . The other mechanism relies on intrinsic generation of charge carriers, which can be induced easily in donor-acceptor blends.<sup>3</sup> Photocarrier production by low energy photons in the bulk of pristine materials is however quite rare and difficult to separate from electrode processes.

First studies in early 1960s already provide evidence of photoconductivity in trimethine cyanine films.<sup>4</sup> Apart from this pioneering study, cyanines have only marginally been studied as solid semiconducting films. Most of the works have dealt with solar cells, photodiodes, and light-emitting electrochemical cells. As has been shown in other systems, creation of photo-shunts by photoconductivity in a particular material component can have detrimental effects on device performance.<sup>5</sup> Photoconductivity in cyanine single crystals of CTIP<sup>6</sup> has revealed some kind of autoionization process which may proceed via vibronic excitations.

Here we present photoconductivity investigations of a typical pentamethine cyanine dye salt in a thin film. It allowed investigating current-voltage characteristics under various conditions of light irradiation and electric fields. In addition, electrodes and poling conditions were

varied in order to scrutinize possible injection effects leading to the efficient photoconductivity yield which we found to exceed 40%. Also, we were able to perform photo-induced charge carrier extraction by a linearly increasing voltage (photon-CELIV) measurements on films with different thicknesses, which allowed us to extract the photo-induced charge carrier density and infer the recombination kinetics. The investigations bring evidence for a bulk photogeneration mechanism rather than an electrode induced effect.

In this chapter, all samples and devices were prepared by the author. All experiments regarding absorbance, fluorescence, profilometry, IPCE, current-voltage characteristic, transient current (poling) and luminance response were performed by the author. Photo-CELIV and optical simulation was performed by Sandra Jenatsch (Empa). Ellipsometry measurements were carried out by Erwin Hack (Empa).

## 4.2 Experimental

### 4.2.1 Device fabrication

Single layer cyanine diodes were fabricated and stored in a glove box under nitrogen ( $\text{H}_2\text{O} < 1$  ppm,  $\text{O}_2 < 10$  ppm). Indium tin oxide-coated glass substrates (ITO, Thin Film Devices, 140 nm, sheet resistance 20 Ohm/square) were sequentially cleaned in acetone, ethanol, detergent and de-ionized water. Anode buffer  $\text{MoO}_3$  (Sigma Aldrich, 99.99%), Al (Kurt J. Lesker, 99.999%) and Ag (Cerac, 99.99%) as well as cathode buffer tris(8-hydroxyquinolino)aluminium ( $\text{Alq}_3$ , Sigma-Aldrich, 99.995%) were deposited by thermal evaporation under high vacuum ( $< 5 \times 10^{-6}$  mbar). Semiconducting films consisting of pentamethine cyanine dye 1,3,3-trimethyl-2-3H-indolium hexafluorophosphate (Cy5-PF6, FEW Chemicals, **Figure 4-1**) were spin coated from filtered acetonitrile. In some cases PEDOT (Clevios P VP Al 4083) was used as anode buffer layer instead of  $\text{MoO}_3$  and was spin-coated from aqueous solutions. The top silver or aluminum electrode was evaporated through a shadow mask to define devices with active areas of 3.1 mm<sup>2</sup> or 7.1 mm<sup>2</sup>.

Single layer devices with architecture ITO/ $\text{MoO}_3$  (10 nm) or PEDOT (80 nm)/Cy5-PF6 (x nm)/ $\text{Alq}_3$  (2 nm)/Ag (80 nm) or Al (40nm) were fabricated by subsequent deposition steps on cleaned ITO substrates. The layer thicknesses x = 40 nm, 50 nm, 65 nm, 100 nm and 130 nm were achieved by varying the concentration and spin-coating speed from 1000 rpm to 6000

rpm and from 16 mg/ml to 40 mg/ml, respectively. Semitransparent devices were fabricated by replacing the thick metal electrode by a thin semitransparent of Ag (12 nm) and Al (8 nm).

#### 4.2.2 Methods

For photocurrent characterization, the substrates were sealed in a vacuum tight box with current feedthroughs and an optical window. Current-voltage characteristics of the solar cells were measured using a Keithley 2400 source/measure unit in the dark and under simulated AM1.5G solar irradiation of  $100 \text{ mW cm}^{-2}$  from a calibrated solar simulator (Spectra-Nova). Increased irradiation intensity was achieved by placing two glass lenses into the diffuse white light beam in order to achieve a maximum irradiation intensity of  $283 \text{ mW/cm}^2$ . For reduced irradiation conditions, the white light intensity  $P_{in}$  was passed through neutral density filters (Andover Corporation Optical Filter). A Cornerstone 130 monochromator (Oriel) was used together with a 300 W Xe lamp to measure the incident photon-to-current conversion efficiencies (IPCE). They were calculated as **Eq. 4-1**

$$IPCE = \frac{hc}{\lambda e} \times J_{sc} \times P_{in}^{-1} \quad (\text{Eq. 4-1})$$

where  $h$  is Planck's constant,  $e$  is the elementary charge and  $\lambda$  is the monochromatic irradiation wavelength. The monochromatic light intensity was determined using a calibrated Si-diode. Reflection losses (10%) at the window of the inert gas measurement chamber were not considered in the calculation.

Photo-CELIV transients were measured using the PAIOS system<sup>7</sup> in a nitrogen-filled glovebox. Samples were illuminated by a 300  $\mu\text{s}$  white LED (Cree® XLamp® XP-G) pulse with a nominal intensity of  $72 \text{ mW/cm}^2$ . To determine recombination kinetics, the photogenerated charges were extracted after a variable delay time  $\tau_{\text{delay}}$  using a voltage sweep rate  $A$  of 10 and 100 V/ms. Prior to the voltage ramp, the applied voltage was iteratively set to  $V_{oc}$  (open circuit condition) during the light pulse in order to avoid preliminary charge extraction. In order to assess the mobility of Cy5-PF6 films, the sweep rate was varied from 1 to 100 V/ms. The simulations were performed using the SETFOS software that has previously been used to extract organic solar cell parameters by combining steady-state and transient techniques<sup>8,9</sup>. The charge carrier mobility and the density of photo-generated charge carriers were calculated from the time taken to reach the photocurrent maximum and by integrating the area under the photo-induced transients.

Poling experiments were performed using constant positive or negative bias to the cell and monitoring the current density. Characteristic poling times were determined at the maximum current density peak.

Fluorescence measurements were performed in a vacuum tight chamber using the optical fiber accessory of a Fluorolog-3 spectrofluorometer (Jobin Yvon Horiba) for emission detection and excitation. For high intensity excitation, a 532 nm emission wavelength solid state laser (Thorlabs) with an intensity of 4.5 mW was employed. Fluorescence quantum yields were determined in an integrating sphere mounted into the sample compartment of the fluorimeter.

Absorption spectra were measured on a Varian Cary 50 UV-vis spectrophotometer. Film thicknesses were determined by profilometry (Ambios XP1). The absorptance of the films was determined by optics simulation software Setfos 3.3 which is based on the transfer matrix formalism for fast calculation of the photon flux across multilayer stacks. The absorptance of some films was double checked with the help of difference time domain (FDTD) simulations using Lumerical FDTD Solution software (Lumerical Inc. Canada). Both calculations utilize the optical constants  $n(\lambda)$  and  $k(\lambda)$  as obtained by variable angle spectral ellipsometry.

### 4.3 Results

Pristine single layer cyanine Cy5-PF6 devices can be fabricated with various thicknesses ranging from 40 nm to 130 nm. Single layer devices were made with PEDOT and MoO<sub>3</sub> anode buffer layers as well as different metal cathodes, both using a 2nm thin Alq<sub>3</sub> cathode buffer layer (**Figure 4-1**). In terms of rectifying properties as well as open-circuit voltage under white light irradiation, diodes with structure ITO/MoO<sub>3</sub>/Cy5-PF6/Alq<sub>3</sub>/Al perform clearly best. In reverse bias, there is a striking linear behavior of the photocurrent under irradiation. The diode breakthrough voltage is as high as -5 V for 40 nm thick films (corresponding to an external applied electric field of  $1.25 \cdot 10^8$  V/m).

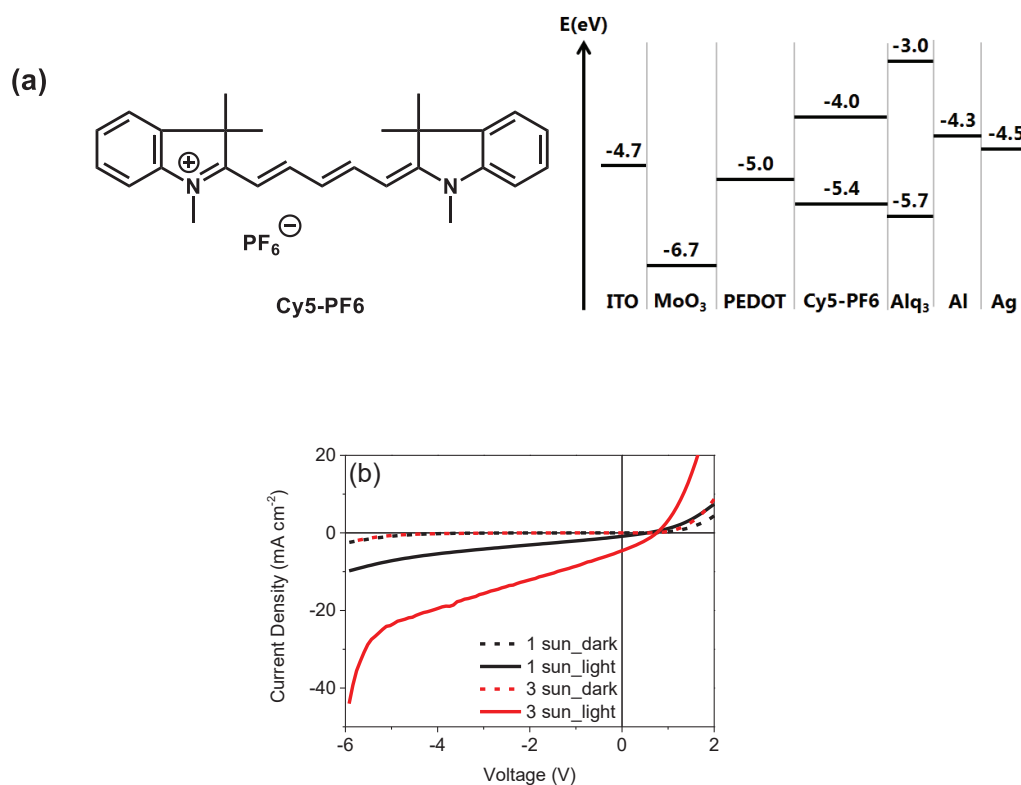


**Figure 4-1:** (a) Chemical structure of Cy5-PF6 and energy level diagram of the layers used in the thin film diodes. (b) Current-voltage curves of single layer Cy5-PF6 (40 nm) devices using MoO<sub>3</sub> as anode buffer layer in the dark and under 1 or 3 sun irradiation.

Devices using PEDOT anode buffer layers and a silver cathode exhibit higher dark current in reverse bias and present non-rectifying J-V characteristics. We have attributed this behavior to insufficient wetting of the dye solution on PEDOT leading to a rough morphology with numerous pinholes. Upon evaporation, Ag can penetrate into the cyanine layer and form micro shunts. Due to the lower diffusion of vapor deposited Al into the organic layer J-V curves are more rectifying, but still present large dark currents in reverse direction. Obviously, MoO<sub>3</sub> presents high hole selectivity and allows excellent rectification.



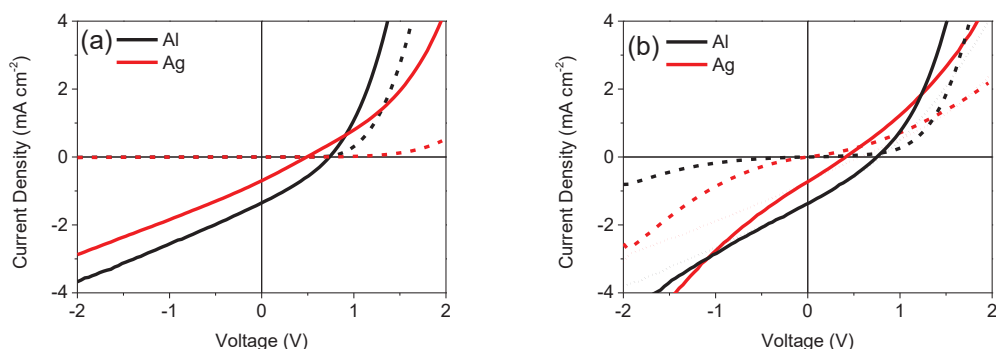


**Figure 4-2:** Current-voltage curves of single layer Cy5-PF6 (40 nm) devices using (a) MoO<sub>3</sub> or (b) PEDOT anode buffer layers. The cathode (Al or Ag) are indicated in the figure legend. Curves monitored in the dark are marked by dashed lines while curves measured under AM1.5 simulated solar light are drawn as full lines. Dotted lines correspond to the difference between current-voltage curves in the dark and under irradiation.

Disregarding rectifying behavior, all devices present a linear photocurrent response in reverse bias. For non-rectifying devices the dark current was subtracted from the current under irradiation (see dotted lines in **Figure 4-2b**). Under simulated solar irradiation these single layer diodes show an open circuit voltage of 0.7 V which depends logarithmically on irradiation intensity (see 4.7 Supporting Information, **Figure 4-8**).

The linear part of the photocurrent in reverse direction allows for determination of the conductivity from the slope of the current-voltage curve:

$$\frac{dJ}{dE} = \sigma = ne\mu \quad (\text{Eq. 4-2})$$

where  $\sigma$  is the conductivity,  $e$  the elementary electronic charge and  $\mu$  the charge carrier mobility. From **Figure 4-2** we see that conductivity is not dependent on the type of electrode or anode buffer layer we apply to the device, although  $V_{oc}$  clearly changes according to the effective work function of the electrode. Furthermore conductivity depends linearly on light intensity (**Figure 4-3a**) with a slight sub-linear response above an intensity of 1.5 suns.

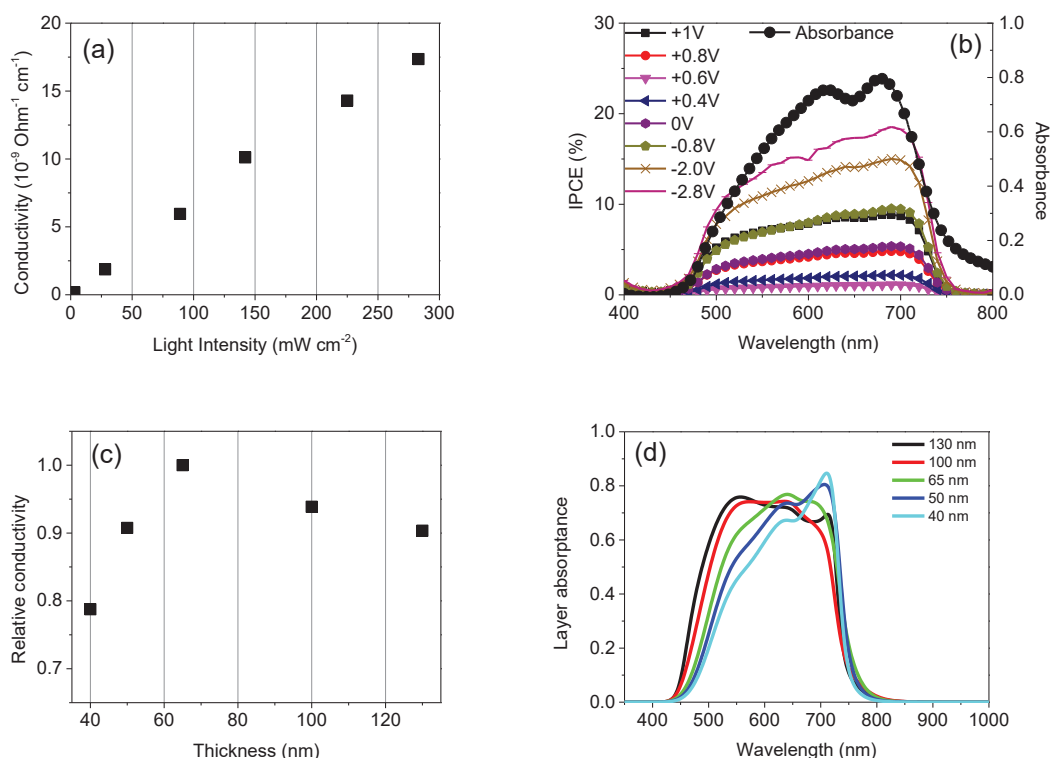


**Figure 4-3:** (a) Conductivity  $\sigma$  extracted from the linear slope of the current-voltage characteristics of an ITO/MoO<sub>3</sub>/Cy5-PF6 (40 nm)/Alq<sub>3</sub>/Al device measured at different light intensities (full curves are shown in 4.7 Supporting Information, **Figure 4-9**). (b) Absorbance spectra of glass/MoO<sub>3</sub> (10 nm)/Cy5-PF6 (40 nm) and IPCE spectra of the same device as in (a) at different bias voltages under 1 sun irradiation. (c) Relative conductivity  $\sigma$  extracted from the linear slope of the current-voltage characteristics of ITO/PEDOT/Cy5-PF6 ( $x$  nm)/Alq<sub>3</sub>/Ag as a function of device thickness  $x$ . (d) Simulated absorbance spectra of the devices in (c).

IPCE spectra do not vary notably with the electrical field in forward or reverse direction (**Figure 4-3b**) indicating that charge generation mechanism is the same within the range of fields measured. The spectrum does not follow the absorbance obtained by Setfos transfer matrix calculation but has a saturated shape. As we will show below this feature is attributed to the fact that photocurrent generation at the absorption band edges is enhanced with respect to the maximum absorption wavelength, due to inhomogeneous photogeneration of charge carriers. This is also the reason why the photoconductivity of the cyanine film achieves a maximum at a thickness of about 70 nm, even though its white light absorption increases slightly (**Figure 4-3d**). At the highest possible applied reverse field of  $1.1 \cdot 10^8$  V/m before diode breakdown occurs (i.e. before the photocurrent signal becomes non-linear), an IPCE

above 30% is obtained by extrapolating the IPCE signal at 700 nm. Considering the absorbance of about 80% at 700 nm for a thickness of 40 nm and subtracting the reflection losses at the window of the sealing chamber of 10%, we arrive at an estimate of the internal quantum efficiency (IQE) of 42%. Performing this calculation at different wavelengths gives the same order of magnitude with a maximum IQE of 84% at 500 nm. We do not exceed 100% and unfortunately the injection onset in the reverse bias does not permit to drive the devices into saturation. Nevertheless, the linear electric field dependence at field strengths  $> 10^6$  V/m is already a strong indication that charge generation is intrinsic to the cyanine film. Injection of charges from the electrodes other than to collect photo-induced charges seems very unlikely at reverse bias, since we would expect non-linear light intensity behavior and a certain sensitivity on the electrode work function.

In order to further investigate possible electrode effects on the photocurrent, devices with semitransparent silver electrodes of 12 nm thickness were fabricated (**Figure 4-4**).

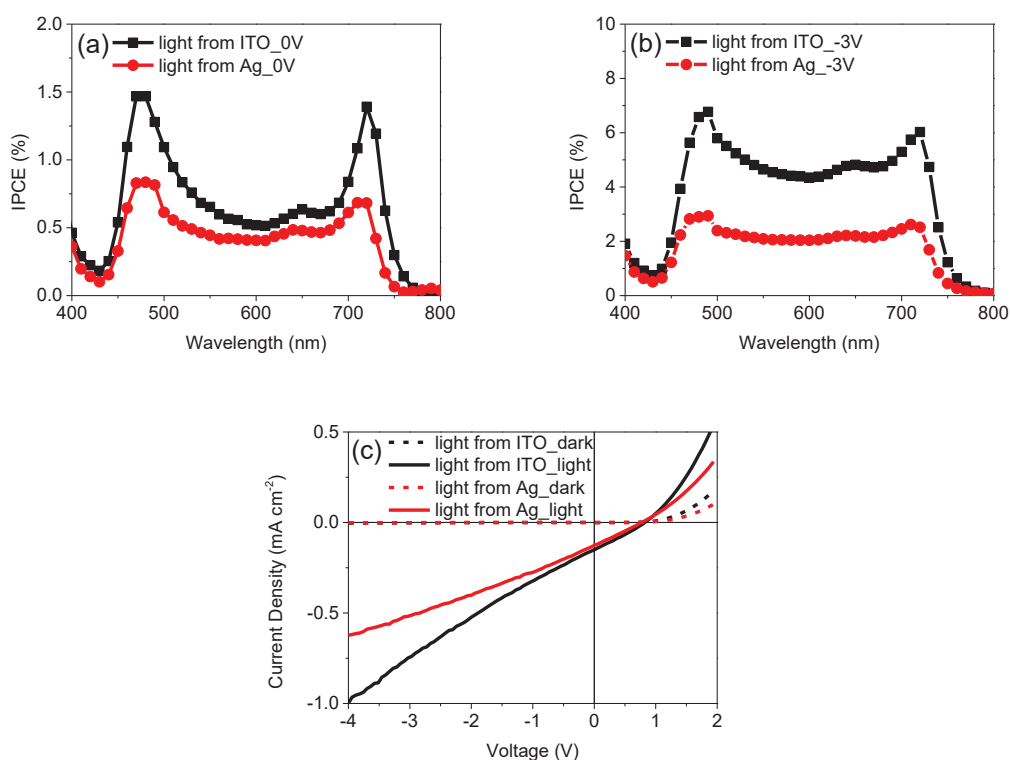


**Figure 4-4:** (a) IPCE spectra of ITO/MoO<sub>3</sub> (10 nm)/Cy5-PF6 (130 nm)/Alq<sub>3</sub> (2 nm)/Ag(12 nm) devices at (a) 0 V or (b) -3 V bias under 1 sun irradiation from the front (ITO) and back side (Ag). (c) Current density-voltage curves in the dark and under illumination.

We clearly observe an increased IPCE at the band edges of the absorption spectrum and a dip where the film most strongly absorbs. At short circuit condition, there is not much difference between light impinging from the ITO or from the semitransparent silver electrode. This feature remains also when using semitransparent aluminum electrodes with a thickness of 8 nm (see 4.7 Supporting Information, **Figure 4-10**). At higher reverse bias the difference between band edge and the spectral region of maximum absorption diminishes. Interestingly also the difference in the IPCE measured at the central absorption region differs by a factor of two when irradiation from front and back side, respectively.

Modifying the electrode interfaces would be another way to scrutinize electrode effects on charge generation. This can be done by poling the devices in forward bias (**Figure 4-5**). As we have shown recently, cyanine films can be poled, if the counterions such as  $\text{PF}_6^-$  are mobile enough.<sup>10</sup> As in conventional electrochemical light-emitting devices, p- and n-doped zones are formed after a sufficient poling time during which negative counterions move to the positively biased anode. In such poled devices the slope of the current-voltage characteristics is almost identical to the one of unpoled devices. The field dependence is perfectly linear which again indicates that charges are likely generated in the bulk of the film and not at specific interfaces. The higher  $V_{\text{oc}}$  indicates that better Ohmic contacts are reached between the intrinsic and doped regions and also show that recombination losses are small. Also a weak LEC emission can be observed (**Figure 4-5a**).

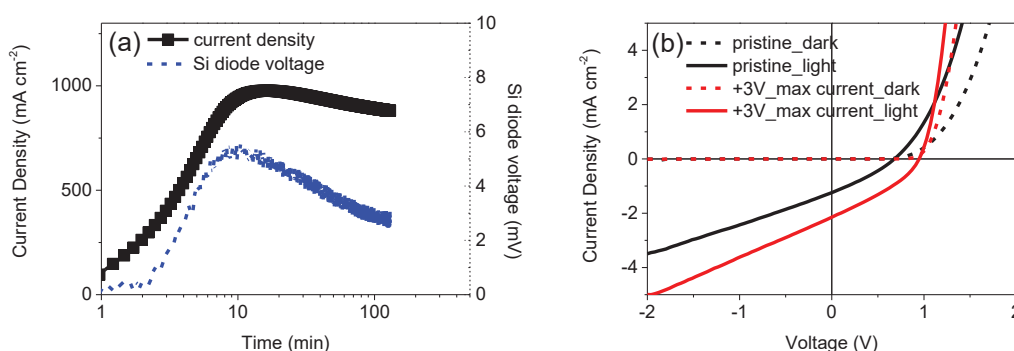


**Figure 4-5:** (a) Poling curve of ITO/MoO<sub>3</sub>/Cy5-PF<sub>6</sub> (40 nm)/Alq<sub>3</sub>/Al devices in forward direction at +3V.

The luminescence emission is indicated in the graph. (b) Corresponding current-voltage characteristics of the same device after a poling time of 25 minutes in forward direction. Dashed and solid lines stand for dark and light J-V characteristics, respectively.

## 4.4 Discussion

We first discuss the photoconductivity observed in pristine Cy5-PF6 single layer devices measured just after fabrication. Anode (ITO/MoO<sub>3</sub>) and cathode (Alq<sub>3</sub>/Al) contacts were chosen in order to obtain efficient injection into the organic semiconductor. We reach a maximum open circuit voltage of 0.7-0.8 V at saturation at a high light intensity of approximately 3 suns. This open circuit voltage is also achieved for thicker dye layers using PEDOT as buffer layer. However, after bias, an increased open circuit voltage of 0.94 V is observed. Since poling induces n- and p-doped layers at the cathode and anode, respectively, the open circuit voltage of the device corresponds to the maximum achievable photovoltage in these single layer devices. Given that the open circuit voltage of 0.7 eV can be achieved either with PEDOT or MoO<sub>3</sub> anode buffer layers, but only with Alq<sub>3</sub>/Al cathodes, we judge that most of all electron injection is ameliorated in poled devices.

Intrinsic charge generation in an organic semiconductor usually requires either strong electric fields, or photon energies well above the optical bandgap of the semiconductor. We measured the electric field quenching of Cy5-PF6 photoluminescence by varying the reverse and forward bias applied to the single layer devices (**Figure 4-6b**).

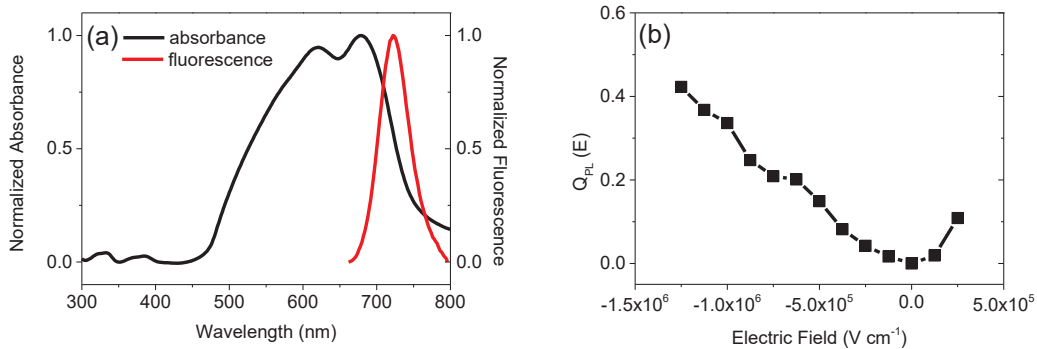


**Figure 4-6:** (a) Absorbance and luminescence spectra of a 40 nm thick Cy5-PF6 layer sandwiched between ITO/MoO<sub>3</sub> and Alq<sub>3</sub>/Al electrodes. The film was excited with a 4.5 mW laser emitting at 532 nm. (b) Field induced quenching efficiency  $Q_{PL}(E)$  of Cy5-PF6 luminescence monitored at 730 nm.

$Q_{PL}(E)$  was calculated from equation (**Eq. 4-3**).

The field induced photoluminescence quenching efficiency  $Q_{PL}(E)$  can be written as

$$Q_{PL}(E) = \frac{I_{PL}(0) - I_{PL}(E)}{I_{PL}(0)} \quad (\text{Eq. 4-3})$$

and has been analyzed by various continuum theories such as the Onsager theory<sup>11</sup> or its extension by Noolandi and Hong<sup>12</sup>. In both theories, photoluminescence quenching is accompanied by charge carrier generation. A simple model allows relating the exciton binding energy to the onset field of luminescence quenching<sup>13</sup>:

$$E_b = 2e \sqrt{\frac{e E_{onset}}{\epsilon \epsilon_0}} \quad (\text{Eq. 4-4})$$

Using  $E_{onset} = 10^7$  V/m and a dielectric constant of 3.6 from ellipsometry measurements (see 4.7 Supporting Information, **Figure 4-11**), a binding energy of 0.45 eV is calculated. This is of the same order of magnitude as experimentally determined exciton binding energy of 0.2 for other cyanine dyes.<sup>14</sup> The weak emission observed from Cy5-PF6 films also has a rather narrow band width (**Figure 4-6a**) indicating that it originates from non-relaxed excitonic states that have not been able to diffuse substantially before recombining radiatively or being quenched by other processes. In particular the generation of charge carriers with a quantum efficiency of more than 40 % was found to be very efficient. In the present work, the photoluminescence quantum yield was below the detection limit of our apparatus ( $< 10^{-4}$ ) at zero field and therefore carrier generation observed in the present case must occur in the absence of an electric field. Further mechanisms could be related to exciton-exciton reactions, such as exciton fusion giving rise to a higher excited state which would be able to be ionized. Indeed, rather low photon fluxes of  $10^{16}$  to  $10^{18}$   $s^{-1}cm^{-2}$  are required to trigger exciton-exciton fusion in aggregated cyanine films at low temperature<sup>15</sup>. In our devices under simulated solar irradiation the calculated flux density  $N_{phot}$  of absorbed photons is  $6.64 \cdot 10^{16}$   $s^{-1}cm^{-2}$  (this is calculated from the simulated absorbance  $A(l)$  by convolution with the AM1.5 solar spectrum  $S(l)$  according to **Eq. 4-5**.

$$N_{phot} = \int A(\lambda)S(\lambda) \frac{\lambda}{hc} d\lambda \quad (\text{Eq. 4-5})$$

Such processes typically depend quadratically on light intensity, which we do not observe in the devices studied in this work. We therefore conclude that photogeneration is a direct process (also called "self-ionization"). Indeed, our previous pulsed laser spectroscopy study using the perchlorate salt of Cy5,<sup>16</sup> revealed fast generation of oxidized species within the 10 ns laser pulse in the absence of an applied electric field.

Direct photogeneration can be due to structural inhomogeneity creating energetic disorder in the film. This is especially important for Cy5-PF6 films that show a very broad spectrum with clear H-aggregate features. Aggregates indeed induce quite important variations of

orbital energy levels up to 0.2-0.3 eV<sup>17</sup>. This would allow for large enough driving forces to have spontaneous charge carrier generation induced by electron transfer, from a monomer species to an aggregate. At the same time, the transport gap would be reduced due to the heterogeneous structure of the film. There have been numerous investigations on the relationship between the open-circuit voltage ( $V_{oc}$ ) and the transport gap of organic semiconductors.<sup>18</sup> Apart from structural disorder,  $V_{oc}$  is mainly affected by the electrode wave functions, exciton binding energy, recombination or charge transfer states. For poled devices, we can exclude electrode effects on  $V_{oc}$  since highly n- and p-doped interface layers form at the respective electrodes. The difference of 0.7 eV between the open circuit voltage of Cy5-PF6 of 0.94 V and the optical bandgap of 1.64 eV is rather low, which may be related to the lower exciton binding energy reported in cyanine semiconductors<sup>14</sup> as well as reduced recombination. We note that the same difference is obtained in single layer devices using trimethine cyanine dye Cy3-PF6 with an optical gap of 2.1 eV and an open circuit voltage of poled devices at 1.4 V (see 4.7 Supporting Information, **Figure 4-12**).

In order to further understand photogeneration and recombination of charges in disordered Cy5-PF6 films, we carried out photo-CELIV measurements on films of 40 nm and 130 nm thickness. Figure 6a displays extracted charge density taken at different delay times after the light pulse. Extraction proceeded typically at a rate of 10 V s<sup>-1</sup> and did not follow an exponential law. Strikingly, recombination kinetics in Cy5-PF6 films turn out to be extremely slow with about 50% of the charge still being extracted at a delay of 1 ms. Such long recombination times have already been observed for polymer-fullerene blends with phase separated domains<sup>19</sup> but is unusual in pristine small molecular materials. On the double logarithmic plot, the thin cyanine layer follows a linear behavior with a slope of -1/7 which would correspond to a kinetic law of order 8. This contrasts to the bimolecular behavior of Langevin recombination rate  $R$ :

$$R = \gamma_L np \quad \text{with} \quad \gamma_L = \frac{e}{\epsilon \epsilon_0} (\mu_e + \mu_h) \quad (\text{Eq. 4-6})$$

where  $\gamma_L$  is the bimolecular recombination coefficient. Such second order kinetics would correspond to a slope of -1 and contrasts to the measured ultraslow recombination kinetics in Cy5-PF6 (**Figure 4-7a**).

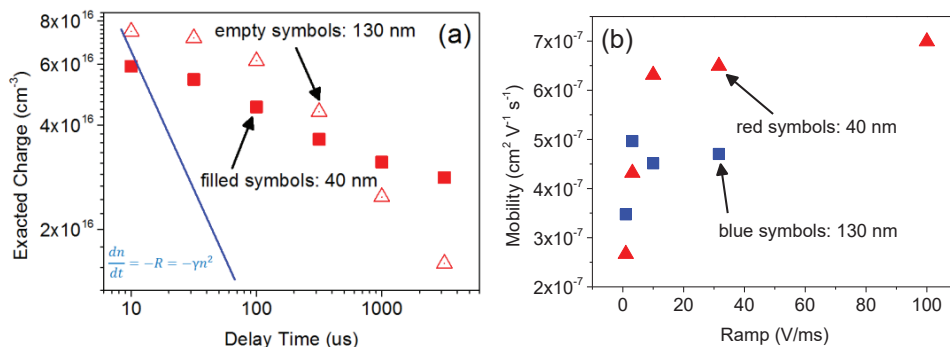


**Figure 4-7:** Photo-CELIV measurements of ITO/MoO<sub>3</sub>/Cy5-PF6 (40 nm or 130 nm)/Alq<sub>3</sub>/Al devices (a) Recombination kinetics measured by time delayed charge carrier extraction. (b) Extracted charge carrier mobility at different sweep rates (film thicknesses indicated in the graph).

**Figure 4-7b** displays extracted charge carrier mobilities as a function of sweep rate and cyanine layer thickness. In all cases voltage sweeps start at  $V_{oc}$  and proceed to  $-3V$ . The RC constant of the electronic circuit was  $0.1 \mu s$  and thus did not interfere with the analysis of the transient curve. The apparent mobility of the charge carriers shows a clear dependence of the voltage sweep rate and the layer thickness. The decrease of apparent mobility at low sweep rates has already been predicted to occur in systems with trap states.<sup>20,21</sup> The average mobility measured is  $5 \cdot 10^{-7} \text{ cm}^2 \text{ V}^{-1} \text{ s}^{-1}$  and includes both holes and electrons. The low carrier mobilities are indicative of charge carrier trapping, but are not able to explain non Langevin behavior. Therefore there must be another mechanism present to screen the charge carriers from attracting each other. Such a mechanism could come from the fact that cyanine are cationic dyes. When reduced by an electron the chromophore becomes neutral. While the chromophore site with its surrounding would still appear negatively charged seen from a far distance, the local fields may mask the negative charge carrier. Additionally, if small displacements of the ions in the film are possible, negative as well as positive charge carriers will be screened.

Slow recombination would also explain the rather large quantum efficiency of photo-induced charge carrier production in the bulk material. We are now able to compare the charge carrier density  $n_{cond}$  obtained from the conductivity with the charge carrier density  $n_{CELIV}$  extracted from CELIV data. The former can be obtained from  $n_{cond} = \sigma/e\mu$ . Using  $\sigma = 6.5 \cdot 10^{-9} \Omega^{-1} \text{ cm}^{-1}$  (**Figure 4-2**) and the average mobility of  $5 \cdot 10^{-7} \text{ cm}^2 \text{ V}^{-1} \text{ s}^{-1}$  a charge carrier density  $n_{cond} = 8 \cdot 10^{16} \text{ cm}^{-3}$ . This compares very well with the density  $n_{CELIV} = 6.4 \cdot 10^{16} \text{ cm}^{-3}$ .



So far we have assumed identical mobility for electron and hole. If this is true we must indeed obtain similar behavior for irradiation through the front electrode (ITO/MoO<sub>3</sub>) and back (semitransparent Ag). As shown in **Figure 4-4**, EQE measured in the central absorption band is almost identical for front and back side irradiation. This is surprising since the two electrodes have an important difference in reflection. Using Setfos, we calculated the absorptance of light in the central absorption region to be 30% for Ag side irradiation and 75% for ITO irradiation. Since most of the radiation is absorbed close to the interface at the maximum absorption wavelength, the current obtained is limited by those carriers traveling farthest. Photogeneration of charge carriers from the ITO side (front side) would mean that electrons travel a larger distance than holes. Even though twice as many electrons are produced by front side irradiation as compared to back side irradiation, the two currents are comparable. This means that electrons are less mobile approximately by a factor of two. The enhanced EQE at the edges of the absorption band is similar for back and front irradiation. This phenomenon is related to charge density dependent mobility of carriers (see 4.7 Supporting Information, **Figure 4-10**). At the maximum absorption wavelength charge density will be very asymmetric leaving regions with very low carrier density and therefore lower mobility. Light with wavelength at the edges of the absorption band will more homogeneously irradiate the films and therefore provide a higher EQE. In thick devices this feature is observed in the IV characteristics where front face illumination has clear field dependence on conductivity while back illumination shows a linear character. At higher reverse bias mobility is enhanced by the electric field and the marked wavelength dependence of EQE reduces.

Finally we discuss Cy5-PF6 films biased in the opposite direction. In the ideal case, we would induce p-type doping at the Al cathode and n-type doping at the ITO electrode. As a matter of fact the J-V characteristics rather look like a short-circuited device, meaning that it is fully doped by one type of charge carrier and that there is no junction formation between p- and n-zones. This is indeed supported by the fact that we do not observe an open circuit voltage in this type of poled device. The inverse poling effect is reversible and not due to device deterioration. (see 4.7 Supporting Information, **Figure 4-13**). The question regarding which type of charge carrier is doping the film arises. It is not easy to be answered, but given the high work function of MoO<sub>3</sub>, we suspect that electron injection from MoO<sub>3</sub> is more difficult than hole injection from the aluminum contact. Due to this asymmetry in charge carrier

injection, a p-doped film grows with time and in the eventually both electrodes equilibrate with the Fermi level of the p-doped cyanine film. However, at the Al electrode, a Schottky junction builds up blocking electron injection and building a barrier for hole transfer at the Al side. Upon irradiation, this Schottky barrier will be lowered, increasing photocurrent generation substantially. We indeed observe photomultiplication with an EQE larger than 100%.

## 4.5 Conclusions

We demonstrate efficient photo-induced charge carrier generation in the bulk of pristine pentamethine cyanine dye films with internal quantum efficiency exceeding 40%. The mechanism of charge generation is found to be independent of the electrodes and compatible with bulk generation. As revealed by CELIV investigations, charges are created in the absence of an electric field. Under reverse bias, charges generated under continuous irradiation lead to a linear dependence of the current-voltage curve. The conductivity extracted from the slope of the latter linearly depends on light intensity and allows inferring the charge carrier density which perfectly matches the one obtained from CELIV measurements. Other mechanisms that would yield similar photoconductivity characteristics can be discarded. Field induced fluorescence quenching does not contribute significantly to the photocurrent due to the very low fluorescence yield. Electrode effects were shown not to be effective based on the photosensitivity spectrum, the independence on the type of electrodes and the perfectly linear current-voltage dependence. The high order recombination rate in these cyanine films with a typical half time of milliseconds points towards a charge screening mechanism in these cationic dye salts.

## 4.6 References

- [1] M. Pope, C. E. Swenberg, *Electronic Processes in organic Crystals and Polymers*, 2nd ed., Oxford University Press, New York, **1999**.
- [2] K. Law, organic photoconductive materials: recent trends and developments, *Chem. Rev.* **1993**, 93, 449-486.

- [3] H. Huang, C. Chou, Y. Che, L. Li, C. Wang, X. Yang, Z. Peng, L. Zang, morphology control of nanofibril donor-acceptor heterojunction to achieve high photoconductivity: exploration of new molecular design rule, *J. Am. Chem. Soc.* **2013**, 135, 16490-16496.
- [4] H. Meier, organic dyes as photoelectric semiconductors, *Angew. Chem. Int. Ed.* **1965**, 4, 619-635.
- [5] W. Tress, K. Leo, M. Riede, photoconductivity as loss mechanism in organic solar cells, *Phys. Status Solidi RRL* **2013**, 7, 401-405.
- [6] D. Hauschildt, W. Fuhs, H. -J. Hesse, photoconduction in single crystals of a pentamethinium cyanine dye, *Phys. Stat. Sol. (b)* **1979**, 91, 447-453.
- [7] w.f.c. PAIOS by Fluxim AG.
- [8] S. Jenatsch, R. Hany, A. C. Veron, M. Neukom, S. Zufle, A. Borgschulte, B. Ruhstaller, F. Nüesch, influence of molybdenum oxide interface solvent sensitivity on charge trapping in bilayer cyanine solar cells, *J. Phys. Chem. C* **2014**, 118, 17036-17045.
- [9] M. T. Neukom, S. Zufle, B. Ruhstaller, reliable extraction of organic solar cell parameters by combining steady-state and transient techniques, *Org. Electronics* **2012**, 13, 2910-2916.
- [10] S. Jenatsch, L. Wang, M. Bulloni, A.C. Veron, B. Ruhstaller, S. Altazin, F. Nuesch, R. Hany, Doping Evolution and Junction Formation in Stacked Cyanine Dye Light-Emitting Electrochemical Cells, *ACS Appl. Mater. Interfaces* **2016**, 8, 6554-6562.
- [11] D. M. Pai, R. C. Enck, onsager mechanism oh photogeneration in amorphous selenium, *Phys. Rev. B* **1975**, 11, 5163-5174.
- [12] J. Noolandi, K. M. Hong, theory of photogeneration and fluorescence quenching, *J. Chem. Phys.* **1979**, 70, 3230-3236.
- [13] S. Tasch, G. Kranzelbinder, G. Leising, U. Scherf, electric-field-induced luminescence quenching in an electroluminescent organic semiconductor, *Phys. Rev. B*, **1997**, 55, 5079-5083.
- [14] T. Tani, T. Suzumoto, K. Ohzeki, energy-gap dependence of efficiency of photoinduced electron-transfer from cyanine dyes to silver bromide microcrystals in spectral sensitization, *J. Phys. Chem.* **1990**, 94, 1298-1301.
- [15] C. Spitz, S. Daehne, low temperature exciton-exciton annihilation in amphi-PIPE J-aggregates, *Int. J. Photoenergy* **2006**, 84950.

- [16] F. A. Castro, H. Benmansour, J. -E. Moser, C. F. O. Graeff, F. Nueesch, R. Hany, photoinduced hole-transfer in semiconducting polymer/low-bandgap cyanine dye blends: evidence for unit charge separation quantum yield, *Phys. Chem. Chem. Phys.* **2009**, 11, 8886-8894.
- [17] B. I. Shapiro, molecular assemblies of polymethine dyes, *Russ. Chem. Rev.* **2006**, 75, 433-456.
- [18] N. K. Elumalai, A. Uddin, open circuit voltage of organic solar cells: an in-depth review, *Energy Environ. Sci.* **2016**, 9, 391-410.
- [19] C. Deibel, A. Baumann, V. Dyakonov, polaron recombination in pristine and annealed bulk heterojunction solar cells, *Appl. Phys. Lett.* **2008**, 93, 163303.
- [20] R. Hanfland, M. A. Fischer, W. Brutting, U. Wurfel, R. C. I. MacKenzie, the physical meaning of charge extraction by linearly increasing voltage transients from organic solar cells, *Appl. Phys. Lett.* **2013**, 103, 063904.
- [21] M. T. Neukom, N. A. Reinke, B. Ruhstaller, charge extraction with linearly increasing voltage: A numerical model for parameter extraction, *Solar Energy* **2011**, 85, 1250-1256.

## 4.7 Supporting Information

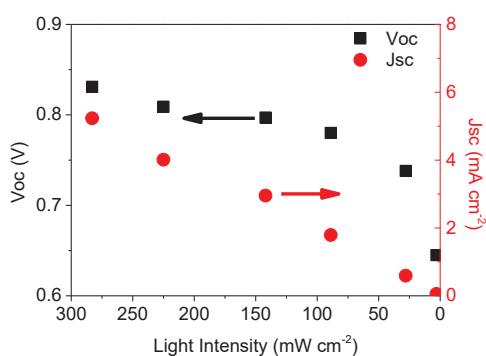


**Figure 4-8:**  $V_{oc}$  and  $J_{sc}$  values of ITO/MoO<sub>3</sub>/Cy5-PF6 (40 nm)/Alq<sub>3</sub>/Al devices irradiated at different light intensities.

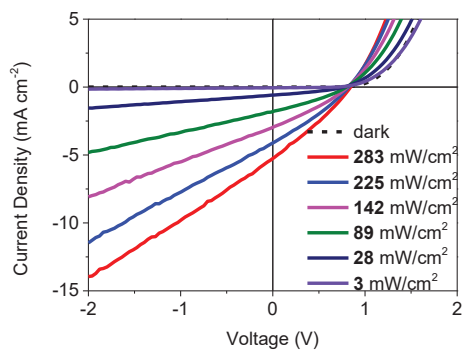


**Figure 4-9:** J-V characteristics of ITO/MoO<sub>3</sub>/Cy5-PF6 (40 nm)/Alq<sub>3</sub>/Al devices irradiated at different light intensities.

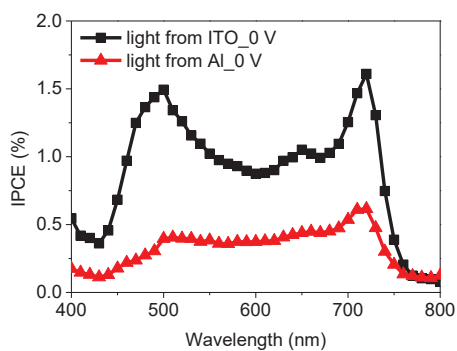


**Figure 4-10:** IPCE spectra of ITO/MoO<sub>3</sub>/Cy5-PF6 (130 nm)/Alq<sub>3</sub> (2 nm)/Al (8 nm) devices at 0 V under 1 sun irradiation from the front (ITO) and back side (Al).

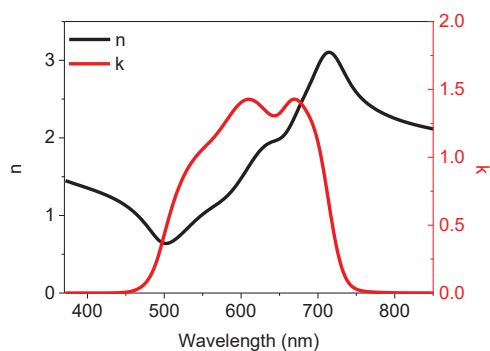


**Figure 4-11:** Ellipsometry measurements of Cy5-PF6.

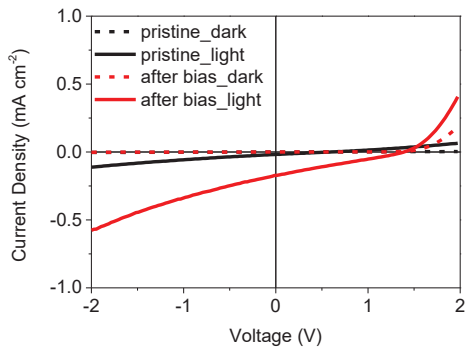


**Figure 4-12:** J-V characteristics of ITO/PEDOT/Cy3-PF6 (130 nm)/Alq<sub>3</sub>/Ag before and after bias at +3V to maximum current.

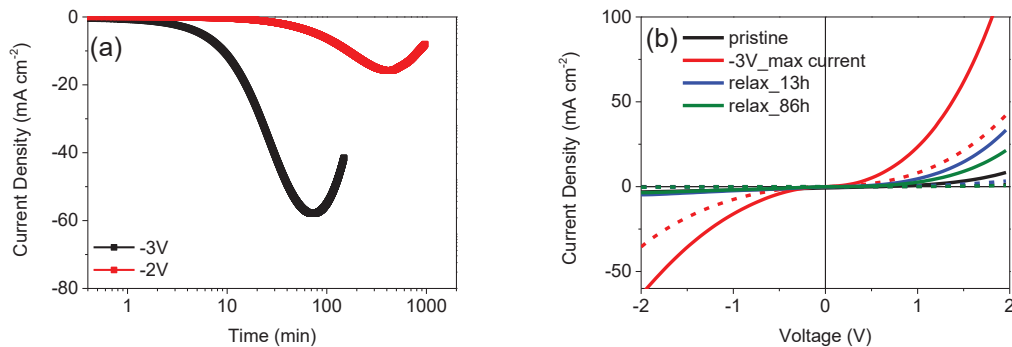


**Figure 4-13:** (a) Poling curve of ITO/MoO<sub>3</sub>/Cy5-PF6 (40 nm)/Alq<sub>3</sub>/Al devices in reverse direction at different voltages. (b) White light (solid lines) and dark (dotted lines) J-V characteristics before and after biasing at -3 V to maximum current.

## Chapter 5: Visible-Light Induced Azide Decomposition in Trimethine Cyanine/Azido-Benzoate Films

### 5.1 Introduction

The aim of this work was the development of a light-triggered nitrene-mediated chemical fixation method for mobile anions in organic thin films. Significant progress is being made with organic materials that feature mixed ionic/electronic conduction for new applications in the fields of optoelectronic, sensors and smart materials.<sup>1</sup> Cyanine dyes are ionic semiconducting organic salts that are accompanied by a counter ion. When applying a voltage bias the ions can be displaced in a thin cyanine film. Ionic interfacial space charge builds up and this has been exploited in bilayer cyanine/acceptor-C<sub>60</sub> and cyanine/donor-polymer solar cells.<sup>2,3</sup>

More recently, cyanine light-emitting electrochemical cells (LECs) have been demonstrated.<sup>4,5</sup> When a voltage larger than the energy gap of the semiconductor is applied between the two electrodes, the ions in the active materials redistribute in a complex manner to facilitate the injection and transport of electrons and holes. The organic material is p-type (at the anode) and n-type (at the cathode) doped and the conductivity increases strongly. These regions grow into the film and form a p-n junction where they meet. Further injected charges travel along the doped material and recombine generating light emission at the junction.

The p-n junction formation process followed by light-emission is dependent on the ionic redistribution; therefore, the turn-on time to light emission of a LEC is dependent on the ionic conductivity as well as on the driving voltage and the active material thickness. Characteristics of a LEC are a low turn-on voltage and the independence of the device operation on the electrode materials. Importantly, all processes in a LEC are reversible, and removal of the external voltage leads to device discharge and redistribution of the ions. The device is not rectifying and slow turn-on times are often observed. Similarly in an ionic organic solar cells, the ions relax back when the driving voltage is turned off, which prevents the continuous operation of the device.

Therefore, it is clear that the dynamic p-n junction should be stabilized by immobilisation of the ions, thereby attaining quick LEC response time and continuous solar cell operation.

Various attempts have been reported to permanently fix a desired ion distribution, thereby decoupling device operation from the slow ionic motion. Originally, ions were physically immobilized by attempting to freeze out ionic mobility.<sup>6</sup> A cationically and anionically functionalized polyacetylene bilayer was fabricated. The bilayer was then electrochemically doped by applying a voltage. The liberated salt was washed away with a solvent, effectively trapping a p-n polymer junction.<sup>7</sup> A chemically fixed junction was demonstrated with ion pair monomers that can be polymerized. The ions were locked during device charging, probably via radical-induced reactions with the radical anions and radical cations that are formed when electrical charge is injected into the organic material.<sup>8,9</sup> This approach was extended by studying crosslinking reactions of polymerizable counter ions and polymerizable ion-transporting material using a radical initiator compound.<sup>10</sup> A permanently fixed p-n junction was prepared by using an organic bilayer consisting of a cationic polyelectrolyte containing fluoride counter anions and a neutral conjugated polymer containing anion-trapping groups. Application of a voltage lead to migration of the fluoride anions into the neutral polymer where they were trapped, establishing a stable junction with fast turn-on time for light emission.<sup>11</sup> For photovoltaic applications, single-component and blended donor-acceptor devices were fabricated by adding a polymerizable salt. Charging with an external voltage established a chemically fixed p-i-n junction. These solar cells showed a promising increase in the open-circuit voltage, but the measured currents and fill factors were rather low.<sup>12</sup>

As an alternative to immobilizing ions after device charging, we tested here anions containing a reactive azide group. Azides form highly reactive nitrene intermediates when irradiated with light in the UV wavelength range which rapidly react with nearby covalent bonds. Organic azides have found widespread use as photoaffinity markers for biomolecules, crosslinking reagents in photoresists, as reagents for the light-induced modification and functionalization of surfaces or as organic synthetic intermediates.<sup>13-15</sup> In organic solar cells, small molecule bis-azides have been recently used to induce UV-photo or thermal crosslinking reactions in organic films composed of blends of polymers and fullerenes.<sup>16-18</sup> The general idea here is to improve the cell long-term stability by fixing favourable blend microstructures after film coating, thereby suppressing the tendency for progressing phase separation on thermal ageing.

As reactive anions we used azido-benzoate and azido-perfluorobenzoate and synthesized in a first step tri- (Cy3), penta- (Cy5) and hepta- (Cy7) cyanine salts via ion-exchange reactions.



However, the concept of displacing the anions in a first step (device charging) followed by photochemical stabilization of the operating device was not successful in our hand. This was due to a distinct tendency of the azido-benzoates towards decomposition during device fabrication already, triggered by light, temperature or electrical charges. Surprisingly, we observed that Cy3/azido-benzoate films also decomposed effectively already when exposed to visible light, and we ascribe this to an endothermic triplet-energy transfer reaction from excited cyanines to the azide group. Detrimental to LEC and solar cell performance, spontaneous azide decomposition resulted in severe quenching of the photoluminescence (PL) and functional devices could not be fabricated. We conclude that performing a selective and electronically non-disruptive chemical reaction between a cyanine chromophore and the accompanying counter anion remains an interesting but challenging task.

In this chapter, all synthesis of Cy-FN3 and Cy-N3 were performed by the author (see Chapter 2). Synthesis of Cy3-T was carried out by Anna Véron (Empa). All experiments regarding absorbance, fluorescence, infrared (IR) and cyclic voltammetry (CV) were carried out by the author. All device fabrication and characterization regarding absorbance variation during device operation, photovoltaic behavior, transient current and luminance measurements were performed by the author. NMR measurements and spectra analysis were performed by the author and Daniel Rentsch (Empa).

## 5.2 Experimental

### 5.2.1 Materials

Cy-FN3 (Cy3-FN3, Cy5-FN3 and Cy7-FN3), Cy-N3 (Cy3-N3 and Cy5-N3) and Cy3-T (Cy3 with  $\Delta$ -TRISPHAT as a counter anion) were prepared in our laboratory (**Figure 5-1**), 1-ethyl-2-[3-(1-ethyl-3,3-dimethyl-1,3-dihydro-indol-2-ylidene)-propenyl]-3,3-dimethyl-3H-indolium hexafluorophosphate (Cy3-PF<sub>6</sub>, FEW Chemicals), 2,2,3,3-tetrafluoro-1-propanol (TFP, Aldrich), acetonitrile (ACN, Sigma-Aldrich), silver (Ag, Cerac), poly(3,4-ethylenedioxythiophene):poly(styrene sulfonate) (PEDOT, Clevios P VP Al 4083), tris-(8-hydroxyquinoline)aluminum (Alq<sub>3</sub>, Aldrich), poly(ethylene oxide) (PEG, Mv~400000, Aldrich), gallium-indium eutectic (EGaln, Aldrich).

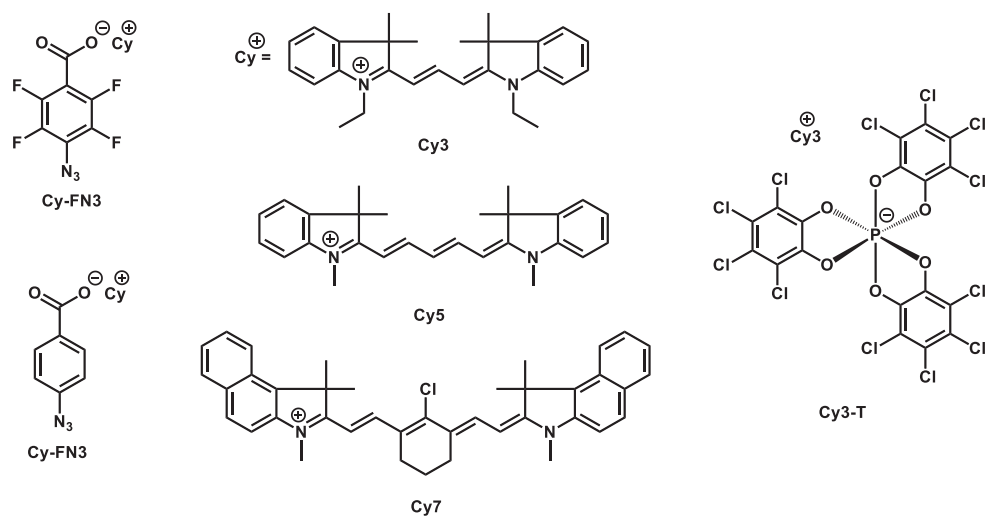


**Figure 5-1:** Chemical structures of Cy-FN3, Cy-N3 and Cy3-T.

## 5.2.2 Methods

NMR spectra were recorded on a Bruker 400 MHz spectrometer. Absorbance spectra were measured on a Varian Cary 50 UV-Vis spectrophotometer. PL spectra were measured on a Horiba Jobin Yvon Fluorolog spectrometer. Cyanine films were coated from ACN or TFP solutions on cleaned glass substrates and were then stored in inert atmosphere in the dark. Na-N<sub>3</sub> films were coated from PEG/water solution since pure Na-N<sub>3</sub> aqueous solution did not form homogeneous films. Absorbance and PL spectra were recorded for freshly coated films, stored films for different time at RT or elevated temperatures, or for irradiated films using UV or visible light. Both absorbance and PL measurements were carried out in air. Each sample was taken out of the inert atmosphere and measured only once. A new film was used for subsequent measurements. To study the effect of thermal metal evaporation on cyanine films, absorbance and PL spectra were recorded before and after 1 h irradiation from a glowing evaporation boat in the vacuum chamber. Attenuated total reflection IR (ATR-IR) spectra were recorded on a Bruker TENSOR 27 FT-IR spectrometer. To investigate IR spectra's variations in the films during storage or upon light irradiation, thick cyanine films (> 200 nm) coated on glass substrates were used as samples and measured before and after treatment. UV irradiation was performed using a medium-pressure Hg lamp (Heraeus Noblelight) with an efficient spectral range between 200 nm to 300 nm and a power density of ~100 W/cm<sup>2</sup>. White light irradiation was performed using a 300 W Xe light source. Optical filters were used to block light below 400 nm or 610 nm, resulting in visible light irradiation without UV

content. Monochromatic light irradiation was performed using a 150 W Xe lamp equipped with a monochromator. The monochromatic light intensities were measured using a calibrated Si-diode: 3.32 W/m<sup>2</sup> (at 580 nm), 2.54 W/m<sup>2</sup> (at 680 nm) and 0.53 W/m<sup>2</sup> (at 880 nm). Elemental analysis was carried out by the micro-laboratory of ETH Zürich. Ion chromatography analysis was carried out on a Metrohm 883 Basic IC plus. Electrospray ionization mass spectroscopy (ESI-MS) was carried out on a Waters Xevo TQD. CV measurements were performed on a PGSTAT 30 potentiostat (Autolab) using a standard three electrodes system with Au as working electrode, Pt as counter electrode and Ag/AgCl as reference electrode. 0.1 M DMF solution of tetrabutyl ammonium chloride and tetrabutyl ammonium perchlorate was used for inner and outer chamber, respectively. The concentration of dyes was ~0.4 mM for Cy3-N3 and ~0.6 mM for Cy3-PF6. The ferrocene/ferrocenium (Fc/Fc<sup>+</sup>) redox couple was used as internal reference.

## 5.3 Results

### 5.3.1 Decarboxylation of fluorobenzoate anion

As observed from <sup>19</sup>F NMR spectra (see 5.7 Supporting Information), 4-azido-2,3,5,6-tetrafluorobenzoate anions degraded partially (1-5%) already during synthesis.

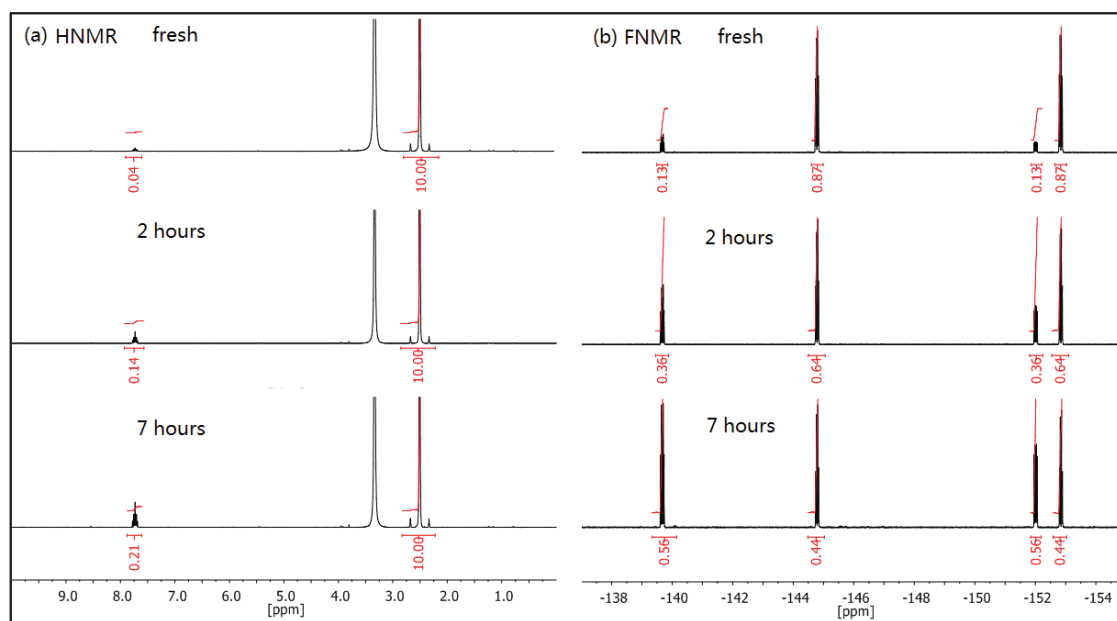


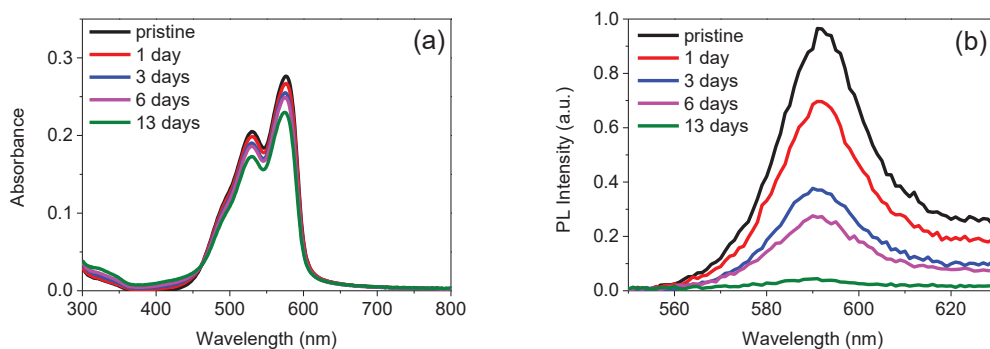
**Figure 5-2:** (a) <sup>1</sup>H and (b) <sup>19</sup>F NMR spectra of Na-FN3 in DMSO-d<sub>6</sub> measured freshly, 2 hours or 7 hours after sample preparation.

From **Figure 5-2**, it can be clearly seen that Na-FN3 is not stable when dissolved in DMSO. In  $^1\text{H}$  NMR spectra, a proton signal appeared at 7.7 ppm and increased with time. Simultaneously, fluorine signals at -152.9 and -144.8 ppm decreased and increased at -152.0 and -139.7 ppm, respectively. These results suggest that the carboxylate group was substituted by a proton, yielding 3-azido-1,2,4,5-tetrafluorobenzene as the main product. A similar decarboxylation reaction was reported for perfluorobenzoate ions.<sup>19,20</sup>

We note that 13% perfluorobenzoate anions were degraded already in a freshly prepared sample. Since the initial 1-5% degradation of anions originated from synthesis, it can be concluded that  $\sim 10\%$  benzoate anions decarboxylated rapidly within the first  $\sim 10$  min (time for NMR sample preparation). Apparently, this reaction became slower over time, generating 36% and 56% decarboxylated product after storage in DMSO for 2 and 7 hours, respectively.

Decarboxylation was also observed for Cy3-FN3 and Cy5 associated with pentafluorobenzoate in DMSO solutions. In these cases,  $^1\text{H}$  NMR spectra showed that both the polymethine chain and side groups of cyanines were chemically attacked. From this, we can conclude that the proton required for decarboxylation was partially abstracted from cyanine chromophores. However, Cy-FN3 were stable in MeOH solution and NMR spectra did not change over 14 days.

### 5.3.2 Thermal stability of Cy-FN3 and Cy-N3 films



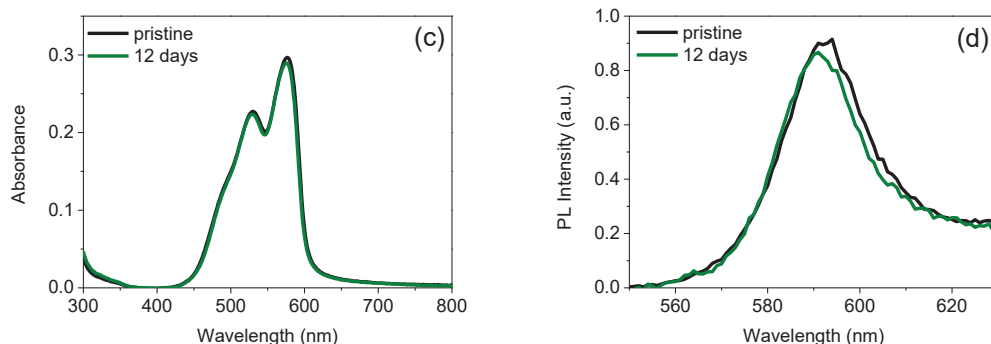


**Figure 5-3:** Absorbance and PL spectra of (a, b) Cy3-FN3 and (c, d) Cy3-N3 thin films coated from ACN and stored in the dark at RT in N<sub>2</sub>.

Cy3-FN3 films showed a continuous absorbance decrease and PL quenching over time (**Figure 5-3a** and **3b**). Over a period of 13 days, the maximum absorbance at 576 nm dropped by ~17% and PL was completely quenched. Similar trends were observed for Cy3-FN3 films coated from TFP. However, <sup>19</sup>F NMR spectra of stored and re-dissolved films were superimposable with the original spectra. ATR-IR spectra of Cy3-FN3 films also remained unchanged after 21 days storage (see 5.7 Supporting Information). From this we conclude that decomposition of Cy3-FN3 films is occurring, however, only to a small extent. Degradation cannot be followed with NMR or IR spectroscopy, but can be tracked with optical spectroscopy. These are very sensitive methods, and small amounts of impurities can quench the PL already substantially.

On the other hand, no trends in absorbance and PL were observed for Cy3-N3 films (**Figure 5-3c** and **3d**), which means that Cy3-N3 films are stable at RT. Also, no change was found in <sup>1</sup>H NMR spectra for Cy3-N3 compounds stored at -25 °C for 2 months. We therefore conclude that no decarboxylation occurred during storage.

Absorbance and PL spectra of Cy3-N3 films stored at elevated temperatures in the dark in N<sub>2</sub> were investigated. At 50 °C, no change was observed in absorbance spectra. However, PL was continuously quenched over time and ~70% PL quenching was detected after storage for 8 h. When heated at 70 °C, both absorbance decrease and PL quenching was found for Cy3-N3 films. We observed that a complete PL quenching occurred after 5 h, accompanied with a ~16% drop of the maximum absorbance at 576 nm (see 5.7 Supporting Information).

### 5.3.3 Visible light induced decomposition of phenyl azide

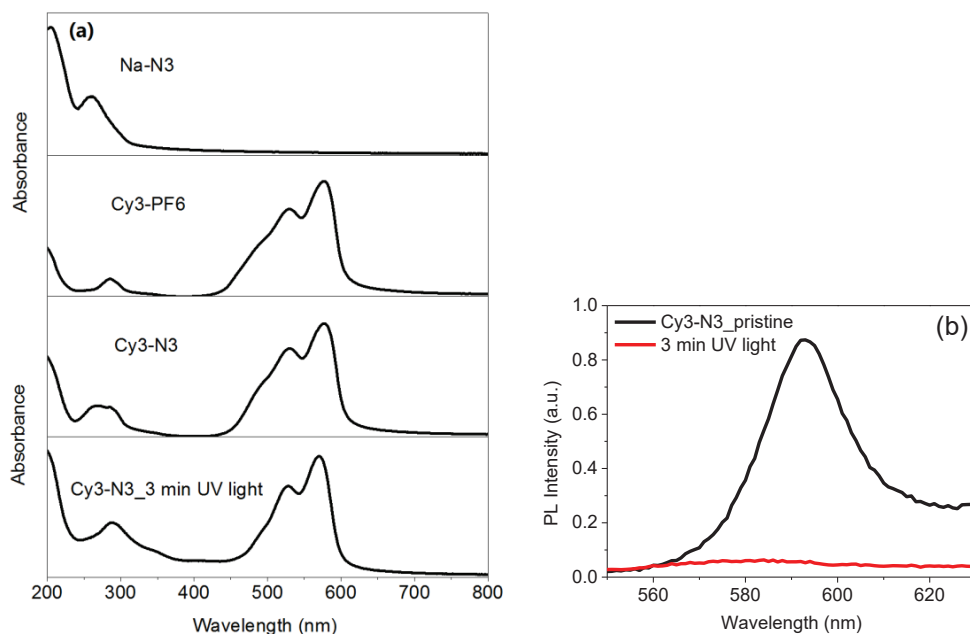


**Figure 5-4:** (a) Absorbance spectra of pristine Na-N3, Cy3-PF6, Cy3-N3 films and irradiated Cy3-N3 film using UV light and (b) PL spectra of Cy3-N3 films before and after UV light irradiation.

Phenyl azides absorb UV light and decompose by expelling  $N_2$ . This generates reactive nitrene intermediates, which can undergo a wide variety of chemical reactions.<sup>13,21,22,23-25</sup> The maximum UV absorption of phenyl azides is usually in the range of 250 nm to 280 nm, depending on the exact chemical structure.<sup>21,26</sup> As can be seen from **Figure 5-4a**, the azide signal of Na-N3 film appears at ~265 nm and Cy3-PF6 absorbs predominately between 450 – 600 nm. Besides, a second absorbance band in Cy3-PF6 film is observed at ~285 nm. Therefore, the broad absorbance between 250 nm and 300 nm in Cy3-N3 film comprises two apparently overlapping signals, which are attributed to the presence of both 4-azido benzoate anions and Cy3 chromophores. Clearly, the azide signal at ~265 nm Cy3-N3 samples disappeared upon UV light irradiation. A full PL quenching was observed in UV light irradiated Cy3-N3 film (**Figure 5-4b**).

We found that the azide partially decomposed already during the process of thermal evaporation of the top electrode (Ag or Al) onto Cy3-N3 films. Small absorbance changes (~3% at 576 nm) and pronounced PL quenching (~50%) was observed for Cy3-N3 films after thermal evaporation (see 5.7 Supporting Information). The temperature at the position of the

film substrate was below 40 °C, and therefore the decomposition cannot be thermally induced. We speculated that the light emission from the glowing evaporation boat induced photodecomposition of the azide. The effect of light with different wavelengths on the azide photolysis was investigated. Surprisingly, illumination in the wavelength range (400 – 610 nm) where the Cy3 chromophore absorbs induced a decomposition of the 4-azido benzoate anion. ATR-IR measurements showed that the intensity of azide signal<sup>13</sup> at  $\sim 2114\text{ cm}^{-1}$  reduced considerably during visible light irradiation of Cy3-N3 films (**Figure 5-5**). Since a very thick film was required for ATR-IR measurement to obtain well-resolved signals, the bottom part of the film was not irradiated efficiently, but was detected by the ATR crystal during the measurement. This explains the remaining azide signal after irradiation. We note that Cy3-N3 only decomposed during visible irradiation when coated as a film. In Cy3-N3/ACN solutions, the azide group was stable (see 5.7 Supporting Information).

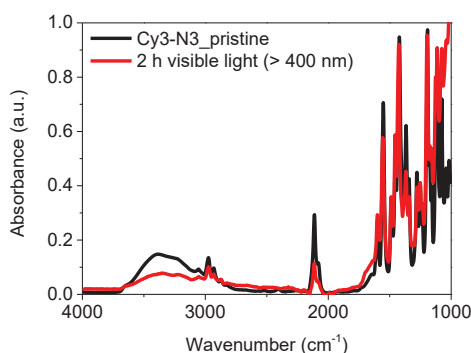


**Figure 5-5:** ATR-IR spectra of Cy3-N3 films before and after 2 h visible light (> 400 nm) irradiation.

For light-emitting electrochemical cells (LECs) of the structure ITO/PEDOT/Cy5-N3/Alq<sub>3</sub>/Ag, however, we observed a pronounced decrease of absorbance induced by the flowing current during biasing. Although not studied in further detail, this can indicate that both the oxidation and reduction leads also to the dissociation of the azide group.<sup>27</sup>

## 5.4 Discussion

### 5.4.1 Decarboxylation of 4-azido-2,3,5,6-tetrafluoro benzoate

In contrast to the statement that “perfluorophenyl azides can be stored under ambient conditions in the dark until use”<sup>14</sup>, our results demonstrate a distinct instability of a trimethine

cyanine (Cy3) associated with the 4-azido-2,3,5,6-tetrafluoro benzoate counter anion. The fluorinated anion can be stabilized in protic solvents, but decomposes rapidly over 1 day in aprotic solvents via a decarboxylation reaction to yield 3-azido-1,2,4,5-tetrafluorobenzene. When stored as a powder or coated as a film, the decarboxylation of Cy3-FN3 still occurs. The decomposition reaction is thermally activated and ~3% anions degraded during a storage period of 5 months at 4 °C. It was reported<sup>19</sup> that unless stabilized by an excess of free acid, pentafluorobenzoate anions undergo decarboxylation in aprotic solvents, e.g. CHCl<sub>3</sub>, ACN and DMSO. This may explain the initial degradation of Cy-FN3 during synthesis since DCM or CHCl<sub>3</sub> was used for the solvent extraction step. In DMSO, decarboxylation was also observed for Cy5 combined with pentafluorobenzoate, which indicates that the azide group is not required for this reaction. ATR-IR measurements demonstrated that the azide group was still present in fully decarboxylated Cy7-FN3 after storage in ACN for 23 h (see 5.7 Supporting Information). As a detrimental additional effect we observed a full PL quenching already in films with less than 20% degraded cyanine dye (**Figure 5-3a** and **3b**).

It has been found<sup>20</sup> that decarboxylation of pentafluorobenzoic acid is much faster than of tetrafluorobenzoic acid. In our case, the non-fluorinated azido benzoate anion was more stable than the fluorinated benzoate anion. The decarboxylation reaction did not occur and films could be stored under inert atmosphere at ambient temperature over 12 days without chemical degradation.

#### 5.4.2 Visible light sensitization of 4-azido benzoate

The long wavelength absorption edge of the 4-azido benzoate anion is at ~300 nm in solution and at ~320 nm in the film. Photoirradiation with UV light expels N<sub>2</sub> and yields the singlet nitrene as the key intermediate.<sup>28</sup> In our case, we measured the decrease of the IR absorption of the azide group<sup>13</sup> at ~2114 cm<sup>-1</sup> and observed the complete azide decomposition when irradiating a 30 nm thick Cy3-N3 film for 3 min by UV light. Irradiation induced a ~40% decrease of the absorbance of the Cy3 chromophore. This means that the nitrene does not selectively react via insertion reactions at the cyanine side groups (the desired reaction) but to a considerable extent reacts at chemical sites of the cyanine core that form the conjugated electron system. The PL of UV irradiated films was completely quenched (**Figure 5-4b**), suggesting that efficient exciton quenchers were generated from the nitrene-cyanine reactions. This is different from Ref. [18] where the nitrene-mediated



photocrosslinking of semiconducting polymers was dominated by alkyl side chain reactions, which did not degrade the semiconductor properties and consequently did not quench the PL.

A ~400 nm thick Cy3-N3 film was irradiated with UV light for 5 min and was then re-dissolved in methanol-d<sub>4</sub>. <sup>1</sup>H NMR measurements were carried out to determine possible reaction products resulting from the azide decomposition. Results indicated that protons belonging to polymethine, phenyl and alkyl groups were converted to a similar extent (~3% - 5%), suggesting that reactive nitrene intermediates underwent reactions in a very non-selective manner. However, the azide decomposition was not accompanied by decarboxylation since the splitting of proton signals belonging to benzoate anions did not change.

Unexpectedly, we observed that the 4-azido benzoate anion in Cy3-N3 films could also be photosensitized in the presence of visible light only. Visible photosensitization was not effective for Na-N3 or Cy3-N3 dissolved in water and ACN, respectively. Also no decomposition was observed when a film of Na-N3 dispersed in PEG was irradiated with visible light (see 5.7 Supporting Information). From this we conclude that Cy3 photoexcitation by visible light sensitizes the azide decomposition, enabled due to the close proximity of the dye and the counter anion in the film.

Several possible mechanisms were considered whereby the azide anion could quench photoexcited Cy3. First, there is no overlap between the Cy3 fluorescence (at ~590 nm) and the 4-azido benzoate anion absorption and therefore a long-range Förster transfer can be ruled out. Although azides can quench donor singlet states<sup>32</sup>, we also rule out an Cy3\* (S1 at ~2.1 eV) → N3\* (S1 at ~4.1 eV) exchange energy transfer in our case because this reaction is strongly endothermic.

The possibility of an electron transfer reaction must be considered. This could occur either from excited Cy3\* to the lowest unoccupied molecular orbital (LUMO) of 4-azido benzoate, or via an electron transfer from the highest occupied molecular orbital (HOMO) of 4-azido benzoate to the lowest singly occupied orbital of Cy3\*. We measured cyclic voltammetry to access the relevant redox levels (**Figure 5-6**).

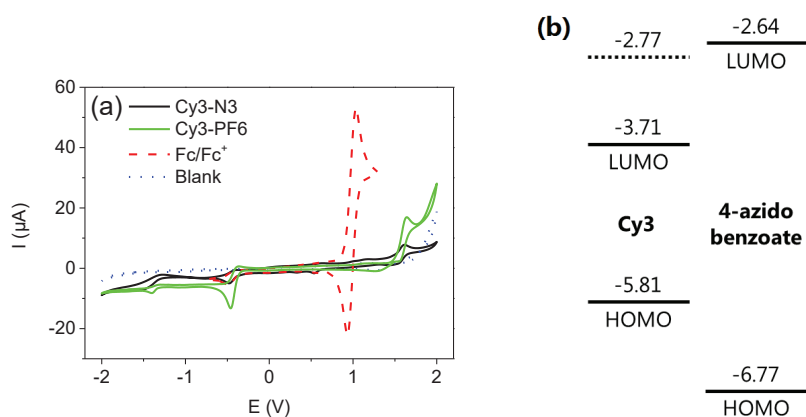


**Figure 5-6:** (a) CV spectra of Cy3-N3, Cy3-PF6 and Fc/Fc<sup>+</sup>, (b) frontier energy levels of Cy3 and 4-azido benzoate anion.

As an approximation of the formal potential of the redox couples, half-wave potentials  $E_{1/2} = \frac{1}{2}(E_{pc} + E_{pa})$  were evaluated, with the cathodic and anodic peak potentials,  $E_{pc}$  and  $E_{pa}$ .  $E_{1/2}$  for Fc/Fc<sup>+</sup> was 0.98 V against the Ag/AgCl reference electrode. The first half-wave reduction potential for both Cy3-N3 and Cy3-PF6 was  $E_{1/2,red} = -1.39$  V against Fc/Fc<sup>+</sup> (**Figure 5-6**). Assuming that  $E_{1/2,red}$  corresponds to the LUMO level of Cy3, and with an energy level of -5.10 eV vs. vacuum for Fc/Fc<sup>+</sup><sup>30</sup>, the redox level of Cy3 (LUMO) vs. vacuum can be calculated to be 3.71 eV. For Cy3-PF6 we measure a second half-wave reduction potential at  $E_{1/2,red} = -2.33$  V against Fc/Fc<sup>+</sup> (-2.77 eV vs. vacuum). For Cy3-N3 this second apparent half-wave reduction potential is slightly shifted (by -0.07 V) and probably presents the overlap between cyanine and the LUMO energy of 4-azido benzoate. To estimate the HOMO energy level we subtracted the optical bandgap for Cy3 and 4-azido benzoate from the corresponding LUMO levels (**Figure 5-6**).

From data shown in Ref. [18] for ethylene bis(4-azido-2,3,5-trifluoro-6-isopropylbenzoate), the HOMO can be estimated at  $\sim 7.7$  eV and the LUMO at  $\sim 2.2$  eV below vacuum. Using cyclic voltammetry, for phenyl azide an oxidation potential of 1.74 V relative to a saturated calomel electrode was reported.<sup>27</sup> From this value the HOMO level of phenyl azide at  $\sim 6.48$  eV below vacuum can be obtained, assuming that the energy level of SCE is situated at -4.74 eV below vacuum.<sup>18</sup> These values are in good agreement with our values for 4-azido benzoate. Importantly, the azide redox energy levels are outside those of Cy3, and both a reductive and oxidative electron transfer reaction between photoexcited Cy3\* and 4-azido benzoate can be ruled out.

Based on the above discussion we rule out singlet energy transfer and electron transfer reactions to be the reason for the observed visible photosensitization of 4-azido benzoate by Cy3. We propose that azide decomposition is triggered via a triplet energy transfer process; this involves intersystem crossing of  $\text{Cy3}^{\text{S1}*} \rightarrow \text{Cy3}^{\text{T1}*}$ , followed by energy transfer to the azide  $\text{N3}^{\text{S0}} \rightarrow \text{N3}^{\text{T1}*}$ . In a following step,  $\text{N3}^{\text{T1}*}$  expels  $\text{N}_2$  and produces a chemically reactive triplet nitrene. The proposed mechanism is summarized in **Figure 5-7**.

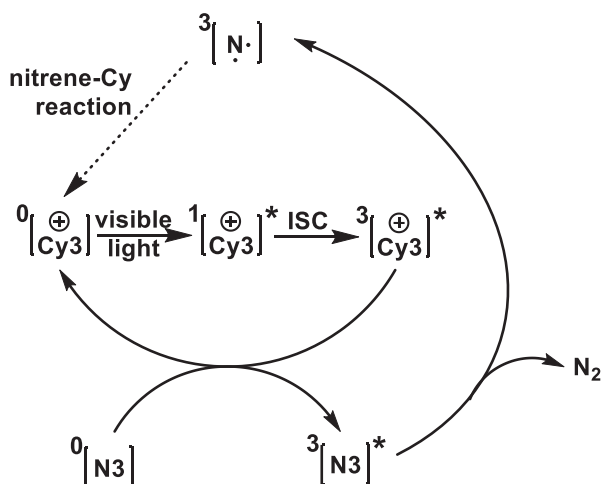


**Figure 5-7:** Schematic mechanism of sensitized azide photodecomposition via triplet energy transfer.

Conclusive evidence for a triplet energy transfer mechanism would involve, for example, first measuring the triplet energy levels of  $\text{Cy3}^{\text{T1}*}$  and  $\text{N3}^{\text{T1}*}$ , and in a second step correlating the quenching rate of  $\text{Cy3}^{\text{T1}*}$  with the formation rate of  $\text{N3}^{\text{T1}*}$  in Cy3-N3 films under visible irradiation. The problem with this approach is that both triplet states are not easily accessible by spectroscopy. In the following we summarize the main processes occurring after photoexcitation of cyanines and azides.

### 5.4.3 Photorelaxation of cyanine dyes

The photophysics and photochemistry of cyanine dyes has been intensively studied. Despite the large structural variety of cyanines, a simplified general picture of the photorelaxation can be formulated. Excited all-trans cyanines can be deactivated via fluorescence, internal conversion, intersystem crossing to the triplet state and trans-cis photoisomerization. In solution of low viscosity and for non-hindered monomers of cyanines with no heavy atoms – either directly attached to the dye chromophore, present as counter anion or as part of the

solvent – the quantum yield of fluorescence is small and often negligibly small for intersystem crossing, and the trans-cis photoisomerization presents a major deactivation pathway. When the temperature is lowered, the isomerization is hindered and the yields of fluorescence and triplet formation increase.<sup>31-33</sup>

Due to the low quantum yield of intersystem crossing, the cyanine triplet state energy has been measured in only a few cases. For a series of monomers and singly covalently linked trimethine indo- and thiocarbocyanines, the S1-T1 gap is ~0.5 eV.<sup>32</sup> From the onset of the phosphorescence spectra at ~720 nm, a T1 energy of 1.72 eV is obtained.<sup>32</sup> For a structurally related trimethine cyanine, the S1-T1 gap was ~0.4 eV and the T1 energy is at ~1.77 eV.<sup>34</sup>

Of relevance to this work is the photorelaxation of cyanines in thin films and in the presence of non-inert counter anions. First, the fluorescence of a pristine trimethine cyanine film decayed on the order of tens of ps<sup>35</sup> with a quantum yield below 1%.<sup>5</sup> This poor yield means that cyanines present an efficient self-quenching mechanism of their fluorescence, because the fluorescence increased strongly as cyanines were diluted into a polymer matrix.<sup>36</sup> It was speculated that cyanine dimer/aggregate formation possibly acted as non-radiative quenching centers.<sup>36</sup> In cyanine films, the photoisomerization seems to be inhibited.<sup>37,38</sup> Likewise, the intersystem crossing yield in the film is low and was at most 0.02 for a monomethine cyanine in thin films of polyvinyl alcohol.<sup>39</sup> By chemically bonding iodine to the chromophore, the maximum triplet yield could be increased to 0.25.<sup>39</sup> A similar heavy-atom effect was observed for benzene solution of cyanine with I<sup>-</sup> as the counter anion; irradiation generated the triplet state and the heavy-atom-induced intersystem crossing was possible, because the dye iodide in benzene exists almost exclusively as an ion pair.<sup>40</sup>

Another deactivation channel for excited cyanines can be opened via an intra-ion pair electron transfer. In one example the photoexcitation of cyanines was followed by an electron transfer from the iodide anion to the excited cyanine leading to the formation of a radical.<sup>41</sup> In several examples, a similar electron transfer has been studied for borate anions. Borate anions can reduce excited cyanines in the film<sup>37,42</sup> or in non-polar solvents, where the cyanine borate exists predominantly as an ion pair.<sup>38,43</sup> Alkyl-substituted borates undergo further carbon-boron cleavage upon oxidation. The free alkyl radicals thus formed may be used for the initiation of polymerization reactions, noteworthy triggered by light absorption of the cyanine in the visible range.

#### 5.4.4 Photolysis of azides

Directly photoexcited azides expel rapidly  $N_2$  and the singlet nitrene is formed. Singlet nitrenes chemically react by ring expansion, insertion and cycloaddition reactions. For aromatic azides, it has been found that the introduction of halogen atoms on the phenyl ring suppresses the ring expansion reactions of singlet nitrenes and favours the insertion reactions.<sup>14,21,44</sup>

Alternatively, singlet nitrenes can intersystem cross to the triplet nitrenes, which react predominantly via H-abstraction reactions or dimerize to the azo compounds. Intersystem crossing from the singlet to the triplet nitrene is a barrier-less process.<sup>15,45</sup> Therefore, thermally activated chemical reactions of the singlet nitrene at lower temperature are relatively suppressed and intersystem crossing is favoured.

The triplet state of arylazides,  $Ph-N_3^{T1*}$ , can efficiently be populated by energy transfer. This occurs, for example in phenacylazides, where photoexcitation produces the triplet state of the keto group, that via an intramolecular energy transfer populates the excited azide triplet state that splits off  $N_2$  to yield  $Ph-N^{T1}$  as reactive intermediate.<sup>13,15</sup> Triplet-sensitized photoreactivity was also demonstrated for a vinylazide containing an acetophenone group.<sup>46</sup>

Alternatively, azide triplet states can be populated by intermolecular energy transfer via triplet sensitizers.<sup>27,28,47-49</sup> Triplet-triplet energy transfer was typically achieved by irradiation of a sensitizer with UV light. Recently, useful photosensitizers that absorb in the visible range of the spectrum have been demonstrated. Visible sensitizing light is attractive because often more complex organic molecules are prone to decomposition when irradiated with UV light. The most commonly used visible light photocatalysts are polypyridyl complexes of ruthenium and iridium. For example, the complex tris(2,2'-bipyridine)ruthenium(II) ( $Ru(bpy)_3^{2+}$ ) absorbs light in the visible and undergoes rapid intersystem crossing to the triplet state with a long lifetime of 1.1  $\mu s$ .  $Ru(bpy)_3^{2+}$  emits at  $\lambda_{max} = 615$  nm from its lowest triplet energy level at 2.03 eV.<sup>50</sup> The long lifetime of the excited state is a prerequisite for energy transfer reactions in solution because too short lifetimes do not allow an efficient diffusive encounter between the sensitizer and quencher at experimentally achievable concentrations. Transition-metal complexes have been used for the visible light triplet sensitization of vinyl azides.<sup>51</sup> Benzoyl azides were used for the direct C-H amidation of heteroarenes in the presence of acid,

$\text{Ru}(\text{bpy})_3^{2+}$  and visible light.<sup>52</sup> Triplet energy transfer was possible because of the favourable T1 energy ( $\sim 1.78$  eV) of benzoyl azides.

Azide triplet energy levels have been calculated in a number of cases. Alternatively, the triplet energy can be estimated from sensitization experiments; as long as the triplet energy of the sensitizer is greater than that of the acceptor, the energy transfer should occur at the diffusion-controlled rate. When the energy transfer is endothermic a rapid fall off is expected. For alkyl azides, T1 is between 3.25 – 3.47 eV;<sup>49,53</sup> for two vinyl azides, T1 = 1.97 eV and 2.25 eV, respectively;<sup>51</sup> for an azidonaphthalene, T1 = 2.69 eV;<sup>51</sup> for phenyl azide, T1 = 2.95 eV.<sup>27</sup>

Interestingly, it has been observed that sensitizers with lower triplet energies were considerably more effective than expected for a classical endothermic energy transfer.<sup>27,29,48,49,53</sup> It has been suggested that the molecules are more stable with a bent than a linear configuration of the azide group in the first excited state. The effective energy transfer was then best explained by vertical excitation of a vibrationally excited bent azide ground state to a low-energy bent excited state.

#### 5.4.5 Quenching of cyanine triplets by 4-azido benzoate

From the published data discussed above, we can estimate the triplet energy levels to  $\text{Cy3}^{\text{T1}^*} \approx 1.75$  eV, and 4-azido benzoate<sup>T1\*</sup>  $\approx 2.5 - 3$  eV. This means that also in our case energy transfer is taking place despite that the process is endothermic. We performed two experiments to support our explanation of the visible-light induced azide decomposition in Cy3-N3 films.

Although the individual efficiencies of the processes shown in **Figure 5-7** are not precisely known, it is clear that the overall efficiency of the reaction sequence " $\text{Cy3}^{\text{S1}^*} \rightarrow \text{N}^{\text{T1}} \rightarrow$  chemical reactions" must be small. This is because of the low intersystem crossing efficiency  $\text{Cy3}^{\text{S1}^*} \rightarrow \text{Cy3}^{\text{T1}^*}$  ( $\Phi_{\text{isc}} < 0.01$ ); in addition the quantum yield for the dinitrogen loss from triplet excited phenyl azide is only  $\sim 0.5$ .<sup>49</sup> We irradiated 50 nm thick Cy3-N3 films with monochromatic light of  $3.32 \text{ W/m}^2$  at 580 nm and measured the decrease of the cyanine film absorbance over time. As we have explained above the full azide decomposition induced a decrease of the cyanine absorbance by  $\sim 40\%$ ; therefore, this spectral change is a measure for the number of produced triplet nitrenes. From the known number of absorbed photons and the number of converted molecules we could calculate the overall efficiency of the photodecomposition

reaction sequence to be in the range of  $1-5 \times 10^{-4}$ . This number is considerably smaller than the combined efficiencies of the cyanine intersystem crossing and triplet nitrene production and therefore not inconsistent with the proposed reaction mechanism.

Overall, the endothermic triplet energy transfer process  $\text{Cy3}^{\text{T1}^*} \rightarrow \text{N3}^{\text{T1}^*}$  is rather inefficient. We figured that the process can be suppressed completely for increased cyanine-azide triplet-triplet energy gaps. Therefore, we synthesized penta- (Cy5) and heptamethine (Cy7) cyanines with the anions 4-azido benzoate and 2,3,5,6-tetrafluoro-4-azido benzoate, respectively. Cy5 and Cy7 absorb at longer wavelengths than Cy3 (**Figure 5-8**). For a pentamethine cyanine delayed fluorescence and phosphorescence was observed.<sup>54</sup> The delayed fluorescence was emitted from the S1 state of trans-cyanine via a thermally activated reverse intersystem crossing from the cis-triplet state to the trans-S1 state. The energy difference between the S1 and T1 states of trans-cyanine was about 0.24 eV ( $T1 = 1.60$  eV).<sup>54</sup> Thin films of Cy3-N3, Cy5-N3 and Cy7-FN3 were irradiated with monochromatic light at the maxima of the absorbance spectra for 1h (**Figure 5-8**). Absorbance spectra taken before and after irradiation showed the decomposition of Cy3 but films of Cy5 and Cy7 remained unaffected. This shows that for penta- and heptamethine cyanine the proposed triplet energy transfer reaction is suppressed.

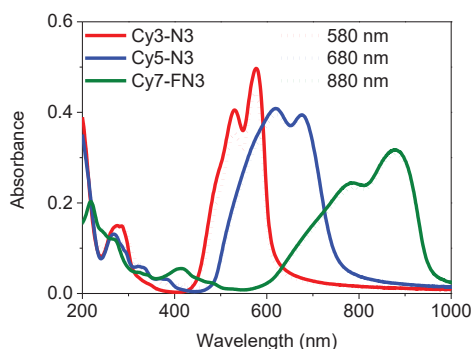


**Figure 5-8:** Absorbance spectra for Cy3-N3, Cy5-N3 and Cy7-FN3 films before (solid lines) and after (dotted lines) monochromatic light irradiation for 1 h.

## 5.5 Conclusions

Our results demonstrate the pronounced degradation tendency of cyanine/4-azido benzoate films that is triggered by heat, electric charges and light, both in the UV and visible range. The concept of displacing the anions first in a thin film, followed by nitrene-mediated

chemical fixation by a UV light trigger was therefore not applicable and all our attempts to fabricate functional LECs and organic photovoltaic (OPV) cells failed. Regardless of the azide reactivity, decarboxylation of the fluorinated benzoate anion resulted in considerable PL quenching in the film. The devices employing Cy-FN3 as active materials were therefore not successful. Further, we demonstrated that the nitrene intermediate upon azide decomposition in the films reacted quite non-selectively with cyanine dye chromophores, destroying the polymethine group and forming very effective exciton quencher. For LECs, no luminance was detected in a device based on Cy3-N3. The most detrimental effect is the finding that already small amounts of azide decomposition resulted in a pronounced PL quenching. If the azides could have been selectively fixed in the p-doped region after device turn-on, light-emission from the intrinsic region could still take place. Devices containing trimethine cyanines with a bulky  $\Delta$ -TRISPHAT ion as counter anion (Cy3-T) and Cy3-N3 blends were fabricated and operated, aiming at moving the relatively small and mobile 4-azido benzoate anion prior to its decomposition in the intrinsic region. The PL quenching, however, was severe and occurred already during evaporation of the metal top electrode in the vacuum chamber, induced by the light emitted by the glowing metal evaporation boat. Hence, several attempts focusing on deposition of a back electrode without light irradiation were carried out. Ag/polydimethylsiloxane (PDMS) or ITO/PEDOT was applied as alternative electrodes via lamination process, which resulted in poor contact between the laminated electrodes and the active materials and consequently irreproducible device performance in LECs. Another attempt was given to spray-coating of silver nanowires (AgNWs) in the dark. However, it was found that the sprayed organic solvents dissolved the cyanine active layers. The use of eutectic gallium-indium (EGaln) as metal electrode was investigated. LEC devices exhibited a typical transient current response during operation under a constant voltage, but no luminance was observed. As found before, this might be attributed to the decomposition of phenyl azides induced by the flowing current during biasing.

To chemically fix ionic junctions in organic electronic devices, an important prerequisite is that the chemical reaction proceeds in a desired manner, which produces harmless products that do not degrade the semiconducting properties. Besides, no degradation of materials should occur during storage under ambient conditions and the chemical fixation should take place solely by specific triggers, which do not include ambient light and temperature. Ideally,



chemical reactions for immobilizing the ions are performed in a highly selective way, which generates a characteristic product and does not yield side products.

## 5.6 References

- [1] J. Leger, M. Berggren, S. Carter, *Iontronics: Ionic Carriers in Organic Electronic Materials and Devices* CRC Press, **2011**.
- [2] H. Benmansour, F. A. Castro, M. Nagel, J. Heier, R. Hany, F. Nüesch, ionic space charge driven organic photovoltaic devices, *Chimia* **2007**, 61, 787-791.
- [3] M. Lenes, H. J. Bolink, ionic space-charge effects in solid state organic photovoltaics, *ACS Appl. Mater. Interfaces* **2010**, 2, 3664-3668.
- [4] S. Jenatsch, L. Wang, M. Bulloni, A. C. Véron, B. Ruhstaller, S. Altazin, F. Nüesch, R. Hany, doping evolution and junction formation in stacked cyanine dye light-emitting electrochemical cells, *ACS Appl. Mater. Interfaces* **2016**, 8, 6554-6562.
- [5] A. Pertegás, D. Tordera, J. J. Serrano-Pérez, E. Ortí, H. J. Bolink, light-emitting electrochemical cells using cyanine dyes as the active components, *J. Am. Chem. Soc.* **2013**, 135, 18008-18011.
- [6] J. Gao, G. Yu, A. J. Heeger, polymer light-emitting electrochemical cells with frozen p-i-n junction, *Appl. Phys. Lett.* **1997**, 71, 1293-1295.
- [7] C. H. W. Cheng, M. C. Lonergan, a conjugated polymer pn junction, *J. Am. Chem. Soc.* **2004**, 126, 10536-10537.
- [8] J. M. Leger, D. B. Rodovsky, G. P. Bartholomew, self-assembled, chemically fixed homojunctions in semiconducting polymers, *Adv. Mater.* **2006**, 18, 3130-3134.
- [9] I. V. Kosilkin, M. S. Martens, M. P. Murphy, J. M. Leger, polymerizable ionic liquids for fixed-junction polymer light-emitting electrochemical cells, *Chem. Mater.* **2010**, 22, 4838-4840.
- [10] S. Tang, K. Irgum, L. Edman, chemical stabilization of doping in conjugated polymers, *Org. Electronics* **2010**, 11, 1079-1087.
- [11] C. V. Hoven, H. Wang, M. Elbing, L. Garner, D. Winkelhaus, G. C. Bazan, chemically fixed p-n heterojunctions for polymer electronics by means of covalent B-F bond formation, *Nature Mater.* **2010**, 9, 249-252.

- [12] J. M. Leger, D. G. Patel, D. B. Rodovsky, G. P. Bartholomew, polymer photovoltaic devices employing a chemically fixed p-i-n junction, *Adv. Funct. Mater.* **2008**, 18, 1212-1219.
- [13] S. Bräse, G. Gil, K. Knepper, V. Zimmermann, organic azides: an exploding diversity of a unique class of compounds, *Angew. Chem. Int. Ed.* **2005**, 44, 5188-5240.
- [14] L. H. Liu, M. Yan, perfluorophenyl azides: new applications in surface functionalization and nanomaterial synthesis, *Acc. Chem. Res.* **2010**, 43, 1434-1443.
- [15] S. Bräse, K. Banert, *organic azides: syntheses and application* **2010**.
- [16] J. W. Rumer, R. S. Ashraf, N. D. Eisenmenger, Z. Huang, I. Meager, C. B. Nielsen, B. C. Schroeder, M. L. Chabiny, I. McCulloch, dual function additives: a small molecule crosslinker for enhanced efficiency and stability in organic solar cells, *Adv. Energy Mater.* **2015**, 5, 1401426.
- [17] L. Derue, O. Dautel, A. Tournebize, M. Drees, H. Pan, S. Berthumeyrie, B. Pavageau, E. Cloutet, S. Chambon, L. Hirsch, A. Rivaton, P. Hudhomme, A. Facchetti, G. Wantz, thermal stabilisation of polymer-fullerene bulk heterojunction morphology for efficient photovoltaic solar cells, *Adv. Mater.* **2014**, 26, 5831-5838.
- [18] R. Q. Png, P. J. Chia, J. C. Tang, B. Liu, S. Sivaramakrishnan, M. Zhou, S. H. Khong, H. S. O. Chan, J. H. Burroughes, L. L. Chua, R. H. Friend, P. K. H. Ho, high-performance polymer semiconducting heterostructure devices by nitrene-mediated photocrosslinking of alkyl side chains, *Nature Mater.* **2010**, 9, 152-158.
- [19] B. Brycki, B. Brzezinski, E. Grech, interaction of 1,8-bis(dimethylamino)naphthalene with pentafluorobenzoic acid in [<sup>2</sup>H<sub>3</sub>] acetonitrile, *J. Chem. Soc. Perkin Trans. 2*, **1991**, 1209-1211.
- [20] B. Gierczyk, G. Wojciechowski, B. Brzezinski, E. Grech, G. Schroeder, study of the decarboxylation mechanism of fluorobenzoic acids by strong N-bases, *J. Phys. Org. Chem.* **2001**, 14, 691-696.
- [21] J. F. W. Keana, S. X. Cai, new reagents for photoaffinity labeling: synthesis and photolysis of functionalized perfluorophenyl azides, *J. Org. Chem.* **1990**, 55, 3640-3647.
- [22] O. Norberg, L. Deng, M. Yan, O. Ramström, photo-click immobilization of carbohydrates on polymeric surfaces-a quick method to functionalize surfaces for biomolecular recognition studies, *Bioconjugate Chem.* **2009**, 20, 2364-2370.
- [23] R. Belloli, nitrenes, *J. Chem. Educ.* **1971**, 48, 422-426.

- [24] G. L'abbe, decomposition and addition reactions of organic azides, *Chem. Rev.* **1969**, 69, 345-363.
- [25] R. A. Abramovitch, E. P. Kyba, chapter 5: decomposition of organic azides, *the azido group (1971)*.
- [26] J. F. W. Keana, S. X. Cai, functionalized perfluorophenyl azides: new reagents for photoaffinity labeling, *J. Fluorine Chem.* **1983**, 43, 151-154.
- [27] L. J. Leyshon, A. Reiser, sensitized photodecomposition of phenyl azide and  $\alpha$ -naphthyl azide, *J. Chem. Soc. Faraday Trans. 2*, **1972**, 68, 1918-1927.
- [28] F. D. Lewis, W. H. Saunders, the intermediates in direct photolysis of alkyl azides, *J. Am. Chem. Soc.* **1968**, 90, 7031-7033.
- [29] F. D. Lewis, J. C. Dalton, quenching of aromatic hydrocarbon singlets by alkyl azides, *J. Am. Chem. Soc.* **1969**, 91, 5260-5263.
- [30] C. M. Cardona, W. Li, A. E. Kaifer, D. Stockdale, G. C. Bazan, electrochemical considerations for determining absolute frontier orbital energy levels of conjugated polymers for solar cell applications, *Adv. Mater.* **2011**, 23, 2367-2371.
- [31] A. K. Chibisov, triplet states of cyanine dyes and reactions of electron transfer with their participation, *J. Photochemistry*, **1976-1977**, 6, 199-214.
- [32] A. K. Chibisov, G. V. Zakharova, H. Goerner, Y. A. Sogulyaev, I. L. Mushkalo, A. I. Tolmahev, photorelaxation processes in covalently linked indocarbocyanine and thiocarbocyanine dyes, *J. Phys. Chem.* **1995**, 99, 886-893.
- [33] A. K. Chibisov, S. V. Shvedov, H. Görner, photosensitized processes in dicarbocyanine dyes induced by energy transfer: delayed fluorescence, trans  $\rightarrow$  cis isomerization and electron transfer, *J. Photochem. Photobiol. A* **2001**, 141, 39-45.
- [34] K. Jia, Y. Wan, A. Xia, S. Li, F. Gong, G. Yang, characterization of photoinduced isomerization and intersystem crossing of the cyanine dye Cy3, *J. Phys. Chem. A* **2007**, 111, 1593-1597.
- [35] A. Devižis, J. D. Jonghe-Risse, R. hany, F. Nüesch, S. Jenatsch, V. Gulbinas, J. Moser, dissociation of charge transfer states and carrier separation in bilayer organic solar cells: a time-resolved electroabsorption spectroscopy study, *J. Am. Chem. Soc.* **2015**, 137, 8192-8198.

- [36] F. A. Castro, H. Benmansour, J. Moser, C. F. O. Graeff, F. Nüesch, R. Hany, photoinduced hole-transfer in semiconducting polymer/low-bandgap cyanine dye blends: evidence for unit charge separation quantum yield, *Phys. Chem. Chem. Phys.* **2009**, 11, 8886-8894.
- [37] J. D. Jonghe-Risse, J. Heier, F. Nüesch, J. Moser, ultrafast charge transfer in solid-state films of pristine cyanine borate and blends with fullerene, *J. Mater. Chem. A* **2015**, 3, 10935-10941.
- [38] S. Chatterjee, P. D. Davis, P. Gottschalk, M. E. Kurz, B. Sauerwein, X. Yang, G. B. Schuster, photochemistry of carbocyanine alkyltriphenylborate salts: intra-ion-pair electron transfer and the chemistry of boranyl radicals, *J. Am. Chem. Soc.* **1990**, 112, 6329-6338.
- [39] A. V. Buettner, radiationless transitions in cyanine dyes, *J. Chem. Phys.* **1967**, 46, 1398-1401.
- [40] B. Sauerwein, G. B. Schuster, external iodine atoms influence over the intersystem crossing rate of a cyanine iodide ion pair in benzene solution, *J. Phys. Chem.* **1991**, 1903-1906.
- [41] A. K. Pandey, P. C. Deakin, R. D. J. Vuuren, P. L. Burn, I. D. W. Samuel, photo-rechargeable battery effect in first generation cationic-cyanine dendrimers, *Adv. Mater.* **2010**, 3954-3958.
- [42] M. C. Etter, B. N. Holmes, R. B. Kress, G. Filipoich, solid-state chemistry of cyanine-type dyes and the effect of two novel counterions on their crystal properties, *Isr. J. Chemistry* **1985**, 25, 264-273.
- [43] S. Chatterjee, P. Gottschalk, P. D. Davis, G. B. Schuster, electron-transfer reactions in cyanine borate ion pairs: photopolymerization initiators sensitive to visible light, *J. Am. Chem. Soc.* **1988**, 110, 2326-2328.
- [44] S. X. Cai, J. C. Nability, M. N. Wybourne, J. F. W. Keana, bis(perfluorophenyl)azides: efficient cross-linking agents for deep-UV and electron beam lithography, *Chem. Mater.* **1990**, 2, 631-633.
- [45] E. Leyva, M. S. Platz, G. Persy, J. Wirz, photochemistry of phenyl azide: the role of singlet and triplet phenylnitrene as transient intermediates, *J. Am. Chem. Soc.* **1986**, 108, 3783-3790.
- [46] S. Rajam, A. V. Jadhav, Q. Li, S. K. Sarkar, P. N. D. Singh, A. Rohr, T. C. S. Pace, R. Li, J. A. Krause, C. Bohne, B. S. Ault, A. D. Gudmundsdottir, triplet sensitized photolysis of a vinyl azide: direct detection of a triplet vinyl azide and nitrene, *J. Org. Chem.* **2014**, 79, 9325-9334.
- [47] O. L. Chapman, J. P. L. Roux, 1-aza-1,2,4,6-cycloheptatetraene, *J. Am. Chem. Soc.* **1978**, 100, 282-285.

[48] F. D. Lewis, W. H. Saunders, photosensitized rearrangements of triarylmethyl azides, *J. Am. Chem. Soc.* **1967**, 89, 645-647.

[49] F. D. Lewis, W. H. Saunders, sensitized photolysis of organic azides. possible case of nonclassical energy transfer, *J. Am. Chem. Soc.* **1968**, 90, 7033-7038.

[50] C. K. Prier, D. A. Rankic, D. W. C. MacMillan, visible light photoredox catalysis with transition metal complexes: applications in organic synthesis, *Chem. Rev.* **2013**, 113, 5322-5363.

[51] E. P. Farney, T. P. Yoon, visible-light sensitization of vinyl azides by transition-metal photocatalysis, *Angew. Chem. Int. Ed.* **2014**, 53, 793-797.

[52] E. Brachet, T. Ghosh, I. Ghosh, B. König, visible light C-H amidation of heteroarenes with benzoyl azides, *Chem. Sci.* **2015**, 6, 987-992.

[53] R. F. Klima, A. D. Gudmundsdóttir, intermolecular triplet-sensitized photolysis of alkyl azides trapping of triplet alkyl nitrenes, *J. Photochem. Photobiol. A* **2004**, 164, 239-247.

[54] Z. Huang, D. Ji, A. Xia, F. Koberling, M. Patting, R. Erdmann, direct observation of delayed fluorescence from a remarkable back-isomerization in Cy5, *J. Am. Chem. Soc.* **2005**, 127, 8064-8066.

## 5.7 Supporting Information

### 5.7.1 NMR measurements of stored Cy3-FN3 film

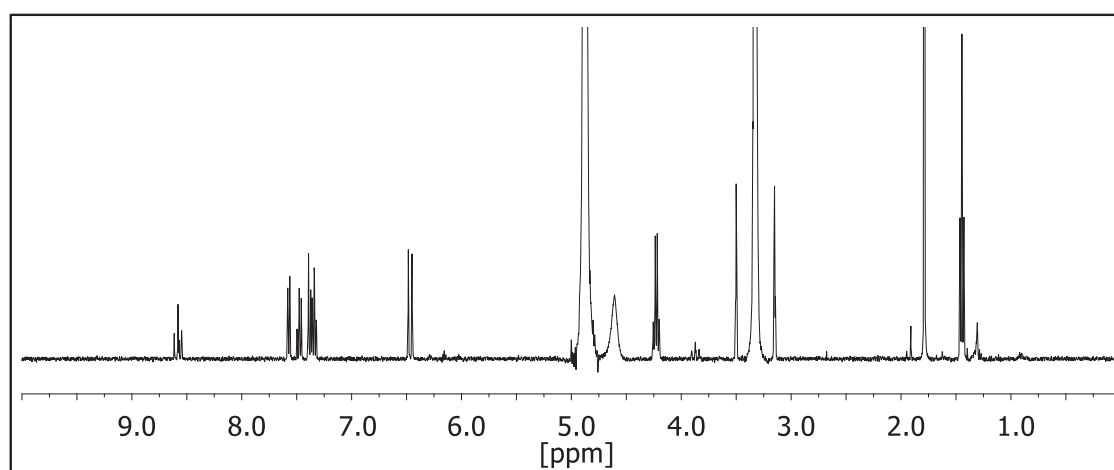


**Figure 5-9:** <sup>1</sup>H NMR spectrum of freshly coated Cy3-FN3 film from TFP (redissolved in methanol-d<sub>4</sub>).

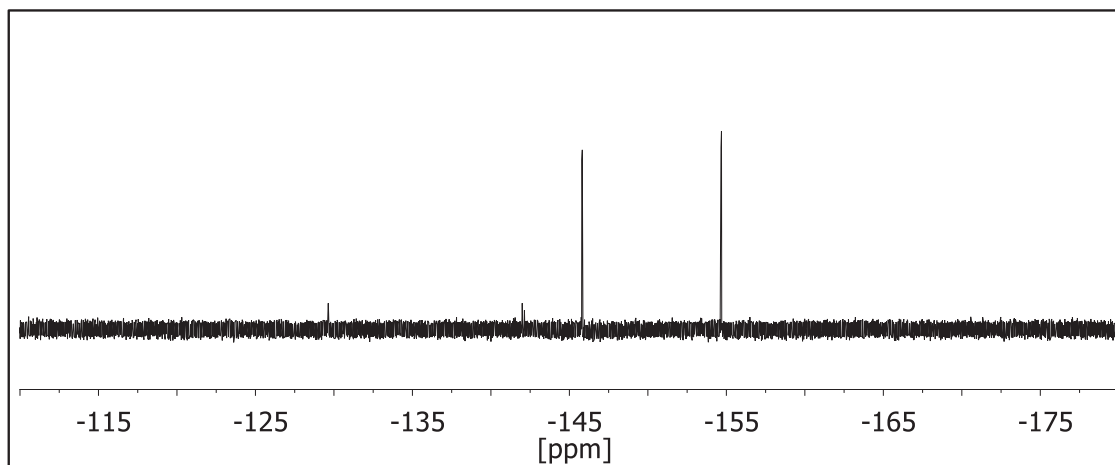


**Figure 5-10:**  $^{19}\text{F}$  NMR spectrum of freshly coated Cy3-FN3 film from TFP (redissolved in methanol- $\text{d}_4$ ).

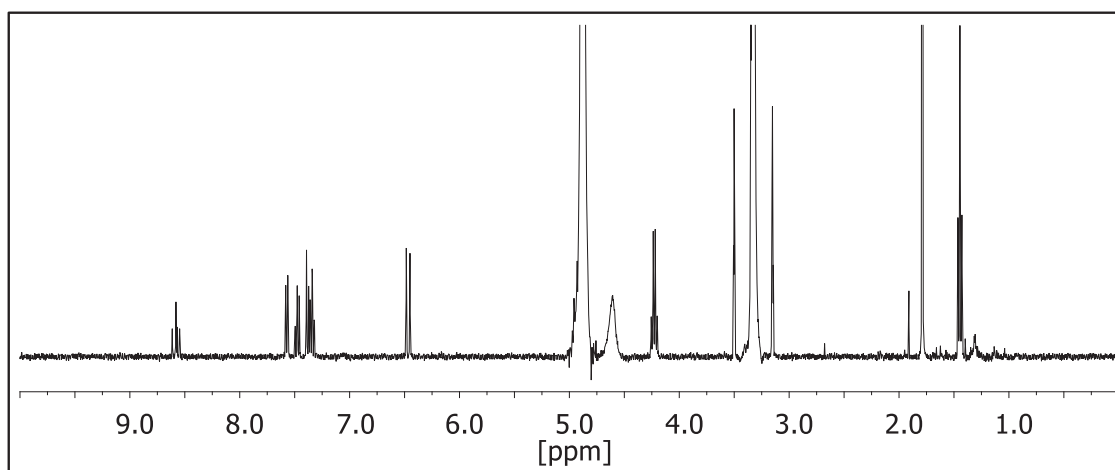


**Figure 5-11:**  $^1\text{H}$  NMR spectrum of 21 days stored Cy3-FN3 film (redissolved in methanol- $\text{d}_4$ ).

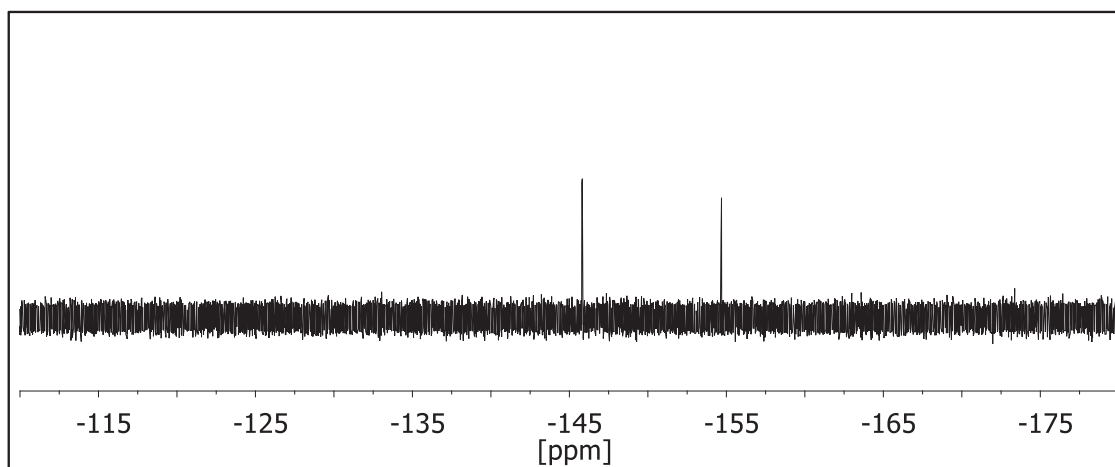


**Figure 5-12:**  $^{19}\text{F}$  NMR spectrum of 21 days stored Cy3-FN3 film (redissolved in methanol- $\text{d}_4$ ).

### 5.7.2 ATR-IR measurements

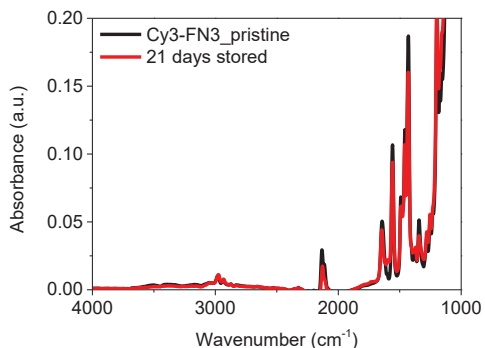


**Figure 5-13:** ATR-IR spectra of Cy3-FN3 films before and after 21 days storage in the dark at RT in N<sub>2</sub>.

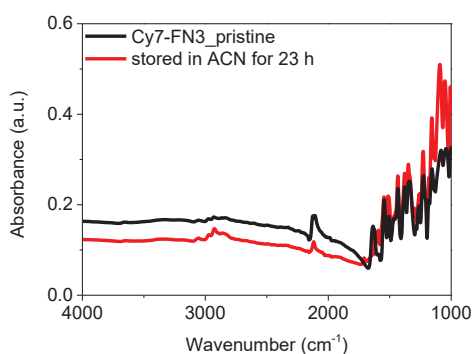


**Figure 5-14:** ATR-IR spectra of Cy7-FN3 before and after storage in ACN for 23 hours (ACN removed before measure).

### 5.7.3 Thermal stability of Cy3-N3 films at elevated temperatures

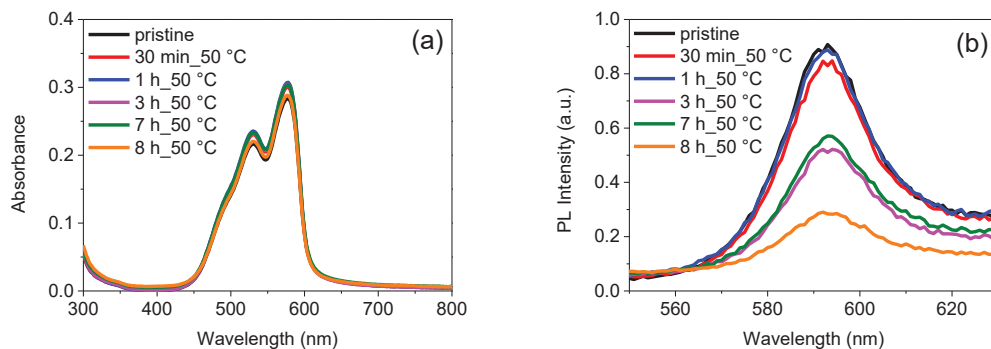


**Figure 5-15:** (a) Absorbance and (b) PL spectra of Cy3-N3 films after different time of heating at 50 °C in the dark in N<sub>2</sub>.

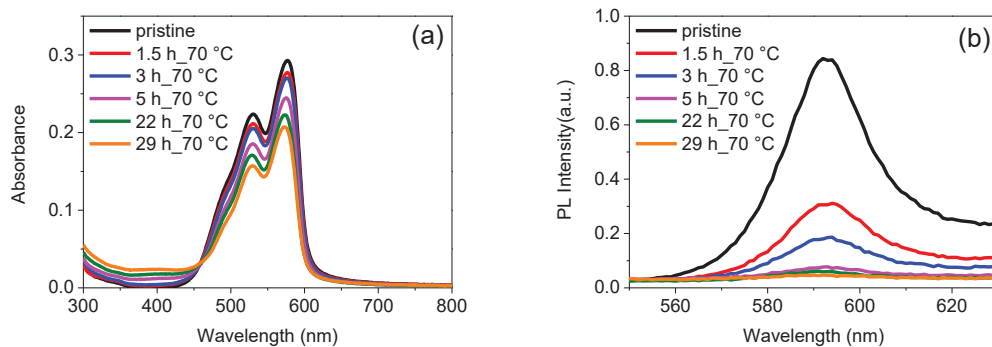


**Figure 5-16:** (a) Absorbance and (b) PL spectra of Cy3-N3 films after different time of heating at 70 °C in the dark in N<sub>2</sub>.

#### 5.7.4 Effect of thermal evaporation

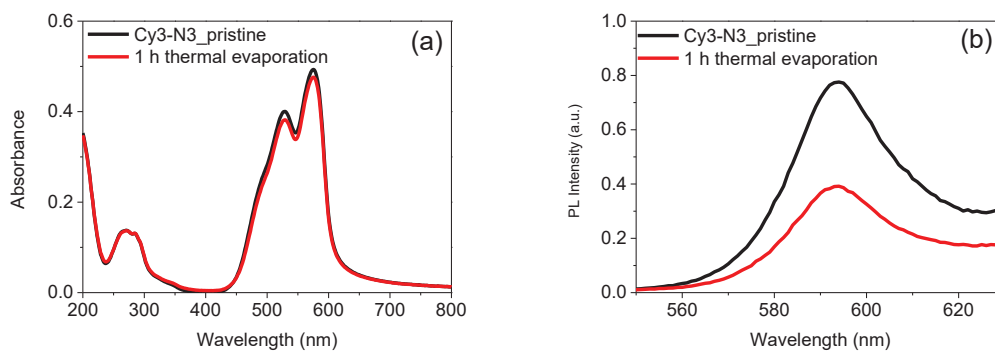


**Figure 5-17:** (a) Absorbance and (b) PL spectra of Cy3-N3 films before and after 1 h thermal evaporation.



### 5.7.5 White light irradiation on Na-N3 and Cy3-N3

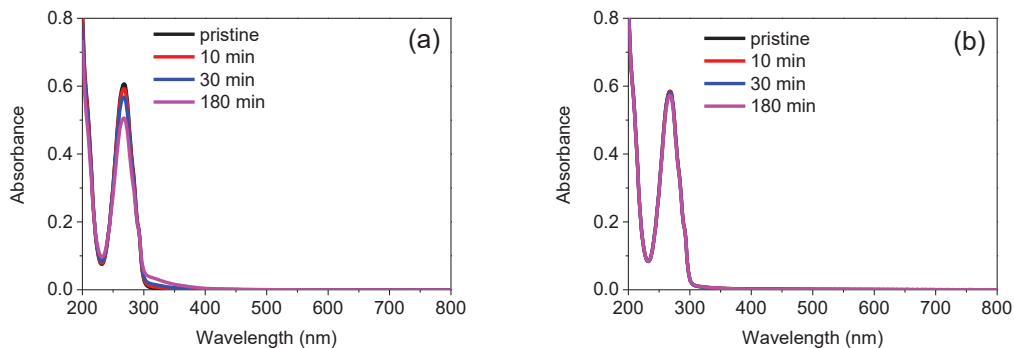


**Figure 5-18:** Absorbance spectra of Na-N3 aqueous solution over time for (a) white light or (b) visible light (> 400 nm) irradiation.

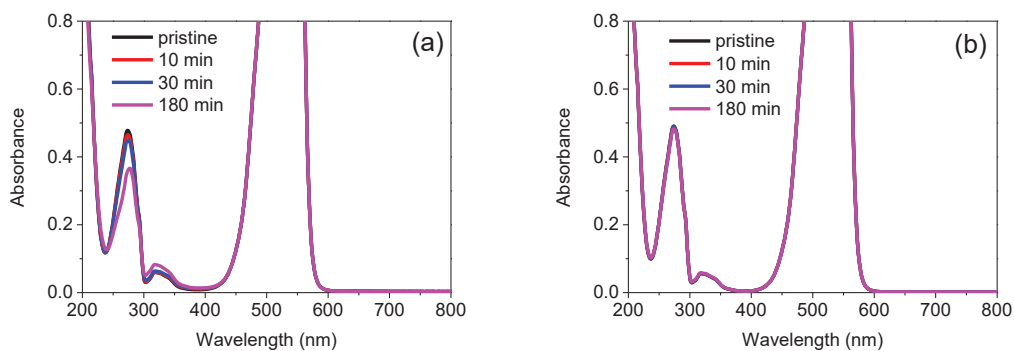


**Figure 5-19:** Absorbance spectra of Cy3-N3/ACN solution over time for (a) white light or (b) visible light (> 400 nm) irradiation.

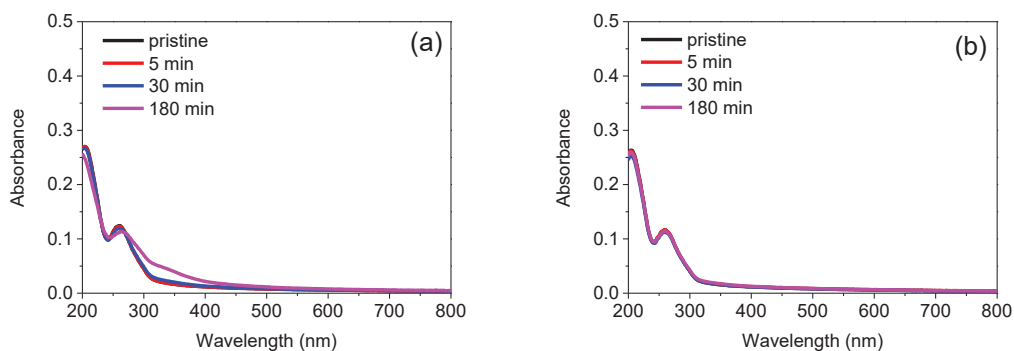


**Figure 5-20:** Absorbance spectra of Na-N3 films over time for (a) white light or (b) visible light (> 400 nm) irradiation.

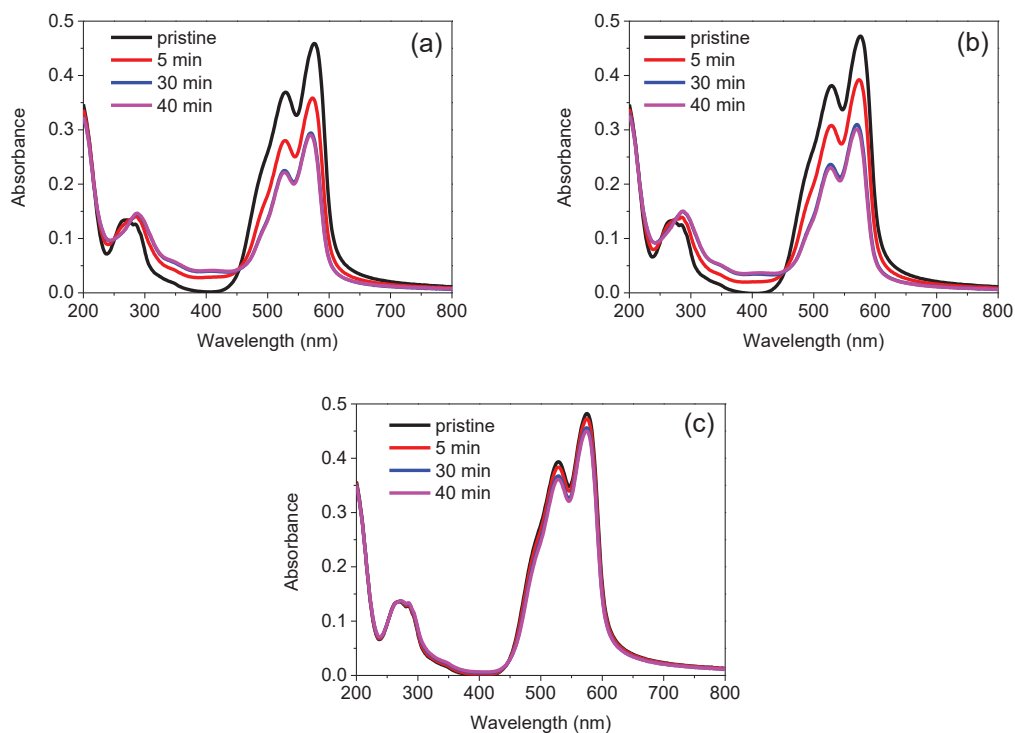


**Figure 5-21:** Absorbance spectra of Cy3-N3 films over time for (a) white light, (b) visible light (> 400 nm) or (c) visible light (> 610 nm) irradiation.

## Chapter 6: Cyanine Dye Polyelectrolytes for Organic Bilayer Heterojunction Solar Cells

### 6.1 Introduction

Polyelectrolytes contain a backbone with pendant groups capable of ionizing in high dielectric media. Their solubility in polar solvent allows fabrication of multilayer organic electronic devices by solution coating techniques in combination with neutral semiconducting materials that are soluble in orthogonal nonpolar solvents.<sup>1</sup>

The best-known polyelectrolyte for organic electronic device applications is probably poly(3,4-ethylenedioxythiophene):poly(styrene sulfonate) (PEDOT), that is coated as a thin film from a water suspension. PEDOT has widely been used as buffer layer on transparent conducting oxide electrodes in organic devices in which light enters or exits.<sup>2</sup>

Polyelectrolytes (and other highly polar polymers<sup>3,4</sup>) have been successfully used as interfacial layer materials in thin-film transistors,<sup>5</sup> organic light-emitting devices<sup>6</sup> and organic solar cells.<sup>7,8</sup> Polyelectrolytes as active layers have been applied in single-component light-emitting electrochemical cells<sup>9</sup> and light-emitting devices.<sup>10</sup>

A double-layer structure was fabricated by using a cationic polyelectrolyte with fluoride anions coated on top of a neutral polymer containing anion-trapping groups. Application of a bias leads to charge injection and fluoride displacement into the neutral layer, where covalent bond formation takes place. Thereby, a stable p-n rectifying heterojunction and fast-responding light-emitting electrochemical behavior was obtained.<sup>11</sup>

In a similar manner, ionic charge was exploited in cyanine dye organic solar cells. Cyanine dyes are charged semiconducting molecules that are accompanied by a counter anion. Therefore, cyanines have intrinsic built-in ionic and electronic charge conductivity. It has been demonstrated that the counter anions are relatively mobile and could be displaced within the cyanine layer and into adjacent layers. Thereby, ionic charge could be used to control the flow of electronic current.<sup>12,13</sup>

Cyanine dyes have a number of interesting property characteristics for organic solar cell applications, such as tunable redox levels and wavelengths of absorption,<sup>14</sup> very high light

extinction coefficients, aggregate formation that facilitates exciton transport and good film forming properties from organic solvents.<sup>15</sup>

Due to excessive phase separation resulting in coarse film morphology, efficient bulk heterojunction devices using blends of cyanines and soluble fullerenes could not be fabricated so far.<sup>14</sup> Regular bilayer electron donor cyanine/acceptor C<sub>60</sub> solar cells with power conversion efficiencies (PCE) of 2.9-3.6% have been demonstrated.<sup>16,17</sup> In these cases, the C<sub>60</sub> film was deposited by evaporation, because no orthogonal solvent for the soluble fullerene derivative [6,6]-phenyl-C<sub>61</sub>-butyric acid methyl ester (PCBM) exists that would leave the cyanine layer unaffected during the coating step.

Clean bilayer C<sub>60</sub> or PCBM/cyanine solar cells in the inverted geometry with PCE = 3.7% were also fabricated.<sup>18,19</sup> In contrast to the regular device architecture, in these cases the cyanines could be coated onto the underlying acceptor from polar alcohols, where the fullerenes are completely insoluble.

Here we demonstrate the first solution processed bilayer cyanine/PCBM regular solar cells. To this end, cyanine polyelectrolytes (Cy-Poly) were synthesized where the cationic dyes are electrostatically bound to an anionic polymer backbone. This is a different synthetic approach from the concept where the light-absorbing dye core constituted the polyelectrolyte backbone.<sup>20</sup> We describe the synthesis of the anionic polyelectrolyte backbone, followed by incorporation of the cyanine. The Cy-Poly showed a strongly decreased solubility in chlorinated solvents, which allowed the fabrication of solution-processed regular cyanine/PCBM solar cells. The optimization of solar cells is described and the low hole mobility in Cy-Poly films is identified as the main reason that currently limits the performance of these devices.

In this chapter, the results are mainly based on the following publication: "Cyanine dye polyelectrolytes for organic bilayer solar cells" by Lei Wang, Christian Hinderling, Sandra Jenatsch, Frank Nüesch, Daniel Rentsch, Roland Steim, Hui Zhang, Roland Hany, *Polymer*, **2014**, 55, 3195-3201. Characterization of Cy-Poly thin films, e.g. morphology, absorption and solubility study, were carried out by the author. Fabrication of all solar cell devices and characterization regarding J-V characteristics and IPCE measurements were performed by the author. Photo-CELIV measurements were carried out by Sandra Jenatsch (Empa).

## 6.2 Experimental

### 6.2.1 Materials and methods

All Cy-Poly (Cy5-Poly20, Cy5-Poly30, Cy5-Poly50, Cy5PEG25Poly50, Cy5-PEG50Poly50, Cy3-Poly20, Cy3-Poly30 and Cy3-Poly50) and Cy-MES (Cy5-MES and Cy3-MES) were synthesized in our laboratory (**Figure 6-1**, for Cy-Poly and Cy-MES synthesis, see Chapter 2). 2,2,3,3-tetrafluoro-1-propanol (TFP, Aldrich), chlorobenzene (CB, Sigma-Aldrich), molybdenum (VI) oxide ( $\text{MoO}_3$ , Aldrich), aluminum (Al, Lesker), calcium (Ca, CERAC), PCBM (Solenne, **Figure 6-1**).

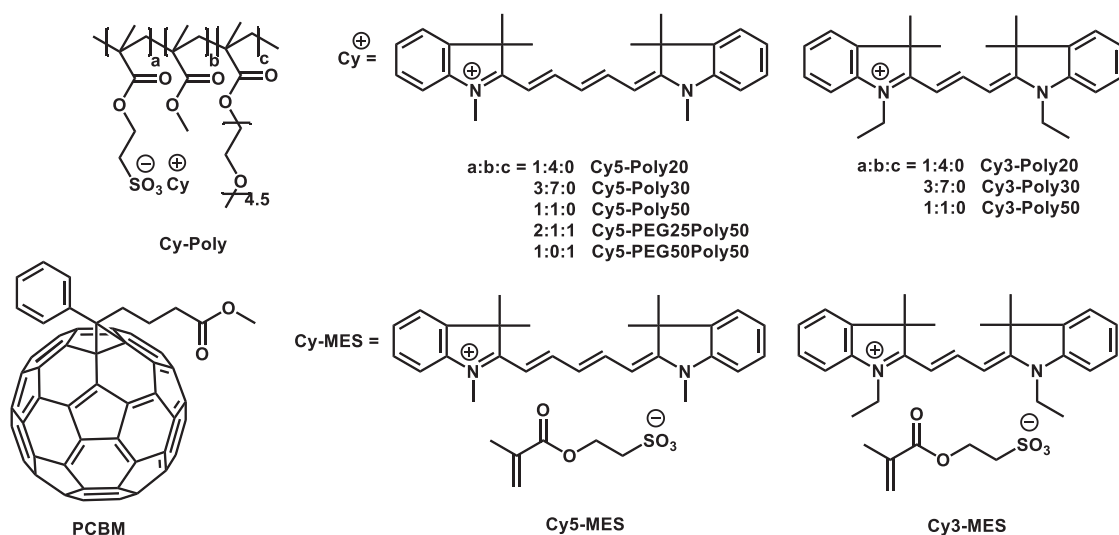


**Figure 6-1:** Chemical structures of Cy-Poly, Cy-MES and PCBM.

UV-Vis spectra were measured on a Varian Cary 50 Scan or using an integrating sphere on a Horiba Jobin Yvon Fluorolog. Charge mobilities were measured using the technique of photo-induced charge carrier extraction by a linearly increasing voltage (photo-CELIV). Measurements were carried out under  $\text{N}_2$  in a glove box with the commercial Paicos system, Fluxim AG. Cy5-Poly/PCBM solar cells were illuminated for 30  $\mu\text{s}$  using a blue LED (430-510 nm) and generated charge carriers were extracted by applying voltage ramps  $A$  ranging between 100 and 300  $\text{V ms}^{-1}$ . Hole mobilities  $\mu_{\text{Cy5}}$  were calculated using the modified formula<sup>21</sup> (**Eq. 6-1**)

$$\mu_{Cy5} = \frac{2d_{Cy5}(d_{Cy5} + d_{PCBM})}{3At_{max}^2} \cdot \frac{1}{(1 + 0.36 \frac{\Delta j}{j_0})} \quad (\text{Eq. 6-1})$$

where  $d_{Cy5}$  and  $d_{PCBM}$  are the layer thicknesses of Cy5-Poly and PCBM respectively,  $t_{max}$  is the peak position of the current,  $\Delta j$  is the peak height and  $j_0$  is the capacitive displacement current. We assumed equal dielectric constants for Cy5-Poly and PCBM, and the formula accounts for the fact that the voltage is applied over the whole organic layer thickness, but that holes are formed at the heterojunction and have to travel only through the Cy5-Poly layer.

### 6.2.2 Solar cell fabrication and characterization

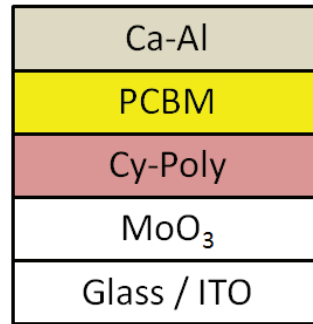


**Figure 6-2:** Schematic of device architecture for Cy-Poly/PCBM bilayer solar cells.

Solar cells were fabricated using a layer stack of ITO/MoO<sub>3</sub>/Cy-Poly/PCBM/(Ca)/Al (**Figure 6-2**). ITO coated glass substrates were successively cleaned by sonication in acetone, ethanol, detergent and de-ionized water. The hole transporting layer MoO<sub>3</sub> (10 nm) was deposited by thermal evaporation at a pressure below  $5 \cdot 10^{-6}$  mbar. Cy-Poly layers were spin coated from TFP solutions (1-5 mg/mL) inside a nitrogen-filled glove box (<1 ppm H<sub>2</sub>O, <6 ppm O<sub>2</sub>), followed by spin coating of PCBM on top from CB solutions (20-50 mg/mL). Devices were then completed by evaporating Al (35 nm) or Ca(8 nm)/Al cathodes through a shadow mask to define eight cells on each substrate with areas of 0.031 cm<sup>2</sup> or 0.071 cm<sup>2</sup>.

For characterization, solar cells were mounted under N<sub>2</sub> into an air-tight homemade transfer box and measured outside the glove box. Current-voltage (J-V) characteristics were measured using 100 mW cm<sup>-2</sup> simulated AM1.5G solar irradiation on a calibrated solar simulator from Spectra Nova. The incident photon-to-current conversion efficiency (IPCE) was measured using a monochromator and the light from a 300 W Xe lamp together with an AM1.5G filter set. The monochromatic light intensity was determined using a calibrated Si-diode. The

thickness of PCBM layers was measured by profilometry (Ambios XP1). ~40 nm thick Cy-Poly films were measured by profilometry and UV-Vis spectroscopy. The thickness of thinner Cy-Poly films as used in solar cells was then determined by comparing the absorptions at the wavelength maxima between thick and thin films. Surface morphology of Cy-Poly and PCBM films was investigated via AFM measurements on a Nanosurf Mobile S in tapping mode at a resonance frequency of 170 kHz using silicon cantilevers.

## 6.3 Results and Discussion

### 6.3.1 Characterization of Cy-Poly thin films

Cy-Poly with 20-50% cyanine content were soluble in polar solvents such as MeOH or TFP. For the non-polar solvent CB, we found a pronounced solubility dependence on the cyanine and PEG content in the polyelectrolytes. Thin films of Cy-Poly were spin coated from TFP solutions on glass substrates. In a next step, pure CB solvent was spin coated (4000 rpm, 60 s) onto these films. Film absorption spectra were measured before and after CB coating. The decrease of the maximum absorption is a measure of the Cy-Poly solubility in CB for experimental conditions that mimic the actual solar cell fabrication process, where a CB solution containing PCBM is coated onto the Cy-Poly films.

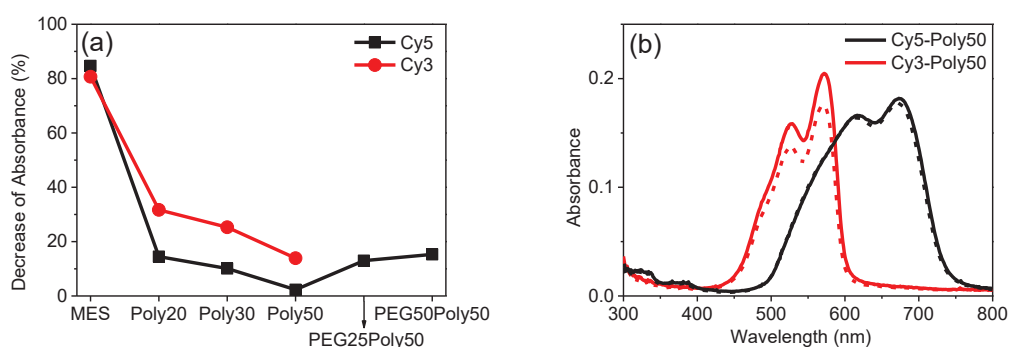


**Figure 6-3:** (a) Decrease of film absorption maxima after CB washing. (b) Absorption spectra of Cy5-Poly50 and Cy3-Poly50 films before (solid lines) and after (dotted lines) CB washing.

Results are shown in **Figure 6-3**. The solubility of the Cy-MES dye monomers in CB is high, and more than 80% of the film was removed during the spin coating process. With increasing cyanine content, the polyelectrolytes solubility decreased strongly, with Cy5-Poly being less soluble than Cy3-Poly. For Cy3-Poly50, 14% was dissolved during CB spin coating, and 2.3%

for Cy5-Poly50. Further, it was found that Cy5-Poly containing polyethylene glycol (PEG) segments and 50% cyanine content have an increased CB solubility with increasing PEG content. ~15% of Cy5-PEG25Poly50 or Cy5-PEG50Poly50 films were removed during the CB washing step.

For a solution-processed bilayer solar cell, the existence of an orthogonal second solvent that does not dissolve the underlying first active layer is essential. Excessive material removal eventually results in the formation of cracks and pinholes. The overlying material then penetrates and contacts both electrodes at the same time. These direct paths between anode and cathode act as a shunt resistance in parallel with the active part, resulting in a lowered open circuit voltage ( $V_{oc}$ ) and eroding the device efficiency partly.

The quality of spin coated Cy5-Poly30 (15 nm thick, from TFP) and Cy5-Poly30 (15 nm)/PCBM (40 nm, from CB) bilayer films was examined with optical microscopy, and both films appeared homogeneous and defect-free. The film surface topography was characterized with AFM. Again, both films were smooth and pinhole-free. For Cy5-Poly30, the root mean square (rms) roughness was 3.2 nm, for PCBM the rms roughness was 0.4 nm. Apparently, PCBM flattened the initial roughness of the polyelectrolyte film considerably, thereby providing a plane surface for deposition of the top electrode in organic solar cells.

Finally, the pure non-solvent CB was spin coated onto Cy5-Poly30 films to examine possible changes in the polyelectrolyte film topography during the actual solar cell fabrication process. AFM images revealed a slightly decreased rms roughness (2.1 nm) but no changes in the surface topography were observed.

### 6.3.2 Cy-Poly/PCBM bilayer solar cells

Cy-Poly/PCBM bilayer organic solar cells were fabricated with the architecture shown in **Figure 6-2**.  $\text{MoO}_3$  was used as the hole extracting buffer layer,<sup>14,16</sup> and Al or Ca/Al was the top electrode.<sup>22,23</sup> Using a 15 nm thick Cy5-Poly20 layer, the PCBM thickness (20 nm-50 nm) was optimized in a first step (**Figure 6-4**).



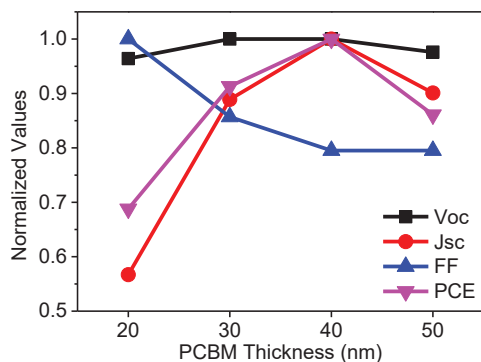


**Figure 6-4:** Effect of PCBM thickness on ITO/MoO<sub>3</sub>/Cy5-Poly20(15 nm)/PCBM/Al solar cells performance characteristics.

Open-circuit voltages ( $V_{oc} = 0.81 \pm 0.1$  V) were independent of the fullerene thickness, while fill factors ( $FF = 31 - 24\%$ ) decreased linearly when increasing the thickness from 20 nm to 50 nm. Short-circuit currents ( $J_{sc} = 1 - 1.7$  mA cm<sup>-2</sup>) and power conversion efficiencies ( $PCE = 0.25 - 0.34\%$ ) increased strongly with increasing PCBM thickness and reached maximum values for an acceptor thickness of 40 nm. This value corresponds to the exciton diffusion length of the structurally closely related C<sub>60</sub> molecule.<sup>24</sup> For small molecule cyanine dye/C<sub>60</sub> solar cells it has recently been shown that a C<sub>60</sub> thickness of 40 nm results in highest PCE values.<sup>16,18</sup>

For a PCBM film thickness fixed at 40 nm, the thickness of Cy5-Poly50 was optimized in a second step (**Figure 6-5**).

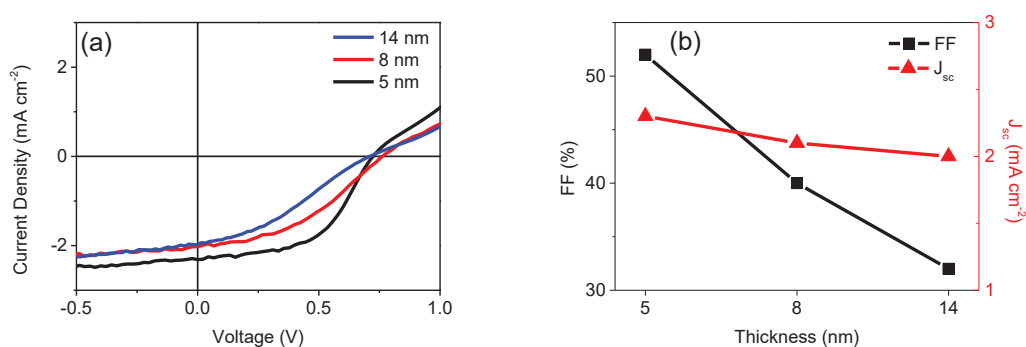


**Figure 6-5:** (a) J-V characteristics of ITO/MoO<sub>3</sub>/Cy5-Poly50/PCBM(40 nm)/Al solar cells with different Cy5-Poly50 thicknesses. (b) Fill factor (FF) and short circuit current ( $J_{sc}$ ) variation as function of Cy5-Poly50 thickness.

Donor layer thickness above ~10 nm resulted in poor FF (< 35%). FF and  $J_{sc}$  increased for thinner cyanine films, and when using an ultrathin Cy-Poly50 film of ~5 nm, FF = 52%,  $J_{sc}$  = 2.4 mA cm<sup>-2</sup>,  $V_{oc}$  = 0.74 V were measured, resulting in a PCE of 0.9%.

Cy5-Poly (without PEG segments) and Cy3-Poly solar cells with cyanine contents of 20%, 30% and 50% were then fabricated by spin coating thin donor layers from 2 mg mL<sup>-1</sup> TFP solutions. This resulted in film thicknesses between ~5 nm and 7.5 nm. For Cy5-Poly,  $V_{oc}$  = (0.72 ± 0.03) V was nearly independent of the cyanine content. In contrast,  $J_{sc}$  and FF clearly increased with increasing cyanine content. For Cy3-Poly cells, similar trends for  $J_{sc}$  and FF were observed. In addition, also higher  $V_{oc}$  values were measured with increasing cyanine content. Due to low  $J_{sc}$  values, Cy3-Poly cells performed considerably less than Cy5-Poly cells (**Table 6-1** and **Figure 6-6**).

**Table 6-1:** Device performance of ITO/MoO<sub>3</sub>/Cy-Poly/PCBM(40 nm)/Al solar cells.

Active layer material	Thickness (nm)	$V_{oc}$ (V)	$J_{sc}$ (mA cm <sup>-2</sup> )	FF (%)	PCE (%)
Cy5-Poly20	7.5	0.74	1.6	42	0.50
Cy5-Poly30	6.4	0.78	1.8	53	0.74
Cy5-Poly50	4.9	0.74	2.4	52	0.92
Cy5-Poly50 <sup>a</sup>	4.9	0.70-0.76	2.2-2.4	51-52	0.81-0.92
Cy3-Poly20	6.6	0.37	0.51	37	0.07
Cy3-Poly30	6.0	0.56	0.57	50	0.16
Cy3-Poly50	5.5	0.63	0.84	51	0.27

<sup>a</sup> Ranges of values from 8 solar cells.

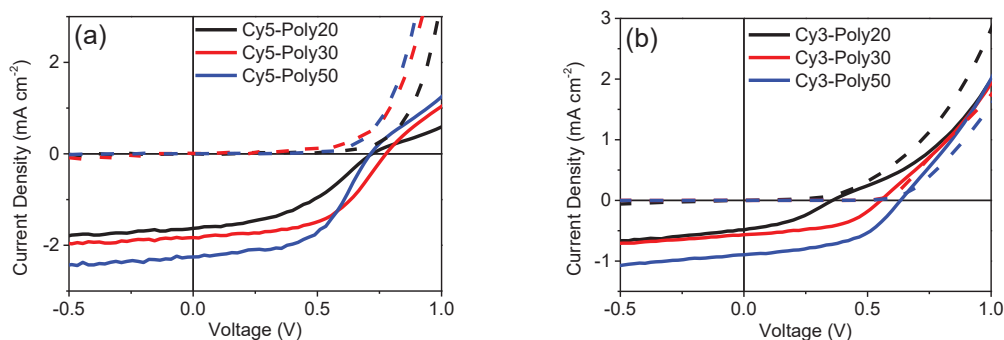


**Figure 6-6:** White light (solid lines) and dark (dotted lines) J-V characteristics of (a) ITO/MoO<sub>3</sub>/Cy5-Poly/PCBM(40 nm)/Al and (b) ITO/MoO<sub>3</sub>/Cy3-Poly/PCBM(40 nm)/Al solar cells.

For Cy5-Poly, absorbances of pure films at  $\lambda_{\max}$  (673 nm) with thicknesses from **Table 6-1** were  $0.078 \pm 0.002$ , for Cy3-Poly at 572 nm  $0.073 \pm 0.007$ . Assuming in a simple model that incident light is reflected by the aluminium cathode and penetrates the active layers twice, only a small (< 30%) fraction of the sunlight is absorbed by the cyanines. Inevitably, this results in small photocurrents, as we observed. IPCE curves of Cy5-Poly and Cy3-Poly cells are shown in **Figure 6-7**. In agreement with  $J_{sc}$  values from **Table 6-1**, IPCE values increase strongly for cyanine contents > 20% in the polyelectrolytes. This trend indicates that the charge generation and/or hole charge extraction yield is sensitively dependent on the cyanine content, since the amount of light absorption is rather similar amongst the Cy5-Poly and Cy3-Poly layers.

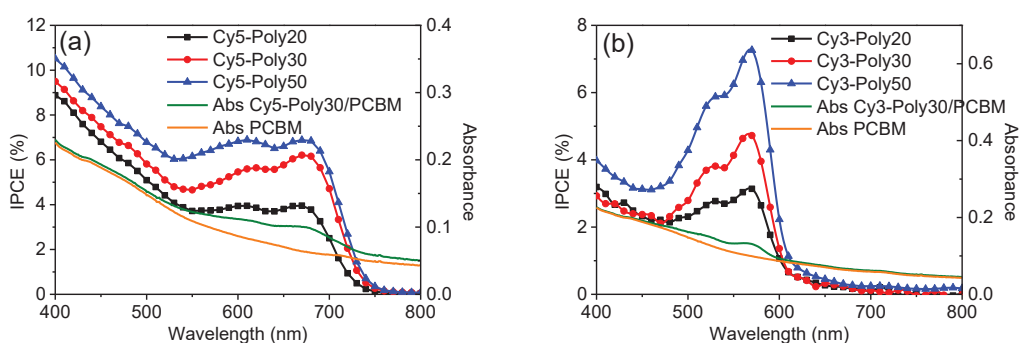


**Figure 6-7:** IPCE and absorption spectra for (a) ITO/MoO<sub>3</sub>/Cy5-Poly/PCBM(40 nm)/Al and (b) ITO/MoO<sub>3</sub>/Cy3-Poly/PCBM(40 nm)/Al solar cells.

In **Figure 6-7a**, we note that between  $\sim 750$  nm and 800 nm the IPCE is very small despite the PCBM absorption spectrum that shows a weak tail in this wavelength region. This spectral feature is discussed in 6.6 Supporting Information.

The S-shape in J-V characteristics for Cy5-Poly50 solar cells could be improved by inserting a Ca layer (8 nm) between the PCBM and Al, yielding an enhancement of FF (**Table 6-2**). Further, Cy5-Poly containing 50% cyanines and different content of PEG segments (Cy5-Poly50, Cy5-PEG25Poly50 and Cy5-PEG50Poly50) were employed as active layer materials and the solar cells ITO/MoO<sub>3</sub>/Cy5-Poly ( $\sim 5$ -15 nm)/PCBM (40 nm)/Ca (8 nm)/Al were fabricated (**Figure 6-8**).

**Table 6-2:** Device performance of ITO/MoO<sub>3</sub>/Cy5-Poly/PCBM(40 nm)/Ca (8 nm)/Al solar cells.

Active layer material	Thickness (nm)	V <sub>oc</sub> (V)	J <sub>sc</sub> (mA cm <sup>-2</sup> )	FF (%)	PCE (%)
Cy5-Poly50	$\sim 5$	0.74-0.82	2.4-2.9	57-62	1.1-1.4
Cy5-PEG25Poly50	$\sim 5$	0.71-0.76	2.7-3.3	61-68	1.2-1.6
Cy5-PEG50Poly50	$\sim 5$	0.55-0.65	2.6-3.0	70-75	1.1-1.4
Cy5-PEG50Poly50	$\sim 10$	0.57-0.66	2.7-3.2	63-69	1.1-1.4
Cy5-PEG50Poly50	$\sim 15$	0.76-0.81	2.7-3.0	47-54	1.1-1.2

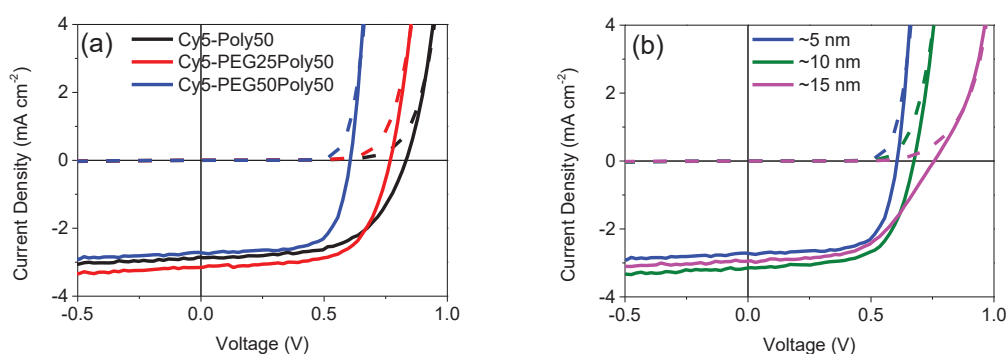


**Figure 6-8:** White light (solid lines) and dark (dotted lines) J-V characteristics of (a) ITO/MoO<sub>3</sub>/Cy5-Poly( $\sim 5$  nm)/PCBM(40 nm)/Ca (8 nm)/Al and (b) ITO/MoO<sub>3</sub>/Cy5-PEG50Poly50( $\sim 5$ -15 nm)/PCBM(40 nm)/Ca(8 nm)/Al solar cells.

Clearly, the insertion of Ca layer improved the device performance by increasing FF, thereby resulting in a higher PCE of  $> 1\%$ . However, as can be seen in **Figure 6-8b** and **Table 6-2**, FF

dropped from 75% to ~50% with increasing Cy5-PEG50Poly50 film thickness, similar as observed for Cy5-Poly50 solar cells (**Figure 6-5**). The higher  $V_{oc}$  obtained in Cy5-PEG50Poly50 solar cells with thicker Cy-Poly layer compensated the drop in FF, consequently leading to a relatively unchanged PCE of ~1.2%.

### 6.3.3 Hole mobility measurement

Hole mobility values of ITO/MoO<sub>3</sub>/Cy5-Poly(15 nm)/PCBM(40 nm)/Al solar cells were measured using the photo-CELIV technique (**Figure 6-9**). Initially, a light pulse is applied to the cell ( $t < 0 \mu\text{s}$ ). The charge carriers created are forced to recombine in the device by adjusting an offset bias to compensate the  $V_{oc}$  of the solar cell. Under these flat-band conditions, no charges are extracted and the measured current density is negligibly small. At  $t = 0 \mu\text{s}$ , the remaining charges are extracted by a linearly increasing voltage ramp  $A$ . In principle, the ionic charge carriers present in cyanine dyes can also be displaced when an external electrical field is applied.<sup>12,13</sup> This is unlikely here, however, because the small anions are chemically fixed into a polymer and ionic mobility could only be caused by displacement of the bulky cyanine cations. We indeed found no evidence for ionic mobility that influences CELIV results (see 6.6 Supporting Information).

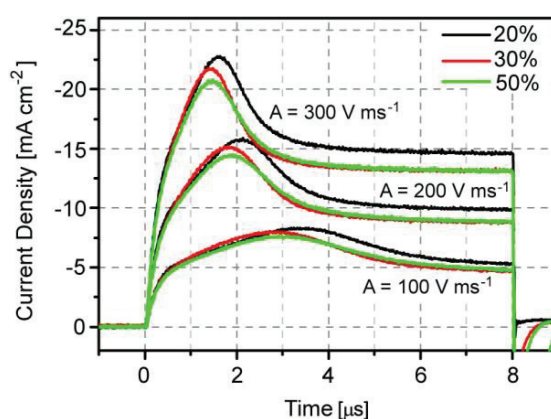


**Figure 6-9:** Photo-current transients of Cy5-Poly/PCBM solar cells for different contents and voltage ramps.

The current transients in **Figure 6-9** for  $t > 0 \mu\text{s}$  are characterized by a capacitance induced displacement current  $j_0$  to which an extraction current with peak height  $\Delta j$  at time  $t_{max}$  is

superimposed. The current offset due to  $j_0$  is proportional to  $A$  and the current peak shifts to shorter times with higher voltage ramps.<sup>25</sup>

Hole mobility was calculated using **Eq. 6-1** with values for  $A$ ,  $t_{\max}$  and  $\Delta j$  from **Figure 6-9**. We found a small ( $\sim 30\%$ ) increase of  $\mu_{h,\text{Cy5-Poly}}$  with increasing voltage slope, indicative of an electric field dependence of the mobility.<sup>21</sup> Average mobility values for Cy5-Poly are shown in **Table 6-3**. These mobility values almost matched the individual mobility values when using a voltage ramp of  $200 \text{ V ms}^{-1}$ .

**Table 6-3:** Average mobility values for Cy5-Poly.

Active material	Mobility ( $\text{cm}^2 \text{V}^{-1} \text{s}^{-1}$ )
Cy5-Poly20	$(4.6 \pm 0.6) \cdot 10^{-6}$
Cy5-Poly30	$(5.4 \pm 0.5) \cdot 10^{-6}$
Cy5-Poly50	$(5.1 \pm 0.7) \cdot 10^{-6}$

Usually, photo-CELIV measurements cannot identify the sign of the carrier detected in the current transient. If both charge carriers are mobile and their mobility is significantly different, two extraction peaks may be measured.<sup>26</sup> In our case, only one peak was detected corresponding to charges with mobility values of  $\sim 5 \cdot 10^{-6} \text{ cm}^2 \text{V}^{-1} \text{s}^{-1}$ .

We assign this value to the hole mobility in the polyelectrolytes layers since the electron mobility in PCBM is known to be much higher. For polymer/PCBM blends, electron mobility values measured with photo-CELIV were in the range of  $(1-9) \cdot 10^{-4} \text{ cm}^2 \text{V}^{-1} \text{s}^{-1}$ .<sup>21,25-27</sup> For pure PCBM films, the electron mobility is  $> 10^{-3} \text{ cm}^2 \text{V}^{-1} \text{s}^{-1}$ .<sup>28</sup> For such high mobility values and thin films as used in our bilayer solar cells, the extraction peak is expected to be at  $t_{\max} < 0.5 \mu\text{s}$ . This short extraction time is comparable to the RC time of our setup ( $\sim 0.15 \mu\text{s}$ ) and cannot be resolved as a single peak.

The low hole mobility values and the large mobility mismatch ( $> 100$ ) between the hole and electron mobility explain the observed J-V trends using different donor layer thicknesses (**Figure 6-5**). The mobility lifetime product  $\mu \cdot \tau$  will determine the average distance charges can travel before recombination.<sup>27</sup> Therefore, holes with a low mobility value will not be efficiently extracted through thicker polyelectrolyte layers, resulting in reduced photocurrents.

In addition, the S-shaped J-V characteristic for thicker donor films (**Figure 6-5**) is probably caused by the strong imbalance between the mobility values for holes and electrons. For planar bilayer organic solar cells, it has been shown that for a mobility mismatch factor larger than  $\sim 100$ , the S-kink and lowering of FF is caused by the active material itself and is not due to a barrier at the contacts.<sup>29</sup> The S-kink is predicted to get more pronounced with increasing layer thickness of the low mobility material, in agreement with J-V curves shown in **Figure 6-5**. We finally confirmed these results for Cy5-PEG50Poly50 cells where a Ca layer was inserted between PCBM and Al. For a thin ( $\sim 5$  nm) polyelectrolyte layer, FF was 75% indicating Ohmic contacts for hole and electron extraction (**Table 6-2**). When increasing the polyelectrolyte thickness to  $\sim 15$  nm, FF decreased to  $\sim 50\%$ . This confirms that the observed S-shape trends are caused by the charge transport properties of the active materials and not by a barrier at the interface to the electrodes.

## 6.4 Conclusions

In this chapter, we investigated the solubility and morphology of Cy-Poly thin films and confirmed that the considerably reduced solubility of Cy-Poly in CB allowed for the fabrication of bilayer solution-processed organic heterojunction solar cells. Device optimization regarding the thickness of PCBM and Cy-Poly was discussed. Results suggested that an ultrathin layer ( $\sim 5$  nm) of polyelectrolytes with the highest cyanine loading (50%) and 40 nm PCBM layer yielded the best performing solar cells. Furthermore, higher FF up to 75% could be achieved by inserting a Ca layer between PCBM and Al, resulting in a higher PCE up to 1.6%. Finally, photo-CELIV technique was applied to identify the low hole mobility in polyelectrolyte layer as the main reason that currently limit solar cell performance.

## 6.5 References

- [1] U. Scherf, counterion pinning in conjugated polyelectrolytes for applications in organic electronics, *Angew. Chem. Int. Ed.* **2011**, 50, 5016-5017.
- [2] A. Elschner, S. Kirchmeyer, W. Lövenich, U. Merker, K. Reuter, *PEDOT, principles and applications of an intrinsically conductive polymer*, CRC Press, Boca Raton, 2011.
- [3] Z. He, C. Zhong, S. Su, M. Xu, H. Wu, Y. Cao, enhanced power-conversion efficiency in polymer solar cells using an inverted device structure, *Nat. Phot.* **2012**, 6, 591-595.

- [4] Y. Zhou, C. Fuentes-Hernandez, J. Shim, J. Meyer, A. J. Giordano, H. Li, P. Winget, T. Papadopoulos, H. Cheun, J. Kim, M. Fenoll, A. Dindar, W. Haske, E. Najafabadi, T. M. Khan, H. Sojoudi, S. Barlow, S. Graham, J. Brédas, S. R. Marder, A. Kahn, B. Kippelen, a universal method to produce low-work function electrodes for organic electronics, *Science*, **2012**, 336, 327-332.
- [5] J. H. Seo, A. Gutacker, B. Walker, S. Cho, A. Garcia, R. Yang, T. Nguyen, A. J. Heeger, G. C. Bazan, improved injection in n-type organic transistors with conjugated polyelectrolytes, *J. Am. Chem. Soc.* **2009**, 131, 18220-18221.
- [6] H. J. Bolink, H. Brine, E. Coronado, M. Sessolo, ionically assisted charge injection in hybrid organic-inorganic light-emitting diodes, *ACS Appl. Mater. Interfaces* **2010**, 2, 2694-2698.
- [7] S. Oh, S. Na, J. Jo, B. Lim, D. Vak, D. Kim, water-soluble polyfluorenes as an interfacial layer leading to cathode-independent high performance of organic solar cells, *Adv. Funct. Mater.* **2010**, 20, 1977-1983.
- [8] J. H. Seo, A. Gutacker, Y. Sun, H. Wu, F. Huang, Y. Cao, U. Scherf, A. J. Heeger, G. C. Bazan, improved high-efficiency organic solar cells via incorporation of a conjugated polyelectrolyte interlayer, *J. Am. Chem. Soc.* **2011**, 133, 8416-8419.
- [9] L. Edman, B. Liu, M. Vehse, J. Swensen, G. C. Bazan, A. J. Heeger, single-component light-emitting electrochemical cell fabricated from cationic polyfluorene: effect of film morphology on device performance, *J. Appl. Phys.* **2005**, 98, 044502.
- [10] S. Kim, J. Jackiw, E. Robinson, K. S. Schanze, J. R. Reynolds, water soluble photo- and electroluminescent alkoxy-sulfonated poly(p-phenylenes) synthesized via palladium catalysis, *Macromolecules* **1998**, 31, 964-974.
- [11] C. V. Hoven, H. Wang, M. Elbing, L. Garner, D. Winkelhaus, G. C. Bazan, chemically fixed p-n heterojunctions for polymer electronics by means of covalent B-F bond formation, *Nat. Mater.* **2010**, 9, 249-252.
- [12] H. Benmansour, F. A. Castro, M. Nagel, J. Heier, R. Hany, F. Nüesch, ionic space charge driven organic photovoltaic devices, *Chimia* **2007**, 61, 787-791.
- [13] M. Lenes, H. J. Bolink, ionic space-charge effects in solid state organic photovoltaics, *ACS Appl. Mater. Interfaces* **2010**, 2, 3664-3668.
- [14] H. Zhang, G. Wicht, C. Gretener, M. Nagel, F. Nüesch, Y. Romanyuk, J. Tisserant, R. Hany, semitransparent organic photovoltaics using a near-infrared absorbing cyanine dye, *Sol. Energy Mater. Sol. Cells* **2013**, 118, 157-164.



- [15] R. Hany, B. Fan, F. A. Castro, J. Heier, W. Kylberg, F. Nüesch, strategies to improve cyanine dye multi layer organic solar cells, *Prog. Photovolt: Res. Appl.* **2011**, 19, 851-857.
- [16] G. Wicht, S. Bücheler, M. Dietrich, T. Jäger, F. Nüesch, T. Offermans, J. Tisserant, L. Wang, H. Zhang, R. Hany, stability of bilayer trimethine cyanine dye/fullerene organic solar cells, *Sol. Energy Mater. Sol. Cells* **2013**, 117, 585-591.
- [17] O. Malinkiewicz, T. Grancha, A. Molina-Ontoria, A. Soriano, H. Brine, H. J. Bolink, efficient, cyanine dye based bilayer solar cells, *Adv. Energy Mater.* **2013**, 3, 472-477.
- [18] E. Berner, T. Jäger, T. Lanz, F. Nüesch, J. Tisserant, G. Wicht, H. Zhang, R. Hany, influence of crystalline titanium oxide layer smoothness on the performance of inverted organic bilayer solar cells, *Appl. Phys. Lett.* **2013**, 102, 183903.
- [19] O. Malinkiewicz, M. Lenes, H. Brine, H. J. Bolink, meniscus coated high open-circuit voltage bi-layer solar cells, *RSC Adv.* **2012**, 2, 3335-3339.
- [20] T. Geiger, H. Benmansour, B. Fan, R. Hany, F. Nüesch, low-band gap polymeric cyanine dyes absorbing in the NIR region, *Macromol. Rapid. Commun.* **2008**, 29, 651-658.
- [21] A. J. Mozer, N. S. Sariciftci, L. Lutsen, D. Vanderzande, R. Österbacka, M. Westerling, G. Juška, charge transport and recombination in bulk heterojunction solar cells studied by the photoinduced charge extraction in linearly increasing voltage technique, *Appl. Phys. Lett.* **2005**, 86, 112104.
- [22] W. Ma, C. Yang, X. Gong, K. Lee, A. J. Heeger, thermally stable, efficient polymer solar cells with nanoscale control of the interpenetrating network morphology, *Adv. Funct. Mater.* **2005**, 15, 1617-1622.
- [23] R. Steim, F. R. Kogler, C. J. Brabec, interface materials for organic solar cells, *J. Mater. Chem.* **2010**, 20, 2499-2512.
- [24] P. Peumans, A. Yakimov, S. R. Forrest, small molecular weight organic thin-film photodetectors and solar cells, *J. Appl. Phys.* **2003**, 93, 3693-3723.
- [25] M. T. Neukom, N. A. Reinke, B. Ruhstaller, charge extraction with linearly increasing voltage: a numerical model for parameter extraction, *Solar Energy* **2011**, 85, 1250-1256.
- [26] B. Tremolet de Villers, C. J. Tassone, S. H. Tolbert, B. J. Schwartz, improving the reproducibility of P3HT:PCBM solar cells by controlling the PCBM/cathode interface, *J. Phys. Chem. C* **2009**, 113, 18978-18982.

[27] A. Pivrikas, N. S. Sariciftci, G. Juška, R. Österbacka, a review of charge transport and recombination in polymer/fullerene organic solar cells, *Prog. Photovolt. Res. Appl.* **2007**, 15, 677-696.

[28] C. Waldauf, P. Schilinsky, M. Perisutti, J. Hauch, C. J. Brabec, solution-processed organic n-type thin-film transistors, *Adv. Mater.* **2003**, 15, 2084-2088.

[29] W. Tress, A. Petrich, M. Hummert, M. Hein, K. Leo, M. Riede, imbalanced mobilities causing S-shaped IV curves in planar heterojunction organic solar cells, *Appl. Phys. Lett.* **2011**, 98, 063301.

## 6.6 Supporting Information

### 6.6.1 Absorption spectra and IPCE in the near-infrared wavelength region

The absorption spectra shown in **Figure 6-7a** are meant to show the individual contributions from the cyanine and PCBM to the photocurrent. These spectra were measured on a commercial UV-Vis spectrophotometer and are, therefore, influenced by light scattering. Light scattering causes an apparent absorbance because less light reaches the detector. To capture scattered light, we have measured the PCBM absorption using an integrating sphere<sup>S1</sup>. A comparison (**Figure 6-10**) shows that there is indeed considerable light scattering from a PCBM film. For Cy5-Poly50/PCBM solar cells (**Figure 6-7a**) the IPCE trend at higher wavelengths agrees with the absorption spectrum of Cy5-Poly50 and drops off at ~750 nm. The remaining absorbance between ~750 and 800 nm is due to PCBM. PCBM films show a weak tail in their absorption spectra extending as far as 1000 nm<sup>S2,S3</sup>. The HOMO-LUMO gap of PCBM is at around 1.8 eV (~700 nm). A literature survey confirms that the generated photocurrent is negligibly small after excitation of PCBM with wavelengths energies below the bandgap<sup>S4,S5</sup>.

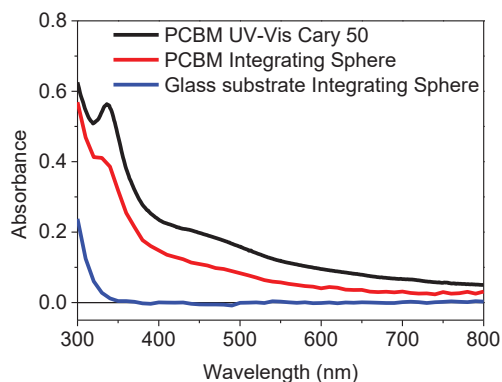


**Figure 6-10:** Absorption spectra of a ~40 nm thick PCBM film on glass measured on a UV-Vis Cary 50 spectrometer or using an integrating sphere. We demonstrate the accuracy of the baseline in the integrating sphere in wavelength regions without absorption with the spectrum of an uncoated glass substrate.

### 6.6.2 Electronic and ionic charges in cyanine dyes

Cyanine dyes are charged cationic molecules that are accompanied by a counter anion. It has been demonstrated that small anions (such as  $\text{Cl}^-$ ,  $\text{PF}_6^-$  or  $\text{ClO}_4^-$ ) are relatively mobile and are displaced within the cyanine layer and into adjacent layers, either by diffusion due to concentration gradients or by internal or applied external electrical fields. The build-up of ionic space charge creates electric fields and induces potential energy shifts at junctions similar to conventional p-n junctions. These processes can have a distinct influence on the mode of operation of cyanine organic solar cells, resulting in time-dependent current-voltage and spectral response characteristics<sup>S6,S7</sup>.

In this work we find no evidence for ionic mobility that influences solar cell performance and CELIV results. In contrast to Ref. [S6,S7], the anions are here chemically fixed into a polymer and ionic mobility could only be caused by displacement of the bulky cyanine cations. In addition, bias voltages of typically a few volts over a time of several minutes were necessary to detect the influence of small migrating cyanine counter anions. We note that these are also typical operating conditions and turn-on times for light-emitting electrochemical cells whose function rely on the separation of ionic charges<sup>S8</sup>.

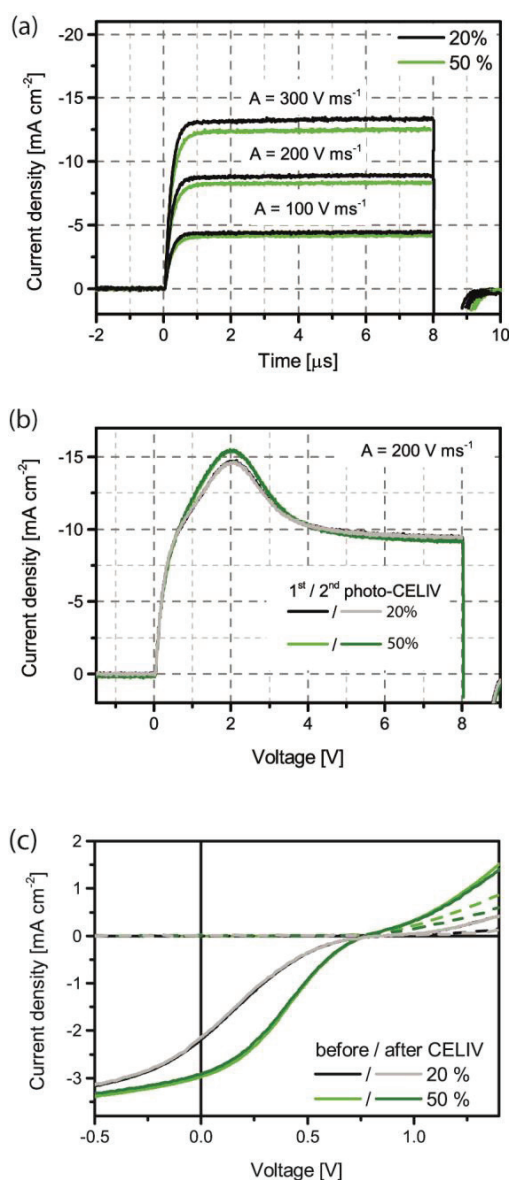


**Figure 6-11:** (a) Dark-CELIV transients of Cy5-Poly/PCBM solar cells for different cyanine contents and voltage ramps. (b) Photo-CELIV transients taken before and after a measurement cycle. (c) J-V characteristics measured before and directly (less than 1 minute) after the CELIV experiments. Both measurements could be carried out on the commercial Paios system (Fluxim AG) without changing the electrical wiring.

Dark-CELIV transients of Cy5-Poly/PCBM solar cells are shown in **Figure 6-11a**. For these conditions no current overshoot is observed which confirms that the extraction current during photo-CELIV (**Figure 6-9**) is due to photo-generated charge carriers. The voltage ramp is applied during  $8 \mu\text{s}$  only, and substantial ionic displacement during that period that influences the photo-CELIV results can be excluded. We verified this by repeatedly measuring

the same cell and found stable current transients (**Figure 6-11b**). Also J-V characteristics recorded before and after the CELIV measurement cycle were identical (**Figure 6-11c**) and showed no indication of mobile ionic charge.

We finally verified that also the J-V characteristics under white light illumination are not influenced by mobile cyanine cations. **Figure 6-12** shows unchanged J-V curves for a cell biased consecutively at +0.5 V, -0.5 V, +1 V and -1 V, for 10 min in each case. J-V curves did not change and  $V_{oc} = 0.71 - 0.72$  V,  $J_{sc} = 2.21 - 2.24$  mA cm<sup>-2</sup> and FF = 58 -59% were measured.

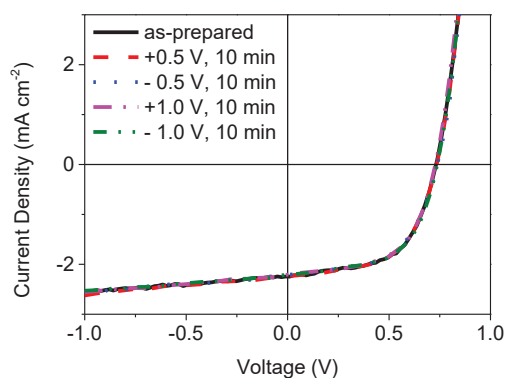


**Figure 6-12:** J-V characteristics of ITO/MoO<sub>3</sub>/Cy5-Poly50/PCBM/Ca/Al solar cells as a function of bias voltage.

[S1] J. C. de Mello, H. F. Wittmann, R. H. Friend, an improved experimental determination of external photoluminescence quantum efficiency, *Adv. Mater.* **1997**, 9, 230-232.

[S2] S. Cook, R. Katoh, A. Furube, ultrafast studies of charge generation in PCBM:P3HT blend films following excitation of the fullerene PCBM, *J. Phys. Chem. C* **2009**, 113, 2547-2552.

[S3] S. Cook, H. Ohkita, Y. Kim, J. J. Benson-Smith, D. D. C. Bradley, J. R. Durrant, a photophysical study of PCBM thin films, *Chem. Phys. Lett.* **2007**, 445, 276-280.

[S4] S. E. Shaheen, C. J. Brabec, N. S. Sariciftci, F. Padinger, T. Fromherz, J. C. Hummelen, 2.5% efficient organic plastic solar cells, *Appl. Phys. Lett.* **2001**, 78, 841-843.

[S5] Y. Kim, S. Cook, S. M. Tuladhar, S. A. Choulis, J. Nelson, J. R. Durrant, D. D. C. Bradley, M. Giles, I. McCulloch, C. Ha, M. Ree, a strong regioregularity effect in self-organizing conjugated polymer films and high-efficiency polythiophene:fullerene solar cells, *Nature Mater.* **2006**, 5, 197-203.

[S6] H. Benmansour, F. A. Castro, M. Nagel, J. Heier, R. Hany, F. Nüesch, ionic space charge driven organic photovoltaic devices, *Chimia* **2007**, 61, 787-791.

[S7] M. Lenes, H. J. Bolink, ionic space-charge effects in solid state organic photovoltaics, *ACS Appl. Mater. Interfaces* **2010**, 2, 3664-3668.

[S8] M. Lenes, G. Garcia-Belmonte, D. Tordera, A. Pertegás, J. Bisquert, H. J. Bolink, operating modes of sandwiched light-emitting electrochemical cells, *Adv. Funct. Mater.* **2011**, 21, 1581-1586.

## Chapter 7: Conclusions and Outlook

### 7.1 Conclusions

Different strategies to alter the cyanine counterions during chemical synthesis were presented and the potential applications of the synthesized cyanines with novel counter anions as active components in organic electronic devices were investigated.

Cyanine polyelectrolytes (Cy-Poly) consisting of an anionic methacrylate backbone and cationic cyanine dye chromophores in the pendant groups were successfully synthesized. The synthetic approach involved the copolymerization of (methyl)methacrylate monomer units containing sulfonic acids or poly(ethylene glycol) (PEG) segments in a different ratio, followed by deprotonation of the sulfonic acids and a salt metathesis reaction to incorporate the dye with elimination of silver halides as side products. Cy-Poly exhibited a considerably reduced solubility in non-polar organic solvents, e.g. chlorobenzene, which made the deposition via solution casting of another film on top of the polyelectrolyte layer possible. The bilayer solution-processed Cy-Poly/PCBM solar cells were fabricated, which possessed a high fill factor (FF) up to 75% and power conversion efficiency (PCE) up to 1.6%. Finally, it was found that the proposed synthetic approach via salt metathesis to incorporate cationic cyanine dyes is quite versatile. Apart from the achieved trimethine (Cy3) and pentamethine (Cy5) polyelectrolytes, other cationic dyes such as heptamethine (Cy7) cyanines or different dye cations could be incorporated into the same anionic backbone.

4-azido (tetrafluoro)benzoate anions were introduced as immobilizable counterions for Cy3, Cy5 and Cy7 dyes during chemical synthesis. For the fluorinated counter anions, we observed a pronounced decarboxylation process of the benzoate groups which occurred during storage of the dyes as solid compounds at 4 °C or as thin films at room temperature. No decarboxylation reaction was detected for non-fluorinated benzoate anions, suggesting that 4-azido benzoate was thermally more stable. Remarkable exciton quenching behavior was observed if the azide anions were stabilized in the films. This resulted from the fact that phenyl nitrenes generated upon UV light exposure reacted with the cyanine dye chromophores, leading to the formation of efficient exciton quenchers. The light-induced exciton quenching effect in the films was already observed during device fabrication, which

was attributed to the sensitized photolysis of phenyl azides enabled by a triplet-triplet energy transfer from the visible light absorbed Cy3 dyes. It could be shown that the undesired triplet-triplet sensitization can be inhibited if cyanine dyes with lower triplet energy are used. This is the case for Cy5 and Cy7. However, the unspecific reactivity of phenyl nitrenes formed upon UV irradiation of the azido-benzoates still presents a major problem. One idea to avoid detrimental reactions with the chromophore would be to provide preferential reaction sites. Unfortunately, our attempts to add PEG chains to the cyanine films were unsuccessful. Other strategies would therefore be required.

Ion exchange reactions were performed for different cyanine dyes, generating Cy3 and monomethine (Cy1) dyes with hexafluorophosphate ( $\text{PF}_6^-$ ) as counter anions and the potential applications of these dyes in host-guest light-emitting electrochemical cells (LECs) were explored. A largely enhanced photoluminescence (PL) was observed in a binary cyanine blend film containing a Cy1 dye as matrix material and a Cy3 dye as emitter, demonstrating that extensive self-quenching effect was prevented.

LECs using commercially available cyanine dyes as the single active component were demonstrated. A method based on the combination of electroluminescence (EL) and PL, incident photon-to-current conversion efficiency (IPCE) measurements and optical modelling was proposed to study the evolution of p-i-n junction and electrochemical doping process during device operation under a constant voltage. Photovoltaic effect of the cyanine dye LECs after bias was investigated and the optimization was carried out by varying the thickness of active layer. Results suggested that LECs with a ~90 nm cyanine layer after bias to the maximum current yielded the optimal photovoltaic performance upon white light illumination.

The mechanism of photocurrent generation in Cy5 films was studied. Single layer devices containing Cy5 with  $\text{PF}_6^-$  as counterions (Cy5-PF6) exhibited a linear current-voltage (J-V) characteristics under white light illumination. The linearity of the J-V curves did not vary by employing different electrode buffer layers in the devices, which indicated that the photo-induced charge carriers were generated in the bulk Cy5-PF6 films. Photoconductivity values in such cyanine films were successfully extracted from the slope of J-V characteristics and the photocurrent generation was proposed to be partially due to the structural inhomogeneity in a highly aggregated film. The electric field induced exciton quenching was confirmed to be only a minor contribution to photocurrent. This study showed that important



photogeneration of charge carriers is occurring in certain cyanine films. While this effect will create losses in the fill factor of photovoltaic devices, it could be interesting in photodiodes working under reversed bias. Photocurrent could thus be generated without the need of an electron acceptor.

## 7.2 Outlook

The present thesis could develop a few solid concepts towards the goal of permanent ionic space charge distributions in thin organic semiconducting films. Unfortunately, the nonspecific reactivity of azides always leads to the formation of exciton quenching sites due to the reaction with the cyanine chromophore. If this approach shall be used in the future, free volume sites with specific reaction targets for such anions have to be present in the film. This could perhaps be engineered by suitable chemical functionalization of the dye molecules or by a blend approach.

Generally, to achieve a chemically fixed ionic junction in cyanine based organic electronic devices, chemical reactions that do not degrade the semiconducting properties of cyanines are required. This implies that fixation of anions should not occur at the  $\pi$ -electron conjugated polymethine chains. A system containing cyanine dyes with polymerizable anions, crosslinkable ionic conductors and photoinitiators could be promising. After biasing, UV light exposure would induce crosslinking reaction between the polymerizable anions and the ionic conductors, yielding a bulky and immobile anionic polymer network. The stabilization of the ionic carriers with desired distribution would thus be achieved.

Dye-polymer electrolytes proved to yield smooth films that allow for subsequent coating of further layers using orthogonal solvents. In particular, the layers showed to be refractory against poling, meaning that the ions constituting the polyelectrolyte have a very low mobility. Additionally, copolymerization with ion conducting moieties was shown to be feasible thus allowing for foreign ions to travel into the polyelectrolyte. This system could therefore be exploited in to study ion motion across an interface and if reactive ions were chosen, a permanent fixation of space charge could be foreseen.

So far, ion mobility in cyanine films was shown to be directly related to the size of the counterions. In ionically conductive devices, it may be interesting to increase ion mobility, e.g. for faster switch-on times in light-emitting electrochemical devices. The way to such new

functionalities in cyanine dyes can also be performed via chemical modification on the dye chromophores during synthesis. This can be achieved by functionalizing the indole precursors in advance with interesting organic groups that are linked to the aromatic rings or the nitrogen atom. Besides, the chloro-substituent on the polymethine chain of heptamethine cyanine dyes provides also possibilities to modify the dye with different functional groups via nucleophilic substitution reactions. In order to promote ionic mobility in these semiconducting salts, incorporation of ethylene glycol moieties would be of particular interest.

Finally, the efficiency of LECs ultimately depends on the light-emission efficiency of the emitting layer. Further investigation of cyanine dye host-guest LECs could be carried out to improve the quantum efficiency of the electroluminescent devices. This involves the chemical synthesis of new cyanine dyes with different bandgaps and the exploration of the best host-guest system employing the most compatible and appropriate matrix and emitter materials. If the self-quenching behavior of the emitting dyes is significantly reduced or disappears, external quantum efficiency (EQE) of the devices that approaches the theoretical maximum could be expected.

## Abbreviations and Symbols

A	simulated absorbance
ACN	acetonitrile
AFM	atomic force microscopy
Ag	silver
AgCl	silver chloride
AgI	silver iodide
AgNO <sub>3</sub>	silver nitrate
AgNWs	silver nanowires
Ag <sub>2</sub> O	silver(I) oxide
AIBN	2,2'-azobis(2-methylpropionitrile)
Al	aluminum
Alq <sub>3</sub>	tris-(8-hydroxyquinoline)aluminum
ATR-IR	attenuated total reflection infrared
BABP	4,4'-bis(azidomethyl)-1,1'-biphenyl
BCP	bathocuproine
BHJ	bulk heterojunction
bis(PFBA)	bis(perfluorophenyl) azide
c	speed of light in vacuum
C <sub>60</sub>	fullerene
Ca	calcium
CB	chlorobenzene
CHCl <sub>3</sub>	chloroform
Cl <sup>-</sup>	chloride anion
ClO <sub>4</sub> <sup>-</sup>	perchlorate anion
CPEs	conjugated polyelectrolytes
CV	cyclic voltammetry

Cy1	monomethine cyanine
Cy3	trimethine cyanine
Cy5	pentamethine cyanine
Cy7	heptamethine cyanine
Cy-Cl	cyanine dye with chloride anion
Cy-FN3	cyanine dye with 4-azido-2,3,5,6-tetrafluorobenzoate anion
Cy-I	cyanine dye with iodide anion
Cy-MES	cyanine dye with 2-sulfoethyl methacrylate anion
Cy-N3	cyanine dye with 4-azido benzoate anion
Cy-NO3	cyanine dye with nitrate anion
Cy-PF6	cyanine dye with hexafluorophosphate anion
Cy-Poly	cyanine polyelectrolytes, Cyaninpolyelektrolyten
Cy-T	cyanine dye with $\Delta$ -TRISPHAT anion
<i>d</i>	layer thickness
DAZH	1,6-diazidohexane
DCM	dichloromethane
DMF	dimethylformamide
DMSO	dimethyl sulfoxide
DQF-COSY	double quantum filtered homonuclear correlation spectroscopy
DSC	differential scanning calorimetry
<i>e</i>	elementary charge
$E_{1/2}$	half-wave potential
$E_{1/2,red}$	first half-wave reduction potential
$E_{pa}$	anodic peak potential
$E_{pc}$	cathodic peak potential
EDLs	electric double layers
EDMA	ethylene glycol dimethacrylate
EGaIn	eutectic gallium-indium

EL	electroluminescence
EPR	electron paramagnetic resonance
EQE	external quantum efficiency
ESI-MS	electrospray ionization mass spectroscopy
EtOH	ethanol
Fc/Fc <sup>+</sup>	ferrocene/ferrocenium
FDTD	finite difference time domain
FF	fill factor, Füllfaktor
gHMBC	gradient selected heteronuclear multiple bond coherence
gHSQC	gradient selected heteronuclear single quantum coherence
GPC	gel permeation chromatography
<i>h</i>	Planck's constant
HCl	hydrochloric acid
HMBC	heteronuclear multiple bond coherence
H-MES	2-sulfoethyl methacrylate
HOMO	highest occupied molecular orbital
HSQC	heteronuclear single quantum coherence
IPCE	incident photon-to-current conversion efficiency
IQE	internal quantum efficiency
ISC	intersystem crossing
iTMCs	ionic transition metal complexes
ITO	indium tin oxide
<i>j</i> <sub>0</sub>	capacitive displacement current
<i>J</i> <sub>max</sub>	current density at maximum power output
<i>J</i> <sub>sc</sub>	short circuit current density
<i>J</i> - <i>V</i>	current density-voltage
<i>k</i>	extinction coefficient
LED	light-emitting diode

LEC	light-emitting electrochemical cell
LECs	light-emitting electrochemical cells
LEZ	lichtemittierende elektrochemische Zellen
Li <sup>+</sup>	lithium cation
LiCF <sub>3</sub> SO <sub>3</sub>	lithium trifluoromethanesulfonate
LUMO	lowest unoccupied molecular orbital
MeOH	methanol
MePc	metal phthalocyanine
MMA	methyl methacrylate
$M_n$	number average molecular weights
MoO <sub>3</sub>	molybdenum (VI) oxide
n	refractive index, charge carrier density
N <sub>2</sub>	nitrogen gas
Na-FN3	sodium with 4-azido-2,3,5,6-tetrafluorobenzoate anion
NaHCO <sub>3</sub>	sodium bicarbonate
Na-N3	sodium with 4-azido benzoate anion
NaN <sub>3</sub>	sodium azide
NaOH	sodium hydroxide
NaPF <sub>6</sub>	sodium hexafluorophosphate
Na <sub>2</sub> SO <sub>4</sub>	sodium sulfate
NIR	near infrared
NMR	nuclear magnetic resonance
$N_{\text{phot}}$	flux density of absorbed photons
OFET	organic field-effect transistor
OFETs	organic field-effect transistors
OLED	organic light-emitting diode
OLEDs	organic light-emitting diodes
OPV	organic photovoltaic

OSC	organic solar cell
OSCs	organic solar cells
PAL	photoaffinity labelling
PANI	polyaniline
PCBM	[6,6]-phenyl-C <sub>61</sub> -butyric acid methyl ester
PCE	power conversion efficiency
PDMS	polydimethylsiloxane
PEDOT	poly(3,4-ethylenedioxythiophene):poly(styrene sulfonate)
PEG	poly(ethylene glycol), poly(ethyl oxide)
PEGMA	poly(ethylene glycol) methyl ether methacrylate
PF <sub>6</sub> <sup>-</sup>	hexafluorophosphate anion
PFPAs	perfluorophenyl azides
photo-CELIV	photo-induced charge carrier extraction by a linearly increasing voltage
P <sub>in</sub>	incident light power density
PL	photoluminescence
P <sub>max</sub>	maximum power output
PPP	poly(p-phenylene)
PPV	polyphenylene vinylene
PT	polythiophene
Q <sub>PL</sub> (E)	field induced photoluminescence quenching efficiency
rms	root mean square
RT	room temperature
Ru(bpy) <sub>3</sub> <sup>2+</sup>	tris(2,2'-bipyridine)ruthenium(II)
sFPA	sterically hindered fluoro-phenyl-azides
SIMS	secondary ion mass spectrometry
SKPM	scanning Kelvin probe microscopy
TFP	2,2,3,3-tetrafluoro-1-propanol
T <sub>g</sub>	glass transition temperature

## Abbreviations and Symbols

---

TGA	thermogravimetric analysis
THF	tetrahydrofuran
TLC	thin layer chromatography
$t_{\max}$	peak position of the current
TS	triplet sensitizer
UV	ultraviolet
UV-Vis	ultraviolet-visible
$V_{\max}$	voltage at maximum power output
$V_{\text{oc}}$	open circuit voltage
XRF	X-ray fluorescence
$\Delta j$	peak height
$\delta$	chemical shifts in ppm
$\eta_{\text{int}}$	internal electroluminescence quantum efficiency
$\lambda$	wavelength
$\mu$	mobility
$\tau$	lifetime
$\tau_{\text{delay}}$	delay time
$\Phi_{\text{isc}}$	intersystem crossing efficiency
$\sigma$	conductivity
$\gamma_{\text{L}}$	bimolecular recombination coefficient



## Curriculum Vitae

### Personal Information

Name: Lei Wang

Nationality: China

Date of birth: 08<sup>th</sup> February 1988

Place of birth: Beijing, China

Email: leiwang8828@gmail.com

Family status: married with one daughter

Languages: Chinese (native), English (fluent), German (fluent)

Address: Room No. 807, Building No. 3, Ziluoyuan Community, Shifoying East, Chaoyang District, Beijing, China

### Education

2013-2016      Ph.D. in Polymer Photovoltaics, Swiss Federal Institute of Technology Lausanne (EPFL), Switzerland

- PhD project conducted at Swiss Federal Institute for Materials Science and Technology (Empa) and Zurich University of Applied Sciences (ZHAW), funded by Swiss National Science Foundation (SNF)

2010-2012      M.Sc. in Polymer Science, Humboldt University Berlin, Free University Berlin, Technical University Berlin, Potsdam University, Germany

- Master project performed at Helmholtz Zentrum Geesthacht (HZG)

2006-2010      B.Sc. in Materials Science and Engineering, Xiamen University, China

### Conferences & Workshops

Aug. 2016      Poster, International Conference on the Physics of Semiconductors (ICPS 2016), Beijing, China

Jan. 2016      Poster (invited), International Symposium on Functional Materials, Okinawa, Japan

- March 2015      Poster, WinsCool 2015 New Materials from Physics to Applications, Champéry, Switzerland
- Sep. 2014      Poster, Swiss Chemical Society Fall Meeting, Zurich, Switzerland
- Sep. 2014      Poster, Rhin-Solar Summer School on Organic Photovoltaics, Strasbourg, France
- July 2014      Talk, IUPAC World Polymer Congress, Chiangmai, Thailand
- June 2014      Poster, Swiss Chemical Society PolyColl 2014, Duebendorf, Switzerland
- Sep. 2013      Poster, Swiss Chemical Society Fall Meeting, Lausanne, Switzerland

## Publications

G. Wicht, S. Bücheler, M. Dietrich, T. Jäger, F. Nüesch, T. Offermans, J. Tisserant, L. Wang, H. Zhang, R. Hany, Stability of bilayer trimethine cyanine dye/fullerene organic solar cells, *Sol. Energy Mater. Sol. Cells* **2013**, 117, 585-591

L. Wang, C. Hinderling, S. Jenatsch, F. Nüesch, D. Rentsch, R. Steim, H. Zhang, R. Hany, Cyanine dye polyelectrolytes for organic bilayer solar cells, *Polymer*, **2014**, 55, 3195-3201

H. Zhang, B. Niesen, E. Hack, S. Jenatsch, L. Wang, A. C. Véron, M. Makha, R. Schneider, Y. Arroyo, R. Hany, F. Nüesch, Cyanine tandem and triple-junction solar cells, *Organic Electronics* **2016**, 30, 191-199

S. Jenatsch, L. Wang, M. Bulloni, A. C. Véron, B. Ruhstaller, S. Altazin, F. Nüesch, R. Hany, Doping evolution and junction formation in stacked cyanine dye light-emitting electrochemical cells, *ACS Appl. Mater. Interfaces* **2016**, 8, 6554-6562

M. Makha, P. Testa, S. B. Anantharaman, J. Heier, S. Jenatsch, N. Leclaire, J. Tisserant, A. C. Véron, L. Wang, F. Nüesch, R. Hany, Ternary semitransparent organic solar cells with a laminated top electrode, *Sci. Tech. Adv. Mater.* **2016**, DOI: 10.1080/14686996.2016.1261602

L. Wang, S. Jenatsch, B. Ruhstaller, C. Hinderling, D. Gesevicius, R. Hany, F. Nüesch, Photoconductivity in ionic cyanine films, in preparation

L. Wang, C. Hinderling, F. Nüesch, R. Hany, Visible-light induced azide decomposition in trimethine cyanine/azido-benzoate films, in preparation

